UNIVERSITY OF OKLAHOMA

GRADUATE COLLEGE

ANALYTICAL AND NUMERICAL ANALYSES OF WELLBORE DRILLED IN ELASTOPLASTIC POROUS FORMATIONS

A DISSERTATION

SUBMITTED TO THE GRADUATE FACULTY

in partial fulfillment of the requirements for the

Degree of

DOCTOR OF PHILOSOPHY

By

SHENGLI CHEN
Norman, Oklahoma
2012

ANALYTICAL AND NUMERICAL ANALYSES OF WELLBORE DRILLED IN ELASTOPLASTIC POROUS FORMATIONS

A DISSERTATION APPROVED FOR THE
MEWBOURNE SCHOOL OF PETROLEUM & GEOLOGICAL ENGINEERING

BY

_____
Dr. Younane N. Abousleiman, Chair

_____
Dr. Gerald A. Miller

_____
Dr. Subhash N. Shah

_____
Dr. Yucel I. Akkutlu

_____
Dr. Deepak Devegowda

ACKNOWLEDGEMENTS

I wish to express my sincerest and deepest gratitude to Dr. Younane N. Abousleiman, my advisor and committee chair, for his constant inspiration, encouragement, and support during the course of my Ph.D. studies at the University of Oklahoma. It was him who introduced me to the challenging and exciting field of petroleum geomechanics, gave me sound academic guidance, and offered me great freedom and flexibility to pursue my research interests. His enthusiasm for science, keen insight into engineering problems, and strong commitment to academic excellence have profoundly impressed me and have always been my motivations to strive for the best in my future career. It was such a wonderful experience working with him!

I would sincerely thank my other committee members, Dr. Gerald A. Miller, Dr. Subhash N. Shah, Dr. Yucel I. Akkutlu, and Dr. Deepak Devegowda, for reviewing this manuscript and for their advice and support offered me during my graduate studies.

I am also deeply thankful to Dr. Kanthasamy K. Muraleetharan for having been serving on my dissertation committee until only recently when he took the sabbatical leave, and for his support, encouragement, and invaluable advice throughout my research program. Discussion with him on the constitutive modelling especially the bounding surface model is definitely enlightening and very helpful.

Special thanks go to my colleagues and friends, Dr. Vinh Xuan Nguyen, Dr. Son Ky Hoang, Mr. Minh Ha Tran, Mr. Amin Mehrabian, Mr. Chao Liu, and Mr. John L. Brumley for many stimulating discussions and personal exchanges. My special thanks must also go to Ms. Carla L. Cates, the Administration and Operations Manager of the integrated PoroMechanics Institute, who always makes sure everything go extremely smoothly and

makes my stay at iPMI an easy and enjoyable experience.

The research is financially supported by the integrated PoroMechanics Institute Industrial Consortium at the University of Oklahoma and the Oklahoma Center for the Advancement of Science and Technology (Grant No. AR081-045), which are gratefully acknowledged. The kind support, help, and encouragement from the following individuals, Prof. Alexander H. D. Cheng (Unviersity of Mississippi), Prof. Longzhu Chen (Shanghai Jiao Tong University), Ms. Yaping Hu (Shanghai Jiao Tong University), Dr. Chunyu Song (Shanghai Jiao Tong University), Prof. Limin Zhang (Hong Kong University of Science and Technology), Dr. Russell T. Ewy (Chevron Energy Technology Co.), and Prof. Jinying Zhu (University of Texas at Austin), are very much appreciated.

Finally I owe my greatest appreciations to my mom and dad (Ms. Zhaoying Wang and Mr. Yuwen Chen) for their unconditional love and everlasting support. For so many years they have been the source of inspiration and the drive for me to succeed. Heartfelt appreciations also go to my parents-in-law (Ms. Ping Liu and Mr. Fuchun Wu) for their long time understanding and unwavering support, and extend to my three sisters (Ms. Bingru Chen, Ms. Taiyi Chen, and Ms. Jinru Chen) and three brothers-in-law (Mr. Weiming Jiang, Mr. Weiyong Hu, and Mr. Hui Lin) for their continuous support and taking over my responsibility in taking care of our dad during my absence.

This thesis is dedicated to my wife, Shanshan Wu, and our son, Xuancheng (Bobby) Chen. Without their love, understanding, and support, it would not have been possible.

TABLE OF CONTENTS

LIST OF TABLES

LIST OF FIGURES

ABSTRACT

The current wellbore stability analyses for analytical solutions are mostly based on the linear elastic or poroelastic theory. The wellbore is regarded as unstable if the determined elastic/poroelastic stresses anywhere around the wellbore satisfy some failure criteria for the rock formation. Rocks, in general, exhibit nonlinear and plastic (hardening/softening) properties with stiffnesses depending on the stress and strain levels. Ignoring the elastoplastic feature of the rock formations tends to give conservative solutions and thus, a substantial overestimate of the critical mud density necessary for stable wellbores.

When elastoplastic constitutive models are taken into account for the rock formations, the wellbore stability boundary value problem usually can only be solved by numerical techniques such as finite element method, though in the past several attempts were made to obtain approximate analytical solutions based on simplified assumptions. This research is aimed to develop a generic class of rigorous, complete analytical solutions for a cylindrical wellbore drilled in elastoplastic porous formations subject to non-isotropic in situ stresses, under both undrained and drained conditions. To cover a range of rock formations such as sandstones and shlaes, different types of elastoplastic models, including the strain hardening Drucker-Prager and Mohr-Coulomb models as well as the Cam Clay and bounding surface models based on the critical state concept, are considered in this analysis.

The key step in the formulation of the wellbore elastoplastic boundary value problem is to establish an incremental relationship between the effective radial, tangential, and vertical stresses and the corresponding stain components, i.e., the elastoplastic

constitutive equations, and then reduce them to a set of differential equations valid for any material point in the plastic zone. For undrained condition, the three stresses can be directly solved from these governing differential equations as an initial value problem, the excess pore pressure then being determined from the radial equilibrium equation. Whereas for the drained condition, the Eulerian radial equilibrium equation must be first transformed into an equivalent one in Lagrangian description, which can be accomplished with the introduction of a suitably chosen auxiliary variable. This transformed equation, together with the aforementioned elastoplastic constitutive relation, again constitute a set of coupled differential equations. The three stress components and the volumetric strain or specific volume thus can be readily solved.

Parametric studies show clearly that the overconsolidation ratio of shale-like formations or soft rocks (the ratio of the maximum stress experienced to the current stress level) has significant influences on the stress and pore pressure distributions as well as on the development and progress of the plastic and failure zones around the wellbore. The computed stress distributions and in particular the stress paths capture well the anticipated elastoplastic failure behaviour of the rocks surrounding the wellbore. The solutions thus are able to contribute to better prediction and design of the wellbore instability problems.

Numerical simulations are also conducted for the drained wellbore problem with the use of ABAQUS, the finite element analysis commercial program. Of importance, a user defined material subroutine (UMAT) for the bounding surface model is developed with FORTRAN following the return mapping algorithm and implemented into the ABAQUS finite element models. The predictions from the analytical solutions and the ABAQUS

analyses are generally in excellent agreement for both modified Cam Clay and bounding surface models.

CHAPTER 1
INTRODUCTION

1.1 Overview

Maintenance of wellbore stability is of fundamental importance during drilling and remains a major concern to drilling engineers in the oil and gas industry. Wellbore instability may cause a stuck pipe due to large borehole deformation or even worse the breakout and hole closure as a result of compressive and shear rock failure (Dusseault, 1994). It is estimated that wellbore instability causes an annual economic loss of US$ 8 billion in the petroleum industry worldwide (Al-Wardy & Urdaneta, 2010; Diwan et al., 2011).

The prevalent method for wellbore stability analysis is based on the linear elastic (Bradley, 1979) or poroelastic/poroviscoelastic theory (Cui et al., 1997; 1999; Hoang, 2011; iPMI, 2011), which simply assumes a linear relationship between stress/pore pressure and strain. Wellbore drilling will be regarded as unstable provided that the calculated elastic/poroelastic/poroviscoelastic stresses anywhere around the wellbore satisfy some failure criteria of the rock formation, e.g., Drucker-Prager and Mohr-Coulomb criteria. A critical mud weight/pressure required to maintain the wellbore stable can therefore be easily determined by comparing the predicted stress components and

distribution near the wellbore with the rock strength. It is well recognized, however, that rocks do exhibit nonlinear and plastic behaviour corresponding to nonlinear or plastic (hardening/softening) properties with stiffnesses depending on the stress and strain levels, before they reach ultimate or residual strength (stability problem) [Charlez, 1994; Potts & Zdravkovic, 1999; Papanastasiou & Zervos, 2004]. Ignoring the elastoplastic feature of rock or soil formations generally gives conservative solutions, thus leading to a substantial overestimate of the critical mud density/pressure (Charlez & Roatesi, 1999). Nevertheless, the incorporation of elastoplastic rock behaviour renders a complete analytical solution to the wellbore drilling problem extremely complex and difficult. Stress and strain analyses for such problem usually are obtained through numerical methods (Carter, 1978; Potts & Zdravkovic, 1999). So far scarce analytical plasticity solutions exist in the literature for the wellbore problem even when major approximations are assumed.

The primary goal of this research is to develop a generic class of rigorous, analytical solutions for a cylindrical wellbore drilled in rock or soil formations exhibiting elastoplastic characteristics while subjected to non-isotropic in situ stresses, under both undrained and drained conditions. To cover a range of rock behaviour, four different models of elastoplasticity are taken into account. The strain hardening Drucker-Prager and Mohr-Coulomb models are used to accommodate hard/soft rock behaviour of great depth, while the Cam Clay (Schofield & Wroth, 1968; Wood, 1990) and bounding surface models (Dafalias & Herrmann, 1980; 1982) based on the critical state concept are used to simulate shale and soft sediment behaviour. Numerical simulations are also conducted with the use of ABAQUS finite element analysis commercial program. In particular, for

the bounding surface model a user defined material subroutine (UMAT) is developed and implemented into ABAQUS for the wellbore stability analysis.

1.2 Literature Review

The wellbore drilling process can be modelled as a cylindrical cavity contraction problem with the cavity pressure gradually reduced from the in situ stress state. For elastic and poroelastic wellbore stability analyses, the reader may refer to Cui et al. (1997; 1999) and Abousleiman & Cui (1998; 2000). Fig. 1.1 shows the scenario of a wellbore of initial radius a_0 drilled in an elastoplastic porous formation subjected to an in-plane (horizontal) in situ stress σ_h and an out-of-plane (vertical) stress σ_v as well as an initial pore pressure p_0, where a is the contracted wellbore radius corresponding to a wellbore pressure p_w and r_p denotes the current position of the elastic-plastic boundary which is occupied by the material particle initially at r_{p0}. From a mathematical perspective, the derivation of the cavity contraction solution can be carried out in essentially a similar fashion as the cavity expansion problem. Attributed primarily to its versatile applications in geomechanics and geotechnical engineering such as the interpretation of pressuremeter tests and analysis of the behaviour of tunnels, the cavity theory, and particularly the cavity expansion in geomaterials, has been the subject of intensive studies over the last few decades (Gibson & Anderson, 1961; Palmer & Mitchell, 1972; Vesic, 1972; Prevost & Hoeg, 1975; Hughes et al., 1977; Randolph et al., 1979; Carter et al., 1986; Yu, 1990; Collins & Stimpson, 1994; Papanastasiou & Durban, 1997; Yu, 2000; Salgado & Randolph, 2001). This section presents a review on the major developments of analytical solutions for both cavity expansion and contraction in elastoplastic materials.

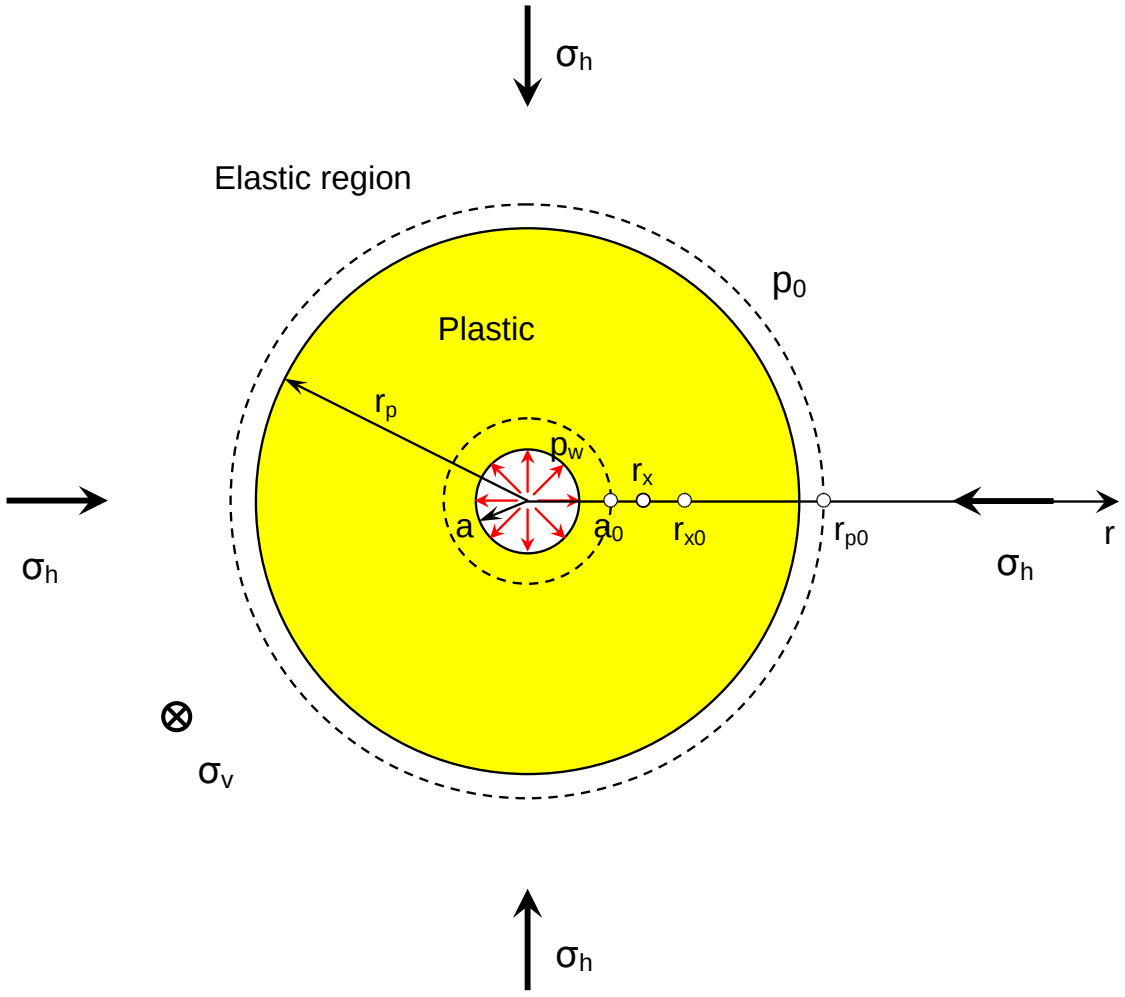

Fig. 1.1. Scenario of wellbore boundary value problem

1.2.1 EXPANSION OF CAVITIES IN ELASTOPLASTIC MATERIALS

The research on the cavity expansion began with Bishop et al. (1945) for the metal indentation problem who solved the elastoplastic finite expansion of a spherical and a cylindrical cavity in an infinite medium by using the elastic-perfectly plastic Tresca

model and neglecting the elastic deformation in the plastic zone. Later Hill (1950) gave a more general large strain solution of the stresses and displacements for the expansion of spherical and cylindrical cavities again with the assumption of Tresca yielding condition. Chadwick (1959) further presented a derivation of the pressure-expansion relationship for the Mohr-Coulomb material by introducing the logarithmic strain and adopting the associated flow rule (the yield surface and flow potential surface are identical). It is worth noting that the first geotechnical application of the cavity expansion theory was made by Gibson & Anderson (1961) for determining the soil properties from pressuremeter test results. Since then, many analytical and semi-analytical solutions for the cavity expansion problem have been developed based on the elastic-perfectly plastic and strain hardening elastoplastic soil/rock models, mainly assuming the Mohr-Coulomb yield criterion, as well as on the Cam Clay critical state models.

For the perfectly plastic models, an important contribution was made by Vesic (1972) who presented approximate solutions for both spherical and cylindrical cavity expansion problems by assuming that the soil behaves as a Mohr-Coulomb material and taking into the account the effects of volume change in the plastic region. Carter et al. (1986) derived an analytical solution for the cavity expansion in non-associated Mohr-Coulomb soils (the yield and plastic potential functions differ) and presented an explicit expression for the pressure-expansion relation by ignoring the convected part of the stress rate in their derivation. Similarly, Bigoni & Laudiero (1989) analyzed the quasi-static finite expansion of a spherical or cylindrical cavity in non-associated Mohr-Coulomb rocks. In their analysis for the cylindrical case, however, the longitudinal normal stress was assumed to be equal to the mean of the other two principal stresses. This restrictive assumption was

later removed by Yu & Houlsby (1991), who provided a unified analytical solution for the expansion of both cylindrical and spherical cavities in dilatant Mohr-Coulomb soils with a more relaxed postulate that the axial principal stress is intermediate with respect to the other two. An explicit expression for the pressure-expansion relation has been derived by the authors by integrating the governing equation with the aid of a series expansion.

In addition to the elastic-perfectly plastic models, cavity expansion analyses incorporating strain hardening into the plastic behaviour of materials have also received considerable attention. For example, Durban & Kubi (1992) proposed a general solution for the pressurized cylindrical tube problem accounting for the arbitrary hardening of Tresca yield function with an associated flow rule. The key feature in Durban & Kubi (1992) is that with the adoption of the logarithmic strain components, the cavity expansion problem can be formulated as a governing differential equation with the equivalent stress as the independent variable and thus be conveniently solved by quadratures. In particular, a comprehensive analysis of the corner zone has been given in their formulation. The similar procedure has subsequently been extended to solve the spherical cavity expansion problem in strain hardening Drucker-Prager material (Durban & Fleck, 1997), and for the cylindrical cavity expansion involving strain hardening Drucker-Prager and Mohr-Coulomb materials (Papanastasiou & Durban, 1997). It is shown (Papanastasiou & Durban, 1997) that the Mohr-Coulomb model requires the numerical solution of a single first-order differential equation, while for the Drucker-Prager model an algebraic constraint in addition to the complex governing differential equation are needed. Note that for the case of Mohr-Coulomb model, the assumption of the axial stress being the intermediate principal stress in Papanastasiou & Durban (1997)

is not necessarily true during the cavity expansion and may violate the plane strain condition in the axial direction (Reed, 1988; Yu & Rowe, 1999).

As far as the critical state soil models are considered, Palmer & Mitchell (1972) appear to have been the first to derive an approximate small strain analytical solution for cylindrical cavity expansion in normally consolidated clay under drained condition, although in their solution a very simple idealized Cam Clay model was adopted and the elastic deformations were ignored for simplicity. Collins et al. (1992) and Collins & Stimpson (1994) presented seminal semianalytical solutions for drained and undrained created cavity problems (zero initial radius) in critical state soils by using the well known similarity solution technique (Hill, 1950). The more general solutions for large strain undrained cavity expansions in critical state soils, with the relaxation of the zero initial radius assumption, were achieved by Collins & Yu (1996) for both the original and modified Cam Clay models. Cao et al. (2001) reconsidered the undrained cavity expansion problem in modified Cam Clay soil following essentially a similar procedure used by Collins & Yu (1996). The shear modulus in Cao et al. (2001), however, was approximated as a constant instead of a variable in proportion to the mean effective stress (Chen & Abousleiman, 2012a). Based on a further simplifying assumption that the deviator stress in the plastic zone is equal to the ultimate deviator stress, they derived approximate closed form expressions for the total stress and excess pore water pressure distributions around the cavity. More recently, the approach of similarity technique has been successfully extended for solving drained cavity expansion problems in crushable sands (Russell & Khalili, 2002; Jiang & Sun, 2011) and also in unsaturated porous media (Russell & Khalili, 2006), to include the effects of particle crushing and suction on the

stress-strain response of soils surrounding the expanding cavities.

Nevertheless, as noted in Chen & Abousleiman (2012a), the aforementioned semi-analytical solutions for drained (Collins et al., 1992; Collins & Stimpson, 1994; Russell & Khalili, 2002; Jiang & Sun, 2011) and undrained (Collins & Yu, 1996; Cao et al, 2001; Russell & Khalili, 2006) cylindrical cavity expansions in critical state soils can only be treated as approximate because in all these solutions more or less simplified rather than rigorous definitions have been used for the deviator and mean effective stresses. The reason for introducing these simplified definitions, which require that both the two effective stress invariants are independent of the axial stress, is merely to simplify the mathematical derivation and allow for the possibility of closed form solutions (Silvestri & Abou-Samra, 2011; 2012).

1.2.2 Contraction of Cavities in Elastoplastic Materials

Cavity contraction theory, of course, has wide applications to the stress and displacement modelling around the drilled wellbore in petroleum engineering and to the design and construction of tunnels in civil engineering as well. However, in contrast to the cavity expansion problem, much less investigations of cavity contraction in soil and rock have been conducted, which is particularly the case when the critical state plastic models are involved.

Earlier analytical solutions reported for the wellbore/tunnel opening problems usually modelled the soils/rocks as associated or non-associated elastic-perfectly plastic materials like linear Mohr-Coulomb and nonlinear Hoek-Brown yield criteria, and under isotropic in situ stress condition. A good review on this topic was provided by Brown et al. (1983) who also presented a series of solutions for the stress and displacement

distributions of a circular opening in the Hoek-Brown rock by using both the elastic-brittle-plastic and elastic strain softening models. However, as the authors pointed out, these elastoplastic solutions may only be regarded as approximate as they were not based on a rigorous theory of incremental plasticity. For the simple elastic-brittle-plastic Hoek-Brown model, a later improvement over the solution of Brown et al. (1983) was made by Wang (1996) using a numerical method and a similar problem was further examined by Sharan (2005) and Bobet (2010).

For the more complex elastic strain hardening/softening models, which suitably capture the important aspects of real soil/rock behavior, some cavity contraction solutions for the wellbore and tunnel problems have recently been developed, though are quite limited. Graziani and Ribacchi (1993) proposed an analytical approach to determine the state of stress and strain for a circular opening excavated in a rock mass and investigated the stability conditions. In their formulation, the rock formation is assumed to obey the non-associated Mohr-Coulomb model and the strain softening behaviour is linked to a simple plastic shear strain by the so-called softening modulus parameter. The same paper by Papanastasiou and Durban (1997) also included the contraction solutions for a cylindrical cavity embedded in strain hardening Drucker-Prager and Mohr-Coulomb geomaterials. Charlez & Roatesi (1999) derived an analytical solution for the wellbore stability problem under undrained condition using a very simple idealized Cam Clay model where the elliptical yield surface was replaced by two straight lines, and the solution is restricted to the volumetric strain hardening rocks with overconsolidation ratio less than 2. Concurrently, Yu & Rowe (1999) provided a set of comprehensive yet still approximate analytical/semi-analytical solutions for the undrained circular excavation

problem using the well known Cam Clay critical state theories (Wood, 1990). Recently, Chen et al. (2012) proposed a closed form approach to predict the development and progress of the plastic zone around a wellbore drilled in linearly hardening or softening Drucker-Prager rocks under drained condition. The main drawback to this approach is that the two stress invariants have again been treated in somewhat approximate fashion and moreover the out-of-plane behaviour was considered to be purely elastic (zero plastic strain in the axial direction).

1.3 Objectives

It is important to realize that although the cavity models have already been well-covered in the literature, exact analytical/semi-analytical elastoplastic solutions for the general cylindrical wellbore drilling problems, whether drained or undrained, are still not available to date. As a matter of fact, in the previous Mohr-Coulomb plasticity-based solutions, the vertical (axial) stress has been exclusively assumed to be everywhere the intermediate principal stress which means that there is no component of plastic strain in the vertical direction (Graziani & Ribacchi, 1993; Papanastasiou & Durban, 1997; Yu & Rowe, 1999). Such an assumption for the vertical stress, as mentioned above, will not remain valid throughout the wellbore drilling process and may cause significant errors to the stress predictions around the wellbore, especially when the in situ stresses are non-isotropic which unfortunately is the general case encountered in the drilling practice. On the other hand, even though the similarity solution procedure proposed by Collins and his coworkers for drained and undrained cavity expansions in critical state plasticity geomaterials is very appealing in that it allows for the determination of the limiting value of cavity pressure with relative ease, such solutions may only be viewed as the

asymptotic solutions valid at intermediate and large times for the finite initial cavity problem. It would not seem possible to be extended for the finite wellbore drilling analysis (Chen & Abousleiman, 2012b), let alone the simplified assumption involved with the mean and deviator stresses in an attempt to obtain the possible semi-analytical solutions.

The overall objective of this thesis is therefore to develop a generic class of novel, exact analytical solutions for a wellbore drilled in poroelastoplastic rock formations subjected to non-isotropic far field in situ stresses, taking into account of both undrained and drained situations and different plasticity models of various complexities. The formulation presented here follows for the first time the standard definitions of the mean effective stress and deviatoric stress so the solutions are rigorous in this sense. The proposed solution procedure also possesses the advantage over the conventional similarity technique in that it is directly applicable to the cavity problem of finite initial radius. These solutions would provide not only a rigorous theoretical framework for predicting the rock behaviour and deformation mechanisms around the wellbore, but also can and are used as benchmarks for verifying the finite element analysis of wellbore drilling problems involving various elastoplastic modelling of wellbore or cavities.

1.4 Organization of Thesis

In Chapter 2 the shear strain hardening Drucker-Prager plasticity model is first adopted to describe the behaviour of sandstone-like formations, and a rigorous analytical solution is derived for undrained/drained wellbore drilling boundary value problem in details. For undrained case, the problem turns out to be equivalent to solving a system of first order ordinary differential equations with the radial, tangential, and vertical effective

stresses being the basic unknowns. For the drained situation, however, the three elastoplastic constitutive equations are coupled with the radial equilibrium equation, the former formulated with respect to a material particle within the Lagrangian description, while the latter in contrast corresponds to the Eulerian formulation for every material point at a specific moment. A suitable auxiliary variable therefore must be introduced to convert the Eulerian equilibrium equation to the Lagrangian form. The three stress components can hence again be solved from a set of simultaneous differential equations together with the volumetric strain.

Chapter 3 proceeds to dealing with the shear strain hardening Mohr-Coulomb model. The main difficulty in using the Mohr-Coulomb model is that since its yield surface in the principal stress space contains six corners, the partial derivatives with respect to the stress components become indeterminate at these corners which makes the derivation of analytical solution almost impossible. To eliminate such shortcoming, the Mohr-Coulomb model will be approximated by a smooth shear hardening Matsuoka-Nakai model (Matsuoka & Nakai, 1974) which passes through the Mohr-Coulomb hexagon at both major and minor vertices. Following a similar procedure outlined in Chapter 2, analytical solution is presented thereafter for the wellbore drilling boundary value problem.

For soft rocks and shale formations which consist mainly of clay minerals, it is commonly accepted that the volumetric hardening plastic models instead of the shear hardening Drucker-Prager and Mohr-Coulomb models would be more suitable to describe their nonlinear stress-strain behaviour. Chapters 4 and 5 presents rather straightforward extension of the wellbore drilling solution to the critical state Cam Clay model (Wood, 1990) and bounding surface model (Dafalias & Herrmann, 1980),

respectively. Extensive parametric studies are made to illustrate the effect of the stress history (overconsolidation ratio) of rocks on the stress and pore pressure distributions as well as the development and progress of the plastic and failure zones around the wellbore. The stress paths and specific volume change due to the wellbore drilling are also presented.

Further numerical analyses for the elastoplastic wellbore drilling problems are conducted in Chapter 6 with the use of ABAQUS software. In particular, a user defined material subroutine (UMAT) for the bounding surface model will be developed using the return mapping algorithm (Borja & Lee, 1990; Neto et al., 2008) and its implementation into ABAQUS be outlined. The predictions from the ABAQUS analyses are generally in excellent agreement with the analytical solutions for both modified Cam Clay and bounding surface models.

Chapter 7 is dedicated to the applications of the analytical solutions proposed in this research, with main attention focused on the prediction of critical mud pressure required to maintain the wellbore stability. It is shown that ignoring the elastoplastic feature of the rock formations does give conservative solutions and would lead to a substantial overestimation of the critical mud pressure (density).

Finally, Chapter 8 ends with the concluding remarks on this dissertation. Recommendations for future study are given.

CHAPTER 2

WELLBORE STABILITY ANALYSIS IN STRAIN HARDENING DRUCKER-PRAGER ROCKS

2.1 Introduction

In this chapter an exact analytical solution for the wellbore boundary value problem is derived, in an elastoplastic porous rock formation. The rock is modelled as Drucker-Prager material with the incorporation of hardening behaviour depending on the evolving of the plastic strain. By adopting the small strain deformation in the elastic region while large strain deformation in the plastic region, the wellbore problems under both drained and undrained conditions are formulated to solve a system of first order ordinary differential equations in the plastic zone. The distributions of the radial, tangential, and vertical effective stresses as well as the pore pressure (undrained case) and volumetric strain (drained case) are plotted against the radial distance around the wellbore. In particular, the mean-deviatoric effective stress paths are illustrated for a material point at the wellbore surface.

2.2 Strain Hardening Drucker-Prager Model

This is an extended version of the ideal Drucker-Prager plasticity model in which the yield surface (cylindrical cone in principal stress space) evolves with the accumulated

plastic strain via the hardening parameter, friction angle β (Wood, 2004). In this model the hardening will be linked solely to the accumulated plastic deviatoric (shear) strain ε_q^p, which is quite realistic for the modelling of soft sandstone-like formations since for such rocks it is basically the rearrangement of the particles that dominates the stress-strain response (Wood, 2004). Fig. 2.1 shows the initial yielding and failure loci separating the elastic, elastoplastic, and inaccessible regions in the $P' - q$ stress plane, with the mean effective and deviatoric stress invariants P' and q defined as

$$P' = \frac{1}{3}(\sigma_r' + \sigma_\theta' + \sigma_z') \tag{2.1}$$

$$q = \sqrt{\frac{1}{2}\left[(\sigma_r' - \sigma_\theta')^2 + (\sigma_r' - \sigma_z')^2 + (\sigma_\theta' - \sigma_z')^2\right]} \tag{2.2}$$

where $\sigma_r' = \sigma_r - p$, $\sigma_\theta' = \sigma_\theta - p$, and $\sigma_z' = \sigma_z - p$ are known as the effective radial, tangential, and vertical principal stresses; σ_r, σ_θ, and σ_z are the total radial, tangential,

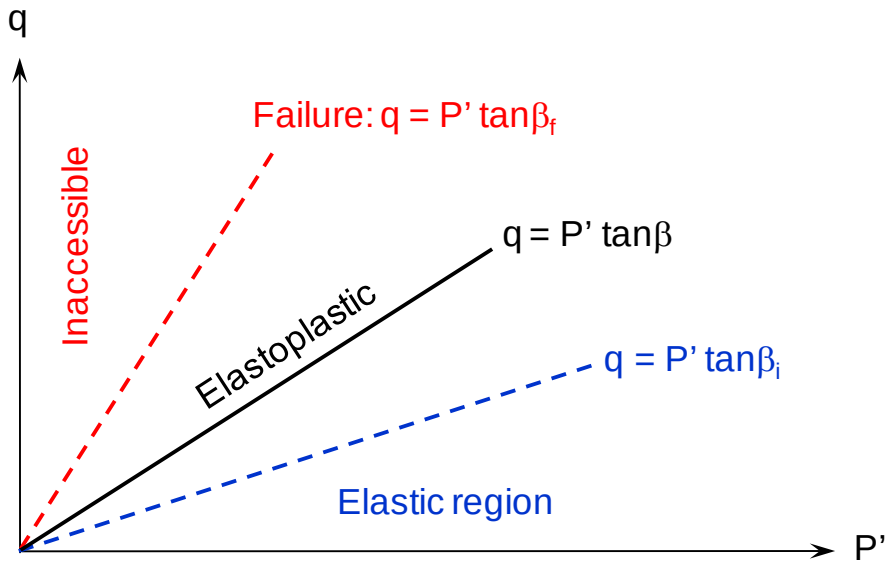

Fig. 2.1. Shear strain hardening plastic Drucker-Prager model

and vertical principal stresses, and p is the pore pressure.

Fig. 2.2 shows the Drucker-Prager yield surface in the principal stress space ($\sigma_1^{'} - \sigma_2^{'} - \sigma_3^{'}$) as well as its circular projection on the deviatoric plane. Also given in Fig. 2.2 is the yield surface associated with Mohr-Coulomb model for comparison, which matches the Drucker-Prager surface at three vertices (triaxial compression).

For frictional granular rocks, the yield function of the strain hardening Drucker-Prager model can be expressed as

$$F(P^{'}, q, \beta) = q - \tan\beta \cdot P^{'} \tag{2.3}$$

where β is the Drucker-Prager fiction angle which as a hardening parameter essentially controls the size of the current yield locus in the $P^{'} - q$ plane (Fig. 2.1).

When an associated flow rule is assumed, the model requires fives material parameters: G, the elastic shear modulus; ν, the drained Poisson's ratio; β_i and β_f, the friction angles corresponding to the initial yield and failure loci, respectively, see Fig. 2.1; and c, a rock parameter which relates the slope of the yield locus, $\tan\beta$, hyperbolically to the plastic deviatoric strain, ε_q^p, as follows

$$\tan\beta = \frac{\varepsilon_q^p}{c+\varepsilon_q^p}\left(\tan\beta_f - \tan\beta_i\right) + \tan\beta_i \tag{2.4}$$

where

$$\varepsilon_q^p = \int d\varepsilon_q^p = \int \frac{\sqrt{2}}{3}\sqrt{(d\varepsilon_r^p - d\varepsilon_\theta^p)^2 + (d\varepsilon_\theta^p - d\varepsilon_z^p)^2 + (d\varepsilon_r^p - d\varepsilon_z^p)^2} \tag{2.5}$$

with $d\varepsilon_q^p$ denoting the plastic deviatoric strain increment, and $d\varepsilon_r^p$, $d\varepsilon_\theta^p$, and $d\varepsilon_z^p$ the plastic strain increments in r, θ, and z directions, respectively.

Fig. 2.3 gives a plot of the above functional relationship where $\tan\beta$ increases asymptotically towards the limiting value of $\tan\beta_f$ as ε_q^p approaches infinity. Note that

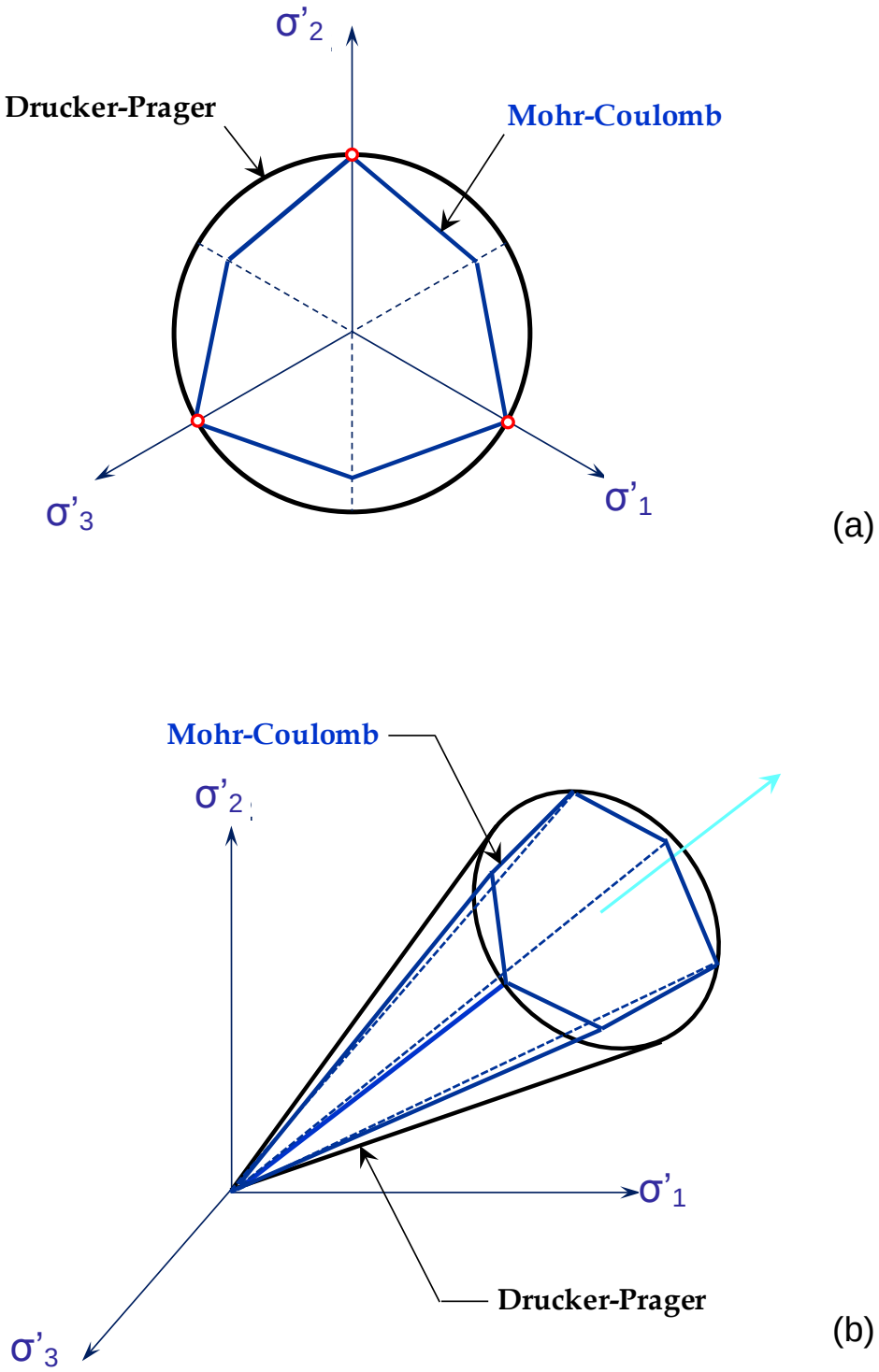

Fig. 2.2. Drucker-Prager and Mohr-Coulomb yield surfaces in: (a) deviatoric plane; (b) principal stress space

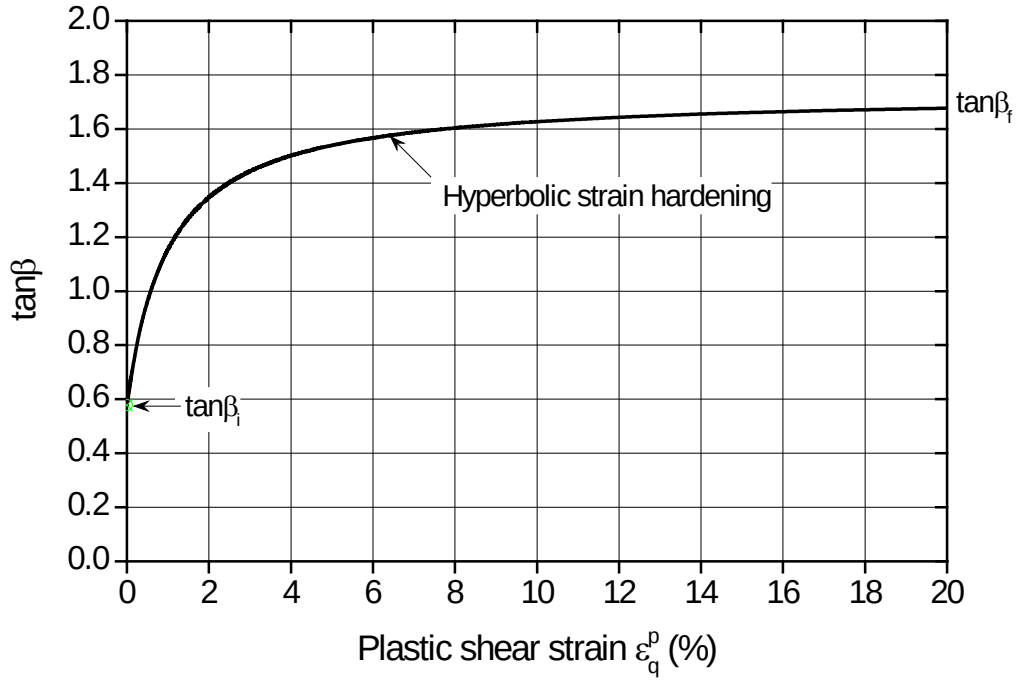

Fig. 2.3. Hyperbolic friction angle hardening curve used in Drucker-Prager model

for sufficiently large and small values of c, the hardening model will degenerate to a perfectly plastic Drucker-Prager model with fixed friction angle equal to β_i and β_f, respectively.

2.3 Undrained Solution

Consider a wellbore having initial radius a_0 drilled in a rock formation with the in situ horizontal, vertical stresses and pore pressure equal to σ_h, σ_v, and p_0, respectively, as shown in Fig. 2.4. The rock is modelled as a strain hardening Drucker-Prager elastoplastic material. As the internal wellbore pressure decreases gradually from its initial value of σ_h, initial yielding first occurs at the wellbore surface. A plastic zone will will then be formed around the borehole with the further decrease of the wellbore

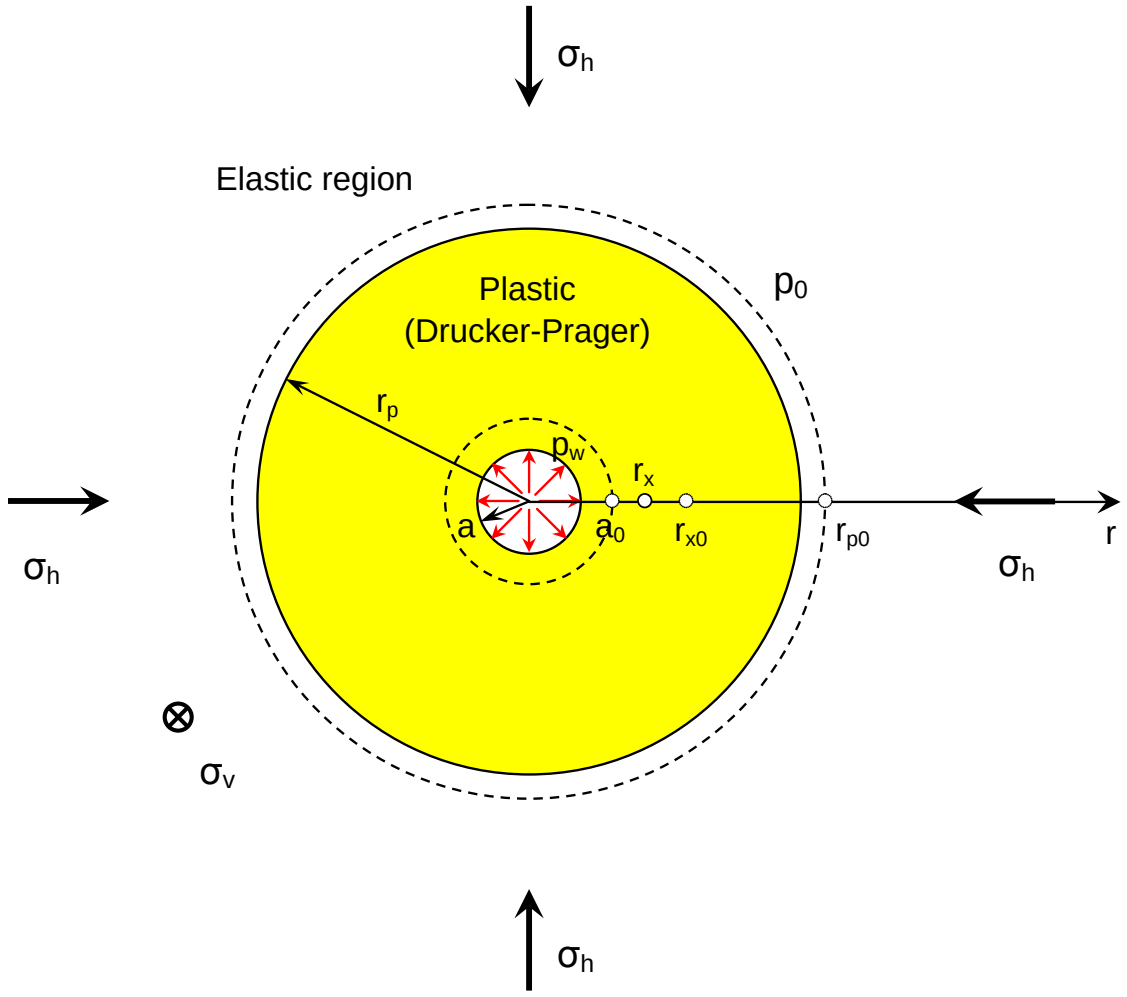

Fig. 2.4. Wellbore boundary value problem (Drucker-Prager model)

pressure, and an internal failure zone may finally develop when the wellbore pressure is sufficiently decreased. Imagine now the situation that the borehole has contracted to the current radius of a corresponding to a wellbore pressure p_w and that plastic deformation is occurring throughout the annulus region $a \leq r \leq r_p$. At this instant a typical particle initially at radial distance r_{x0} will have moved inward to a new position denoted by r_x (see Fig. 2.4). The material remains in an elastic state beyond the elastic-plastic interface

$r = r_p$.

In both the elastic and plastic regions, the radial equilibrium equation in the current configuration can be written as

$$\frac{\partial \sigma_r}{\partial r} + \frac{\sigma_r - \sigma_\theta}{r} = 0 \tag{2.6}$$

or in the effective form,

$$\frac{\partial \sigma_r^{'}}{\partial r} + \frac{\partial p}{\partial r} + \frac{\sigma_r^{'} - \sigma_\theta^{'}}{r} = 0 \tag{2.7}$$

where the compressive stresses and pore pressure p are considered positive.

For the undrained condition, the volumetric strain may be assumed to vanish everywhere. This gives the following relationship between the current and initial positions of an arbitrary point, r_x and r_{x0}, and of the wellbore surface, a and a_0

$$r_x^2 - a^2 = r_{x0}^2 - a_0^2 \tag{2.8a}$$

or the normalized form

$$\frac{r_{x0}}{a} = \sqrt{\left(\frac{r_x}{a}\right)^2 + \left(\frac{a_0}{a}\right)^2 - 1} \tag{2.8b}$$

which indicates that for any particle having the current coordinate of $r = r_x$ corresponding to a contracted borehole radius of a, its original location r_{x0} can be uniquely determined from Eq. (2.8) in terms of a, a_0, and r_x. As will be shown later, the existence of such a simple equation will greatly simplify the subsequent formulation for the undrained elastoplastic wellbore drilling boundary value problem.

2.3.1 Elastic Analysis

In the elastic region $r \geq r_p$, the deformations are very small. The radial and tangential total strain increments $d\varepsilon_r$ and $d\varepsilon_\theta$ at r can be written as

$$d\varepsilon_r = -\frac{\partial du_r}{\partial r} \tag{2.9}$$

$$d\varepsilon_\theta = -\frac{du_r}{r} \tag{2.10}$$

where du_r is the displacement increment for a material point currently at position r, radially outwards direction taken as positive.

The elastic stress strain relationship can be expressed in terms of the effective stresses as

$$\begin{Bmatrix} d\varepsilon_r \\ d\varepsilon_\theta \\ d\varepsilon_z \end{Bmatrix} = \frac{1}{E}\begin{bmatrix} 1 & -\nu & -\nu \\ -\nu & 1 & -\nu \\ -\nu & -\nu & 1 \end{bmatrix} \cdot \begin{Bmatrix} d\sigma_r' \\ d\sigma_\theta' \\ d\sigma_z' \end{Bmatrix} \tag{2.11a}$$

or in terms of the total stresses

$$\begin{Bmatrix} d\varepsilon_r \\ d\varepsilon_\theta \\ d\varepsilon_z \end{Bmatrix} = \frac{1}{E_u}\begin{bmatrix} 1 & -\nu_u & -\nu_u \\ -\nu_u & 1 & -\nu_u \\ -\nu_u & -\nu_u & 1 \end{bmatrix} \cdot \begin{Bmatrix} d\sigma_r \\ d\sigma_\theta \\ d\sigma_z \end{Bmatrix} \tag{2.11b}$$

where $d\varepsilon_z$ is the incremental total strain in z direction; $d\sigma_r'$, $d\sigma_\theta'$, $d\sigma_z'$ and $d\sigma_r$, $d\sigma_\theta$, $d\sigma_z$ are, respectively, the effective and total radial, tangential, and axial principal stress increments; ν and ν_u are the drained and undrained Poisson's ratio (For an incompressible material $\nu_u = 0.5$); and E and E_u are the drained and undrained Young's modulus given by

$$E = 2G(1+\nu), \qquad E_u = 2G(1+\nu_u) \tag{2.12}$$

From Eq. (2.11a) one has

$$d\varepsilon_v = d\varepsilon_r + d\varepsilon_\theta + d\varepsilon_z = \frac{1-2\nu}{E} dP' \tag{2.13}$$

where $d\varepsilon_v$ is the volumetric strain increment. Since the total volume strain rate is zero ($d\varepsilon_v = 0$) in an undrained deformation, Eq. (2.13) gives

$$dP' = 0 \tag{2.14}$$

i.e., the mean effective stress must remain constant during the elastic deformation.

Now combining Eqs. (2.6), (2.9), (2.10) and (2.11b), the solutions for total stresses and radial displacement can be easily shown to be (Timoshenko & Goodier, 1970; Yu, 2000)

$$\sigma_r = \sigma_h + (\sigma_p - \sigma_h)\left(\frac{r_p}{r}\right)^2 \tag{2.15}$$

$$\sigma_\theta = \sigma_h - (\sigma_p - \sigma_h)\left(\frac{r_p}{r}\right)^2 \tag{2.16}$$

$$\sigma_z = \sigma_v \tag{2.17}$$

$$u_r = \frac{\sigma_p - \sigma_h}{2G}\frac{r_p^2}{r} \tag{2.18}$$

where σ_p denotes the total radial stress at the elastic-plastic boundary $r = r_p$.

By adding Eqs. (2.15)-(1.17) it is found that for any particle in the external elastic region there is no variation in the mean total stress *P* and consequently, no excess pore pressure would be induced because as noted above the mean effective stress P' is constant during the elastic deformation. Therefore,

$$p = p_0 \tag{2.19}$$

2.3.2 ELASTOPLASTIC ANALYSIS

For strain hardening Drucker-Prager model with an associated flow rule, from Eqs. (2.1)-(2.3) the three components of incremental plastic strain $d\varepsilon_r^p$, $d\varepsilon_\theta^p$, and $d\varepsilon_z^p$ can be expressed as follows

$$d\varepsilon_r^p = \Lambda\frac{\partial F}{\partial \sigma_r'} = \Lambda\left(\frac{\partial F}{\partial P'}\cdot\frac{\partial P'}{\partial \sigma_r'} + \frac{\partial F}{\partial q}\cdot\frac{\partial q}{\partial \sigma_r'}\right) = \Lambda\left\{-\frac{1}{3}\tan\beta + \frac{3(\sigma_r' - P')}{2q}\right\} \tag{2.20a}$$

$$d\varepsilon_\theta^p = \Lambda\frac{\partial F}{\partial \sigma_\theta'} = \Lambda\left(\frac{\partial F}{\partial P'}\cdot\frac{\partial P'}{\partial \sigma_\theta'} + \frac{\partial F}{\partial q}\cdot\frac{\partial q}{\partial \sigma_\theta'}\right) = \Lambda\left\{-\frac{1}{3}\tan\beta + \frac{3(\sigma_\theta' - P')}{2q}\right\} \tag{2.20b}$$

$$d\varepsilon_z^p = \Lambda \frac{\partial F}{\partial \sigma_z'} = \Lambda \left(\frac{\partial F}{\partial P'} \cdot \frac{\partial P'}{\partial \sigma_z'} + \frac{\partial F}{\partial q} \cdot \frac{\partial q}{\partial \sigma_z'} \right) = \Lambda \left\{ -\frac{1}{3}\tan\beta + \frac{3(\sigma_z' - P')}{2q} \right\} \quad (2.20c)$$

where Λ is a scalar multiplier.

From Eqs. (2.20a)-(2.20c) the expressions for plastic volumetric and deviatoric strain increments, $d\varepsilon_p^p$ and $d\varepsilon_q^p$, can be easily shown to be

$$d\varepsilon_p^p = d\varepsilon_r^p + d\varepsilon_\theta^p + d\varepsilon_z^p = -\Lambda \cdot \tan\beta \equiv \Lambda \frac{\partial F}{\partial P'} \quad (2.21a)$$

$$d\varepsilon_q^p = \frac{\sqrt{2}}{3} \sqrt{(d\varepsilon_r^p - d\varepsilon_\theta^p)^2 + (d\varepsilon_\theta^p - d\varepsilon_z^p)^2 + (d\varepsilon_r^p - d\varepsilon_z^p)^2} = \Lambda \equiv \Lambda \frac{\partial F}{\partial q} \quad (2.21b)$$

Whilst the shear hardening rule, Eq. (2.4), can be rewritten in the incremental form as follows

$$d\varepsilon_q^p = c \frac{\tan\beta_f - \tan\beta_i}{(\tan\beta_f - \tan\beta)^2} d(\tan\beta) = c \frac{\tan\beta_f - \tan\beta_i}{(\tan\beta_f - \tan\beta)^2} d\left(\frac{q}{P'}\right) = c \frac{\tan\beta_f - \tan\beta_i}{(\tan\beta_f - \tan\beta)^2} \frac{P' dq - q dP'}{P'^2} \quad (2.22)$$

Substituting Eq. (2.22) [note $d\varepsilon_q^p = \Lambda$] back into Eqs. (2.20a)-(2.20c), and with the aid of

$$dP' = \frac{1}{3}(d\sigma_r' + d\sigma_\theta' + d\sigma_z') \quad (2.23a)$$

$$dq = \frac{\partial q}{\partial \sigma_r'} d\sigma_r' + \frac{\partial q}{\partial \sigma_\theta'} d\sigma_\theta' + \frac{\partial q}{\partial \sigma_z'} d\sigma_z' \quad (2.23b)$$

one can write the plastic stress strain response in the matrix equation

$$\begin{Bmatrix} d\varepsilon_r^p \\ d\varepsilon_\theta^p \\ d\varepsilon_z^p \end{Bmatrix} = y \begin{bmatrix} a_r^2 & a_r a_\theta & a_r a_z \\ a_\theta a_r & a_\theta^2 & a_\theta a_z \\ a_z a_r & a_z a_\theta & a_z^2 \end{bmatrix} \cdot \begin{Bmatrix} d\sigma_r' \\ d\sigma_\theta' \\ d\sigma_z' \end{Bmatrix} \quad (2.24)$$

where the following notations have been defined to abbreviate the mathematical representation

$$a_r = -\frac{q}{3P'} + \frac{3(\sigma_r' - P')}{2q} \quad (2.25a)$$

$$a_\theta = -\frac{q}{3P'} + \frac{3(\sigma_\theta' - P')}{2q} \quad (2.25b)$$

$$a_z = -\frac{q}{3P'} + \frac{3(\sigma_z' - P')}{2q} \tag{2.25c}$$

$$y = c\frac{(\tan\beta_f - \tan\beta_i)P'}{(P' \cdot \tan\beta_f - q)^2} \tag{2.25d}$$

On the other hand, in strain hardening Drucker-Prager model the elastic stress strain relationship can be expressed in the matrix form

$$\begin{Bmatrix} d\varepsilon_r^e \\ d\varepsilon_\theta^e \\ d\varepsilon_z^e \end{Bmatrix} = \frac{1}{E}\begin{bmatrix} 1 & -\nu & -\nu \\ -\nu & 1 & -\nu \\ -\nu & -\nu & 1 \end{bmatrix} \cdot \begin{Bmatrix} d\sigma_r' \\ d\sigma_\theta' \\ d\sigma_z' \end{Bmatrix} \tag{2.26}$$

where $d\varepsilon_r^e$, $d\varepsilon_\theta^e$, and $d\varepsilon_z^e$ are the elastic strain increments in r, θ, and z directions, respectively.

Eqs. (2.24) and (2.26) can be combined to give the elastoplastic constitutive equation

$$\begin{Bmatrix} d\varepsilon_r \\ d\varepsilon_\theta \\ d\varepsilon_z \end{Bmatrix} = \begin{bmatrix} \frac{1}{E} + ya_r^2 & -\frac{\nu}{E} + ya_r a_\theta & -\frac{\nu}{E} + ya_r a_z \\ -\frac{\nu}{E} + ya_\theta a_r & \frac{1}{E} + ya_\theta^2 & -\frac{\nu}{E} + ya_\theta a_z \\ -\frac{\nu}{E} + ya_z a_r & -\frac{\nu}{E} + ya_z a_\theta & \frac{1}{E} + ya_z^2 \end{bmatrix} \cdot \begin{Bmatrix} d\sigma_r' \\ d\sigma_\theta' \\ d\sigma_z' \end{Bmatrix} \tag{2.27}$$

or inversely

$$\begin{Bmatrix} d\sigma_r' \\ d\sigma_\theta' \\ d\sigma_z' \end{Bmatrix} = \frac{1}{\Delta}\begin{bmatrix} b_{11} & b_{12} & b_{13} \\ b_{21} & b_{22} & b_{23} \\ b_{31} & b_{32} & b_{33} \end{bmatrix} \cdot \begin{Bmatrix} d\varepsilon_r \\ d\varepsilon_\theta \\ d\varepsilon_z \end{Bmatrix} \tag{2.28}$$

where

$$b_{11} = \frac{1}{E^2}[1 - \nu^2 + Ea_\theta^2 y + 2E\nu a_\theta a_z y + Ea_z^2 y] \tag{2.29a}$$

$$b_{12} = \frac{1}{E^2}[-Ea_r(a_\theta + \nu a_z)y + \nu(1 + \nu - Ea_\theta a_z y + Ea_z^2 y)] \tag{2.29b}$$

$$b_{13} = \frac{1}{E^2}[-Ea_r(\nu a_\theta + a_z)y + \nu(1 + \nu + Ea_\theta^2 y - Ea_\theta a_z y)] \tag{2.29c}$$

$$b_{22} = \frac{1}{E^2}[1 - \nu^2 + Ea_r^2 y + 2E\nu a_r a_z y + Ea_z^2 y] \tag{2.29d}$$

$$b_{23} = \frac{1}{E^2}[\nu + \nu^2 + E\nu a_r^2 y - E a_\theta a_z y - E\nu a_r(a_\theta + a_z)y] \tag{2.29e}$$

$$b_{33} = \frac{1}{E^2}[1 - \nu^2 + E a_r^2 y + 2E\nu a_r a_\theta y + E a_\theta^2 y] \tag{2.29f}$$

$$b_{21} = b_{12} \tag{2.29g}$$

$$b_{31} = b_{13} \tag{2.29h}$$

$$b_{32} = b_{23} \tag{2.29i}$$

$$\Delta = -\frac{1+\nu}{E^3}[(-1 + \nu + 2\nu^2) + E(-1+\nu)a_r^2 y + E(-1+\nu)a_\theta^2 y - 2E\nu a_\theta a_z y$$

$$-E a_z^2 y + E\nu a_z^2 y - 2E\nu a_r(a_\theta + a_z)y] \tag{2.29j}$$

which are all explicit functions of the three stress components $\sigma_r^{'}$, $\sigma_\theta^{'}$, and $\sigma_z^{'}$.

In order to account for the effect of large deformations in the plastic zone, the natural (or logarithmic) strains are adopted which take the incremental form

$$d\varepsilon_r = -\frac{\partial(dr)}{\partial r} \tag{2.30}$$

$$d\varepsilon_\theta = -\frac{dr}{r} \tag{2.31}$$

Note that in Eqs. (2.30)-(2.31) r is the radial coordinate associated with a given material particle and dr is the infinitesimal change in position of that particle (Lagrangian description). For undrained cylindrical wellbore drilling problem $d\varepsilon_v = 0$, and also $d\varepsilon_z = 0$ as a result of plane strain deformation, it thus follows that

$$d\varepsilon_r = -d\varepsilon_\theta = \frac{dr}{r} \tag{2.32}$$

Substituting Eq. (2.32) into (2.28) the constitutive relationship reduces to three first order ordinary differential equations

$$\frac{D\sigma_r^{'}}{Dr} - \frac{b_{11} - b_{12}}{\Delta r} = 0 \tag{2.33a}$$

$$\frac{D\sigma_\theta^{'}}{Dr} - \frac{b_{21} - b_{22}}{\Delta r} = 0 \tag{2.33b}$$

$$\frac{D\sigma_z^{'}}{Dr} - \frac{b_{31}-b_{32}}{\Delta r} = 0 \tag{2.33c}$$

where $\frac{D}{Dr}$ denotes the material derivative taken along the particle motion path (Lagrangian description). Eqs. (2.33a)-(2.33c) are valid for any material point r_x in the plastic zone (see Fig. 2.4), and contain three unknown stresses $\sigma_r^{'}$, $\sigma_\theta^{'}$, and $\sigma_z^{'}$ as functions of a single variable r, which varies from r_{xp} to r_x. Here r_{xp} represents the position of the specific particle when it just enters into the plastic state. To solve these differential equations one needs a prior knowledge of r_{xp} as well as the corresponding initial values $\sigma_r^{'}(r_{xp})$, $\sigma_\theta^{'}(r_{xp})$, and $\sigma_z^{'}(r_{xp})$, which is discussed below.

2.3.3 Position and Stresses at Elastic-Plastic Boundary

It will be shown in this section that the solution in the outer elastic region fully specifies the value of r_{xp} and the corresponding stress components as well. For the general case when the in situ stresses are non-isotropic, one can write

$$\sigma_{r0}^{'} = \sigma_{\theta 0}^{'} = (\sigma_h - p_0) = K_0\sigma_{z0}^{'} = K_0(\sigma_v - p_0) \tag{2.34}$$

where $\sigma_{r0}^{'}$, $\sigma_{\theta 0}^{'}$, and $\sigma_{z0}^{'}$ are the initial effective stresses; and K_0 represents the coefficient of earth pressure at rest.

Eq. (2.34) can be rewritten in the normalized form

$$\frac{\sigma_{r0}^{'}}{P_0^{'}} = \frac{\sigma_{\theta 0}^{'}}{P_0^{'}} = \frac{3K_0}{1+2K_0}, \qquad \frac{\sigma_{z0}^{'}}{P_0^{'}} = \frac{3}{1+2K_0} \tag{2.35}$$

where $P_0^{'}$ denotes the initial mean effective stress.

As shown in Eq. (2.14), under undrained condition the change of the mean effective stress P' is zero during the elastic deformation. This indicates that the $P^{'} - q$ stress path of the material point r_p will be a vertical line until it reaches the initial yield locus,

represented by point $(P_0^{'}, q_p)$ where

$$q_p = \tan\beta_i \cdot P_0^{'} \tag{2.36}$$

Since r_p is the position of the elastic-plastic boundary, from Eqs. (2.15)-(2.17), (2.19) and (2.35) one obtains

$$\sigma_{rp}^{'} + \sigma_{\theta p}^{'} = \sigma_{r0}^{'} + \sigma_{\theta 0}^{'} = \frac{6K_0}{1+2K_0} P_0^{'} \tag{2.37}$$

$$\sigma_{zp}^{'} = \sigma_{z0}^{'} = \frac{3}{1+2K_0} P_0^{'} \tag{2.38}$$

where $\sigma_{rp}^{'} = \sigma_r^{'}(r_p)$, $\sigma_{\theta p}^{'} = \sigma_\theta^{'}(r_p)$, and $\sigma_{zp}^{'} = \sigma_z^{'}(r_p)$. On the other hand, at r_p the material point is at initial yield so the same stresses must obey the following relation

$$\frac{1}{\sqrt{2}}\sqrt{\left[\sigma_{rp}^{'} - \sigma_{\theta p}^{'}\right]^2 + \left[\sigma_{\theta p}^{'} - \sigma_{zp}^{'}\right]^2 + \left[\sigma_{rp}^{'} - \sigma_{zp}^{'}\right]^2} = q_p \tag{2.39}$$

Combining Eqs. (2.37)-(2.39) the effective radial and tangential stresses can be obtained as

$$\sigma_{rp}^{'} = \sigma_{r0}^{'} - \sqrt{\sigma_{r0}^{'\,2} - \frac{1}{3}(4\sigma_{r0}^{'\,2} + \sigma_{z0}^{'\,2} - 2\sigma_{r0}^{'}\sigma_{z0}^{'} - q_p^2)} \tag{2.40}$$

$$\sigma_{\theta p}^{'} = \sigma_{r0}^{'} + \sqrt{\sigma_{r0}^{'\,2} - \frac{1}{3}(4\sigma_{r0}^{'\,2} + \sigma_{z0}^{'\,2} - 2\sigma_{r0}^{'}\sigma_{z0}^{'} - q_p^2)} \tag{2.41}$$

Eqs. (2.38) and (2.40)-(2.41) together with Eq. (2.36) provide explicit expressions for the stress components at the current elastic-plastic interface r_p. Note that $\sigma_{rp}^{'} < \sigma_{\theta p}^{'}$ according to the sign convention used in this dissertation. Note also that these stresses are independent of the position of the elastic-plastic boundary and therefore the initial values $\sigma_r^{'}(r_{xp})$, $\sigma_\theta^{'}(r_{xp})$, and $\sigma_z^{'}(r_{xp})$ required for solving Eqs. (2.33a)-(2.33c) corresponding to the material particle r_x are given by the same equations.

It remains now to find the position of the material particle, r_{xp}, at the instant that particle becomes plastic. To accomplish this recall Eq. (2.18) for the radial displacement

u_r which is still valid immediately after yielding. This gives

$$r_{xp} - r_{x0} = \frac{\sigma'_{rp} - \sigma'_{r0}}{2G} r_{xp} \tag{2.42}$$

Substituting Eq. (2.8b) into (2.42) thus determines r_{xp} in terms of a, a_0, and r_x

$$\frac{r_{xp}}{a} = \frac{1}{1 - \frac{\sigma'_{rp} - \sigma'_{r0}}{2G}} \sqrt{\left(\frac{r_x}{a}\right)^2 + \left(\frac{a_0}{a}\right)^2 - 1} \tag{2.43}$$

In addition, in order to analyze the stress distributions around the borehole, the location of the current elastic-plastic interface r_p is needed. This can be calculated from Eq. (2.43) as a special case by equating both r_{xp} and r_x to r_p, giving

$$\frac{r_p}{a} = \sqrt{\frac{\left(\frac{a_0}{a}\right)^2 - 1}{\left(\frac{\sigma'_{rp} - \sigma'_{r0}}{2G}\right)^2 - \frac{\sigma'_{rp} - \sigma'_{r0}}{G}}} \tag{2.44}$$

So far all the initial conditions related to the governing differential equations (2.33a)-(2.33c) have been identified, as given in Eqs. (2.38), (2.40), (2.41), and (2.43). The stresses for any material point in the plastic region, as represented by r_x, thus can be readily solved as an initial value problem starting at r_{xp}. Here use is made of the standard ordinary differential equation system solver implemented in Wolfram Mathematica 7.0 (2008) for this purpose. An important point however to note is that these equations are valid only in case that the material point has been experiencing certain plastic deformation, i.e., an annular plastic zone is formed outside the borehole. This constraint will be satisfied as long as

$$\frac{a_0}{a} > \frac{a_0}{a_p} \tag{2.45}$$

where a_p denotes the reduced borehole radius which corresponds to the onset of yielding at the wellbore surface and can be obtained by setting $r_p = a = a_p$ in Eq. (2.44)

$$\frac{a_p}{a_0} = \frac{1}{1-\frac{\sigma'_{rp}-\sigma'_{r0}}{2G}} \tag{2.46}$$

2.3.4 EXCESS PORE PRESSURE IN PLASTIC ZONE

Having known the effective stresses in the plastic zone $a \le r \le r_p$, it is a matter of ease to calculate from the equilibrium equation (2.7) the distribution of pore pressure $p(r_x)$. Integrating Eq. (2.7) from the elastic-plastic interface up to the point r_x (Eulerian description),

$$p(r_x) = \sigma'_{rp} + p_0 - \sigma'_r(r_x) - \int_{r_p}^{r_x} \frac{\sigma'_r - \sigma'_\theta}{r} dr \tag{2.47}$$

the pore pressure and consequently the excess pore pressure $\Delta p(r_x) = p(r_x) - p_0$ are then determined.

2.4 Drained Solution

The formulation for the drained wellbore drilling problem would be much more challenging since in this case the volumetric strain is no longer equal to zero and thus no additional simplification like Eq. (2.8) could be introduced into the analysis. Actually for the drained case, the volumetric strain on its own needs to be determined. Nevertheless, it is shown in this section that with the introduction of a carefully chosen auxiliary variable, i.e., the ratio of the particle displacement in radial direction to its present radial position, the drained problem can still be reduced to solving a set of first-order simultaneous differential equations in the plastic zone, with the radial, tangential, and vertical stresses in addition to the volumetric strain being the four basic unknowns.

It should be pointed out that when the wellbore is drilled under drained condition, the pore pressure p is eventually constant equal to the in situ value of p_0 and can be

subtracted out of the analysis (Carter, 1978; Collins et al., 1992). The equilibrium equation (2.7) therefore reduces to

$$\frac{\partial \sigma_r^{'}}{\partial r} + \frac{\sigma_r^{'} - \sigma_\theta^{'}}{r} = 0 \tag{2.48}$$

2.4.1 ELASTIC ANALYSIS

Again within the elastic region $r \geq r_p$ (Fig. 2.4), the displacements and strains will be infinitesimal. Note that Eqs. (2.9)-(2-10) for the total strain increments $d\varepsilon_r$ and $d\varepsilon_\theta$ and the constitutive equation (2.11a) also apply for the drained case, so together with Eq. (2.48), the solutions for effective stresses and radial displacement can be obtained as follows

$$\sigma_r^{'} = \sigma_h^{'} + (\sigma_p^{'} - \sigma_h^{'}) \left(\frac{r_p}{r}\right)^2 \tag{2.49}$$

$$\sigma_\theta^{'} = \sigma_h^{'} - (\sigma_p^{'} - \sigma_h^{'}) \left(\frac{r_p}{r}\right)^2 \tag{2.50}$$

$$\sigma_z^{'} = \sigma_v^{'} \tag{2.51}$$

$$u_r = \frac{\sigma_p^{'} - \sigma_h^{'}}{2G} \frac{r_p^2}{r} \tag{2.52}$$

where $\sigma_h^{'} = \sigma_h - p_0$; $\sigma_v^{'} = \sigma_v - p_0$; and $\sigma_p^{'}$ denotes the effective radial stress at the elastic-plastic boundary $r = r_p$.

2.4.2 ELASTOPLASTIC ANALYSIS

As in the undrained case, the elastoplastic incremental constitutive relation during the plastic deformation is still given by (2.28). However, for the drained wellbore drilling problem, $d\varepsilon_v = d\varepsilon_r + d\varepsilon_\theta \neq 0$, the three rows in the matrix equation (2.28) therefore becomes, upon elimination of $d\varepsilon_r$

$$d\sigma_r^{'} = \frac{1}{\Delta}[b_{11}d\varepsilon_v + (b_{12} - b_{11})d\varepsilon_\theta] = \frac{1}{\Delta}[b_{11}d\varepsilon_v + (b_{12} - b_{11})(-\frac{dr}{r})] \quad (2.53a)$$

$$d\sigma_\theta^{'} = \frac{1}{\Delta}[b_{21}d\varepsilon_v + (b_{22} - b_{21})d\varepsilon_\theta] = \frac{1}{\Delta}[b_{21}d\varepsilon_v + (b_{22} - b_{21})(-\frac{dr}{r})] \quad (2.53b)$$

$$d\sigma_z^{'} = \frac{1}{\Delta}[b_{31}d\varepsilon_v + (b_{32} - b_{31})d\varepsilon_\theta] = \frac{1}{\Delta}[b_{31}d\varepsilon_v + (b_{32} - b_{31}))(-\frac{dr}{r})] \quad (2.53c)$$

where b_{ij} and Δ have been defined in Eq. (2.29), which are are all explicit functions of the three stress components $\sigma_r^{'}$, $\sigma_\theta^{'}$, and $\sigma_z^{'}$.

Introduce now an auxiliary independent variable ξ, defined as

$$\xi = \frac{u_r}{r} = \frac{r - r_0}{r} \quad (2.54)$$

where u_r is known as the radial displacement and r_0 the original position of the particle. The differentiation of Eq. (2.54) gives $d\xi = \frac{r_0}{r^2}dr$ and so

$$\frac{dr}{r} = \frac{d\xi}{1-\xi} \quad (2.55)$$

Combining Eq. (2.55) with Eqs. (2.53a)-(2.53c) [Observe also that for a given material point, ε_v must be a function only of its current position r and also only of the auxiliary variable ξ], it follows that

$$\frac{D\sigma_r^{'}}{D\xi} = \frac{b_{11}}{\Delta}f - \frac{b_{12} - b_{11}}{\Delta(1-\xi)} \quad (2.56a)$$

$$\frac{D\sigma_\theta^{'}}{D\xi} = \frac{b_{21}}{\Delta}f - \frac{b_{22} - b_{21}}{\Delta(1-\xi)} \quad (2.56b)$$

$$\frac{D\sigma_z^{'}}{D\xi} = \frac{b_{31}}{\Delta}f - \frac{b_{32} - b_{31}}{\Delta(1-\xi)} \quad (2.56c)$$

$$\frac{D\varepsilon_v}{D\xi} = f \quad (2.56d)$$

where $\frac{D}{D\xi}$ denotes the material derivative with respect to ξ following a given particle (Lagrangian description). Eqs. (2.56a)-(2.56d) constitute a system of first order differential equations with ξ being the single independent variable and are valid for any

material point currently located in the plastic zone. However, there are five unknown functions needs to be solved for in these differential equations, i.e., $\sigma_r^{'}$, $\sigma_\theta^{'}$, $\sigma_z^{'}$, ε_v, and f, but only four available equations. The additional one should be sought from the radial equilibrium condition, as discussed below.

With the aid of the auxiliary variable ξ, Eq. (2.48) can be rewritten as

$$\frac{\partial \sigma_r^{'}}{\partial \xi}\left(-\frac{u_r}{r^2}+\frac{1}{r}\frac{du_r}{dr}\right)+\frac{\sigma_r^{'}-\sigma_\theta^{'}}{r}=0 \tag{2.57}$$

which, on the basis of Eq. (2.56a), yields

$$-(\sigma_r^{'}-\sigma_\theta^{'})=\left[\frac{b_{11}}{\Delta}f-\frac{b_{12}-b_{11}}{\Delta(1-\xi)}\right]\left(-\xi+\frac{du_r}{dr}\right) \tag{2.58}$$

where $\frac{du_r}{dr}$ represents the relative displacement of a neighboring point with respect to the particle instantaneously at position r (Eulerian description), which should not be confused with the material derivative $\left.\frac{du_r}{dr}\right|_{r_0}$ as the latter actually turns out to be equal to 1 for a given particle with fixed value of r_0.

On the other hand, the natural radial strain is defined as

$$\varepsilon_r = -\ln\left(\frac{dr}{dr_0}\right) \tag{2.59}$$

which can be rearranged to give

$$e^{-\varepsilon_r} = \frac{dr}{dr_0}=\frac{d(r_0+u_r)}{dr_0}=1+\frac{du_r}{dr}\frac{dr}{dr_0}=1+\frac{du_r}{dr}e^{-\varepsilon_r} \tag{2.60}$$

and therefore

$$\frac{du_r}{dr}=1-e^{\varepsilon_r} \tag{2.61}$$

Making use of the relation

$$\varepsilon_r=\varepsilon_v-\varepsilon_\theta=\varepsilon_v+\ln\left(\frac{r}{r_0}\right)=\varepsilon_v+\ln\left(\frac{1}{1-\xi}\right) \tag{2.62}$$

Eq. (2.61) can be further expressed as

$$\frac{du_r}{dr} = 1 - \frac{e^{\varepsilon_v}}{1-\xi} \tag{2.63}$$

The Eulerian spatial derivative $\frac{du_r}{dr}$ in the neighbourhood of a given particle thus has been converted to the Lagrangian form in terms of the field variables (ε_v and ξ) corresponding only to that material particle. Elimination of $\frac{du_r}{dr}$ from Eqs. (2.58) and (2.63), and after some manipulations, then results in an equation relating f to the other four variables $\sigma_r^{'}$, $\sigma_\theta^{'}$, $\sigma_z^{'}$, and ε_v as follows

$$f = \frac{\Delta}{b_{11}}\left[-\frac{\sigma_r^{'}-\sigma_\theta^{'}}{1-\xi-\frac{e^{\varepsilon_v}}{1-\xi}} - \frac{b_{11}-b_{12}}{\Delta(1-\xi)}\right] \tag{2.64}$$

Substituting Eq. (2.64) into Eqs. (2.56a)-(2.56d), the four governing differential equations finally reduce to

$$\frac{D\sigma_r^{'}}{D\xi} = -\frac{\sigma_r^{'}-\sigma_\theta^{'}}{1-\xi-\frac{e^{\varepsilon_v}}{1-\xi}} \tag{2.65a}$$

$$\frac{D\sigma_\theta^{'}}{D\xi} = -\frac{b_{21}}{b_{11}}\left[\frac{\sigma_r^{'}-\sigma_\theta^{'}}{1-\xi-\frac{e^{\varepsilon_v}}{1-\xi}} + \frac{b_{11}-b_{12}}{\Delta(1-\xi)}\right] - \frac{b_{22}-b_{21}}{\Delta(1-\xi)} \tag{2.65b}$$

$$\frac{D\sigma_z^{'}}{D\xi} = -\frac{b_{31}}{b_{11}}\left[\frac{\sigma_r^{'}-\sigma_\theta^{'}}{1-\xi-\frac{e^{\varepsilon_v}}{1-\xi}} + \frac{b_{11}-b_{12}}{\Delta(1-\xi)}\right] - \frac{b_{32}-b_{31}}{\Delta(1-\xi)} \tag{2.65c}$$

$$\frac{D\varepsilon_v}{D\xi} = -\frac{\Delta}{b_{11}}\left[\frac{\sigma_r^{'}-\sigma_\theta^{'}}{1-\xi-\frac{e^{\varepsilon_v}}{1-\xi}} + \frac{b_{11}-b_{12}}{\Delta(1-\xi)}\right] \tag{2.65d}$$

which can be readily solved as an initial value problem with the independent variable starting at $\xi = \xi_0$, provided that the initial values of $\sigma_r^{'}(\xi_0)$, $\sigma_\theta^{'}(\xi_0)$, $\sigma_z^{'}(\xi_0)$, and $\varepsilon_v(\xi_0)$ are given. Here ξ_0 corresponds to the value of $\frac{u_r}{r}$ of the specific particle when it is just entering into the plastic state.

2.4.3 ELASTIC-PLASTIC BOUNDARY AND INITIAL CONDITIONS

At the elastic-plastic interface r_p, it is clear that the stresses $\sigma_r^{'}(\xi_p)$, $\sigma_\theta^{'}(\xi_p)$, $\sigma_z^{'}(\xi_p)$ and the displacement $u_r(\xi_p)$, where $\xi_p = \left(\frac{u_r}{r}\right)_{r=r_p}$, must satisfy the elastic region solutions given by Eqs. (2.49)-(2.52), which leads to

$$\sigma_r^{'}(\xi_p) + \sigma_\theta^{'}(\xi_p) = \sigma_{r0}^{'} + \sigma_{\theta 0}^{'} = \frac{6K_0}{1+2K_0} P_0^{'} \tag{2.66}$$

$$\sigma_z^{'}(\xi_p) = \sigma_{z0}^{'} = \frac{3}{1+2K_0} P_0^{'} \tag{2.67}$$

$$\xi_p = \left(\frac{u_r}{r}\right)_{r=r_p} = \frac{\sigma_r^{'}(\xi_p) - \sigma_h^{'}}{2G} \tag{2.68}$$

$$\varepsilon_v(\xi_p) = 0 \tag{2.69}$$

$$P^{'}(\xi_p) = P_0^{'} \tag{2.70}$$

On the other hand, at r_p the material point is just starting to yield which demands the mean and deviator stress point to be located on the initial yield surface. That is

$$q(\xi_p) \equiv \sqrt{\frac{1}{2}\left\{\left[\sigma_r^{'}(\xi_p) - \sigma_\theta^{'}(\xi_p)\right]^2 + \left[\sigma_\theta^{'}(\xi_p) - \sigma_z^{'}(\xi_p)\right]^2 + \left[\sigma_r^{'}(\xi_p) - \sigma_z^{'}(\xi_p)\right]^2\right\}}$$

$$= \tan\beta_i \cdot P_0^{'} \tag{2.71}$$

If Eqs. (2.66), (2.67), and (2.71) are combined it is found that

$$\sigma_r^{'}(\xi_p) = \sigma_{r0}^{'} - \sqrt{{\sigma_{r0}^{'}}^2 - \frac{1}{3}[4{\sigma_{r0}^{'}}^2 + {\sigma_{z0}^{'}}^2 - 2\sigma_{r0}^{'}\sigma_{z0}^{'} - (\tan\beta_i \cdot P_0^{'})^2]} \tag{2.72}$$

$$\sigma_\theta^{'}(\xi_p) = \sigma_{r0}^{'} + \sqrt{{\sigma_{r0}^{'}}^2 - \frac{1}{3}[4{\sigma_{r0}^{'}}^2 + {\sigma_{z0}^{'}}^2 - 2\sigma_{r0}^{'}\sigma_{z0}^{'} - (\tan\beta_i \cdot P_0^{'})^2]} \tag{2.73}$$

Eqs. (2.67)-(2.69), together with Eqs. (2.72) and (2.73), allow to explicitly determine the stresses and volumetric strain in addition to the auxiliary variable at the current elastic-plastic interface r_p. Again, these expressions are independent of the radial

position of the elastic-plastic boundary, they are therefore also the solutions for ξ_0, $\sigma_r^{'}(\xi_0)$, $\sigma_\theta^{'}(\xi_0)$, $\sigma_z^{'}(\xi_0)$, and $\varepsilon_v(\xi_0)$ that serve as the initial conditions for solving the differential equation (2.65a)-(2.65d) pertaining to the given material particle. Once these initial values are obtained, then for any material point in the plastic region currently located at r, its stresses and volumetric strain can be readily solved as an initial value problem starting from $\xi = \xi_0$. In particular at the wellbore surface, the solutions can be found by putting $\xi(a) = \frac{a-a_0}{a} = 1 - \frac{a_0}{a}$ where a is already known.

However, it should be noted that the above differential equations (2.65a)-(2.65d) are expressed with respect to the auxiliary variable ξ rather than the particle position r. To complete the solutions, it is therefore necessary to establish a link between ξ and r. This can be achieved by rewriting Eq. (2.63) as

$$\frac{du_r}{dr} = \xi + r\frac{d\xi}{dr} = 1 - \frac{e^{\varepsilon_v}}{1-\xi} \tag{2.74}$$

and therefore

$$\frac{dr}{r} = \frac{d\xi}{1-\xi-\frac{e^{\varepsilon_v}}{1-\xi}} \tag{2.75}$$

where dr should be understood as the infinitesimal vector between two neighbouring points in the plastic zone ($\frac{dr}{r} \neq -d\varepsilon_\theta$). Integrating the above equation starting from the radius of the wellbore surface, one obtains

$$\frac{r}{a} = e^{\int_{\xi(a)}^{\xi} \frac{d\xi}{1-\xi-\frac{e^{\varepsilon_v}}{1-\xi}}} \tag{2.76}$$

which gives the current position of a particle r as a function of ξ in the integral form [the distribution of $\varepsilon_v(\xi)$ in the plastic zone, $\xi_p < \xi < \xi(a)$, is obtainable by solving Eqs. (2.65a)-(2.65d)]. As a special case, the position of the current elastic-plastic interface r_p

can be calculated as

$$\frac{r_p}{a} = e^{\int_{\xi(a)}^{\xi_p} \frac{d\xi}{1-\xi-\frac{e^{\xi}v}{1-\xi}}} \tag{2.77}$$

Finally, it is remarked that as with the undrained case, the solution procedure in this section for the plastic zone applies only to the situation that the wellbore pressure p_w (or the contracted borehole radius a) is small enough to produce plastic deformation around the wellbore. The critical borehole radius a_p corresponding to the onset of yielding at the wellbore surface can be determined in a similar way from Eq. (2.52) as

$$\frac{a_p}{a_0} = \frac{1}{1-\frac{\sigma_r'(\xi_p)-\sigma_h'}{2G}} \tag{2.78}$$

2.5 Results and Discussions

In this section some numerical results are presented for the wellbore drilling curves (the wellbore pressure p_w versus contracted radius a), the distributions of effective stresses, pore pressure (undrained case), and volumetric strain (drained case) around the borehole, as well as for the effective stress path (ESP) followed by a rock particle in the $P' - q$ plane. Table 2.1 summarizes all the parameters used in the calculation with the Drucker-Prager plastic hardening properties $\beta_i = 30^\circ$, $\beta_f = 60^\circ$, and $c = 0.01$.

Fig. 2.5 shows the variations of wellbore pressure p_w and the generated excess pore pressure at wellbore surface, $\Delta p(a)$, with the normalized wellbore radius $\frac{a_0}{a}$ for the undrained case. As expected, the borehole continually contracts ($\frac{a_0}{a}$ increases) when the wellbore pressure is gradually reduced, yielding initiating at the wellbore surface corresponding to a value of $p_w = 17.69$ MPa. After that, the plastic deformations will

Table 2.1. Parameters used in example analyses with hardening Drucker-Prager model

Plastic parameters: $\beta_i = 30°$, $\beta_f = 60°$, and $c = 0.01$								
$\sigma_{r0}^{'}$ (MPa)	$\sigma_{\theta 0}^{'}$ (MPa)	$\sigma_{z0}^{'}$ (MPa)	p_0 (MPa)	$P_0^{'}$ (MPa)	q_0 (MPa)	K_0	ν	G (MPa)
11.25	11.25	15	10	12.5	3.75	0.75	0.25	300

occur and $\frac{a_0}{a}$ increases more rapidly as the wellbore pressure decreases accompanied by the generation of significant negative pore pressure.

Fig. 2.6a shows the distributions of $\sigma_r^{'}$, $\sigma_\theta^{'}$, and $\sigma_z^{'}$ along the radial distance corresponding to a reduced wellbore pressure of $p_w = 0$ (the contracted wellbore radius $\frac{a_0}{a} = 1.046$), the radial axis being normalized with respect to the current borehole radius a. As can be seen, the effective radial stress exhibits a substantial relaxation in the plastic zone $1 < \frac{r}{a} < 2.82$, which is a well known feature of the elastoplastic solutions for cavity expansion and contraction problems (Hill, 1950; Yu, 2000). Fig. 2.6b displays the distributions of mean effective stress P', deviator stress q, and the excess pore pressure Δp around the borehole, also plotted against the normalized radial distance. It is found that the value of negative excess pore pressure increases steadily with the logarithm of $\frac{r}{a}$ near the wellbore, and becomes virtually equal to zero in the external elastic zone, which is indeed expected. The figure also clearly demonstrates that in the elastic region, both the effective vertical stress and mean stress remain constants and equal to their initial values. Note that since the material particles at different locations follow exactly the same

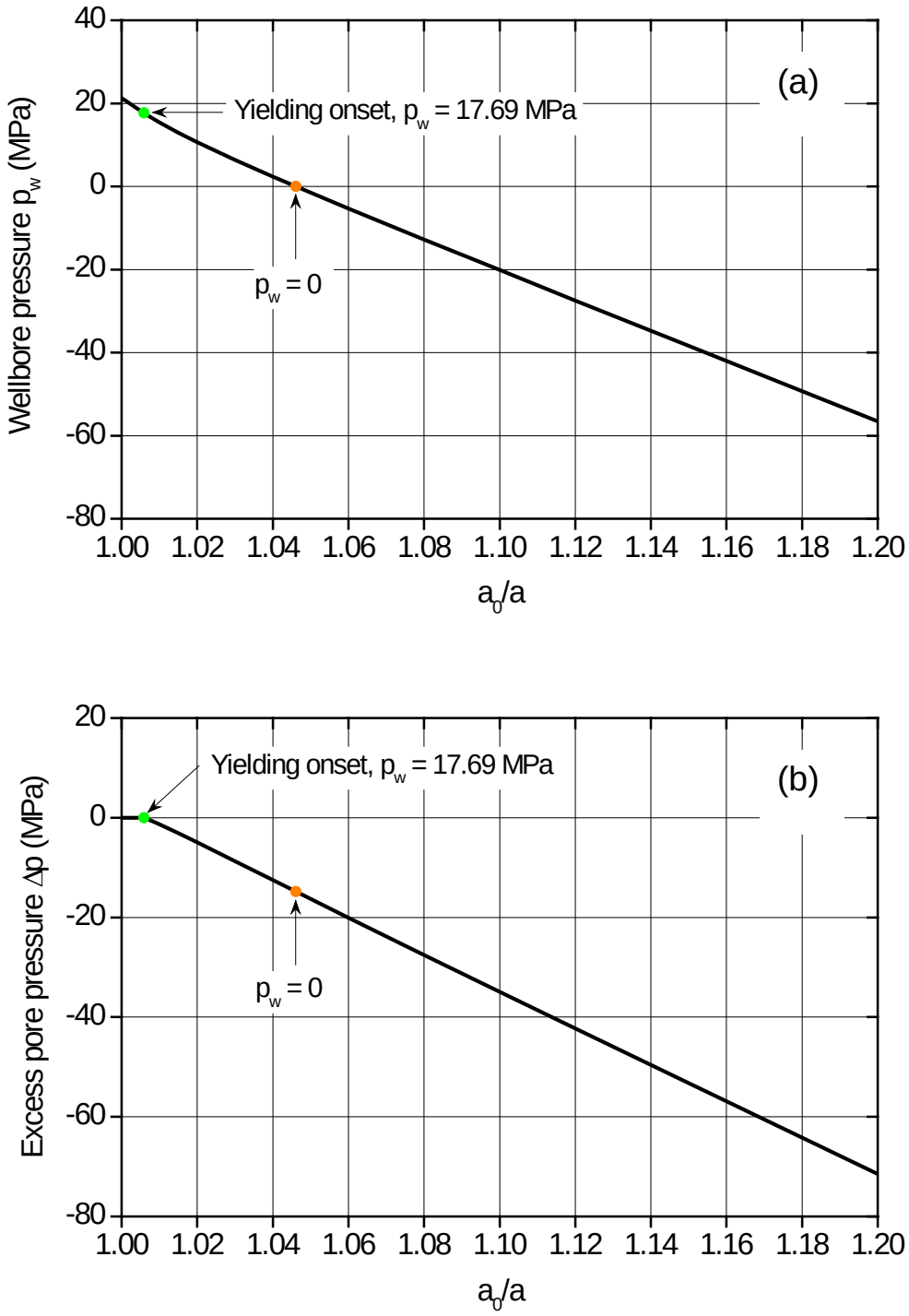

Fig. 2.5. Variations of (a) wellbore pressure; (b) pore pressure with normalized wellbore radius for undrained case

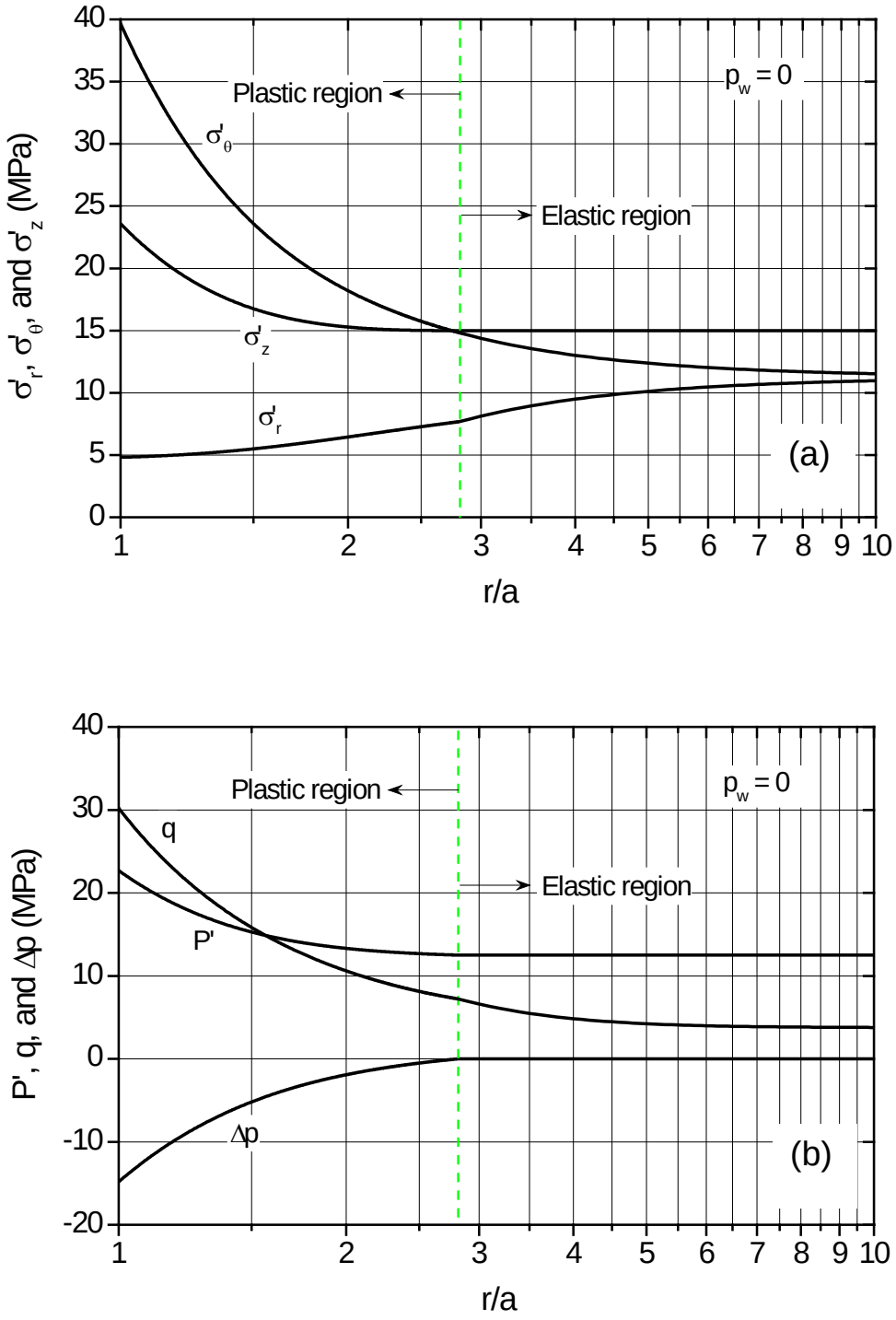

Fig. 2.6. Distributions of (a) effective radial, tangential, and vertical stresses; (b) effective mean, deviatoric stresses and excess pore pressure around the wellbore for undrained case

stress paths (but end at different positions), the curves in Fig. 2.6 represent also the stress and pore pressure changes experienced by any particular material particle.

Fig. 2.7 further plots the undrained effective stress path (ESP) followed in the $P' - q$ plane for a rock point at the wellbore surface. The in situ stress point (P_0', q_0) is located within the initial yield locus $F(P', q, \beta_i) = q - \tan\beta_i \cdot P'$. When the wellbore is drilled, the stress path first moves along a vertical line in the $P' - q$ plane until it hits the initial yield locus. After that the rock will experience plastic hardening and the yield locus has to expand (increasing β) to accommodate the new stress state. The stress path then turns upper-right and heads slowly towards the failure locus $F(P', q, \beta_f) = q - \tan\beta_f \cdot P'$.

Finally, Figs. 2.8-2.10 show the corresponding results for the drained situation, in which case the effective wellbore pressure is defined as $p_w' = p_w - p_0$ and the general features are found similar to those for the undrained condition. The characteristic relaxation of the effective radial stress, however, is not pronounced (Fig. 2.9a). Note that under drained condition, the excess pore pressure is essentially zero, so in Fig. 2.9b ε_v instead of Δp is included which decreases largely from zero to -0.0544 (in dilation) as $\frac{r}{a}$ decreases in the plastic zone $1 < \frac{r}{a} < 1.83$. Fig. 2.10 also indicates that under drained condition the $P' - q$ trajectory approaches more rapidly towards the failure line in comparison with the undrained case, even through for both cases the rock particle follows the same stress path during the elastic phase of deformation.

2.6 Summary

This chapter presents a rigorous analytical solution for undrained/drained wellbore

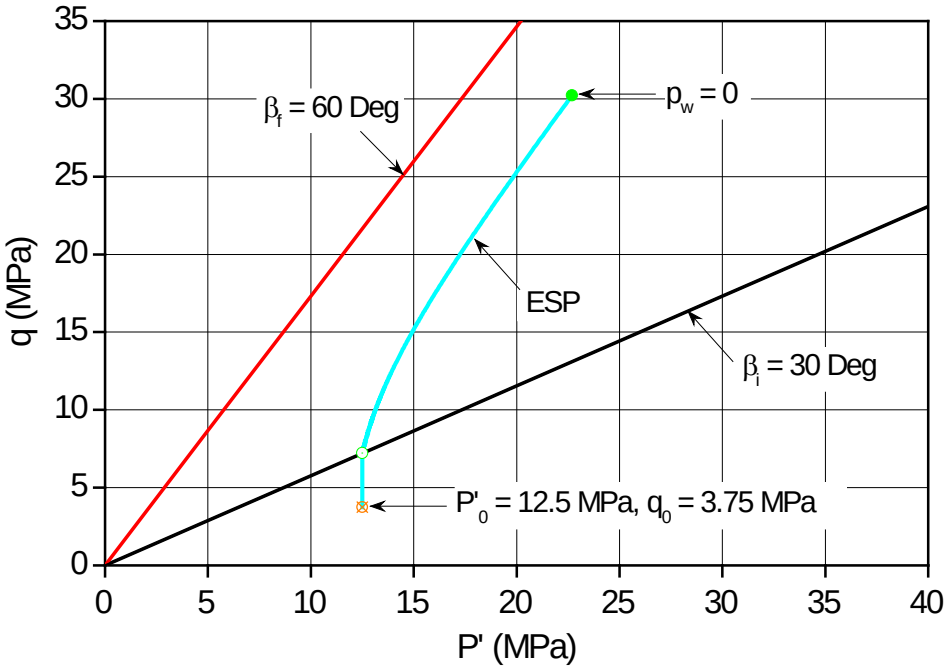

Fig. 2.7. P'-q stress path at wellbore surface for undrained case

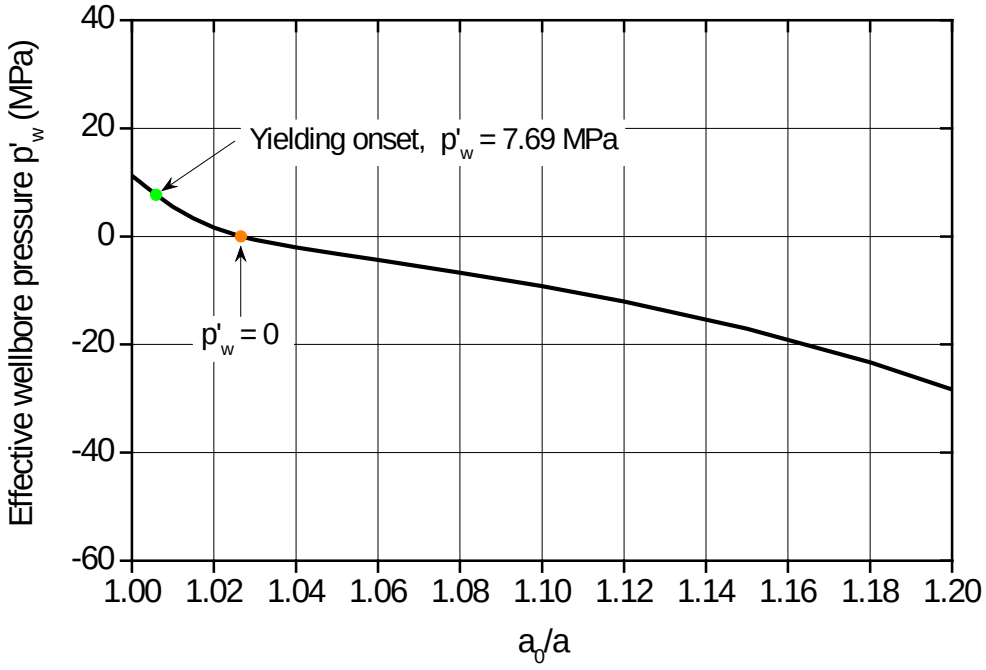

Fig. 2.8. Variations of wellbore pressure with normalized wellbore radius for drained case

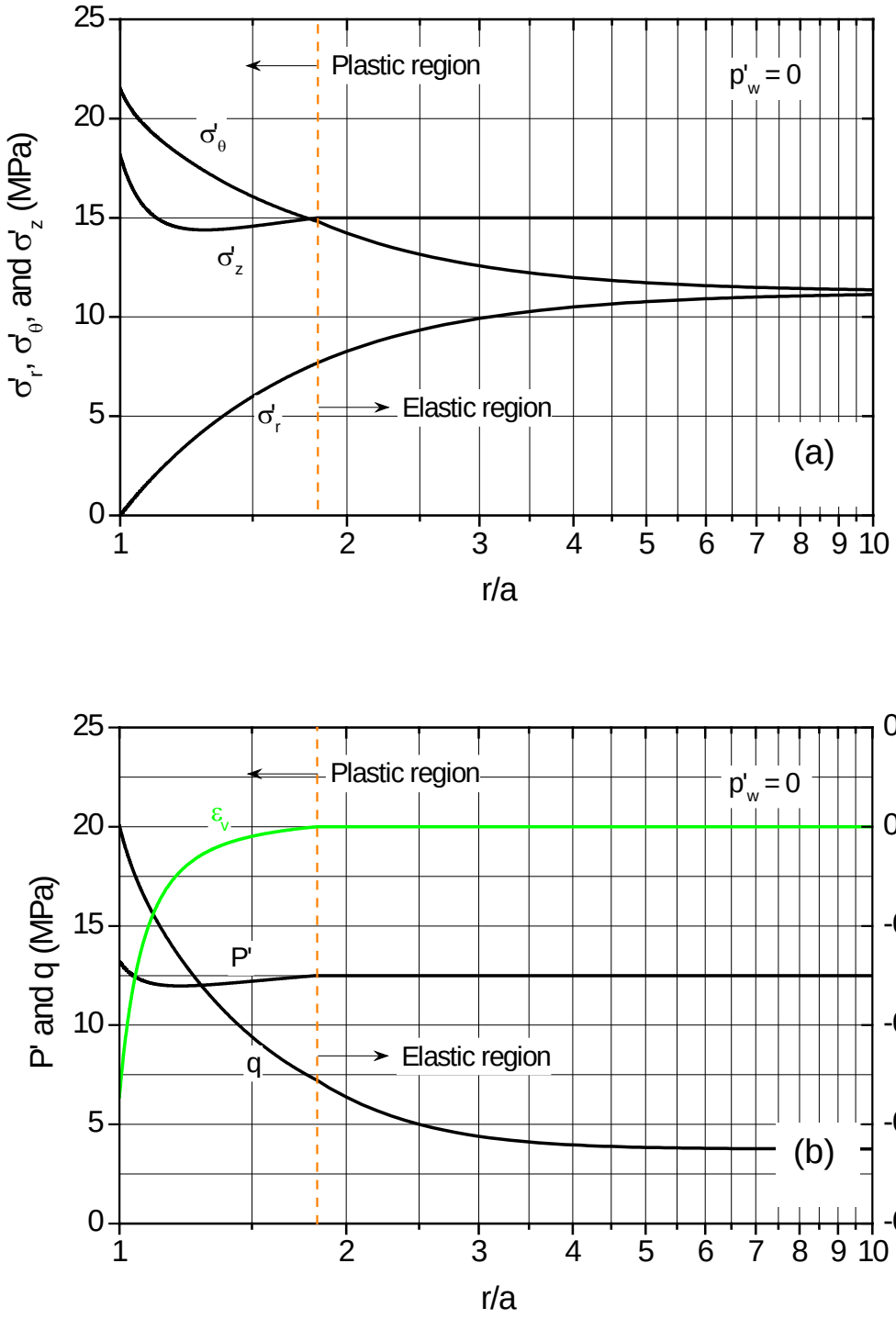

Fig. 2.9. Distributions of (a) effective radial, tangential, and vertical stresses; (b) effective mean, deviatoric stresses and volumetric strain around the wellbore for drained case

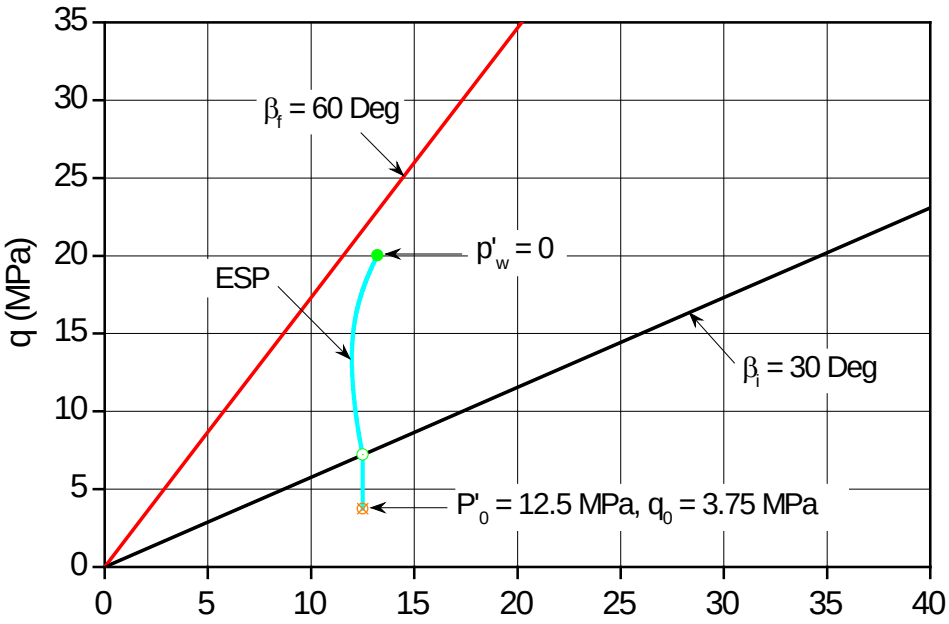

Fig. 2.10. P'-q stress path at wellbore surface for drained case

drilling boundary value problem by adopting the shear strain hardening Drucker-Prager plasticity model to describe the rock formation behaviour. The problem is found to be equivalent to solving a system of first order ordinary differential equations with the initial conditions known at the elastic-plastic boundary, and thus allows the radial, tangential, and vertical effective stresses as well as the excess pore pressure (undrained) and volumetric strain (drained) to be exactly determined. The results show that for undrained problem, the pore pressure remains constant during the elastic deformation but significant negative excess pore pressure may develop after the plastic yielding occurs. While for drained problem, the volumetric strain decreases rapidly from zero in going from the elastic-plastic boundary to the wellbore surface so the rock undergoes substantial dilation in the plastic region. For both the two cases, the $P' - q$ stress paths are first directed

vertically upwards, hitting the initial yield locus, and then move towards the failure yield locus.

CHAPTER 3

WELLBORE STABILITY ANALYSIS IN STRAIN HARDENING MOHR-COULOMB ROCKS

3.1 Introduction

The Mohr-Coulomb model is the most common plastic model employed in the context of geomaterials, in particular rocks. It differs from the previous Drucker-Prager model in that for Mohr-Coulomb model, both yield and strength are dependent on the third stress invariable, Lode's angle θ, in addition to on the mean effective stress P' and deviatoric stress q. In the three dimensional principal stress space Mohr-Coulomb yield function defines an irregular hexagonal cone, while the Drucker-Prager yield function gives a smooth cylindrical cone (see Fig. 2.2).

For the widely used elastic-perfectly plastic Mohr-Coulomb model, there is no hardening/softening law required so the yield surface is fixed in the space of principal stresses. However, as with the strain hardening Drucker-Prager model used in the previous chapter, in treating the wellbore drilling problem this chapter will adopt the shear strain hardening Mohr-Coulomb model to describe the rock formation behaviour where the friction angle is again assumed to vary hyperbolically with respect to the developed plastic shear strain. To simplify the mathematical derivation and allow for the possibility of analytical solutions, in the analysis the Mohr-Coulomb failure criterion is

approximated by the well known Matsuoka-Nakai criterion (Matsuoka & Nakai, 1974), and accordingly the friction hardening Mohr-Coulomb model will be adapted as the shear hardening Matsuoka-Nakai model. Following a similar approach as proposed in Chapter 2, the wellbore drilling problems under both drained and undrained conditions can still be reduced to solving a set of first-order simultaneous differential equations in the plastic zone, with the radial, tangential, and vertical stresses as well as the volumetric strain (for drained case only) being the basic unknowns. As an illustration example, the distributions of stress components, excess pore pressure (undrained case), and the volumetric strain (drained case) are presented against the radial distance, and the mean-deviatoric effective stress paths for a rock point at the wellbore surface are also examined.

3.2 Smoothed Strain Hardening Mohr-Coulomb Model (Matsuoka-Nakai Model)

The main drawback of Mohr-Coulomb model lies in that its yield surface in the principal stress space has six corners where the yield function is no more differentiable as in the Drucker-Prager model. The existence of such singular corner points will not only cause significant numerical difficulties in finite element analysis (Potts & Zdravkovic, 1999), but also make the derivation of analytical solution for wellbore drilling problem almost intractable due to the ununiqueness of partial derivatives with respect to the stress components, which are needed to determine the plastic strain increments [Eqs. (2.20a)-(2.20c)]. A good way to overcome such shortcoming is to round off the corners so that a smooth yield surface may be obtained. To achieve this, here a modified version of the Mohr-Coulomb criterion which was originally proposed by Matsuoka & Nakai (1974) will be used for the wellbore analysis.

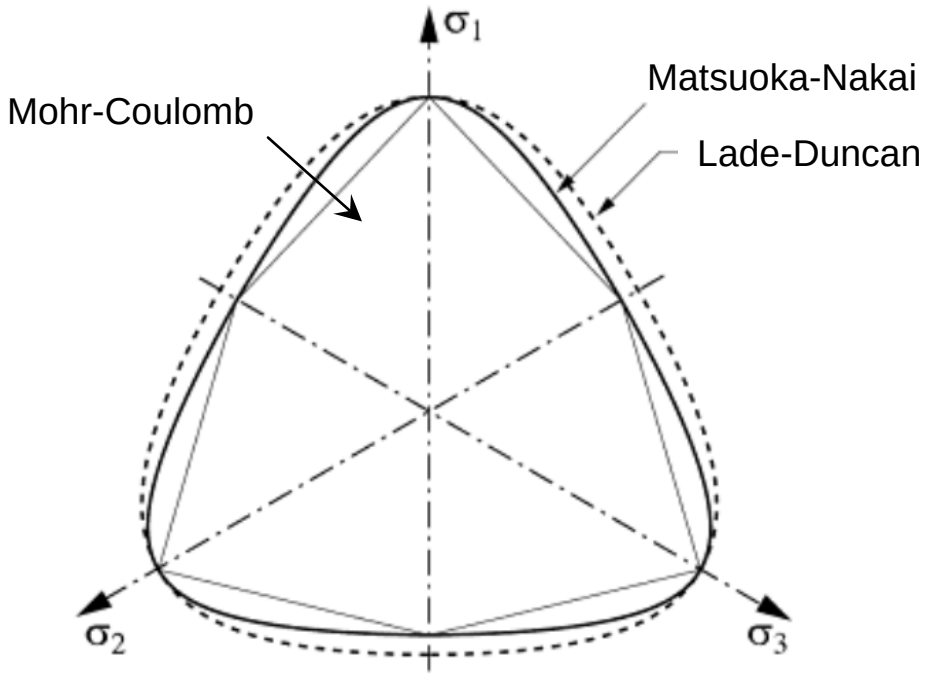

Fig. 3.1. Mohr-Coulomb, Matsuoka-Nakai, and Lade-Duncan's yield surfaces on deviatoric plane (modified after Hicher & Shao, 2008)

The Matsuoka-Nakai criterion matches the Mohr-Coulomb hexagon at both major and minor vertices. In Fig. 3.1 the cross section on the deviatioric plance of the Matsuoka-Nakai yield surface is compared with those of the Mohr-Coulomb and Lade-Duncan surfaces (Yu, 2006; Hicher & Shao, 2008). For wellbore drilling problem in which the radial, tangential, and vertical stresses are the three principal stresses, the yield function for the Matsuoka-Nakai model can be written as (Davis & Selvadurai, 2002)

$$F(\sigma_r^{'}, \sigma_\theta^{'}, \sigma_z^{'}, \chi) = \chi(\varphi)P^{'}(\sigma_r^{'}\sigma_\theta^{'} + \sigma_\theta^{'}\sigma_z^{'} + \sigma_r^{'}\sigma_z^{'}) - \sigma_r^{'}\sigma_\theta^{'}\sigma_z^{'} \quad (3.1)$$

where φ is the friction angle in Mohr-Coulomb model, and χ is a material parameter

which, to ensure that the Matsuoka-Nakai yield surface circumscribes the cohesionless Mohr-Coulomb hexagon, is related to φ by (Davis & Selvadurai, 2002)

$$\chi(\varphi) = \frac{3(1-\sin\varphi-\sin^2\varphi+\sin^3\varphi)}{9-9\sin\varphi-\sin^2\varphi+\sin^3\varphi} \tag{3.2}$$

Note that Eq. (3.1) is restricted to cohesionless rocks as it passes through the origin. Note also that as a smooth approximation of the shear hardening Mohr-Coulomb model, the hardening behaviour of the Matsuoka-Nakai model is reflected in parameter χ via φ. Returning to the Mohr-Coulomb model, the following hyperbolic relationship between φ and plastic deviatoric strain ε_q^p is assumed [recall Eq. (2.4)]

$$\tan\varphi = \frac{\varepsilon_q^p}{c+\varepsilon_q^p}\left(\tan\varphi_f - \tan\varphi_i\right) + \tan\varphi_i \tag{3.3}$$

where φ_i and φ_f are, respectively, the Mohr-Coulomb friction angles corresponding to the initial yield and failure loci; c is again a rock parameter which controls the shape of the hyperbolic function. Obviously, during the plastic hardening the Matsuoka-Nakai's parameter χ may vary from $\chi_i = \chi(\varphi_i)$ to $\chi_f = \chi(\varphi_f)$ with respect to ε_q^p through Eq. (3.2).

3.3 Undrained Solution

The derivation of the undrained solution for the wellbore boundary value problem using the above shear hardening Matsuoka-Nakai model is completely analogous to that for the Drucker-Prager model described in Chapter 2. Referring to Fig. 3.2, the equilibrium equation in the current configuration, for both the elastic and plastic regions, can be expressed in the total stress form as

$$\frac{\partial\sigma_r}{\partial r} + \frac{\sigma_r-\sigma_\theta}{r} = 0 \tag{3.4}$$

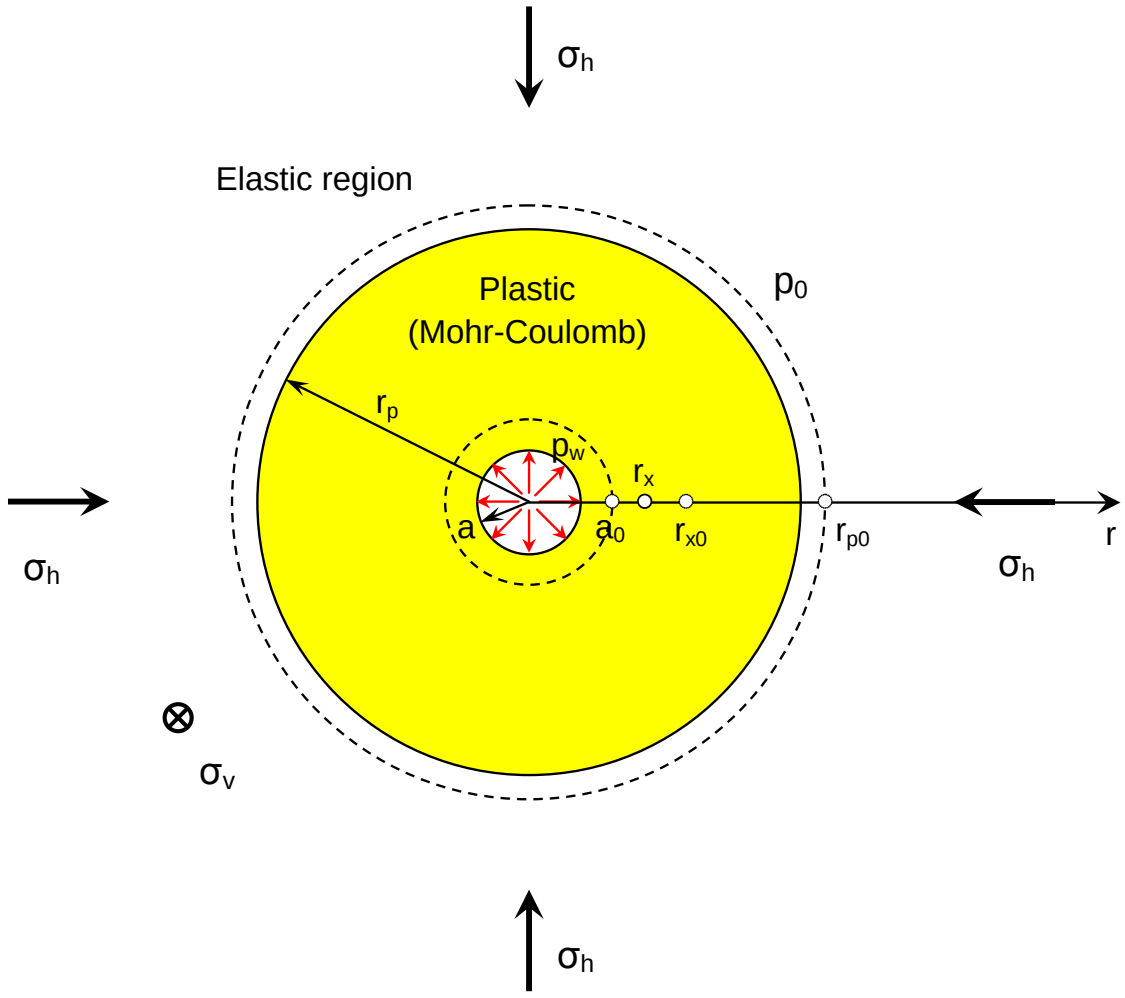

Fig. 3.2. Wellbore boundary value problem (Mohr-Coulomb model)

or alternatively,

$$\frac{\partial \sigma_r^{'}}{\partial r} + \frac{\partial p}{\partial r} + \frac{\sigma_r^{'} - \sigma_\theta^{'}}{r} = 0 \tag{3.5}$$

and the kinematic equation remains unchanged as

$$\frac{r_{x0}}{a} = \sqrt{\left(\frac{r_x}{a}\right)^2 + \left(\frac{a_0}{a}\right)^2 - 1} \tag{3.6}$$

3.3.1 ELASTIC ANALYSIS

In the elastic region $r \geq r_p$, the solutions for total stresses, radial displacement, and pore pressure are exactly the same as those in Chapter 2:

$$\sigma_r = \sigma_h + (\sigma_p - \sigma_h)\left(\frac{r_p}{r}\right)^2 \tag{3.7}$$

$$\sigma_\theta = \sigma_h - (\sigma_p - \sigma_h)\left(\frac{r_p}{r}\right)^2 \tag{3.8}$$

$$\sigma_z = \sigma_v \tag{3.9}$$

$$u_r = \frac{\sigma_p - \sigma_h}{2G}\frac{r_p^2}{r} \tag{3.10}$$

$$p = p_0 \tag{3.11}$$

where as before σ_p denotes the total radial stress at the elastic-plastic boundary $r = r_p$.

3.3.2 ELASTOPLASTIC ANALYSIS

For strain hardening Matsuoka-Nakai model assuming an associated condition, the plastic strain increments are obtained by differentiating Eq. (3.1)

$$d\varepsilon_r^p = \Lambda\frac{\partial F}{\partial \sigma_r'} = \Lambda\left\{\chi P'(\sigma_\theta' + \sigma_z') + \frac{1}{3}\chi(\sigma_r'\sigma_\theta' + \sigma_\theta'\sigma_z' + \sigma_r'\sigma_z') - \sigma_\theta'\sigma_z'\right\} \tag{3.12a}$$

$$d\varepsilon_\theta^p = \Lambda\frac{\partial F}{\partial \sigma_\theta'} = \Lambda\left\{\chi P'(\sigma_r' + \sigma_z') + \frac{1}{3}\chi(\sigma_r'\sigma_\theta' + \sigma_\theta'\sigma_z' + \sigma_r'\sigma_z') - \sigma_r'\sigma_z'\right\} \tag{3.12b}$$

$$d\varepsilon_z^p = \Lambda\frac{\partial F}{\partial \sigma_z'} = \Lambda\left\{\chi P'(\sigma_r' + \sigma_\theta') + \frac{1}{3}\chi(\sigma_r'\sigma_\theta' + \sigma_\theta'\sigma_z' + \sigma_r'\sigma_z') - \sigma_r'\sigma_\theta'\right\} \tag{3.12c}$$

From Eqs. (3.12a)-(3.12c) the required deviatoric plastic strain increments, $d\varepsilon_q^p$, can be found to be

$$d\varepsilon_q^p = \frac{\sqrt{2}}{3}\sqrt{(d\varepsilon_r^p - d\varepsilon_\theta^p)^2 + (d\varepsilon_\theta^p - d\varepsilon_z^p)^2 + (d\varepsilon_r^p - d\varepsilon_z^p)^2} = \frac{\sqrt{2}}{3}\Lambda\vartheta \tag{3.13}$$

where

$$\vartheta = \{(\sigma_r^{'} - \sigma_\theta^{'})^2(\chi P^{'} - \sigma_z^{'})^2 + (\sigma_r^{'} - \sigma_z^{'})^2(\chi P^{'} - \sigma_\theta^{'})^2 + (\sigma_z^{'} - \sigma_\theta^{'})^2(\chi P^{'} - \sigma_r^{'})^2\}^{1/2} \quad (3.14)$$

Whilst the shear hardening rule, Eq. (3.3), can be rewritten in the incremental form as follows

$$d\varepsilon_q^p = c\frac{\tan\varphi_f - \tan\varphi_i}{(\tan\varphi_f - \tan\varphi)^2}\frac{1}{\cos^2\varphi}d\varphi \quad (3.15)$$

On the other hand, carrying out the differentiation of the yield equation (3.1) gives

$$d\chi = \chi^{'}(\varphi)d\varphi = -\frac{\frac{\partial F}{\partial \sigma_r^{'}}d\sigma_r^{'} + \frac{\partial F}{\partial \sigma_\theta^{'}}d\sigma_\theta^{'} + \frac{\partial F}{\partial \sigma_z^{'}}d\sigma_z^{'}}{P^{'}(\sigma_r^{'}\sigma_\theta^{'} + \sigma_\theta^{'}\sigma_z^{'} + \sigma_r^{'}\sigma_z^{'})} \quad (3.16)$$

where

$$\chi^{'}(\varphi) = \frac{3A(\varphi)}{(9 - 9\sin\varphi - \sin^2\varphi + \sin^3\varphi)^2} \quad (3.17)$$

and

$$A(\varphi) = (9 - 9\sin\varphi - \sin^2\varphi + \sin^3\varphi)(-\cos\varphi - \sin 2\varphi + 3\sin^2\varphi\cos\varphi) - (1 - \sin\varphi - \sin^2\varphi + \sin^3\varphi)(-9\cos\varphi - \sin 2\varphi + 3\sin^2\varphi\cos\varphi) \quad (3.18)$$

Substituting Eqs. (3.15)-(3.17) back into Eq. (3.13) then results in the following

$$\Lambda = y\left\{\frac{\partial F}{\partial \sigma_r^{'}}d\sigma_r^{'} + \frac{\partial F}{\partial \sigma_\theta^{'}}d\sigma_\theta^{'} + \frac{\partial F}{\partial \sigma_z^{'}}d\sigma_z^{'}\right\} \quad (3.19)$$

where

$$y = -\frac{1}{\sqrt{2}}\frac{c(\tan\varphi_f - \tan\varphi_i)}{\vartheta(\tan\varphi_f - \tan\varphi)^2\cos^2\varphi} \cdot \frac{(9 - 9\sin\varphi - \sin^2\varphi + \sin^3\varphi)^2}{A(\varphi)P^{'}(\sigma_r^{'}\sigma_\theta^{'} + \sigma_\theta^{'}\sigma_z^{'} + \sigma_r^{'}\sigma_z^{'})} \quad (3.20)$$

Defining the following notations

$$a_r = \frac{\partial F}{\partial \sigma_r^{'}} = \chi P^{'}(\sigma_\theta^{'} + \sigma_z^{'}) + \frac{1}{3}\chi(\sigma_r^{'}\sigma_\theta^{'} + \sigma_\theta^{'}\sigma_z^{'} + \sigma_r^{'}\sigma_z^{'}) - \sigma_\theta^{'}\sigma_z^{'} \quad (3.21a)$$

$$a_\theta = \frac{\partial F}{\partial \sigma_\theta^{'}} = \chi P^{'}(\sigma_r^{'} + \sigma_z^{'}) + \frac{1}{3}\chi(\sigma_r^{'}\sigma_\theta^{'} + \sigma_\theta^{'}\sigma_z^{'} + \sigma_r^{'}\sigma_z^{'}) - \sigma_r^{'}\sigma_z^{'} \quad (3.21b)$$

$$a_z = \frac{\partial F}{\partial \sigma_z^{'}} = \chi P^{'}(\sigma_r^{'} + \sigma_\theta^{'}) + \frac{1}{3}\chi(\sigma_r^{'}\sigma_\theta^{'} + \sigma_\theta^{'}\sigma_z^{'} + \sigma_r^{'}\sigma_z^{'}) - \sigma_r^{'}\sigma_\theta^{'} \quad (3.21c)$$

and substituting Eqs. (3.19) into Eqs. (3.12a)-(3.12c) gives the desired expressions for the plastic strain increments as follows

$$\begin{Bmatrix} d\varepsilon_r^p \\ d\varepsilon_\theta^p \\ d\varepsilon_z^p \end{Bmatrix} = y \begin{bmatrix} a_r^2 & a_r a_\theta & a_r a_z \\ a_\theta a_r & a_\theta^2 & a_\theta a_z \\ a_z a_r & a_z a_\theta & a_z^2 \end{bmatrix} \cdot \begin{Bmatrix} d\sigma_r^{'} \\ d\sigma_\theta^{'} \\ d\sigma_z^{'} \end{Bmatrix} \tag{3.22}$$

Note that according to Eq. (3.2),

$$\varphi = \arcsin\sqrt{\frac{9\chi-3}{\chi-3}} \tag{3.23}$$

so y, a_r, a_θ, and a_z on the right hand side of Eq. (3.22) are all explicit functions of the three stress components $\sigma_r^{'}$, $\sigma_\theta^{'}$, and $\sigma_z^{'}$.

It is useful to recognize that Eq. (3.22) has the same form as Eq. (2.24) for the Drucker-Prager model, except that y, a_r, a_θ, and a_z should now be replaced by Eqs. (3.20) and (3.21a)-(3.21c) corresponding to the present Matsuoka-Nakai model. Consequently, Eqs. (2.25)-(2.33c) in Chapter 2 for determining the stress components would also be applicable and the three first order ordinary differential equations are

$$\frac{D\sigma_r^{'}}{Dr} - \frac{b_{11}-b_{12}}{\Delta r} = 0 \tag{3.24a}$$

$$\frac{D\sigma_\theta^{'}}{Dr} - \frac{b_{21}-b_{22}}{\Delta r} = 0 \tag{3.24b}$$

$$\frac{D\sigma_z^{'}}{Dr} - \frac{b_{31}-b_{32}}{\Delta r} = 0 \tag{3.24c}$$

where b_{ij} and Δ have been previously defined in Eqs. (2.29a)-(2.29j). As discussed in Section 2.3, this set of equations are valid for any material point r_x currently located in the plastic zone (see Fig. 3.2), and to solve the three stress components one needs a prior knowledge of r_{xp} as well as the corresponding initial values $\sigma_r^{'}(r_{xp})$, $\sigma_\theta^{'}(r_{xp})$, and $\sigma_z^{'}(r_{xp})$, where r_{xp} represents the position of the specific particle when it just enters into the

plastic state.

3.3.3 Initial Stress Conditions and Elastic-Plastic Boundary

The determination of the value of r_{xp} and the corresponding stress components is quite similar to the one for the Drucker-Prager model. On one hand, the three effective stresses must satisfy the elastic solutions (3.7)-(3.9) and (3.11), which gives

$$\sigma_r^{'}(r_{xp}) + \sigma_\theta^{'}(r_{xp}) = \sigma_{r0}^{'} + \sigma_{\theta 0}^{'} = \frac{6K_0}{1+2K_0} P_0^{'} \tag{3.25}$$

$$\sigma_z^{'}(r_{xp}) = \sigma_{z0}^{'} = \frac{3}{1+2K_0} P_0^{'} \tag{3.26}$$

where $\sigma_{r0}^{'}$, $\sigma_{\theta 0}^{'}$, and $\sigma_{z0}^{'}$ are the initial effective stresses; and K_0 the coefficient of earth pressure at rest.

On the other hand, the same stresses need to be located on the initial yield surface which requires

$$\chi(\varphi_i) P_0^{'}\left[\sigma_r^{'}(r_{xp})\sigma_\theta^{'}(r_{xp}) + \sigma_\theta^{'}(r_{xp})\sigma_z^{'}(r_{xp}) + \sigma_r^{'}(r_{xp})\sigma_z^{'}(r_{xp})\right] - \sigma_r^{'}(r_{xp})\sigma_\theta^{'}(r_{xp})\sigma_z^{'}(r_{xp}) = 0 \tag{3.27}$$

where use is made of $P^{'}(r_{xp}) = P_0^{'}$ since according to Eqs. (3.7)-(3.9) and (3.11), the mean effective stress remains unchanged during the elastic deformation. On combining Eqs. (3.25)-(3.27), one obtains

$$\sigma_r^{'}(r_{xp})\sigma_\theta^{'}(r_{xp}) = \frac{\chi(\varphi_i)\left(\frac{3}{1+2K_0}P_0^{'}\right)\left(\frac{6K_0}{1+2K_0}P_0^{'}\right)}{\frac{3}{1+2K_0} - \chi(\varphi_i)} \tag{3.28}$$

and

$$\sigma_r^{'}(r_{xp}) = \frac{3K_0}{1+2K_0} P_0^{'} - \sqrt{\left(\frac{3K_0}{1+2K_0} P_0^{'}\right)^2 - \frac{\chi(\varphi_i)\left(\frac{3}{1+2K_0}P_0^{'}\right)\left(\frac{6K_0}{1+2K_0}P_0^{'}\right)}{\frac{3}{1+2K_0} - \chi(\varphi_i)}} \tag{3.29}$$

$$\sigma_\theta^{'}(r_{xp}) = \frac{3K_0}{1+2K_0}P_0^{'} + \sqrt{\left(\frac{3K_0}{1+2K_0}P_0^{'}\right)^2 - \frac{\chi(\varphi_i)\left(\frac{3}{1+2K_0}P_0^{'}\right)\left(\frac{6K_0}{1+2K_0}P_0^{'}\right)}{\frac{3}{1+2K_0}-\chi(\varphi_i)}} \tag{3.30}$$

Finally, in analogous to the analysis for Drucker-Prager model, the corresponding expressions for r_{xp}, r_p, and the critical borehole radius a_p in the Matsuoka-Nakai case are given by

$$\frac{r_{xp}}{a} = \frac{1}{1-\frac{\sigma_{rp}^{'}-\sigma_{r0}^{'}}{2G}}\sqrt{\left(\frac{r_x}{a}\right)^2 + \left(\frac{a_0}{a}\right)^2 - 1} \tag{3.31}$$

$$\frac{r_p}{a} = \sqrt{\frac{\left(\frac{a_0}{a}\right)^2-1}{\left(\frac{\sigma_{rp}^{'}-\sigma_{r0}^{'}}{2G}\right)^2-\frac{\sigma_{rp}^{'}-\sigma_{r0}^{'}}{G}}} \tag{3.32}$$

$$\frac{a_p}{a_0} = \frac{1}{1-\frac{\sigma_{rp}^{'}-\sigma_{r0}^{'}}{2G}} \tag{3.33}$$

3.3.4 Excess Pore Pressure in Plastic Zone

In the plastic zone $a \le r \le r_p$, the calculated effective stresses as given by Eqs. (3.24a)-(3.24c) allows the distribution of pore pressure $p(r_x)$ to be determined from the equilibrium equation (3.5) by integration as follows

$$p(r_x) = \sigma_{rp}^{'} + p_0 - \sigma_r^{'}(r_x) - \int_{r_p}^{r_x}\frac{\sigma_r^{'}-\sigma_\theta^{'}}{r}dr \tag{3.34}$$

and the excess pore pressure is therefore $\Delta p(r_x) = p(r_x) - p_0$.

3.4 Drained Solution

The drained wellbore drilling problem in shear hardening Matsuoka-Nakai rocks can again be dealt with using the same procedure as outlined in Section 2.4, Chapter 2 for the strain hardening Drucker-Prager model. Since all the equilibrium and deformation

equations in addition to the flow rule and boundary conditions take almost the same forms for these two models, the resulting solutions must exhibit close similarity to each other. The only exception is that for shear strain hardening Matsuoka-Nakai model, the counterpart expressions of y, a_r, a_θ, and a_z, i.e., Eqs. (3.20) and (3.21a)-(3.21c), will be needed in the derivation of the four governing differential equations for the plastic zone solution. In the following only some key equations for the drained problem in Matsuoka-Nakai rock formations will be listed for completeness.

3.4.1 Elastic Analysis

The solutions for effective stresses and radial displacement in the elastic region $r \geq r_p$:

$$\sigma_r^{'} = \sigma_h^{'} + (\sigma_p^{'} - \sigma_h^{'}) \left(\frac{r_p}{r}\right)^2 \tag{3.35}$$

$$\sigma_\theta^{'} = \sigma_h^{'} - (\sigma_p^{'} - \sigma_h^{'}) \left(\frac{r_p}{r}\right)^2 \tag{3.36}$$

$$\sigma_z^{'} = \sigma_v^{'} \tag{3.37}$$

$$u_r = \frac{\sigma_p^{'} - \sigma_h^{'}}{2G} \frac{r_p^2}{r} \tag{3.38}$$

where $\sigma_h^{'} = \sigma_h - p_0$; $\sigma_v^{'} = \sigma_v - p_0$; and $\sigma_p^{'}$ denotes the effective radial stress at the elastic-plastic boundary $r = r_p$.

3.4.2 Elastoplastic Analysis

The four governing differential equations in the plastic region $a \leq r \leq r_p$:

$$\frac{D\sigma_r^{'}}{D\xi} = -\frac{\sigma_r^{'} - \sigma_\theta^{'}}{1 - \xi - \frac{e^{\varepsilon} v}{1-\xi}} \tag{3.39a}$$

$$\frac{D\sigma_\theta^{'}}{D\xi} = -\frac{b_{21}}{b_{11}}\left[\frac{\sigma_r^{'}-\sigma_\theta^{'}}{1-\xi-\frac{e^{\varepsilon v}}{1-\xi}} + \frac{b_{11}-b_{12}}{\Delta(1-\xi)}\right] - \frac{b_{22}-b_{21}}{\Delta(1-\xi)} \tag{3.39b}$$

$$\frac{D\sigma_z^{'}}{D\xi} = -\frac{b_{31}}{b_{11}}\left[\frac{\sigma_r^{'}-\sigma_\theta^{'}}{1-\xi-\frac{e^{\varepsilon v}}{1-\xi}} + \frac{b_{11}-b_{12}}{\Delta(1-\xi)}\right] - \frac{b_{32}-b_{31}}{\Delta(1-\xi)} \tag{3.39c}$$

$$\frac{D\varepsilon_v}{D\xi} = -\frac{\Delta}{b_{11}}\left[\frac{\sigma_r^{'}-\sigma_\theta^{'}}{1-\xi-\frac{e^{\varepsilon v}}{1-\xi}} + \frac{b_{11}-b_{12}}{\Delta(1-\xi)}\right] \tag{3.39d}$$

where $\xi = \frac{u_r}{r} = \frac{r-r_0}{r}$ is an auxiliary independent variable introduced to transform the radial equilibrium equation in Eulerian description to an equivalent one in Lagrangian description, i.e., Eq. (3.39d). The above equations enable us to solve the four basic unknowns, $\sigma_r^{'}$, $\sigma_\theta^{'}$, $\sigma_z^{'}$, and ε_v, as an initial value problem with the independent variable starting at $\xi = \xi_0$, where the initial values of $\sigma_r^{'}(\xi_0)$, $\sigma_\theta^{'}(\xi_0)$, $\sigma_z^{'}(\xi_0)$, and $\varepsilon_v(\xi_0)$ can be specified from the external elastic solutions together with the initial yielding condition. Be reminded that ξ_0 corresponds to the value of $\frac{u_r}{r}$ of the specific particle when it enters into the plastic state.

3.4.3 INITIAL CONDITIONS AND ELASTIC-PLASTIC BOUNDARY

The initial values of ξ_0 and stresses at the instant the material particle starts to yield:

$$\xi_0 = \left(\frac{u_r}{r}\right)_{r=r_{xp}} = \frac{\sigma_r^{'}(\xi_0)-\sigma_h^{'}}{2G} \tag{3.40}$$

$$\sigma_r^{'}(\xi_0) = \frac{3K_0}{1+2K_0}P_0^{'} - \sqrt{\left(\frac{3K_0}{1+2K_0}P_0^{'}\right)^2 - \frac{\chi(\varphi_i)\left(\frac{3}{1+2K_0}P_0^{'}\right)\left(\frac{6K_0}{1+2K_0}P_0^{'}\right)}{\frac{3}{1+2K_0}-\chi(\varphi_i)}} \tag{3.41}$$

$$\sigma_\theta^{'}(\xi_0) = \frac{3K_0}{1+2K_0}P_0^{'} + \sqrt{\left(\frac{3K_0}{1+2K_0}P_0^{'}\right)^2 - \frac{\chi(\varphi_i)\left(\frac{3}{1+2K_0}P_0^{'}\right)\left(\frac{6K_0}{1+2K_0}P_0^{'}\right)}{\frac{3}{1+2K_0}-\chi(\varphi_i)}} \tag{3.42}$$

$$\sigma_z^{'}(\xi_0) = \sigma_{z0}^{'} = \frac{3}{1+2K_0}P_0^{'} \tag{3.43}$$

$$\varepsilon_v(\xi_0) = 0 \tag{3.44}$$

and the relation between particle position r and the auxiliary variable ξ

$$\frac{r}{a} = e^{\int_{\xi(a)}^{\xi} \frac{d\xi}{1-\xi-\frac{e^{\varepsilon_v}}{1-\xi}}} \tag{3.45}$$

where the distribution of $\varepsilon_v(\xi)$ in the plastic zone, $\xi_0 < \xi < \xi(a) = 1 - \frac{a_0}{a}$, is obtainable by solving Eqs. (3.39a)-(3.39d). As a special case, the position of the current elastic-plastic interface r_p can be calculated as

$$\frac{r_p}{a} = e^{\int_{\xi(a)}^{\xi_0} \frac{d\xi}{1-\xi-\frac{e^{\varepsilon_v}}{1-\xi}}} \tag{3.46}$$

Finally, the critical borehole radius a_p

$$\frac{a_p}{a_0} = \frac{1}{1-\frac{\sigma_r'(\xi_p)-\sigma_h'}{2G}} \tag{3.47}$$

3.5 Results and Discussions

In this section some numerical results are presented in Figs. 3.3-3.5 for the undrained solution and in Figs. 3.6-3.8 for the drained solution. They are based on the parameters listed in Table 3.1 which are almost the same as those for the hardening Drucker-Prager model (Table 2.1) except for the two frictions angles ($\varphi_i = 15^\circ$ and $\varphi_f = 45^\circ$).

Fig. 3.3 shows the wellbore pressure p_w and the induced excess pore pressure at wellbore surface, $\Delta p(a)$, as functions of normalized wellbore radius $\frac{a_0}{a}$ for the undrained case. The variation trends are basically similar to those for the strain hardening Drucker-Prager model. For instance, during the elastic phase of deformation no excess pore pressure builds up but it could become very large (negative) after the plastic deformation

Table 3.1. Parameters used in example analyses with hardening Mohr-Coulomb model

Plastic parameters: $\varphi_i = 15^\circ$ ($\chi_i = 0.313$), $\varphi_f = 45^\circ$ ($\chi_f = 0.176$), and $c = 0.01$								
$\sigma_{r0}^{'}$ (MPa)	$\sigma_{\theta 0}^{'}$ (MPa)	$\sigma_{z0}^{'}$ (MPa)	p_0 (MPa)	$P_0^{'}$ (MPa)	q_0 (MPa)	K_0	ν	G (MPa)
11.25	11.25	15	10	12.5	3.75	0.75	0.25	300

occurs. The wellbore pressure corresponding to the onset of yielding at the wellbore surface is $p_w = 18.55$ MPa, which is comparable with the value of $p_w = 17.69$ MPa for the Drucker-Prager model as a result of similar parameters used in these two calculations.

The distributions of $\sigma_r^{'}$, $\sigma_\theta^{'}$, and $\sigma_z^{'}$ as well as of P', q, and Δp along the distance from the borehole are given in Figs. 3.4. The results are presented, once more, for the situation of zero wellbore pressure, which corresponds to a contracted wellbore radius of $\frac{a_0}{a} = 1.049$. Analogous to Fig. 2.6a, the substantial relaxation of the effective radial stress $\sigma_r^{'}$ is again clearly observed in Fig. 3.4a for the plastic zone $1 < \frac{r}{a} < 3.33$. Notice that in the elastic region, the excess pore pressure is always equal to zero and both $\sigma_z^{'}$ and P' remain unchanged equal to their initial values.

Fig. 3.5 shows the undrained $P^{'} - q$ stress path of a rock particle located at the wellbore surface during the reduction of wellbore pressure from $p_w = 21.25$ MPa to 0. The initial stress state is given by point A. When the stress path moves vertically reaching the initial yield surface with friction angle $\varphi_i = 15^\circ$ ($\chi_i = 0.313$) at point B, the rock tends to harden plastically, and the yield surface will expand as the plastic deviatoric

strain increases (increasing φ but decreasing χ). Simultaneously, the stress path will bend upper-right towards the failure surface with $\varphi = \varphi_f$, until it reaches point C when $p_w = 0$. It is worth noting that in Fig. 3.5 the projection of the Matsuoka-Nakai yield surface on the $P' - q$ plane is not a single straight line but instead a fan-shaped area bounded by two lines which correspond to the triaxial compression and triaxial extension conditions, respectively. This is because for Matsuoka-Nakai (or Mohr-Coulomb) model, the yield surface in the principal stress space is no longer a surface of revolution about the hydrostatic axis ($\sigma_r' = \sigma_\theta' = \sigma_z'$), but Lode's angle dependent. As a consequence, even though the stress path shoots into the fan-shaped area relevant to the failure surface ($\varphi_f = 45°$), it does not necessarily mean that the stress points are in failure state (lie on the failure yield surface).

The results for the drained condition are further plotted in Figs. 3.6-3.8. For this case, the effective wellbore pressure $p_w' = p_w - p_0$ falls down sharply as $\frac{a_0}{a}$ increases and quickly reaches a limiting value of $p_w' = 0$. Therefore, in Figs. 3.7-3.8 for the stress distributions and stress path history, a wellbore pressure of $p_w' = 1$ MPa instead of zero is used for the calculation. It is also interesting to note that after yielding (point B in Fig. 3.8), unlike the undrained situation, the stress path bends over and moves towards decreasing P' and q provided that the wellbore pressure has sufficiently decreased. However, the stress ratio $\frac{q}{P'}$ is found to have been increasing continuously from point B to C even when the two stress invariants tend to approach zero.

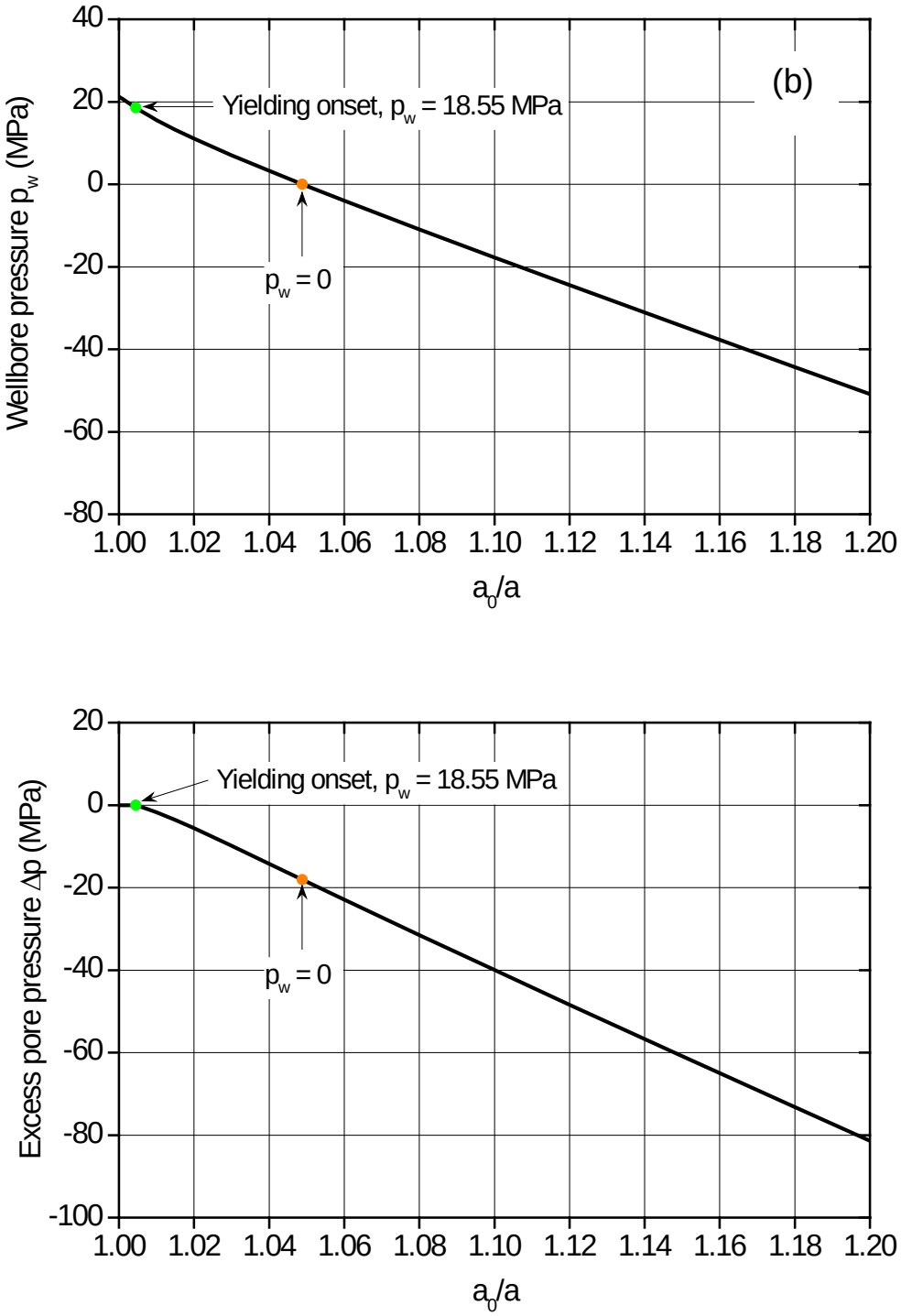

Fig. 3.3. Variations of (a) wellbore pressure; (b) pore pressure with normalized wellbore radius for undrained case

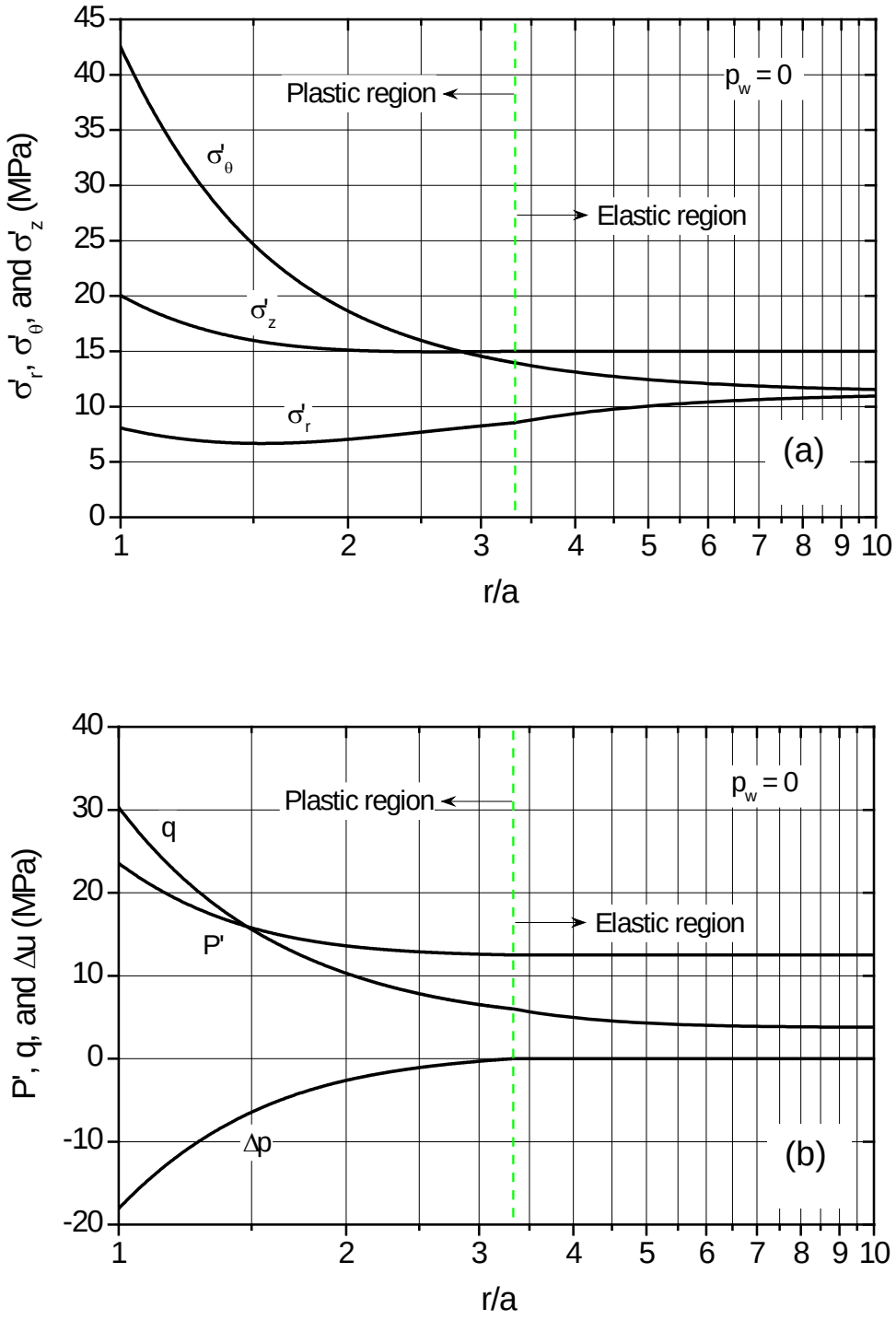

Fig. 3.4. Distributions of (a) effective radial, tangential, and vertical stresses; (b) effective mean, deviatoric stresses and excess pore pressure around the wellbore for undrained case

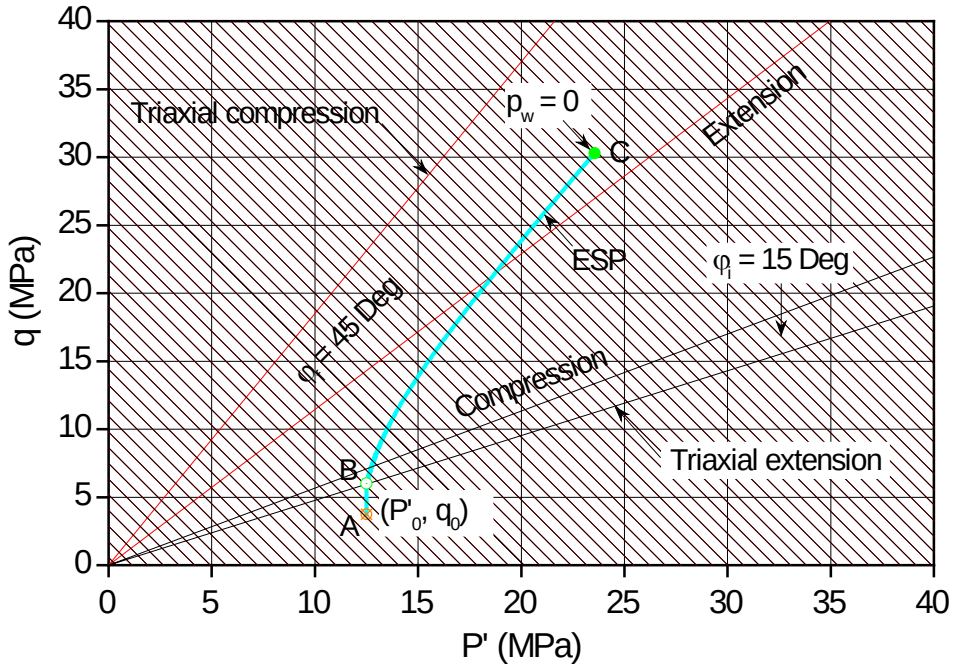

Fig. 3.5. P'-q stress path at wellbore surface for undrained case

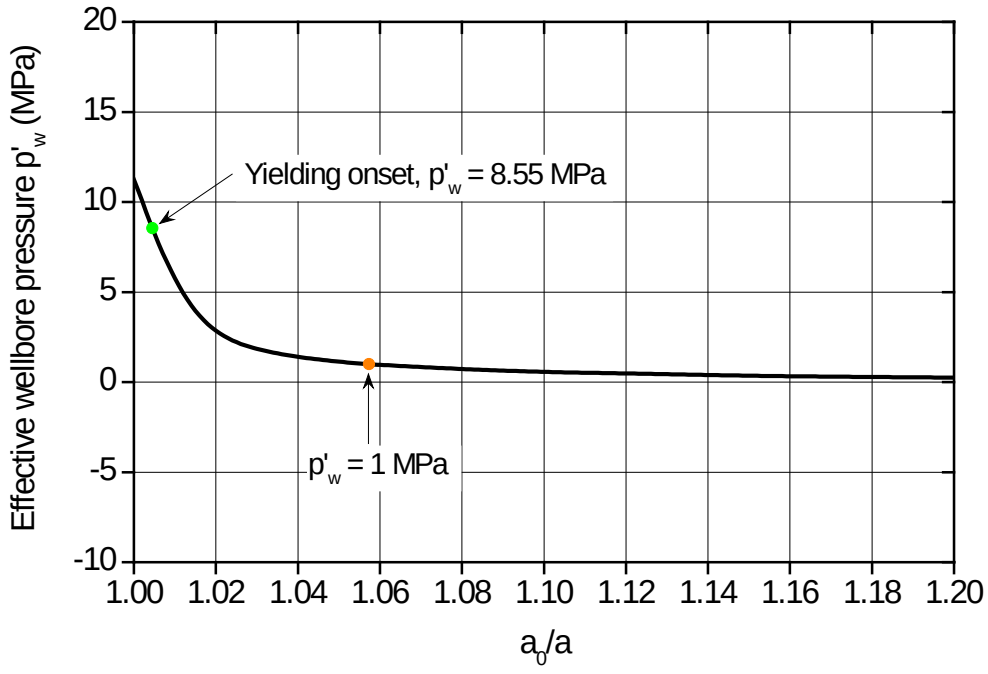

Fig. 3.6. Variations of wellbore pressure with normalized wellbore radius for drained case

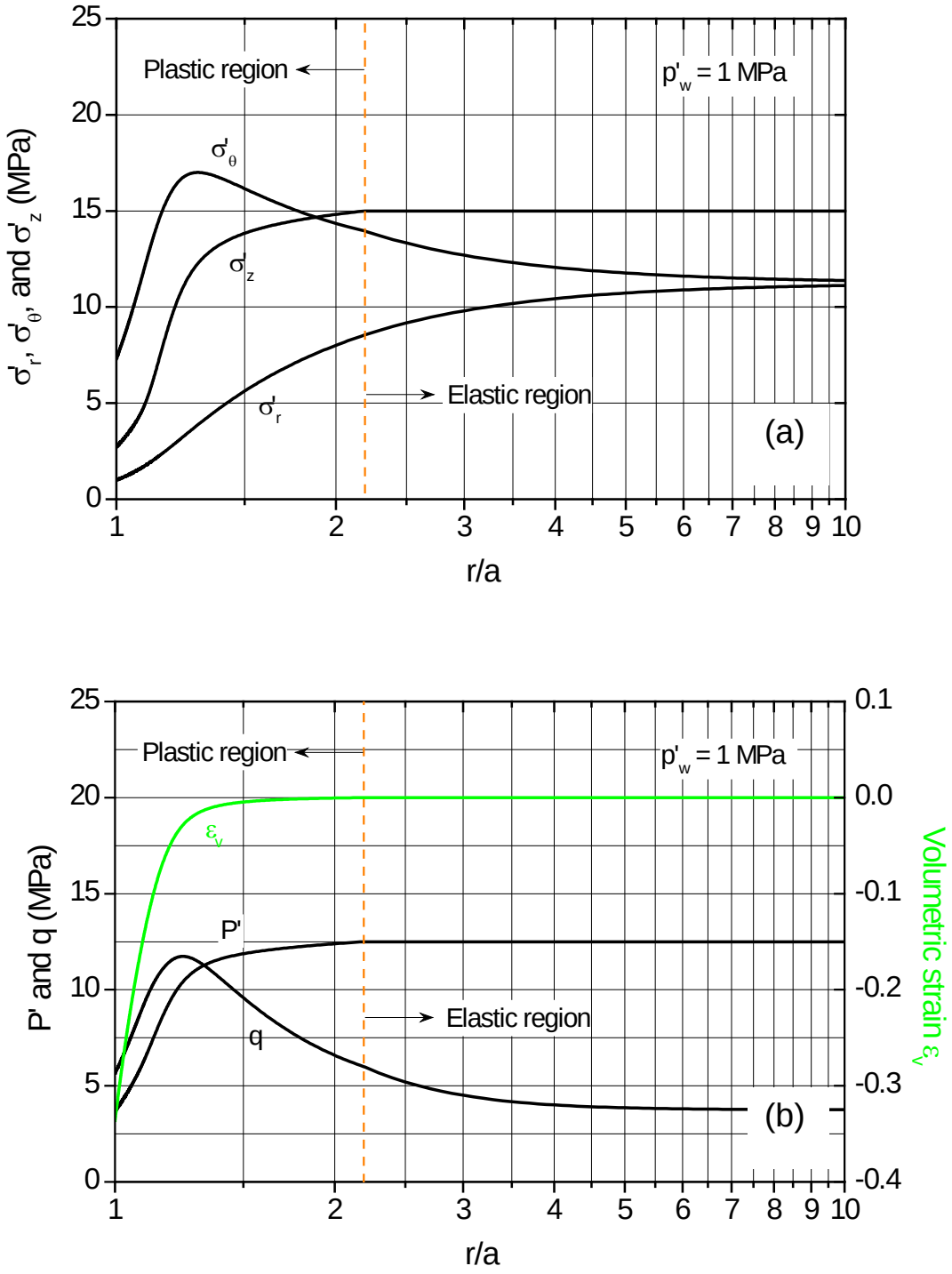

Fig. 3.7. Distributions of (a) effective radial, tangential, and vertical stresses; (b) effective mean, deviatoric stresses and volumetric strain around the wellbore for drained case

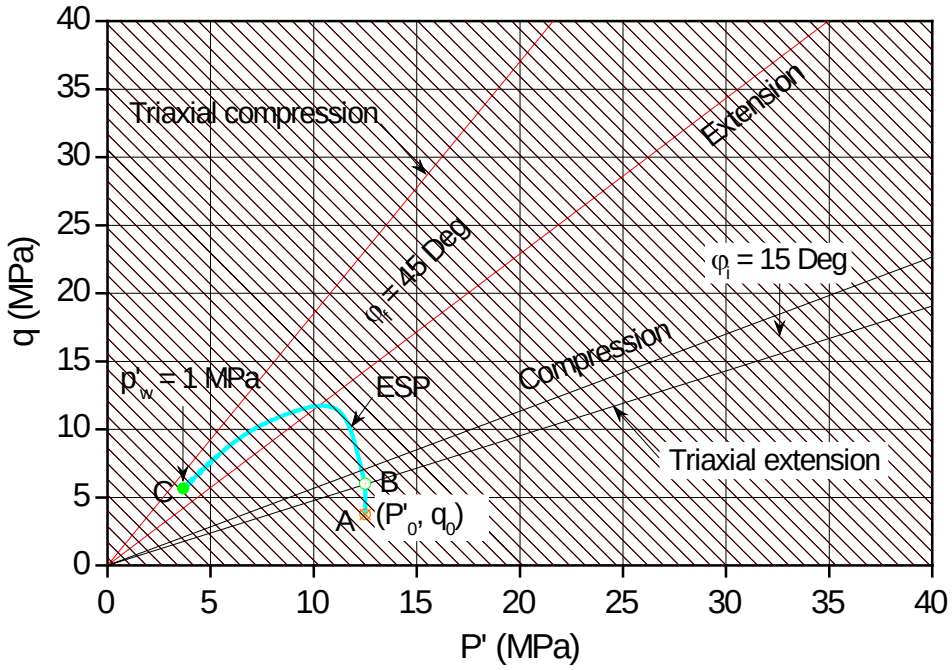

Fig. 3.8. P'-q stress path at wellbore surface for drained case

3.6 Summary

This chapter attempts to provide an analytical solution for the wellbore drilling problem in shear hardening Mohr-Coulomb rock formations. In order to avoid the singular corner problem so that rigorous solutions could be reached, the Mohr-Coulomb model has been approximated by the smooth shear hardening Matsuoka-Nakai model which passes through the Mohr-Coulomb hexagon at both major and minor vertices. Following a similar procedure outlined in the previous chapter for the hardening Drucker-Prager model, the problem is formulated as a set of first-order simultaneous differential equations in the plastic zone by assuming again small strain deformation in the elastic region and large strain deformation in the plastic region. The distributions of the stress

components, the excess pore pressure/volumetric strain as well as the effective stress path history for both undrained and drained conditions are presented through an example analysis.

CHAPTER 4
WELLBORE STABILITY ANALYSIS IN MODIFIED CAM CALY CRITICAL STATE ROCKS

4.1 Introduction

In the previous two chapters, analytical solutions were presented for wellbore drilling problem in rocks modelled by strain hardening Drucker-Prager and Mohr-Coulomb models, the latter was eventually approximated by the smooth Matsuoka-Nakai model in an effort to seek the analytical solution. As described earlier, the Drucker-Prager and Mohr-Coulomb models are quite realistic in modelling the sandstone-like formations as they capture reasonably well the particle rearrangement and the frictional sliding between material particles. However, for soft rocks and shale formations which consist mainly of clay minerals, it would be more preferable to use the volumetric hardening plastic models, such as Cam Clay model (Schofield & Wroth, 1968; Wood, 1990) and more advanced bounding surface model (Dafalias & Herrmann, 1980; 1982), to describe their nonlinear stress-strain behaviour. For this reason, this chapter develops additional solutions for the undrained/drained wellbore drilling problems using the modified Cam Clay model. Solutions based on the bounding surface model will be presented in the next chapter.

4.2 Modified Cam Clay Model

The modified Cam Clay elastoplastic model, developed by Roscoe and his colleagues in Cambridge (Roscoe & Burland 1968; Wood 1990; Nova, 2010), is firmly rooted in critical state soil mechanics and remains thus far the most widely used plasticity model for characterizing the stress-strain behaviour of cohesive soils incorporating the effect of stress history. The success of the modified Cam Clay model resides in its capability to capture the important features such as pressure sensitivity, hardening and softening responses typical in soils, using relatively simple formulations within a unitary conceptual framework. It also serves as a base for more sophisticated constitutive models like bounding surface model (Dafalias & Herrmann, 1980; 1982) and MIT soil models (Kavvadas, 1982; Whittle, 1987), and recently has been extended to describe the plastic properties of rocks, especially for the shale materials (Charlez, 1991; Charlez & Roatesi, 1999).

In the modified Cam Clay model, it is assumed that the elastic volumetric strain change, $d\varepsilon_p^e$, accompanies any change in mean effective stress, dP', according to the expression (Wood, 1990)

$$d\varepsilon_p^e = -\frac{dv}{v} = \frac{\kappa}{v}\frac{dP'}{P'} \tag{4.1}$$

where κ is a material parameter known as the slope of loading-reloading line in $v - \ln P'$ plane. Eq. (4.1) implies a nonlinear elastic response and gives the elastic bulk modulus, K, as

$$K = \frac{dP'}{d\varepsilon_p^e} = \frac{vP'}{\kappa} \tag{4.2}$$

which depends on both the specific volume v and the mean effective stress P'.

The shear modulus G can now be expressed as

$$G = \frac{3(1-2\nu)}{2(1+\nu)}K = \frac{3(1-2\nu)\nu P'}{2(1+\nu)\kappa} \tag{4.3}$$

again P' and ν dependent. Note that for modified Cam Clay model a constant Poisson's ratio ν is usually assumed.

The yield surface for the modified Cam Clay model is assumed to be an ellipse passing through the origin of the $P' - q$ stress plane, as shown in Fig. 4.1. The yield function therefore can be expressed as (Wood, 1990)

$$F(P', q, p_C') = q^2 - M^2[P'(P_C' - P')] \tag{4.4}$$

where M is another parameter defining the shape of the ellipsoidal yield locus, or the slope of critical state line (CSL); P_C' is the yield pressure under isotropic compression which as a hardening parameter essentially controls the size of the yield locus, and is related to the plastic volumetric strain, $d\varepsilon_p^p$, by

$$\frac{dP_C'}{P_C'} = \frac{\nu}{\lambda-\kappa}d\varepsilon_p^p \tag{4.5}$$

which essentially describes the volumetric hardening nature of the model. Here the material parameter λ denotes the slope of normal compression in $\nu - \ln P'$ plane.

The modified Cam Clay model assumes an associated flow (normality), i.e., the yield surfaces and plastic potential surfaces are identical (see Fig. 4.1), so the plastic volumetric and deviatoric strain increments, $d\varepsilon_p^p$ and $d\varepsilon_q^p$, can be expressed as (Wood, 1990)

$$d\varepsilon_p^p = \frac{(\lambda-\kappa)}{\nu P'(M^2+\eta^2)}[(M^2 - \eta^2)dP' + 2\eta dq] \tag{4.6a}$$

$$d\varepsilon_q^p = \frac{(\lambda-\kappa)}{\nu P'(M^2+\eta^2)}\left[2\eta dP' + \frac{4\eta^2}{M^2-\eta^2}dq\right] \tag{4.6b}$$

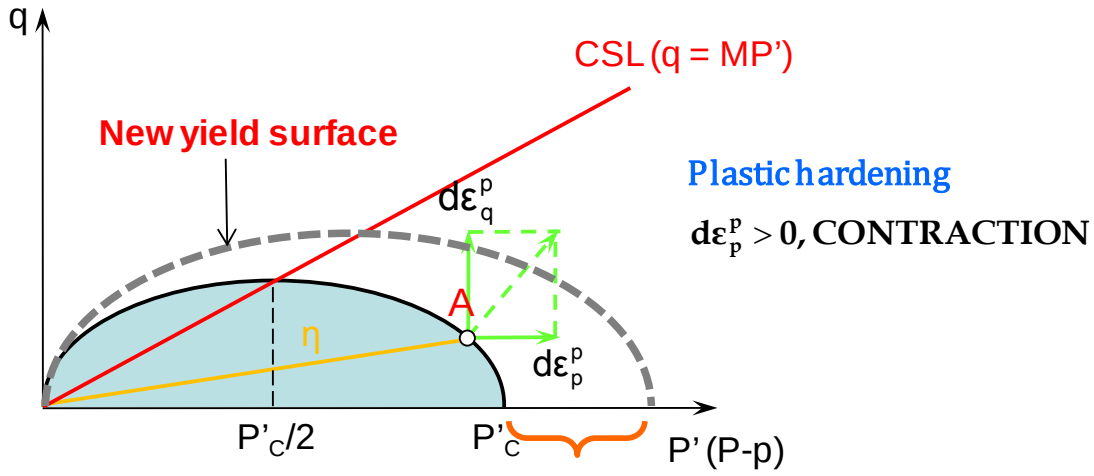

(a) $\mathbf{A:\eta<M\,(wet\ side),\ d\varepsilon_p^p>0\rightarrow dP_C^{'}>0}$

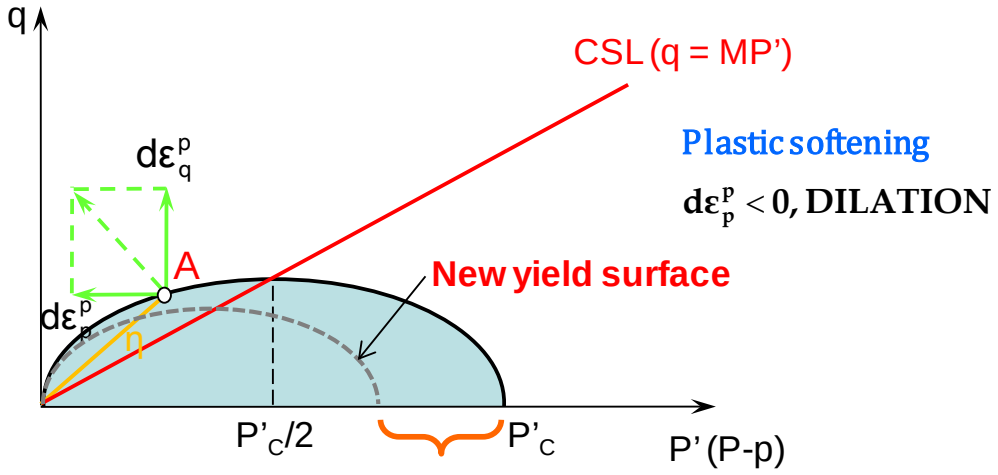

(b) $\mathbf{A:\eta>M\,(dry\ side),\ d\varepsilon_p^p<0\rightarrow dP_C^{'}<0}$

Fig. 4.1. Elliptical yield locus for modified Cam Clay model in P'-q plane: (a) strain hardening in wet side; (b) strain softening in dry side

where $\eta = \frac{q}{P'}$ is the stress ratio. For a stress point A located on the "wet" side of the critical state line ($\eta < M$, Fig. 4.1a), it is clear that during plastic straining the plastic volumetric strain $d\varepsilon_p^p > 0$, the yield surface therefore expands according to Eq. (4.5) and the material exhibits plastic hardening behaviour. On the contrary, when A is located on the "dry" side ($\eta > M$, Fig. 4.1b), the yield surface will contract associated with negative plastic volumetric strain ($d\varepsilon_p^p < 0$) and strain softening occurs.

The modified Cam Clay model requires totally five material parameters. In addition to the above mentioned two elastic parameters κ and ν (or G), and the two plastic ones λ and M, one needs to specify the value of specific volume, v_{cs}, at a reference stress of $P' = 1$ kPa on the critical state line in $v - \ln P'$ plane (Wood, 1990; 2004). This final parameter eventually defines the state boundary surface in the three dimensional $P' - q - v$ space so that the initial specific volume v_0 can be calculated.

4.3 Undrained Solution

Eqs. (2.6)-(2.8) are equilibrium and kinematics equations and apply for all the geomaterials. For completeness, these equations are repeated here for the wellbore drilling in modified Cam Clay rocks as follows

$$\frac{\partial \sigma_r}{\partial r} + \frac{\sigma_r - \sigma_\theta}{r} = 0 \tag{4.7}$$

$$\frac{\partial \sigma_r'}{\partial r} + \frac{\partial p}{\partial r} + \frac{\sigma_r' - \sigma_\theta'}{r} = 0 \tag{4.8}$$

$$\frac{r_{x0}}{a} = \sqrt{\left(\frac{r_x}{a}\right)^2 + \left(\frac{a_0}{a}\right)^2 - 1} \tag{4.9}$$

where all the variables in these equations are defined in Fig. 4.2 and in the previous two chapters.

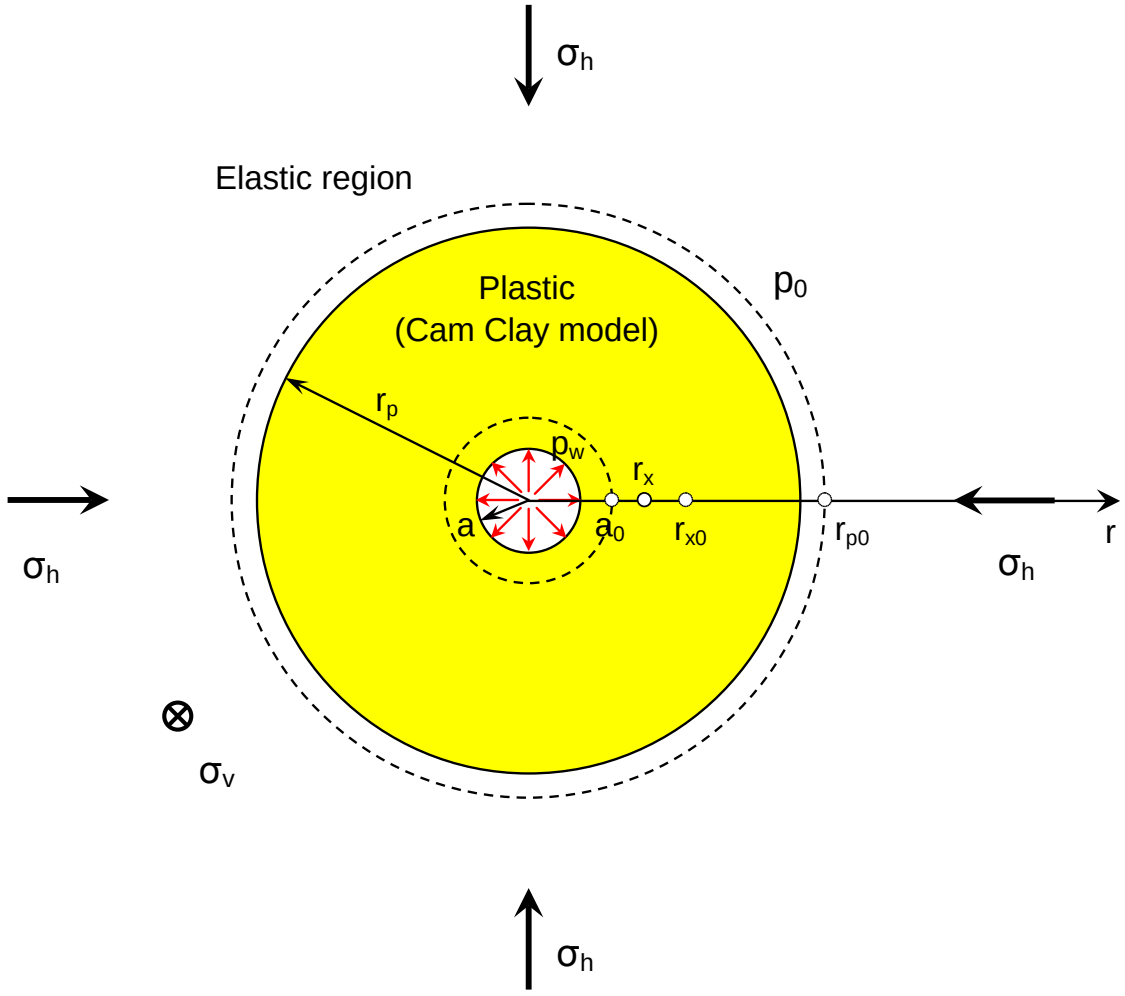

Fig. 4.2. Wellbore boundary value problem (Modified Cam Clay model)

4.3.1 Elastic Analysis

Again, the deformation in the elastic region $r \geq r_p$ is assumed to be infinitesimal. The incremental elastic stress strain relationship for modified Cam Clay model, in terms of the effective stresses, takes the form

$$\begin{Bmatrix} d\varepsilon_r \\ d\varepsilon_\theta \\ d\varepsilon_z \end{Bmatrix} = \frac{1}{E}\begin{bmatrix} 1 & -\nu & -\nu \\ -\nu & 1 & -\nu \\ -\nu & -\nu & 1 \end{bmatrix} \cdot \begin{Bmatrix} d\sigma_r^{'} \\ d\sigma_\theta^{'} \\ d\sigma_z^{'} \end{Bmatrix} \tag{4.10a}$$

and in terms of the total stress form

$$\begin{Bmatrix} d\varepsilon_r \\ d\varepsilon_\theta \\ d\varepsilon_z \end{Bmatrix} = \frac{1}{E_u}\begin{bmatrix} 1 & -\nu_u & -\nu_u \\ -\nu_u & 1 & -\nu_u \\ -\nu_u & -\nu_u & 1 \end{bmatrix} \cdot \begin{Bmatrix} d\sigma_r \\ d\sigma_\theta \\ d\sigma_z \end{Bmatrix} \tag{4.10b}$$

where ν and ν_u are the drained and undrained Poisson's ratio ($\nu_u = 0.5$); and the drained and undrained Young's modulus E and E_u are given by

$$E = 2G(1+\nu), \qquad E_u = 2G(1+\nu_u) \tag{4.11}$$

Note that in modified Cam Clay model the Young's moduli E and E_u are no longer constants as for the Drucker-Prager and Mohr-Coulomb models, but vary in general with $P^{'}$ and v via Eq. (4.3).

By adding Eq. (4.10a), it follows that

$$d\varepsilon_v = d\varepsilon_r + d\varepsilon_\theta + d\varepsilon_z = \frac{3(1-2\nu)}{E} dP^{'} \tag{4.12}$$

where $d\varepsilon_v$ is the volumetric strain increment which is related to the specific volume by

$$d\varepsilon_v = -\frac{dv}{v} \tag{4.13}$$

Clearly the total volume strain rate is zero in an undrained deformation, Eqs. (4.12) and (4.13) thus give

$$dv = dP^{'} = 0 \tag{4.14}$$

i.e., both the specific volume and effective mean stress must remain constant during the elastic phase of deformation and hence from Eqs. (4.3) and (4.11), the instantaneous Young's modulus E and shear modulus G should also remain unchanged and equal to their initial values E_0 and G_0, respectively.

Given the constant E and G, the elastic solutions for total stresses, radial

displacement, and pore pressure in the region $r \geq r_p$ now turn out to be the same as those for the Drucker-Prager and Mohr-Coulomb models (Timoshenko & Goodier, 1970; Yu, 2000), i.e.,

$$\sigma_r = \sigma_h + (\sigma_p - \sigma_h)\left(\frac{r_p}{r}\right)^2 \tag{4.15}$$

$$\sigma_\theta = \sigma_h - (\sigma_p - \sigma_h)\left(\frac{r_p}{r}\right)^2 \tag{4.16}$$

$$\sigma_z = \sigma_v \tag{4.17}$$

$$u_r = \frac{\sigma_p - \sigma_h}{2G_0}\frac{r_p^2}{r} \tag{4.18}$$

$$p = p_0 \tag{4.19}$$

where σ_p corresponds to the total radial stress at the elastic-plastic boundary.

4.3.2 ELASTOPLASTIC ANALYSIS

For modified Cam Clay model following an associated flow rule, the three components of incremental plastic strain in r, θ, and z directions can be expressed as follows

$$d\varepsilon_r^p = \Lambda\frac{\partial F}{\partial \sigma_r'} = \Lambda\left(\frac{\partial F}{\partial P'}\cdot\frac{\partial P'}{\partial \sigma_r'} + \frac{\partial F}{\partial q}\cdot\frac{\partial q}{\partial \sigma_r'}\right) = \Lambda\left\{\frac{P'(M^2-\eta^2)}{3} + 3(\sigma_r' - P')\right\} \tag{4.20a}$$

$$d\varepsilon_\theta^p = \Lambda\frac{\partial F}{\partial \sigma_\theta'} = \Lambda\left(\frac{\partial F}{\partial P'}\cdot\frac{\partial P'}{\partial \sigma_\theta'} + \frac{\partial F}{\partial q}\cdot\frac{\partial q}{\partial \sigma_\theta'}\right) = \Lambda\left\{\frac{P'(M^2-\eta^2)}{3} + 3(\sigma_\theta' - P')\right\} \tag{4.20b}$$

$$d\varepsilon_z^p = \Lambda\frac{\partial F}{\partial \sigma_z'} = \Lambda\left(\frac{\partial F}{\partial P'}\cdot\frac{\partial P'}{\partial \sigma_z'} + \frac{\partial F}{\partial q}\cdot\frac{\partial q}{\partial \sigma_z'}\right) = \Lambda\left\{\frac{P'(M^2-\eta^2)}{3} + 3(\sigma_z' - P')\right\} \tag{4.20c}$$

where Λ is a scalar multiplier. It is to be emphasized here that, in deriving the above expressions, use has been made of the following rigorous definitions for the means effective and deviatoric stresses

$$P' = \frac{1}{3}(\sigma_r' + \sigma_\theta' + \sigma_z') \tag{4.21}$$

$$q = \sqrt{\frac{1}{2}\left[(\sigma_r^{'} - \sigma_\theta^{'})^2 + (\sigma_r^{'} - \sigma_z^{'})^2 + (\sigma_\theta^{'} - \sigma_z^{'})^2\right]} \tag{4.22}$$

which differs from the existing literatures (Collins & Yu, 1996; Charlez & Roatesi, 1999; Yu & Rowe, 1999; Cao et al., 2001) where the two stress invariants are usually treated in somewhat approximate fashion. For example, in Collins & Yu (1996) and Cao et al. (2001) for the cavity expansion problem, they are defined, respectively, as $P^{'} = \frac{1}{2}(\sigma_r^{'} + \sigma_\theta^{'})$, $q = \sigma_r^{'} - \sigma_\theta^{'}$ and $P^{'} = \frac{1}{2}(\sigma_r^{'} + \sigma_\theta^{'})$, $q = \frac{\sqrt{3}}{2}(\sigma_r^{'} - \sigma_\theta^{'})$ to simplify the analyses and obtain the solutions.

Since $d\varepsilon_p^p = d\varepsilon_r^p + d\varepsilon_\theta^p + d\varepsilon_z^p$, it follows from Eqs. (4.6a) and (4.20a)-(4.20c) that

$$\Lambda = \frac{(\lambda-\kappa)}{vP^{'2}(M^2+\eta^2)}\left[dP^{'} + \frac{2\eta}{(M^2-\eta^2)}dq\right] \tag{4.23}$$

Substituting Eq. (4.23) back into Eqs. (4.20a)-(4.20c), one obtains, in matrix notation, the following plastic stress strain response

$$\begin{Bmatrix} d\varepsilon_r^p \\ d\varepsilon_\theta^p \\ d\varepsilon_z^p \end{Bmatrix} = y \begin{bmatrix} a_r^2 & a_r a_\theta & a_r a_z \\ a_\theta a_r & a_\theta^2 & a_\theta a_z \\ a_z a_r & a_z a_\theta & a_z^2 \end{bmatrix} \cdot \begin{Bmatrix} d\sigma_r^{'} \\ d\sigma_\theta^{'} \\ d\sigma_z^{'} \end{Bmatrix} \tag{4.24}$$

which, once again, takes the same form as Eq. (2.24) and Eq. (3.22) as derived for the Drucker-Prager and Mohr-Coulomb models, with the only exception that a_r, a_θ, a_z, and y become now

$$a_r = \frac{P^{'}(M^2-\eta^2)}{3} + 3(\sigma_r^{'} - P^{'}) \tag{4.25a}$$

$$a_\theta = \frac{P^{'}(M^2-\eta^2)}{3} + 3(\sigma_\theta^{'} - P^{'}) \tag{4.25b}$$

$$a_z = \frac{P^{'}(M^2-\eta^2)}{3} + 3(\sigma_z^{'} - P^{'}) \tag{4.25c}$$

$$y = \frac{\lambda-\kappa}{vP^{'3}(M^4-\eta^4)} \tag{4.25d}$$

Eq. (4.24), on combining with the elastic stress strain relationship, Eq. (4.10a), may be inverted

$$\begin{Bmatrix} d\sigma_r^{'} \\ d\sigma_\theta^{'} \\ d\sigma_z^{'} \end{Bmatrix} = \frac{1}{\Delta} \begin{bmatrix} b_{11} & b_{12} & b_{13} \\ b_{21} & b_{22} & b_{23} \\ b_{31} & b_{32} & b_{33} \end{bmatrix} \cdot \begin{Bmatrix} d\varepsilon_r \\ d\varepsilon_\theta \\ d\varepsilon_z \end{Bmatrix} \tag{4.26}$$

which, subjected to the large deformation assumption in the plastic zone, results in again the three desirable first order ordinary differential equations

$$\frac{D\sigma_r^{'}}{Dr} - \frac{b_{11}-b_{12}}{\Delta r} = 0 \tag{4.27a}$$

$$\frac{D\sigma_\theta^{'}}{Dr} - \frac{b_{21}-b_{22}}{\Delta r} = 0 \tag{4.27b}$$

$$\frac{D\sigma_z^{'}}{Dr} - \frac{b_{31}-b_{32}}{\Delta r} = 0 \tag{4.27c}$$

where b_{ij} and Δ are identical to those defined in Eqs. (2.29a)-(2.29j).

4.3.3 Initial Stress Conditions and Elastic-Plastic Boundary

Recall that Eqs. (4.27a)-(4.27c) are valid for any material point r_x currently located in the plastic zone (see Fig. 4.2), and can be readily solved as an initial value problem with the single variable r starting from $r = r_{xp}$, provided that the initial values of $\sigma_r^{'}(r_{xp})$, $\sigma_\theta^{'}(r_{xp})$, and $\sigma_z^{'}(r_{xp})$ are given. Here r_{xp} represents the position of the specific particle when it is just becoming plastic.

Assume that the formation has an overconsolidation ratio OCR, defined as $OCR = \frac{P_C^{'}}{P_A^{'}}$ where $P_A^{'}$ is the intersection of an ellipse passing through the initial mean and deviator stress point $(P_0^{'}, q_0)$ with the P' axis and $P_C^{'}$ has been previously defined, see Fig. 4.3. As shown in Eq. (4.14), under undrained condition the change of the effective mean stress P' is zero during the elastic deformation. This indicates that the $P^{'} - q$ stress path of the

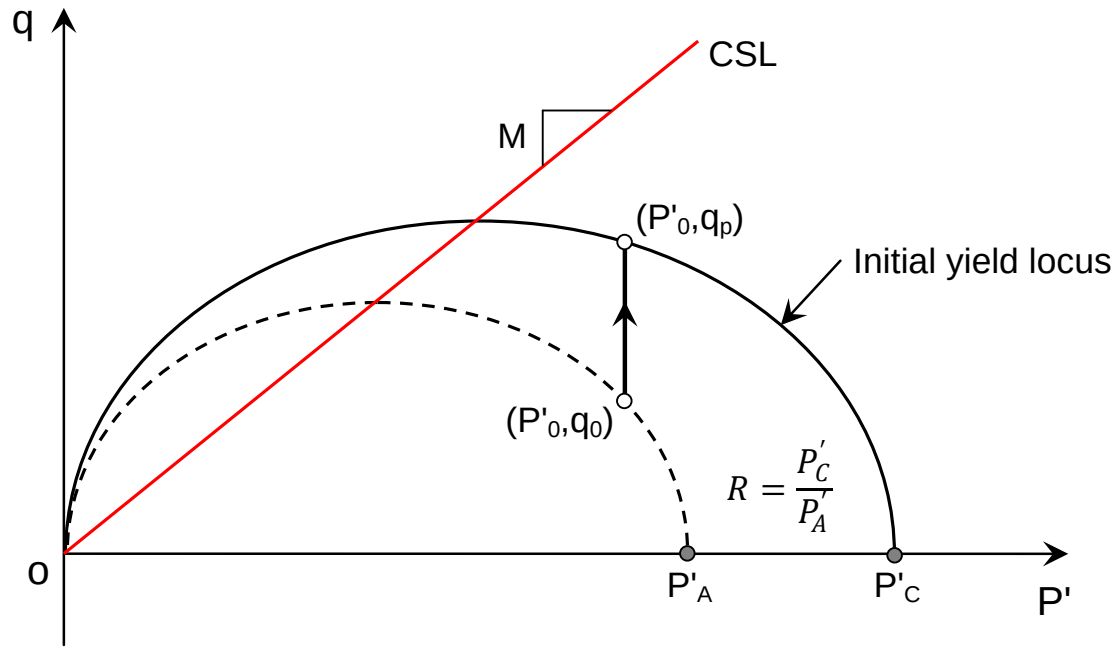

Fig. 4.3. Overconsolidation ratio and stress path during elastic deformation phase

material point r_x will be a vertical line until it reaches the initial yield locus, represented by point $(P_0^{'}, q_p)$ in Fig. 4.3. Note that q_p is related to the overconsolidation ratio OCR, from the simple geometry of Fig. 4.3, as

$$q_p = MP_0^{'}\sqrt{OCR\left[1+\frac{1}{M^2}\left(\frac{q_0}{P_0^{'}}\right)^2\right]-1} \tag{4.28}$$

It is obvious that at the position r_{xp} the material point is at initial yield, so that

$$\frac{1}{\sqrt{2}}\sqrt{\left[\sigma_r^{'}(r_{xp})-\sigma_\theta^{'}(r_{xp})\right]^2+\left[\sigma_r^{'}(r_{xp})-\sigma_z^{'}(r_{xp})\right]^2+\left[\sigma_\theta^{'}(r_{xp})-\sigma_z^{'}(r_{xp})\right]^2}=q_p \tag{4.29}$$

and on the other hand, these effective stresses must satisfy the elastic solutions (4.15)-(4.17) and (4.19), giving

$$\sigma_r^{'}(r_{xp}) + \sigma_\theta^{'}(r_{xp}) = \sigma_{r0}^{'} + \sigma_{\theta 0}^{'} = \frac{6K_0}{1+2K_0} P_0^{'} \tag{4.30}$$

$$\sigma_z^{'}(r_{xp}) = \sigma_{z0}^{'} = \frac{3}{1+2K_0} P_0^{'} \tag{4.31}$$

where $\sigma_{r0}^{'}$, $\sigma_{\theta 0}^{'}$, and $\sigma_{z0}^{'}$ are the initial effective stresses; and K_0 is the coefficient of earth pressure at rest. Thus, from Eqs. (4.29)-(4.31), the effective radial and tangential stresses can be determined as

$$\sigma_{rp}^{'} = \sigma_{r0}^{'} - \sqrt{\sigma_{r0}^{'\,2} - \frac{1}{3}(4\sigma_{r0}^{'\,2} + \sigma_{z0}^{'\,2} - 2\sigma_{r0}^{'}\sigma_{z0}^{'} - q_p^2)} \tag{4.32}$$

$$\sigma_{\theta p}^{'} = \sigma_{r0}^{'} + \sqrt{\sigma_{r0}^{'\,2} - \frac{1}{3}(4\sigma_{r0}^{'\,2} + \sigma_{z0}^{'\,2} - 2\sigma_{r0}^{'}\sigma_{z0}^{'} - q_p^2)} \tag{4.33}$$

In a similar manner, the corresponding expressions for r_{xp}, r_p, and the critical borehole radius a_p in the modified Cam Clay case are given by

$$\frac{r_{xp}}{a} = \frac{1}{1-\frac{\sigma_{rp}^{'} - \sigma_{r0}^{'}}{2G_0}} \sqrt{\left(\frac{r_x}{a}\right)^2 + \left(\frac{a_0}{a}\right)^2 - 1} \tag{4.34}$$

$$\frac{r_p}{a} = \sqrt{\frac{\left(\frac{a_0}{a}\right)^2 - 1}{\left(\frac{\sigma_{rp}^{'} - \sigma_{r0}^{'}}{2G_0}\right)^2 - \frac{\sigma_{rp}^{'} - \sigma_{r0}^{'}}{G_0}}} \tag{4.35}$$

$$\frac{a_p}{a_0} = \frac{1}{1-\frac{\sigma_{rp}^{'} - \sigma_{r0}^{'}}{2G_0}} \tag{4.36}$$

The excess pore pressure shall be calculated as

$$\Delta p(r_x) = p(r_x) - p_0 = \sigma_{rp}^{'} - \sigma_r^{'}(r_x) - \int_{r_p}^{r_x} \frac{\sigma_r^{'} - \sigma_\theta^{'}}{r} dr \tag{4.37}$$

4.3.4 ISOTROPIC IN SITU STRESS CONDITION

It is interesting to note that in the special case of isotropic in situ stress state, the vertical stress $\sigma_z^{'}$ is always equal to the mean of radial stress $\sigma_r^{'}$ and tangential stress $\sigma_\theta^{'}$ throughout the wellbore drilling. This can be proved as follows. Since in this case the rock is initially under isotropic stress condition, $\sigma_h = \sigma_v$, it is evident from Eqs. (4.15)-(4.17) and (4.19) that during the elastic phase the following relationship applies

$$\sigma_z^{'} = \frac{1}{2}(\sigma_r^{'} + \sigma_\theta^{'}) \tag{4.38}$$

and so at the onset of yielding

$$\sigma_r^{'}(r_{xp}) + \sigma_\theta^{'}(r_{xp}) - 2\sigma_z^{'}(r_{xp}) = 0 \tag{4.39}$$

During the plastic phase of drilling, the three governing equations given by (4.27a)-(4.27c) can be combined to obtain

$$\frac{D}{Dr}(\sigma_r^{'} + \sigma_\theta^{'} - 2\sigma_z^{'}) = -\frac{3(1-2\nu)(a_r - a_\theta)(\sigma_r^{'} + \sigma_\theta^{'} - 2\sigma_z^{'})y}{E\Delta r} \tag{4.40}$$

From Eqs. (4.39) and (4.40) it now becomes obvious that the change of $\sigma_r^{'} + \sigma_\theta^{'} - 2\sigma_z^{'}$ is zero and therefore Eq. (4.38) still holds during the plastic straining. This demonstrates that the simplified assumption used for P' and q in Cao et al. (2001) happens to be correct under the special condition of $K_0 = 1$ (despite the fact that a constant G rather than a variable one proportional to P' [Eq. (4.3)] is adopted in their derivation), and probably explains why the error due to the simplifications of P' and q in Collins & Yu (1996) for cylindrical cavity problem is negligible in comparison with the more rigorous finite element numerical results (Sheng et al., 2000). However, it should be remarked that for the general case where the horizontal in situ stress is different from the vertical one, i.e., $K_0 \neq 1$, no such simple relationship as Eq. (4.38) will exist and the wellbore drilling

problem has to be solved using the present approach to obtain the exact solution.

4.4 Drained Solution

This section deals with the wellbore drilling problem under drained condition. Although the development is closely analogous to those above for the Drucker-Prager and Mohr-Coulomb models, a subtle problem is encountered for the modified Cam Clay model which arises from the fact that in the drained situation, the specific volume v generally changes during the drilling process and, consequently, so does the Young's modulus E (or shear modulus G). Specific care has to be taken, therefore, in deriving the stress and displacement solutions in the elastic zone, as shown below. Also, noting that the specific volume is an important variable for the modified Cam Clay model, in this section it is quite natural to chose v as the fourth basic unknown (replacing the volumetric strain ε_v as used for the Drucker-Prager and Mohr-Coulomb models) in the formulation of the governing differential equations.

4.4.1 Elastic Analysis

It is recalled here that the incremental elastic stress strain relation for the modified Cam Clay model is

$$\begin{Bmatrix} d\varepsilon_r \\ d\varepsilon_\theta \\ d\varepsilon_z \end{Bmatrix} = \frac{1}{E}\begin{bmatrix} 1 & -\nu & -\nu \\ -\nu & 1 & -\nu \\ -\nu & -\nu & 1 \end{bmatrix} \cdot \begin{Bmatrix} d\sigma_r' \\ d\sigma_\theta' \\ d\sigma_z' \end{Bmatrix} \tag{4.41}$$

where $E = 2G(1+\nu) = \frac{3(1-2\nu)vP'}{\kappa}$ as previously defined in Section 4.2.

At the first instant of the wellbore drilling, the deformation of the rock formation is purely elastic with the Young's modulus E and shear modulus G equal to their initial

values E_0 and G_0, respectively. Following the theory of elasticity, the incremental solutions for the stresses and radial displacement can be easily found to be (Timoshenko & Goodier, 1970; Yu, 2000)

$$d\sigma_r^{'} = dp_w^{'}\left(\frac{a_0}{r}\right)^2 \tag{4.42}$$

$$d\sigma_\theta^{'} = -dp_w^{'}\left(\frac{a_0}{r}\right)^2 \tag{4.43}$$

$$d\sigma_z^{'} = 0 \tag{4.44}$$

$$du_r = \frac{dp_w^{'}}{2G_0}\frac{a_0^2}{r} \tag{4.45}$$

where $dp_w^{'}$ is the radial stress decrement at the wellbore surface over its initial value of $\sigma_h^{'}$. It should be emphasized that the above expressions are valid only in case that E and G are constants for any material particle in the elastic zone.

From Eqs. (4.42)-(4.44) one has

$$dP' = \frac{1}{3}(d\sigma_r^{'} + d\sigma_\theta^{'} + d\sigma_z^{'}) = 0 \tag{4.46}$$

which combined with Eq. (4.41) gives

$$d\varepsilon_v = d\varepsilon_r + d\varepsilon_\theta + d\varepsilon_z = \frac{3(1-2\nu)}{E}dP' = 0 \tag{4.47}$$

where $d\varepsilon_v = -\frac{dv}{v}$ is the volumetric strain increment.

Eqs. (4.46) and (4.47) indicate that both the specific volume and mean effective stress must remain constants for any point in the elastic region when the wellbore pressure is decreased by an infinitesimal amount of $dp_w^{'}$. This is a desirable property for the cylindrical wellbore problem. As a consequence, E and G should also stay constants after this loading reduction. Eqs. (4.42)-(4.45) therefore can again be used to obtain the corresponding changes of stress and displacement for the next decrease in the wellbore

pressure, which invariably ends up with constant Young's modulus and shear modulus equal to E_0 and G_0, respectively, in the whole elastic region. The process can thus be repeated until the wellbore pressure is finally decreased to the current value of $p_w^{'}$. The only point however to note is that, after the plastic zone has been formed outside the wellbore, a_0 and $dp_w^{'}$ appearing in Eqs. (4.42)-(4.45) should be replaced by the position of the elastic-plastic interface and the corresponding radial stress at that interface.

From the above analysis it is quite evident that the Young's modulus and shear modulus always remain unchanged in the external elastic region, throughout the wellbore drilling process. The solutions for stresses and radial displacement thus can be directly obtained as

$$\sigma_r^{'} = \sigma_h^{'} + (\sigma_p^{'} - \sigma_h^{'}) \left(\frac{r_p}{r}\right)^2 \tag{4.48}$$

$$\sigma_\theta^{'} = \sigma_h^{'} - (\sigma_p^{'} - \sigma_h^{'}) \left(\frac{r_p}{r}\right)^2 \tag{4.49}$$

$$\sigma_z^{'} = \sigma_v^{'} \tag{4.50}$$

$$u_r = \frac{\sigma_p^{'} - \sigma_h^{'}}{2G_0} \frac{r_p^2}{r} \tag{4.51}$$

which again are the same as those above for the undrained case and also those derived for the Drucker-Prager and Mohr-Coulomb models.

4.4.2 ELASTOPLASTIC ANALYSIS

Proceeding as in Section 2.4.2, one may derive the governing differential equations for the drained wellbore drilling problem in modified Cam Clay rock formation. Combine the elastoplastic incremental constitutive relation, Eq. (4.26), with the strain definitions $d\varepsilon_v = -\frac{dv}{v}$ and $d\varepsilon_\theta = -\frac{dr}{r}$, one reaches the following results

$$d\sigma_r^{'} = \frac{1}{\Delta}[b_{11}d\varepsilon_v + (b_{12} - b_{11})d\varepsilon_\theta] = \frac{1}{\Delta}[b_{11}(-\frac{dv}{v}) + (b_{12} - b_{11})(-\frac{dr}{r})] \quad (4.52a)$$

$$d\sigma_\theta^{'} = \frac{1}{\Delta}[b_{21}d\varepsilon_v + (b_{22} - b_{21})d\varepsilon_\theta] = \frac{1}{\Delta}[b_{21}(-\frac{dv}{v}) + (b_{22} - b_{21})(-\frac{dr}{r})] \quad (4.52b)$$

$$d\sigma_z^{'} = \frac{1}{\Delta}[b_{31}d\varepsilon_v + (b_{32} - b_{31})d\varepsilon_\theta] = \frac{1}{\Delta}[b_{31}(-\frac{dv}{v}) + (b_{32} - b_{31})(-\frac{dr}{r})] \quad (4.52c)$$

The auxiliary independent variable, ξ, is chosen as the ratio of the particle displacement in radial direction to its present radial position, i.e.,

$$\xi = \frac{u_r}{r} = \frac{r - r_0}{r} \quad (4.53)$$

Differentiation of Eq. (4.53) then results in following

$$\frac{dr}{r} = \frac{d\xi}{1-\xi} \quad (4.54)$$

Substituting this into Eqs. (4.52a)-(4.52c) gives

$$\frac{D\sigma_r^{'}}{D\xi} = -\frac{b_{11}}{\Delta}\frac{f}{v} - \frac{b_{12} - b_{11}}{\Delta(1-\xi)} \quad (4.55a)$$

$$\frac{D\sigma_\theta^{'}}{D\xi} = -\frac{b_{21}}{\Delta}\frac{f}{v} - \frac{b_{22} - b_{21}}{\Delta(1-\xi)} \quad (4.55b)$$

$$\frac{D\sigma_z^{'}}{D\xi} = -\frac{b_{31}}{\Delta}\frac{f}{v} - \frac{b_{32} - b_{31}}{\Delta(1-\xi)} \quad (4.55c)$$

$$\frac{Dv}{D\xi} = f \quad (4.55d)$$

where $\frac{D}{D\xi}$ is well understood as the material derivative with respect to ξ following a given particle (Lagrangian description). Note that in contrast to the cases of Drucker-Prager and Mohr-Coulomb models, the volumetric strain ε_v has been here replaced by the specific volume v in these four equations. However, there still exist five unknowns, i.e., σ_r, σ_θ, σ_z, v, and f, that need to be solved for and one thus shall seek an additional equation from the radial equilibrium condition.

Now, recall that at every point in the rock formation, the equation of equilibrium

must be satisfied

$$\frac{\partial \sigma_r^{'}}{\partial r} + \frac{\sigma_r^{'} - \sigma_\theta^{'}}{r} = 0 \tag{4.56}$$

which, with the aid of Eq. (4.55a), reduces to

$$-(\sigma_r^{'} - \sigma_\theta^{'}) = \left[-\frac{b_{11}}{\Delta}\frac{f}{v} - \frac{b_{12} - b_{11}}{\Delta(1-\xi)}\right]\left(-\xi + \frac{du_r}{dr}\right) \tag{4.57}$$

where $\frac{du_r}{dr}$ represents the relative displacement of a neighboring point with respect to the particle instantaneously at position r (Eulerian description).

On the other hand, since $e^{\varepsilon_v} = \frac{v_0}{v}$ for large deformation, Eq. (2.63), which still holds for the modified Cam Clay model, can be rewritten as

$$\frac{du_r}{dr} = 1 - \left[\frac{v}{v_0}(1-\xi)\right]^{-1} \tag{4.58}$$

Elimination of $\frac{du_r}{dr}$ from Eqs. (4.57) and (4.58) therefore results in

$$f = \frac{v\Delta}{b_{11}}\left[\frac{\sigma_r^{'} - \sigma_\theta^{'}}{1-\xi-\frac{v_0}{v(1-\xi)}} + \frac{b_{11} - b_{12}}{\Delta(1-\xi)}\right] \tag{4.59}$$

Substituting Eq. (4.59) into Eqs. (4.55a)-(4.55d), the four governing differential equations finally reduce to

$$\frac{D\sigma_r^{'}}{D\xi} = -\frac{\sigma_r^{'} - \sigma_\theta^{'}}{1-\xi-\frac{v_0}{v(1-\xi)}} \tag{4.60a}$$

$$\frac{D\sigma_\theta^{'}}{D\xi} = -\frac{b_{21}}{b_{11}}\left[\frac{\sigma_r^{'} - \sigma_\theta^{'}}{1-\xi-\frac{v_0}{v(1-\xi)}} + \frac{b_{11} - b_{12}}{\Delta(1-\xi)}\right] - \frac{b_{22} - b_{21}}{\Delta(1-\xi)} \tag{4.60b}$$

$$\frac{D\sigma_z^{'}}{D\xi} = -\frac{b_{31}}{b_{11}}\left[\frac{\sigma_r^{'} - \sigma_\theta^{'}}{1-\xi-\frac{v_0}{v(1-\xi)}} + \frac{b_{11} - b_{12}}{\Delta(1-\xi)}\right] - \frac{b_{32} - b_{31}}{\Delta(1-\xi)} \tag{4.60c}$$

$$\frac{Dv}{D\xi} = \frac{v\Delta}{b_{11}}\left[\frac{\sigma_r^{'} - \sigma_\theta^{'}}{1-\xi-\frac{v_0}{v(1-\xi)}} + \frac{b_{11} - b_{12}}{\Delta(1-\xi)}\right] \tag{4.60d}$$

which can be readily solved for any material particle r_x as an initial value problem with

the independent variable starting at $\xi = \xi_0$. Here ξ_0 corresponds to the value of $\frac{u_r}{r}$ of the specific particle when it is just entering into the plastic state.

4.4.3 INITIAL STRESS CONDITIONS AND ELASTIC-PLASTIC BOUNDARY

It will be shown in this section that the solution in the outer elastic region fully specifies the value of ξ_0 and the corresponding stress components and specific volume $\sigma_r^{'}(\xi_0)$, $\sigma_\theta^{'}(\xi_0)$, $\sigma_z^{'}(\xi_0)$, and $v(\xi_0)$ as well. As previously analyzed in Section 2.4.3, these variables must satisfy the elastic region solutions given by

$$\sigma_r^{'}(\xi_0) + \sigma_\theta^{'}(\xi_0) = \sigma_{r0}^{'} + \sigma_{\theta 0}^{'} = \frac{6K_0}{1+2K_0} P_0^{'} \tag{4.61}$$

$$\sigma_z^{'}(\xi_0) = \sigma_{z0}^{'} = \frac{3}{1+2K_0} P_0^{'} \tag{4.62}$$

$$\xi_0 = \frac{\sigma_r^{'}(\xi_0) - \sigma_h^{'}}{2G_0} \tag{4.63}$$

$$v(\xi_0) = v_0 \tag{4.64}$$

$$P'(\xi_0) = P_0^{'} \tag{4.65}$$

and also the following initial yielding condition

$$q(\xi_0) \equiv \sqrt{\frac{1}{2}\left\{\left[\sigma_r^{'}(\xi_0) - \sigma_\theta^{'}(\xi_0)\right]^2 + [\sigma_r^{'}(\xi_0) - \sigma_z^{'}(\xi_0)]^2 + [\sigma_r^{'}(\xi_0) - \sigma_z^{'}(\xi_0)]^2\right\}}$$

$$= MP_0^{'}\sqrt{OCR\left[1 + \frac{1}{M^2}\left(\frac{q_0}{P_0^{'}}\right)^2\right] - 1} \tag{4.66}$$

where K_0, $P_0^{'}$, and q_0 have been previously defined in Section 4.3.3. From Eqs. (4.61), (4.62), and (4.66), one obtains

$$\sigma_r^{'}(\xi_0) = \sigma_{r0}^{'} - \sqrt{\sigma_{r0}^{'2} - \frac{1}{3}\left[4{\sigma_{r0}}^2 + \sigma_{r0}^{'2} - 2\sigma_{r0}^{'}\sigma_{z0}^{'} - q(\xi_0)^2\right]} \tag{4.67}$$

$$\sigma_\theta^{'}(\xi_0) = \sigma_{r0}^{'} + \sqrt{\sigma_{r0}^{'2} - \frac{1}{3}\left[4{\sigma_{r0}}^2 + \sigma_{r0}^{'2} - 2\sigma_{r0}^{'}\sigma_{z0}^{'} - q(\xi_0)^2\right]} \tag{4.68}$$

Furthermore, to establish a linking between the auxiliary variable ξ and the particle position r, one needs to start from Eq. (4.58), which can be rewritten as

$$\frac{du_r}{dr} = \xi + r\frac{d\xi}{dr} = 1 - \frac{v_0}{v(\xi)(1-\xi)} \tag{4.69}$$

and therefore

$$\frac{dr}{r} = \frac{d\xi}{1-\frac{v_0}{v(\xi)(1-\xi)}-\xi} \tag{4.70}$$

Integrating the above equation from the current wellbore radius a, results in

$$\frac{r}{a} = e^{\int_{\xi(a)}^{\xi}\frac{d\xi}{1-\frac{v_0}{v(\xi)(1-\xi)}-\xi}} \tag{4.71}$$

Especially, the position of the current elastic-plastic interface r_p can be calculated as

$$\frac{r_p}{a} = e^{\int_{\xi(a)}^{\xi 0}\frac{d\xi}{1-\frac{v_0}{v(\xi)(1-\xi)}-\xi}} \tag{4.72}$$

Finally, the critical borehole radius a_p can be determined as

$$\frac{a_p}{a_0} = \frac{1}{1-\frac{\sigma_r^{'}(\xi_0)-\sigma_h^{'}}{2G_0}} \tag{4.73}$$

4.5 Results and Discussions

The five modified Cam Clay model parameters used for the analyses are $M = 0.88$, $\lambda = 0.25$, $\kappa = 0.05$, $\nu = 0.16$, and $v_{cs} = 4.04$, as shown in Table 4.1. The numerical results are obtained for four different values of $OCR = 1$, 1.2, 3, and 5 to cover a wide range of overconsolidation ratios. Note that in Table 4.1, the initial specific volume before drilling, v_0, is calculated from (Wood, 1990)

$$v_0 = v_{cs} + (\lambda-\kappa)\ln 2 - \lambda\ln[OCR P_0^{'}(1+\frac{q_0^2}{M^2 P_0^{'2}})] + \kappa\ln[OCR(1+\frac{q_0^2}{M^2 P_0^{'2}})] \tag{4.74}$$

and the initial shear modulus can be determined from Eq. (4.3), i.e., $G_0 = \frac{3(1-2\nu)v_0 P_0^{'}}{2(1+\nu)\kappa}$.

Table 4.1. Parameters used in example analyses with modified Cam Clay model

$M = 0.88$, $\lambda = 0.25$, $\kappa = 0.05$, $\nu = 0.16$, and $v_{cs} = 4.04$								
OCR	$\sigma_{r0}^{'}$ (MPa)	$\sigma_{\theta 0}^{'}$ (MPa)	$\sigma_{z0}^{'}$ (MPa)	p_0 (MPa)	$P_0^{'}$ (MPa)	q_0 (MPa)	v_0	G_0 (MPa)
1	11.25	11.25	15	10	12.5	3.75	1.798	395
1.2	11.25	11.25	15	10	12.5	3.75	1.762	387
3	11.25	11.25	15	10	12.5	3.75	1.579	347
5	11.25	11.25	15	10	12.5	3.75	1.476	325

4.5.1 UNDRAINED CASE

Fig. 4.4 shows the variations of the wellbore pressure p_w and excess pore pressure (suction) $\Delta p(a)$ at wellbore surface $r = a$ with the normalized wellbore radius $\frac{a_0}{a}$ for the cases of $OCR = 1$, 1.2, 3, and 5. It is seen that both p_w and $\Delta p(a)$ decrease very rapidly with the contracted wellbore radius if $\frac{a_0}{a}$ is less than 2 but more slowly beyond this value. The wellbore pressure decreases significantly as OCR increases from 1 for normally consolidated rock to 5 for heavily overconsolidated rock, and so does the induced excess pore pressure.

Figs. 4.5-4.8 show the distributions of $\sigma_r^{'}$, $\sigma_\theta^{'}$, and $\sigma_z^{'}$ and also of P', q, and Δp along the radial distance corresponding to a zero wellbore pressure ($p_w = 0$) for all the overconsolidation ratios in the range 1 to 5, the radial axis again being normalized with respect to the current wellbore radius a. It is interesting to note that for normally consolidated ($OCR = 1$) and slightly overconsolidated ($OCR = 1.2$) rocks, all the stresses

in the vicinity of the wellbore remain almost unchanged. This implies that the rock of this range has essentially reached the critical state. However, as the overconsolidation ratio increases ($OCR = 3$ and 5), such an internal critical state zone disappears and there usually exists a unique plastic zone outside the wellbore. More interestingly, it is found that in the critical state zone the vertical stress is eventually equal to the average of radial and tangential stresses, which is true for both the two values of $OCR = 1$ and 1.2 considered. This feature is actually well reflected in Eq. (4.40) where $\frac{D}{Dr}(\sigma_r^{'} + \sigma_\theta^{'} - 2\sigma_z^{'}) = 0$ as a result of the constant stress components in the critical state zone, and therefore, the only possible zero term on the right hand side, $\sigma_r^{'} + \sigma_\theta^{'} - 2\sigma_z^{'}$, must also vanish thus giving $\sigma_z^{'} = \frac{1}{2}(\sigma_r^{'} + \sigma_\theta^{'})$. Note that for $OCR = 1$ (Fig. 4.5), the Cam Clay model predicts plastic yielding responses for all the material particles immediately after drilling, so that there is no elastic zone around the wellbore in this case. However, when $OCR > 1$, there will usually exist an external elastic zone in addition to the plastic and failure zones developed around the wellbore, see Figs. 4.6-4.8. As is evident, the overconsolidation ratio OCR has a pronounced influence on the distributions of the three effective stresses and excess pore pressure, and on the sizes of the failure, plastic, and elastic zones. The higher the value of OCR, the smaller failure and plastically deformed regions and larger elastic region will be developed outside the wellbore.

It is worth to note from Figs. 4.5b and 4.6b that the negative excess pore pressure generated increases nearly linearly with the logarithm of $\frac{r}{a}$ in the critical state failure zone, and becomes virtually equal to zero in the external elastic zone. This is in agreement with the finite element results for pile driving problem reported by Randolph et al. (1979) where an approximate linear variation of Δp versus $\ln r$ was suggested to estimate the

pore pressure development in the failure zone. On the other hand, both the effective mean stress and deviatoric stress remain largely unchanged (at the critical state) near the wellbore surface, but may increase or decrease with the radial distance in the plastic zone depending essentially on the value of OCR. For all the values of OCR considered, in the elastic region the effective mean stresses remain constant and equal to the initial value of $P_0^{'} = 12.5$ MPa, which is indeed expected. Note that since the material particles at different locations follow exactly the same stress paths, the curves in Figs. 4.5-4.8 represent also the stress and pore pressure changes experienced by any particular material particle.

Figs. 4.9-4.12 further plots the effective stress paths (ESP) followed in the $P^{'} - q$ plane for a material particle located at the wellbore surface. For $OCR = 1$, the initial yield locus passes through the in situ stress point $P_0^{'} = 12.5$ MPa and $q_0 = 3.75$ MPa. Fig. 4.9 shows that in this case, the mean effective stress will decrease but the deviator stress increase during the wellbore drilling so that the stress path continues to move up to the left. The yield locus therefore expands progressively until the stress path intersects the critical state line at point F. At that point the critical state failure is reached and the stress path will thereafter remain stationary there. For OCR greater than 1, the in situ stress point is always located within the initial yield locus. So, as may be seen from Figs. 4.10-4.12, the stress path for a material particle at the wellbore surface first moves along a vertical line in the $P^{'} - q$ diagram until it hits the initial yield locus. After that the stress path will turn up to the left from the 'wet' side ($\eta < M$) or rightward from the 'dry' side ($\eta > M$) both towards the critical state line, and again terminate at the failure point F if the critical state is ultimately reached (Fig. 4.10).

4.5.2 DRAINED CASE

Figs. 4.13-4.16 present the variations of $\sigma_r^{'}$, $\sigma_\theta^{'}$, and $\sigma_z^{'}$ against the normalized radial distance $\frac{r}{a}$ as well as the corresponding results for the mean effective stress P', deviator stress q, and the specific volume v, again relevant to $p_w^{'} = 0$ and overconsolidation ratios $OCR = 1$, 1.2, 3, and 5. It is emphasized that, unlike the previous undrained case where $\sigma_r^{'}$, $\sigma_\theta^{'}$, and $\sigma_z^{'}$ remain largely unchanged near the wellbore surface for normally consolidated and lightly overconsolidated rocks, all the three stress components for the drained situation generally increase rapidly with $\frac{r}{a}$ in the vicinity of the wellbore, implying that the stress state at the wellbore surface still has not reached the critical state. Figs. 4.13-4.16 again clearly demonstrate that the overconsolidation ratio has a significant influence on the stress distributions as well as on the development of plastic zone around the wellbore. As a matter of fact, for the large value of $OCR = 5$ (Fig. 4.16), the plastic zone does not exist at all and the stresses around the wellbore is purely elastic.

Figs. 4.17-4.20 further illustrate the projections of the stress paths on the $P' - q$ plane and on the $v - P'$ plane for a rock particle at the wellbore surface. For $OCR = 1$, the in situ stress point $P_0^{'} = 12.5$ MPa and $q_0 = 3.75$ MPa lies on the initial yield locus, see Fig. 4.17a. During the wellbore drilling process the $P^{'} - q$ stress path first moves upper-left accompanied by progressive expansion of the yield locus, until the stress state is at the crest of the elliptical yield locus (point C). It will then turn down to the left associated with the shrinking of yield locus and with the occurrence of plastic softening. Simultaneously, the $v - P'$ trajectory in the compression plane, which starts from the point $P_0^{'} = 12.5$ KPa and $v_0 = 1.798$ (Fig. 4.17b), moves almost horizontally at the

initial stage of the drilling and then bends towards increasing specific volume after crossing the critical line which can be expressed as (Wood, 1990)

$$v = v_{cs} - \lambda \ln P' \tag{4.75}$$

It perhaps now seems surprising that the $P' - q$ and $v - P'$ diagrams for $OCR = 1$ pass through the critical state line from the wet side to the dry side, rather than terminated at certain point on the critical line during the continuing plastic deformation. However, that is true because the stress paths are found to cross the critical state line parallel to the P' axis, as is clearly illustrated in Figs. 4.17a, which means that when the stress state is on the critical state line the stress increment is tangential to the current yield locus and is actually along the neutral loading direction. Therefore, it makes possible for the $P' - q$ and $v - P'$ trajectories to overshoot the critical state line, changing from the plastic hardening to the plastic softening behaviour, and subsequently move towards the critical line at lower means and deviator stress yet higher specific volume. Similar results have been reported in Collins & Stimpson (1994) for the similarity solution of created cavity problem using the simplified P' and q expressions and also in Chen & Abousleiman (2012b) for the rigorous analysis of finite expansion problem.

For OCR greater than 1, as expected, the in situ stress state always lies inside the initial yield locus (Fig. 4.18a, 4.19a, and 4.20a). The $P' - q$ stress path must rise at constant P' until the initial yield locus is reached and the corresponding $v - P'$ diagram shrinks into a single point as a result of elastic deformation. After that, the rock may experience plastic hardening then softening ($OCR = 1.2$) or plastic softening ($OCR = 3$) depending essentially on the value of overconsolidation ratio. Especially for the case of $OCR = 5$, the modified Cam Clay model predicts purely elastic responses so the effective

mean stress and specific volume must retain their initial values of $P_0^{'}$ and v_0 during the whole process of drilling, as shown in Fig. 4.20.

4.6 Summary

In this chapter, the undrained/drained wellbore drilling problem is analyzed by adopting the widely used volumetric strain-hardening/softening modified Cam Clay model to describe the elastoplastic behaviour of shale formations. The analytical solutions developed follow the rigorous definitions for the two effective stress invariants instead of approximate ones, as usually assumed in the existing literatures for the critical state models. The solution procedure is again very similar to those described before for the Drucker-Prager and Mohr-Coulomb models, although difficulties may arise due to the nonlinear elastic property of the modified Cam Clay model, in particular under the drained situation.

The results show that the overconsolidation ratio has a pronounced influence on the stress distributions around the wellbore and on the size of the plastically deformed region. The higher the value of OCR, the smaller failure and plastic zones and larger elastic zone will be developed outside the wellbore. For the undrained case, in the critical state zone the vertical stress is found to be equal to the average of radial and tangential stresses, and the excess pore pressure varies nearly linearly with the logarithm of the radial distance. The $P^{'} - q$ stress path during the drilling process generally approaches the critical state line from the wet or dry side depending much on the value of OCR. For the drained case, it is observed that the three stress components decrease rapidly in the vicinity of the wellbore, indicating that the stress state at the wellbore surface still has not reached the critical state. More importantly, for normally consolidated and slightly overconsolidated

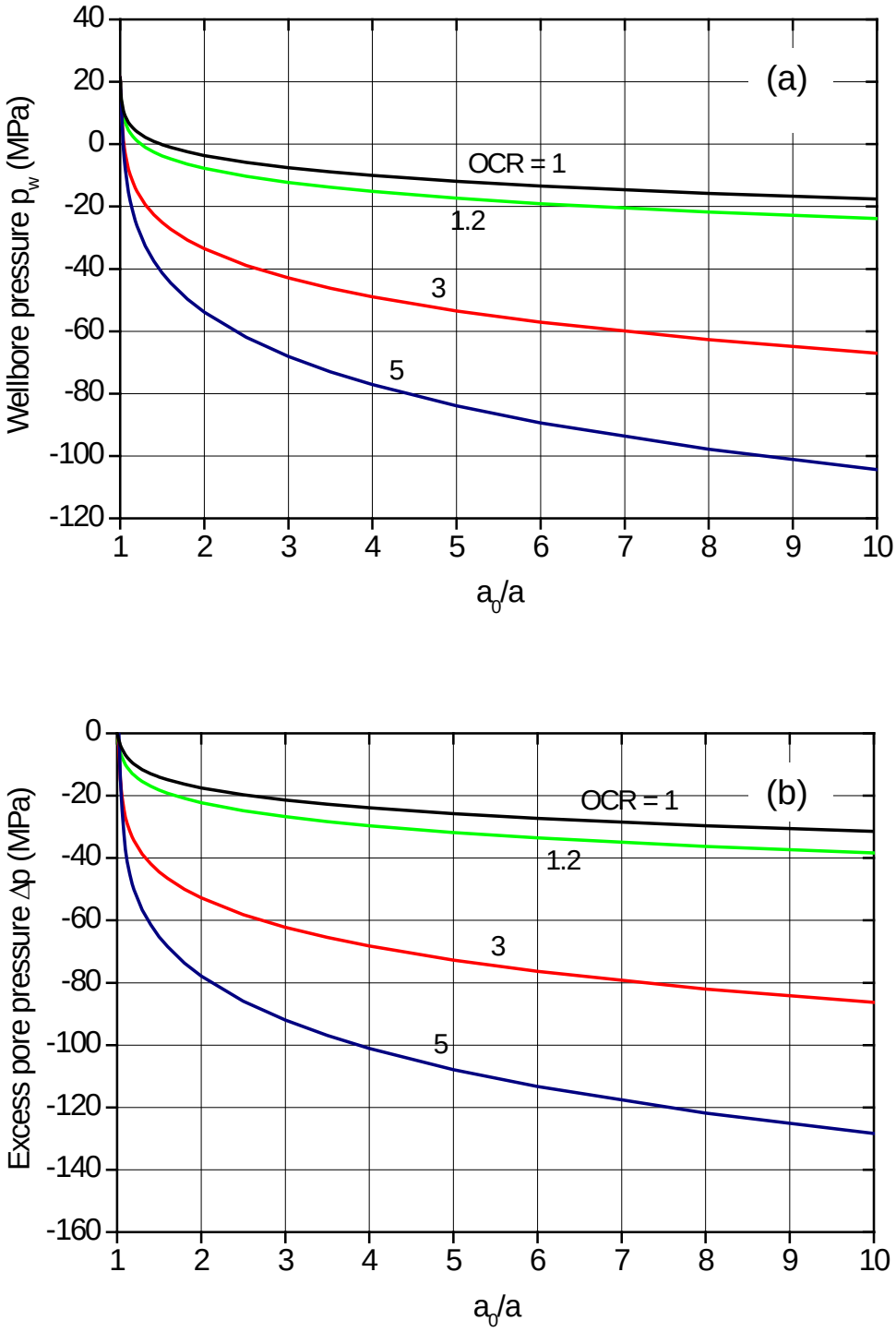

Fig. 4.4. Variations of (a) wellbore pressure; (b) pore pressure with normalized wellbore radius for undrained case (modified Cam Clay model)

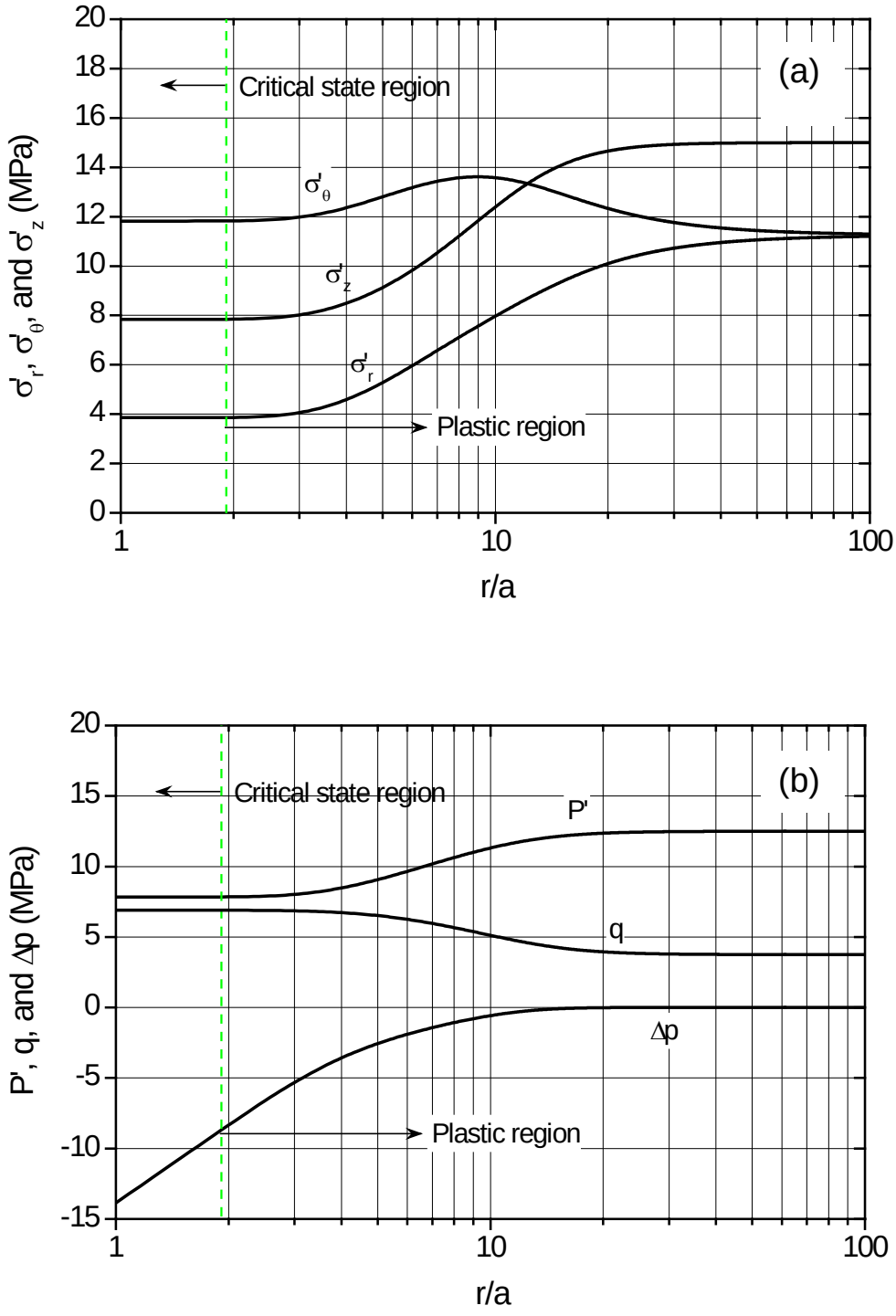

Fig. 4.5. Distributions of (a) effective radial, tangential, and vertical stresses; (b) effective mean, deviatoric stresses and excess pore pressure around the wellbore for OCR = 1, undrained case (modified Cam Clay model)

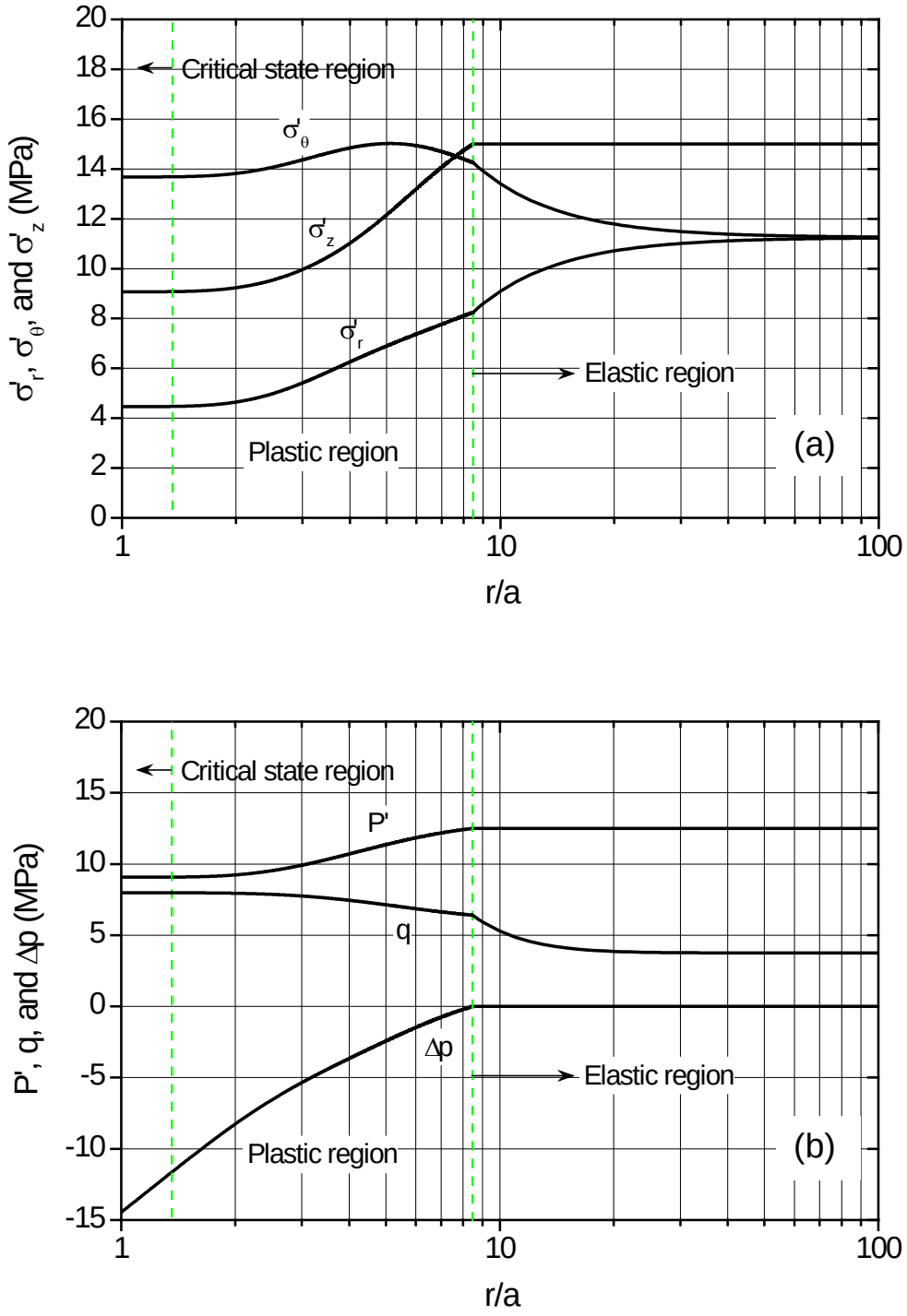

Fig. 4.6. Distributions of (a) effective radial, tangential, and vertical stresses; (b) effective mean, deviatoric stresses and excess pore pressure around the wellbore for OCR = 1.2, undrained case (modified Cam Clay model)

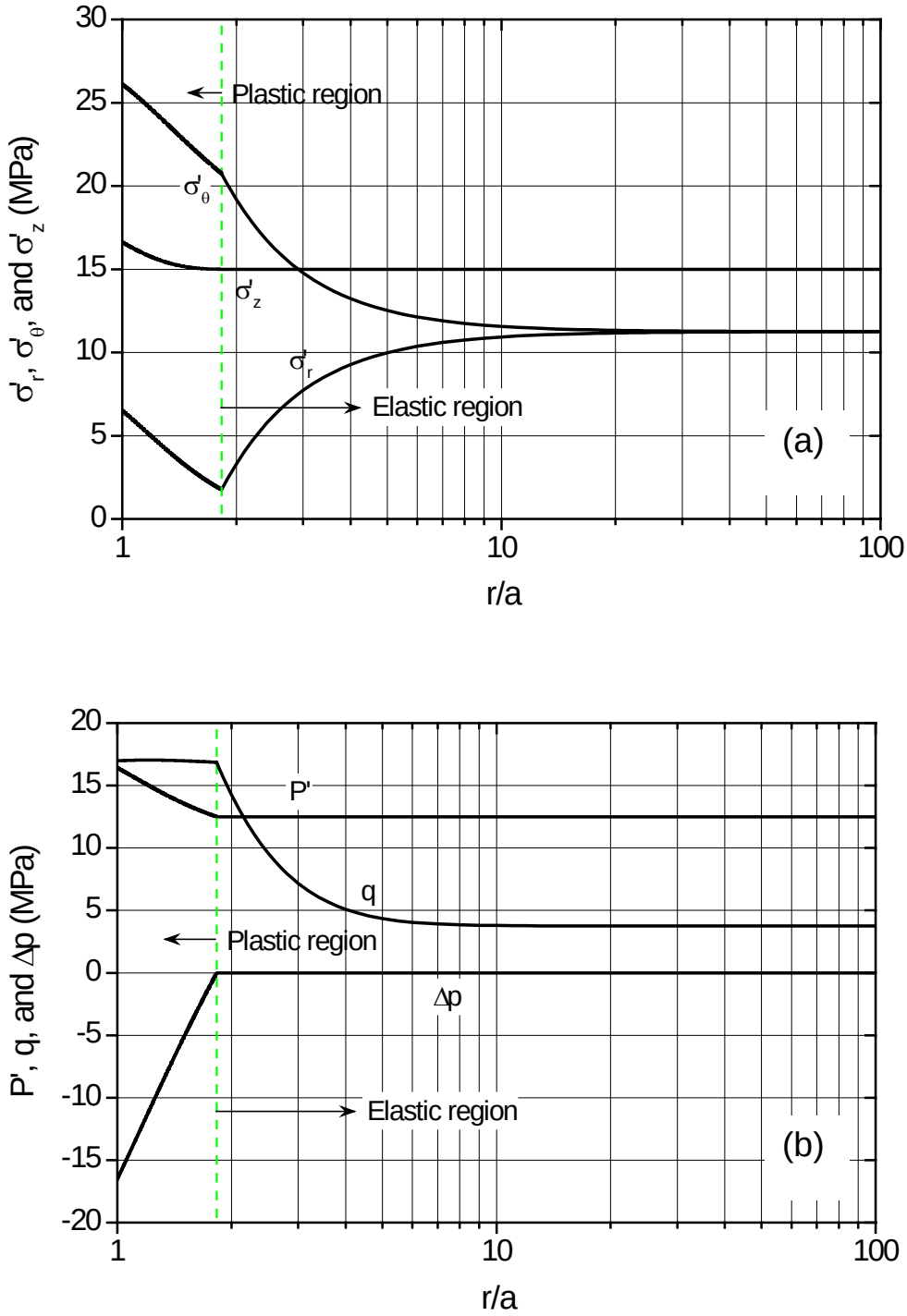

Fig. 4.7. Distributions of (a) effective radial, tangential, and vertical stresses; (b) effective mean, deviatoric stresses and excess pore pressure around the wellbore for OCR = 3, undrained case (modified Cam Clay model)

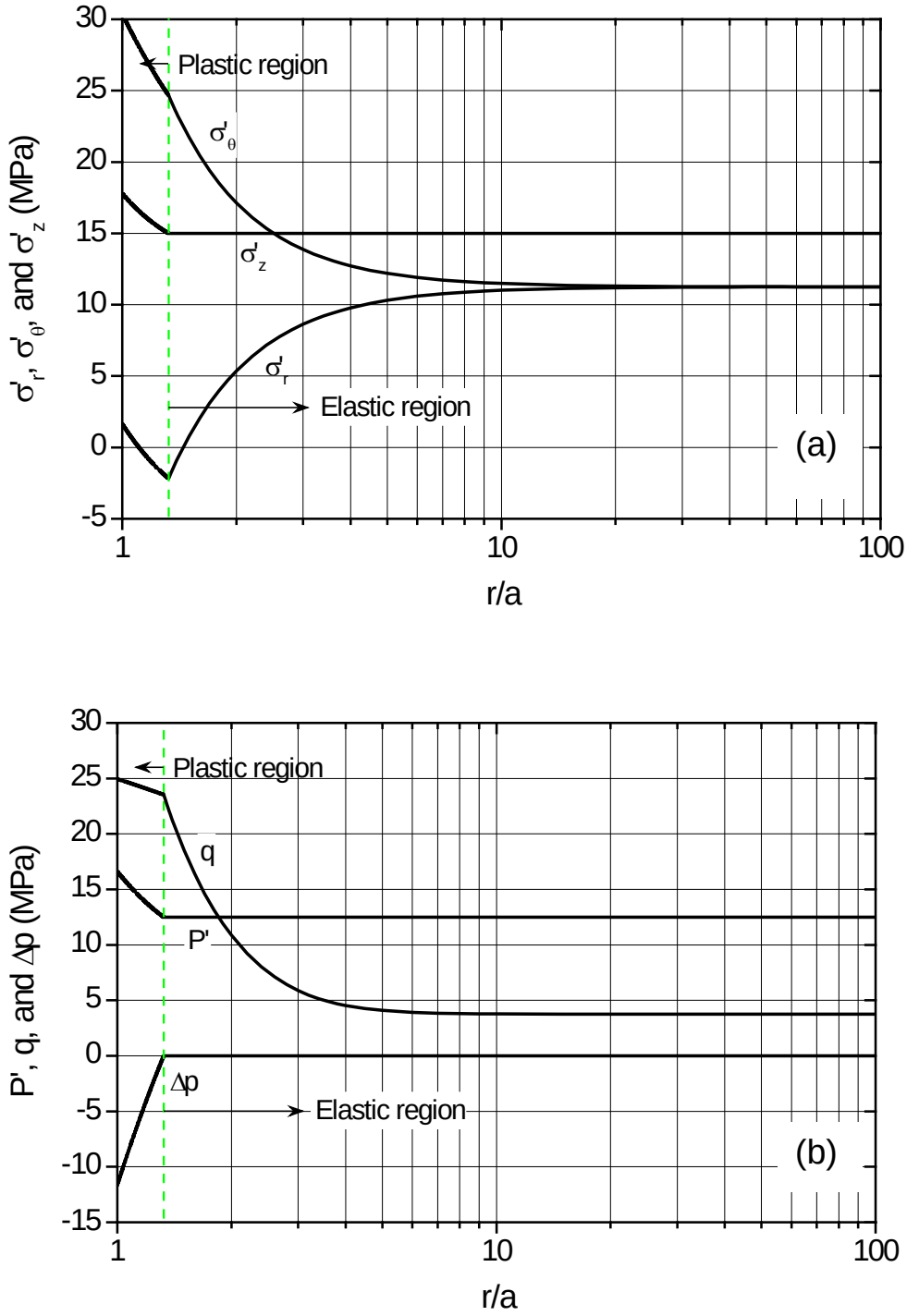

Fig. 4.8. Distributions of (a) effective radial, tangential, and vertical stresses; (b) effective mean, deviatoric stresses and excess pore pressure around the wellbore for OCR = 5, undrained case (modified Cam Clay model)

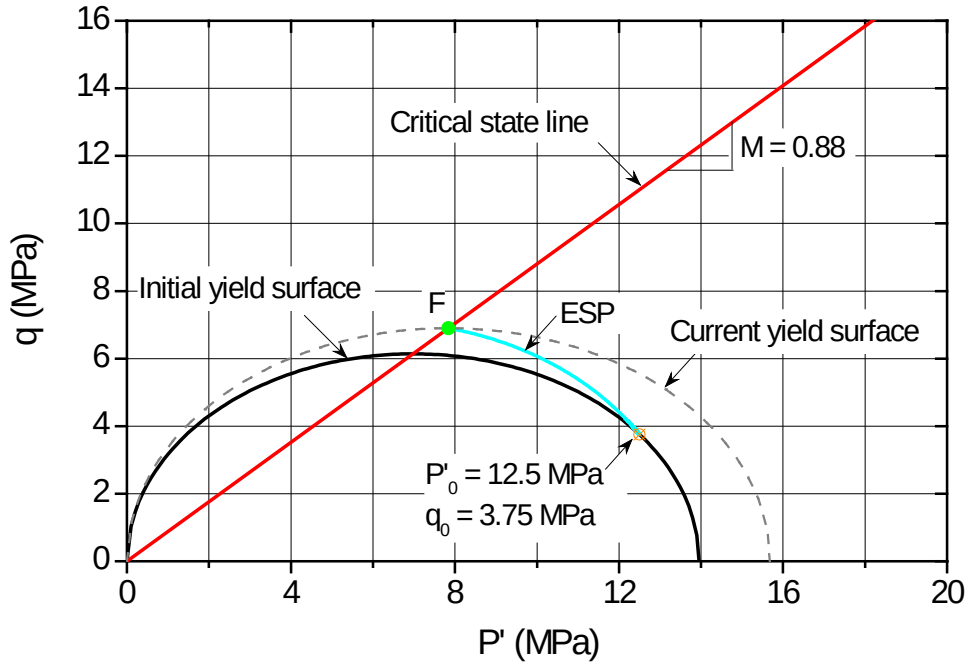

Fig. 4.9. Undrained P'-q stress path at wellbore surface for OCR = 1

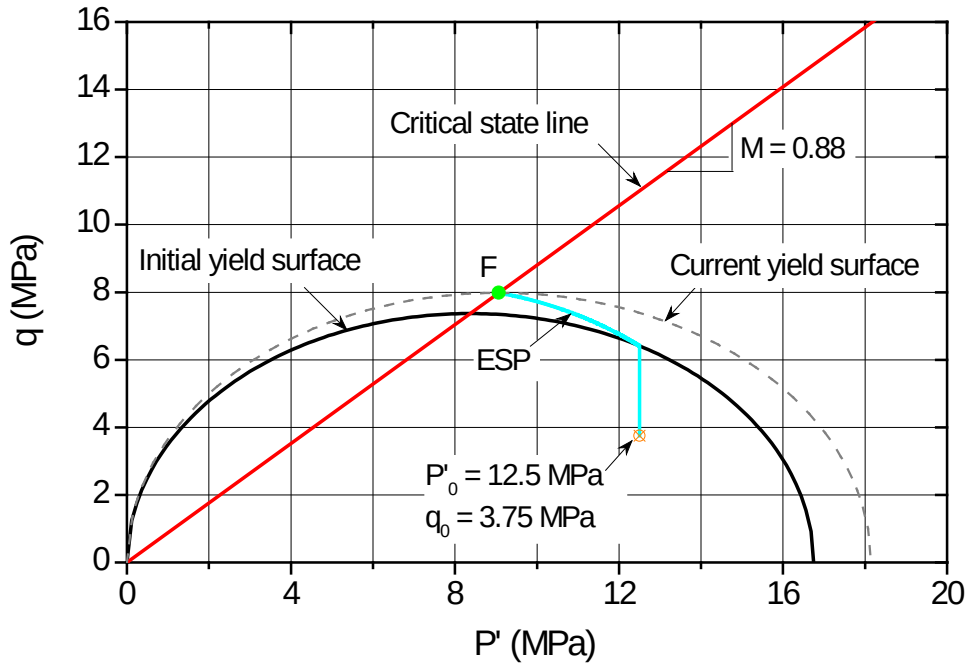

Fig. 4.10. Undrained P'-q stress path at wellbore surface for OCR = 1.2

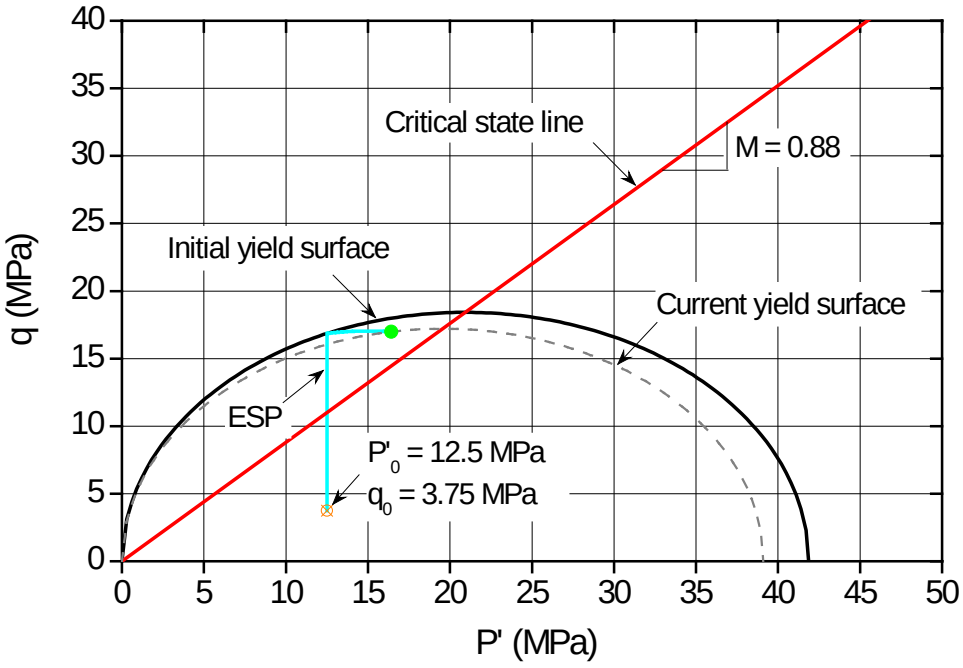

Fig. 4.11. Undrained P'-q stress path at wellbore surface for OCR = 3

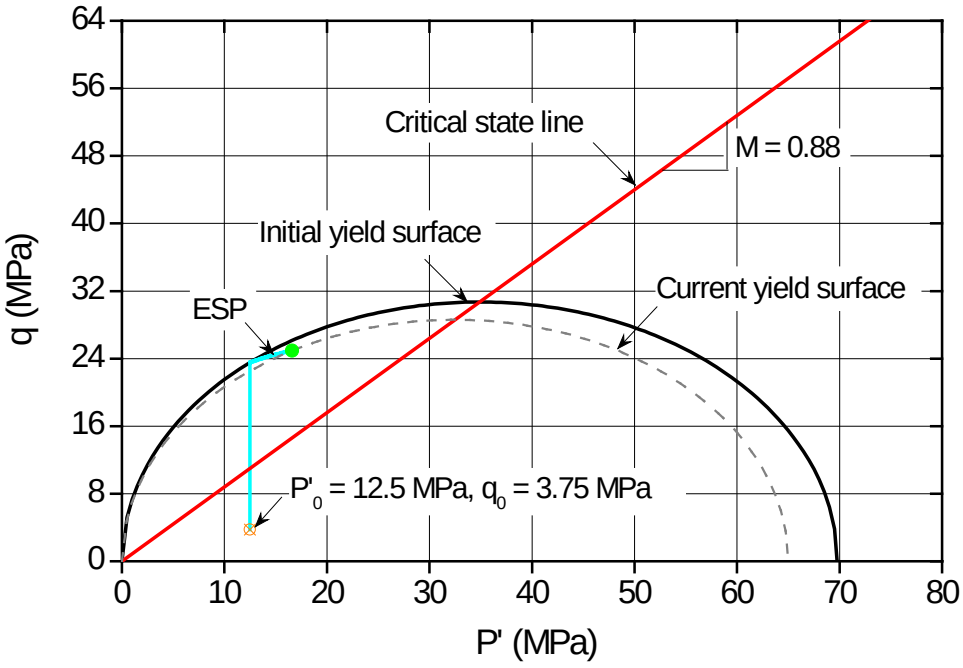

Fig. 4.12. Undrained P'-q stress path at wellbore surface for OCR = 5

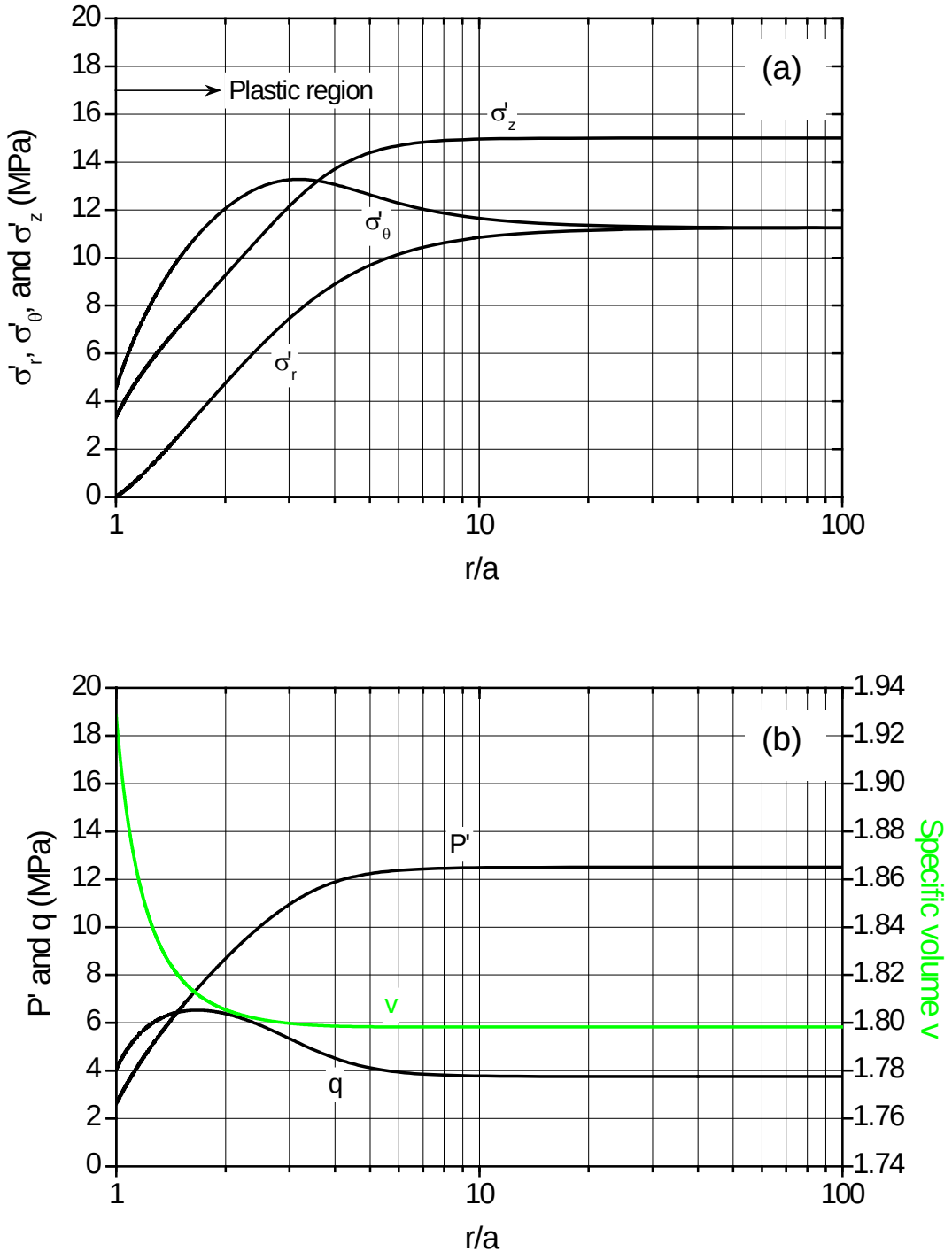

Fig. 4.13. Distributions of (a) effective radial, tangential, and vertical stresses; (b) effective mean, deviatoric stresses and excess pore pressure around the wellbore for OCR = 1, drained case (modified Cam Clay model)

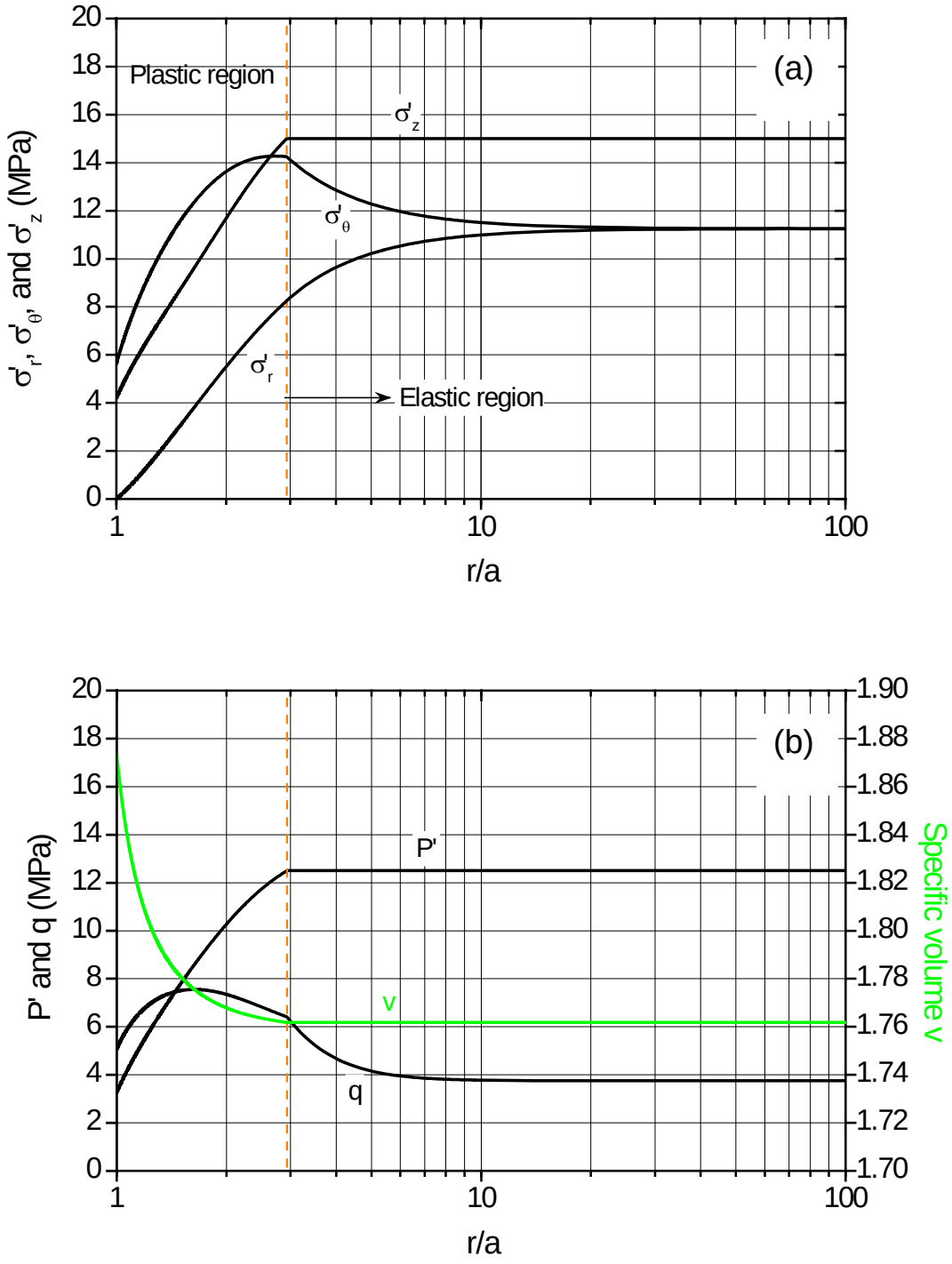

Fig. 4.14. Distributions of (a) effective radial, tangential, and vertical stresses; (b) effective mean, deviatoric stresses and excess pore pressure around the wellbore for OCR = 1.2, drained case (modified Cam Clay model)

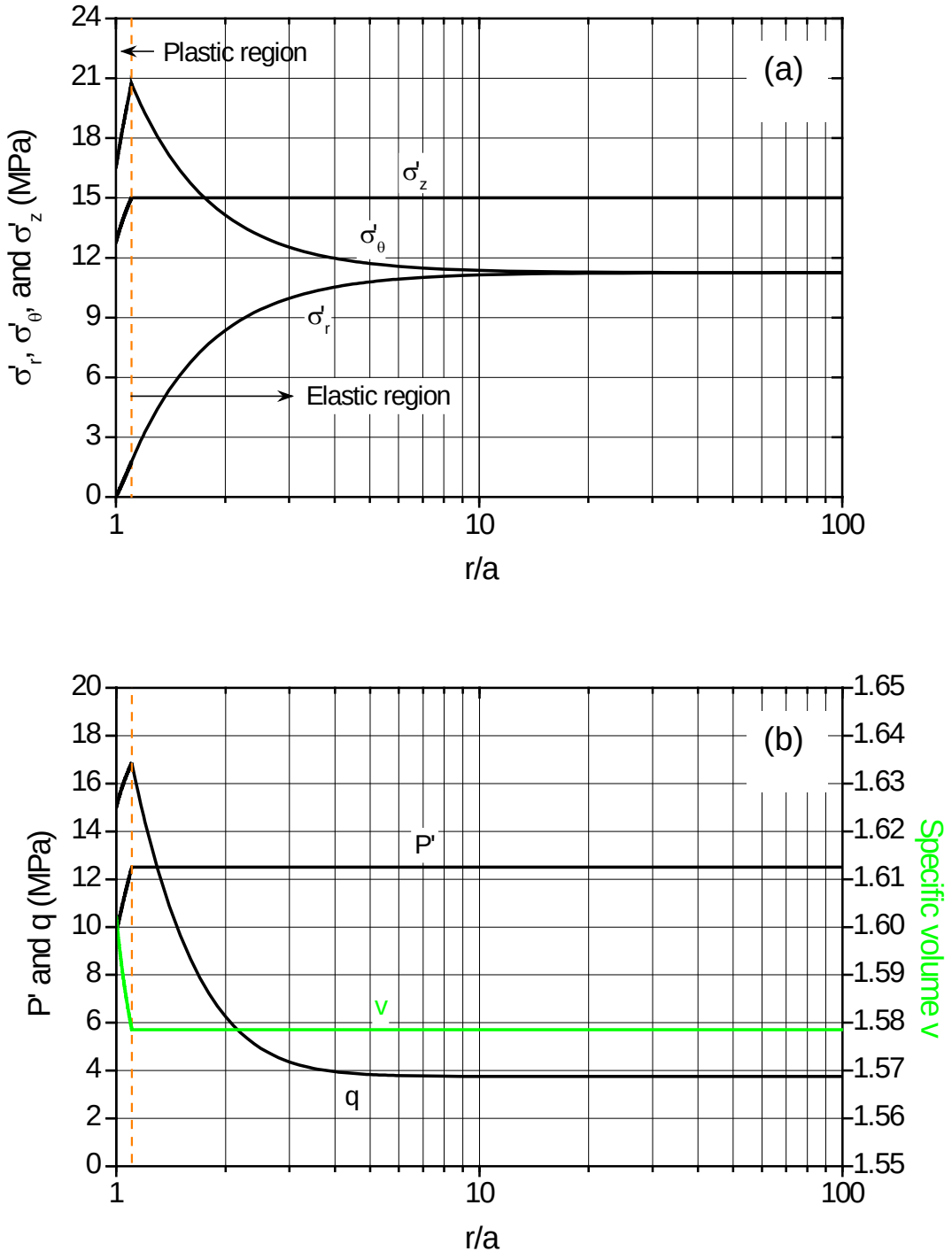

Fig. 4.15. Distributions of (a) effective radial, tangential, and vertical stresses; (b) effective mean, deviatoric stresses and excess pore pressure around the wellbore for OCR = 3, drained case (modified Cam Clay model)

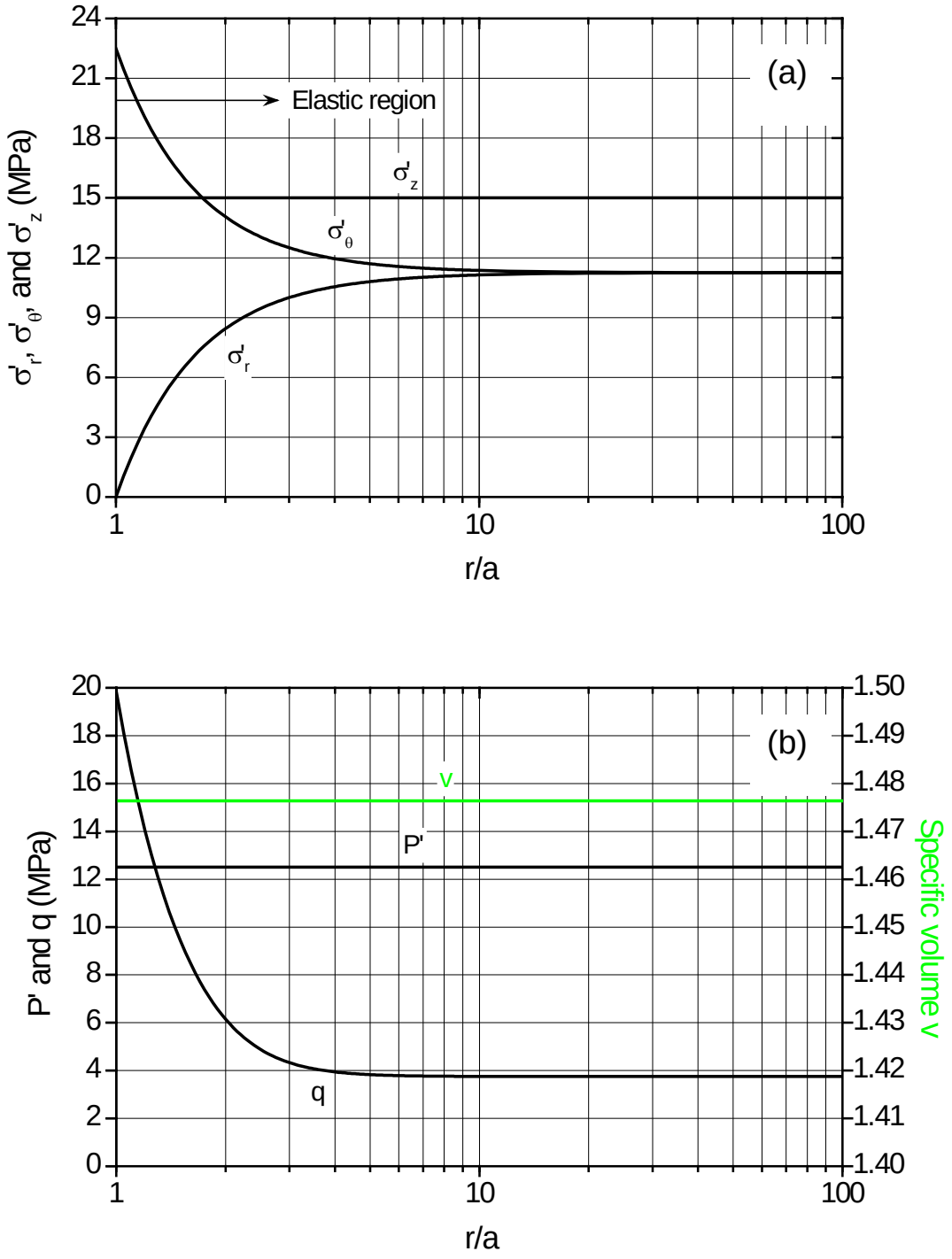

Fig. 4.16. Distributions of (a) effective radial, tangential, and vertical stresses; (b) effective mean, deviatoric stresses and excess pore pressure around the wellbore for OCR = 5, drained case (modified Cam Clay model)

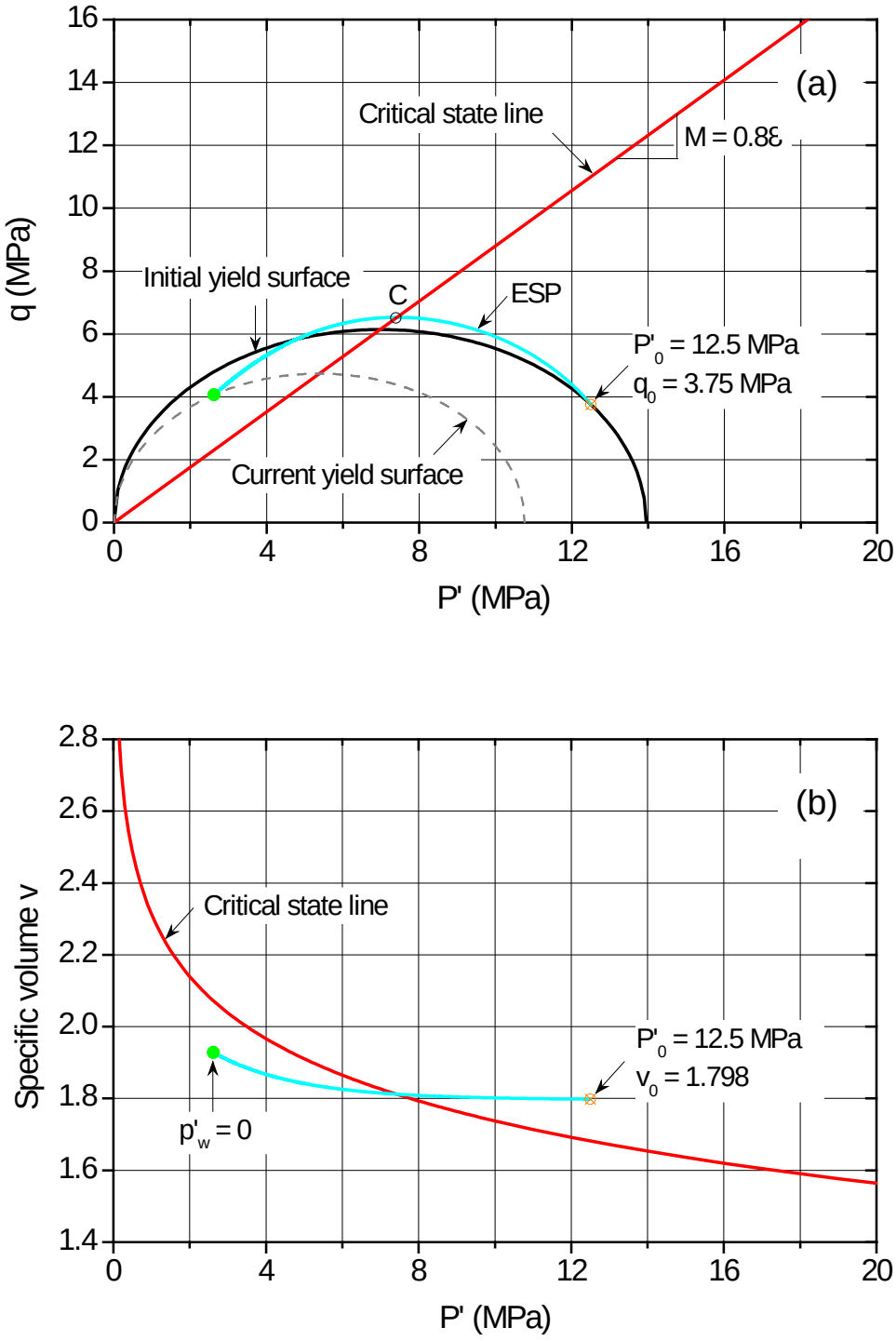

Fig. 4.17. Drained stress path in P'-q-v space at wellbore surface for normally consolidated rock, OCR = 1: (a) projection on P'-q plane; (b) projection on v-P' plane

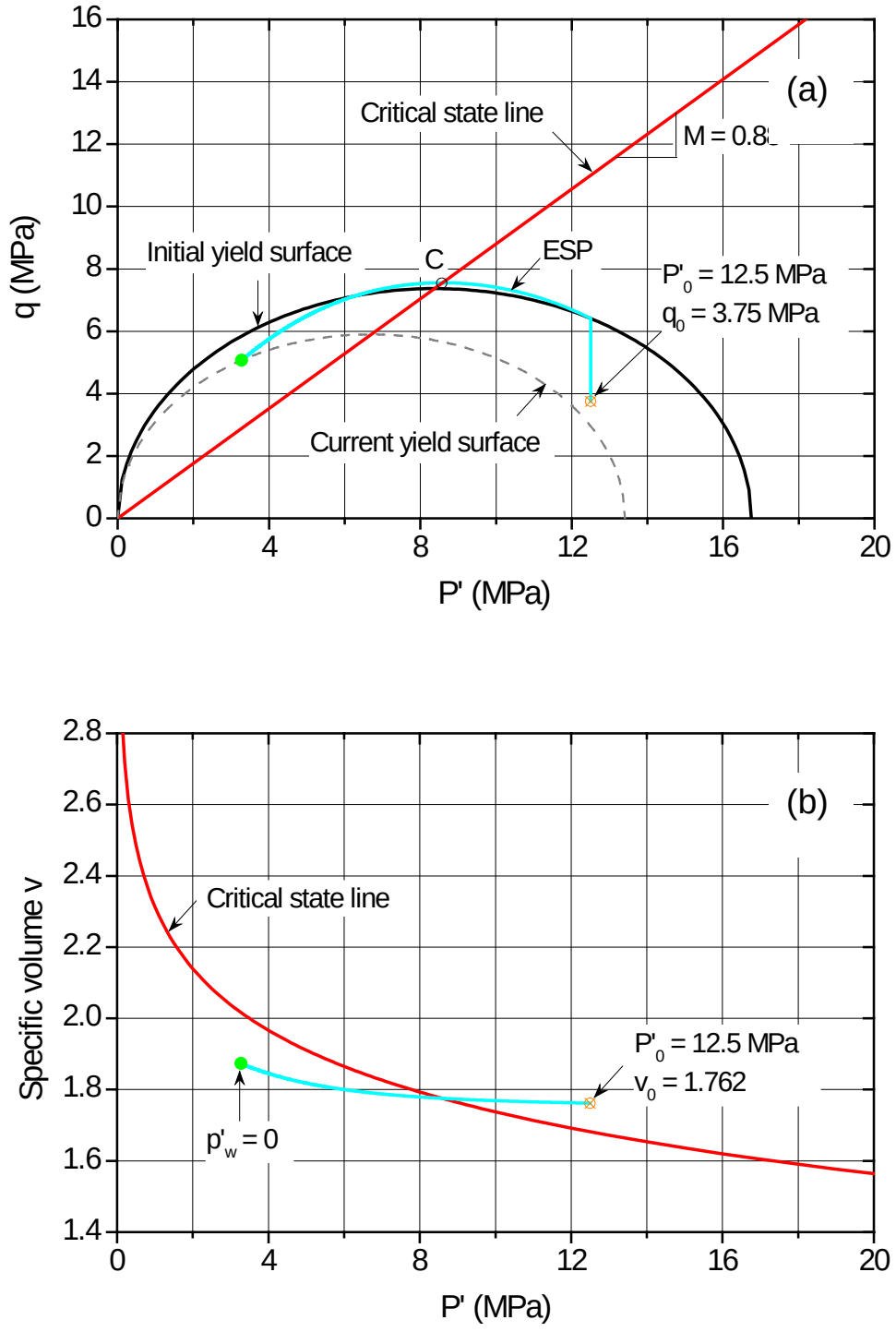

Fig. 4.18. Drained stress path in P'-q-v space at wellbore surface for lightly overconsolidated rock, OCR = 1.2: (a) projection on P'-q plane; (b) projection on v-P' plane

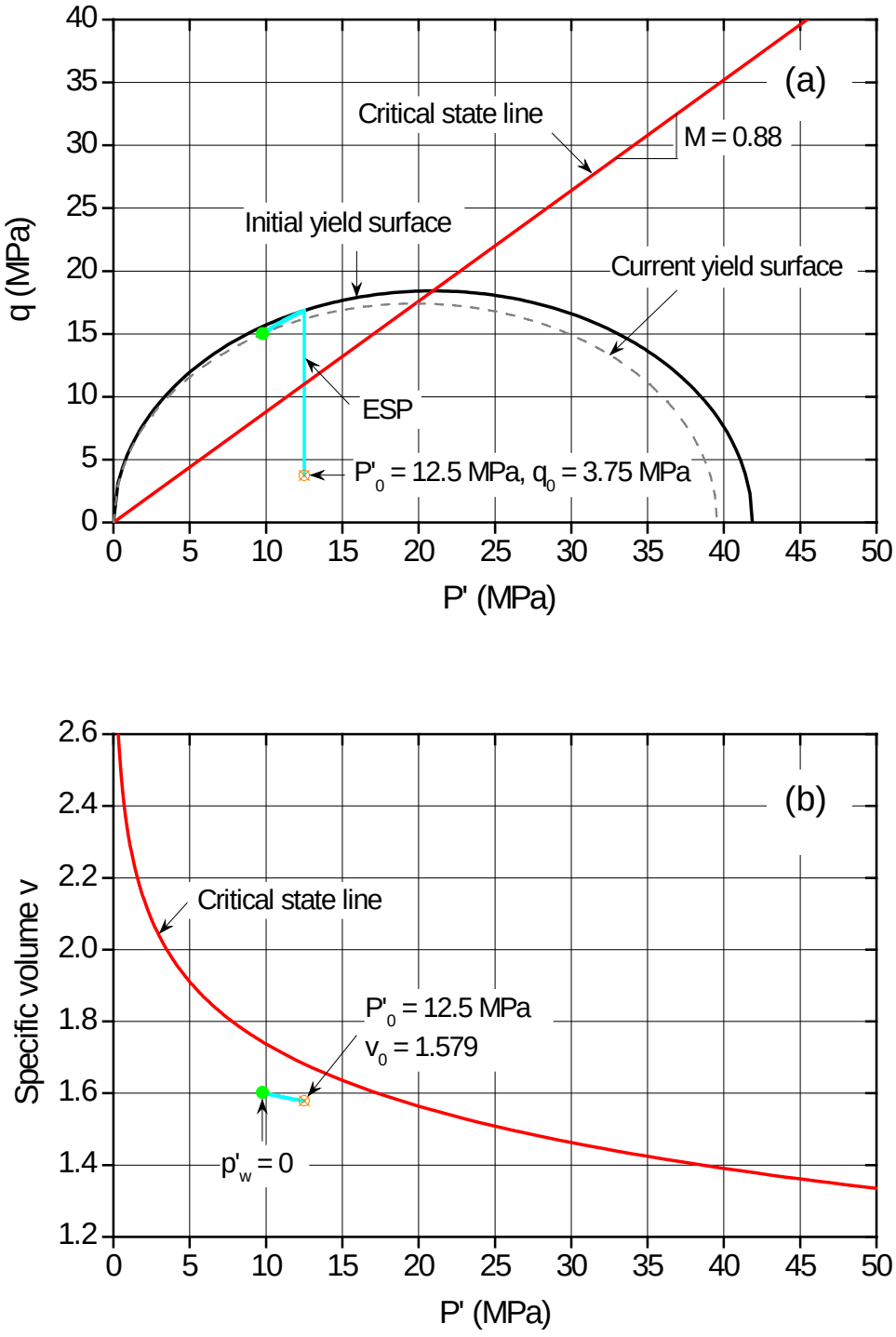

Fig. 4.19. Drained stress path in P'-q-v space at wellbore surface for moderately overconsolidated rock, OCR = 3: (a) projection on P'-q plane; (b) projection on v-P' plane

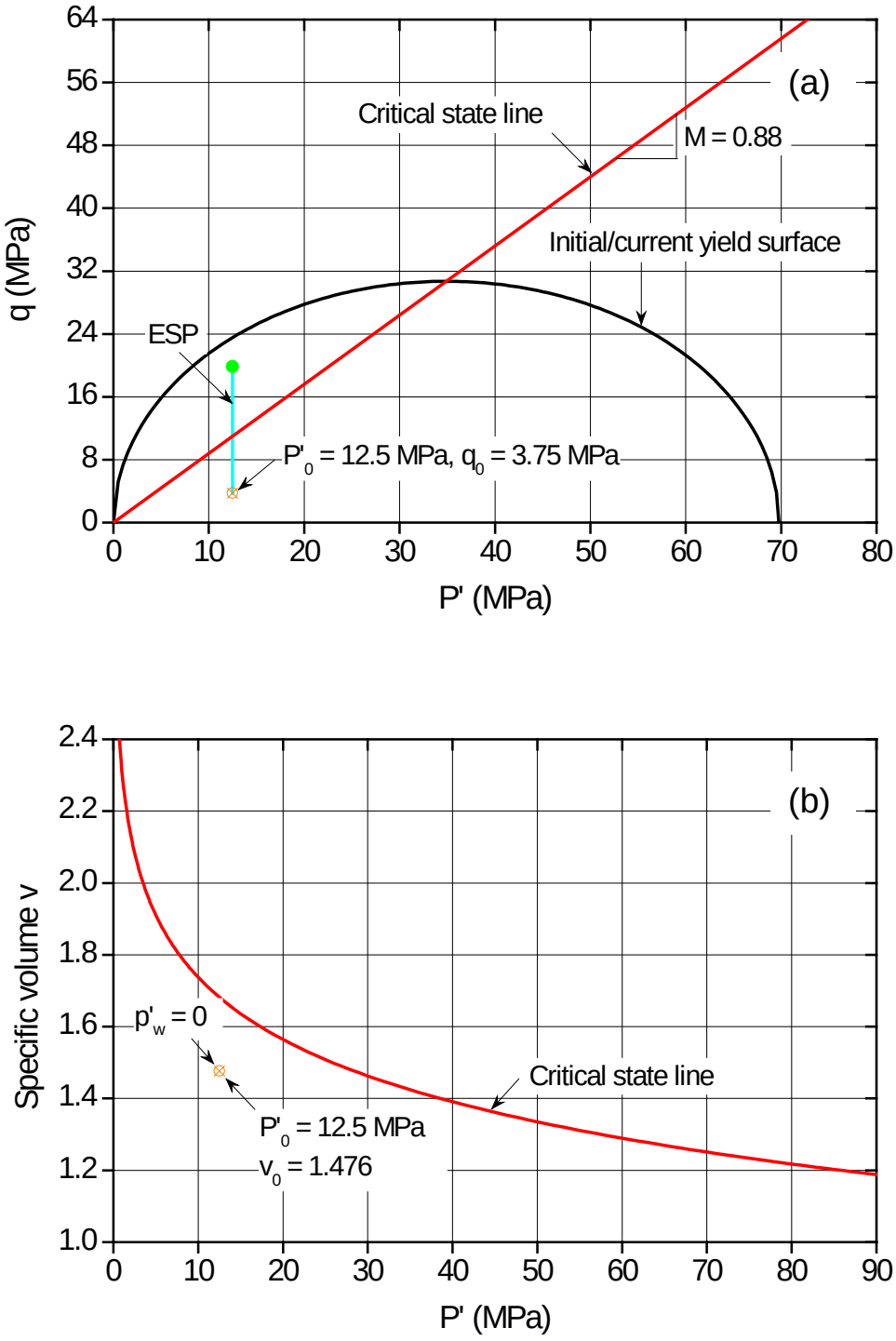

Fig. 4.20. Drained stress path in P'-q-v space at wellbore surface for heavily overconsolidated rock, OCR = 5: (a) projection on P'-q plane; (b) projection on v-P' plane

rocks, the $P' - q$ trajectories may initially overshoot the critical state line in parallel with the P' axis (undergoing the transition from the plastic hardening to the plastic softening behaviour), and then return towards the critical line at lower means and deviator stress yet higher specific volume.

CHAPTER 5

WELLBORE STABILITY ANALYSIS IN BOUNDING SURFACE ROCKS

5.1 Introduction

This chapter considers further the wellbore drilling boundary value problem involving the critical state based bounding surface model (Dafalias & Herrmann, 1980; 1982). The prominent feature of this model, with the concept of the bounding surface in stress space, is that inelastic deformation can occur for stress points within the bounding surface at a pace depending on the proximity of the current stress state to the bounding surface (Kaliakin et al., 1987), so that the realistic non-recoverable behaviour of soils/rock observed on unloading and reloading can be well recovered. The drained/ undrained analytical solution presented in this chapter is suitable for the shale formations and complements the one in Chapter 4 based on the modified Cam Clay model.

5.2 Bounding Surface Model

The well established bounding surface formulation for clay was originally introduced by Dafalias & Herrmann (1980; 1982) within the framework of critical state soil plasticity. The basic idea of their formulation is that an isotropically expanding or contracting surface, rather than a yield surface, is used in the model. This surface is

known as the bounding surface which depends only on the plastic volumetric strain (or plastic void ratio). In addition, the bounding surface model uses a simple radial mapping to determine a unique image point on the bounding surface that corresponds to the current stress point inside the bounding surface. The value of the plastic modulus is assumed to be a function of the distance between the stress point and its image, while the gradient of the bounding surface at the image point defines the loading-unloading direction. The salient feature of this model is that plastic deformation may occur for stress point even inside the surface.

Fig. 5.1 shows a schematic illustration of the bounding surface model. A stress state $\sigma_{ij}^{'}$ lies always within or on the bounding surface which, mathematically, can be expressed as

$$\bar{F}\left(\bar{\sigma}_{ij}^{'}, e^{p}\right) = 0 \tag{5.1}$$

where a bar over stress quantities $\sigma_{ij}^{'}$ indicates points on the bounding surface $\bar{F} = 0$ and e^{p}, the plastic void ratio, is the only plastic internal variable defining the hardening/ softening behaviour of the bounding surface. This is different from the strain hardening Drucker-Prager and Mohr-Coulomb (or Matkuosa-Nakai) models used in Chapters 2 and 3, for which it is nevertheless the plastic deviatoric strain ε_{q}^{p} that controls the manner of hardening. Note that the plastic void ratio e^{p} is related to the plastic volumetric strain ε_{p}^{p} and the elastic void ratio e^{e} as follows

$$de^{p} = -(1 + e)d\varepsilon_{p}^{p} \tag{5.2}$$

$$e^{e} + e^{p} = v - v_{0} \tag{5.3}$$

where e is the total void ratio; v is the specific volume ($v = 1 + e$); v_{0} is the initial specific volume; and de^{p} and $d\varepsilon_{p}^{p}$ are the increments of plastic void ratio and plastic

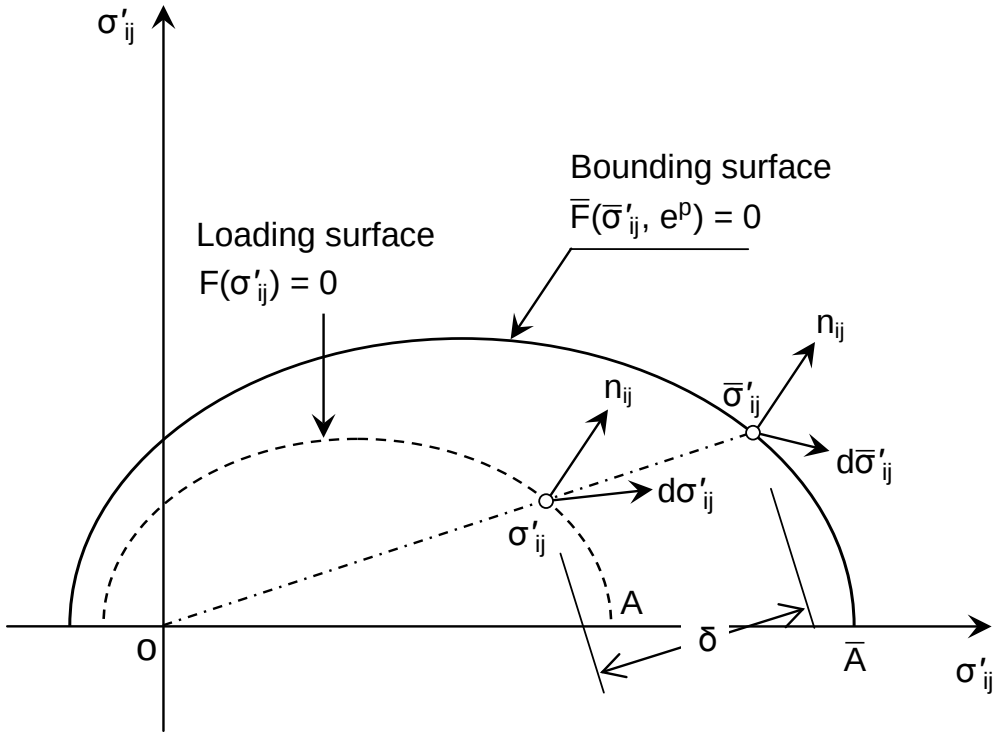

Fig. 5.1. Schematic illustration of bounding surface and radial mapping rule

volumetric strain, respectively.

In addition to the bounding surface, at any stress point $\sigma_{ij}^{'}$ a surface homeothetic to the bounding surface with respect to the origin *o* can be indirectly defined (shown by a dashed line in Fig. 5.1)

$$F\left(\sigma_{ij}^{'}\right) = 0 \tag{5.4}$$

Such a surface is referred to as the loading surface in Dafalias & Herrmann (1980; 1982), which specifies a quasi-elastic domain but is actually not a yield surface since an inward motion of $\sigma_{ij}^{'}$ will eventually induce loading after an initial path of unloading before $\sigma_{ij}^{'}$

reaches the surface again.

The plastic constitutive relations for the bounding surface model, in the general stress space, can be expressed as (Dafalias & Herrmann, 1980)

$$d\varepsilon_{ij}^{p} = \langle L \rangle n_{ij} \tag{5.5}$$

$$L = \frac{1}{K} d\sigma_{kl}^{'}\, n_{kl} = \frac{1}{K_b} d\bar{\sigma}_{kl}^{'} n_{kl} \tag{5.6}$$

where n_{ij} denotes the unit normal at stress point $\sigma_{ij}^{'}$ or its image point $\bar{\sigma}_{ij}^{'}$ on the bounding surface, see Fig. 5.1; K is the actual plastic modulus associated with $d\sigma_{kl}$; K_b is a plastic modulus on the bounding surface associated with $d\bar{\sigma}_{kl}$; the Macauley bracket $\langle \cdot \rangle$ define the operation $\langle L \rangle = h(L) \cdot L$, h being the heaviside step function; L is usually called the loading function. The bounding surface plastic modulus K_b is obtained from the consistency condition

$$d\bar{F} = \frac{\partial \bar{F}}{\partial \bar{\sigma}_{ij}^{'}} d\bar{\sigma}_{ij}^{'} + \frac{\partial \bar{F}}{\partial e^{p}} de^{p} = 0 \tag{5.7}$$

with the aid of Eq. (5.2), as follows

$$K_b = \frac{1+e}{\left[\frac{\partial \bar{F}}{\partial \bar{\sigma}_{ij}^{'}} \frac{\partial \bar{F}}{\partial \bar{\sigma}_{ij}^{'}}\right]} \frac{\partial \bar{F}}{\partial e^{p}} \frac{\partial \bar{F}}{\partial \bar{\sigma}_{kk}^{'}} \tag{5.8}$$

Note that in the above two equations the summation convention over repeated indices applies.

The plastic modulus K needed to determine the plastic strain increment at the current stress point $\sigma_{ij}^{'}$ is related to K_b by

$$K = K_b + H(\sigma_{ij}^{'}, e^{p}) \frac{\delta}{\delta_0\left(\sigma_{ij}^{'}, e^{p}\right) - \delta} \tag{5.9}$$

where H is the hardening function; δ is the distance between $\sigma_{ij}^{'}$ and $\bar{\sigma}_{ij}^{'}$; and δ_0 is a properly chosen reference stress.

5.3 Undrained Solution

It should be emphasized that for a wellbore drilled in a bounding surface rock formation, plastic deformations occur immediately after drilling for all the material particles so there is no elastic zone existing around the wellbore, see Fig. 5.2. This is the

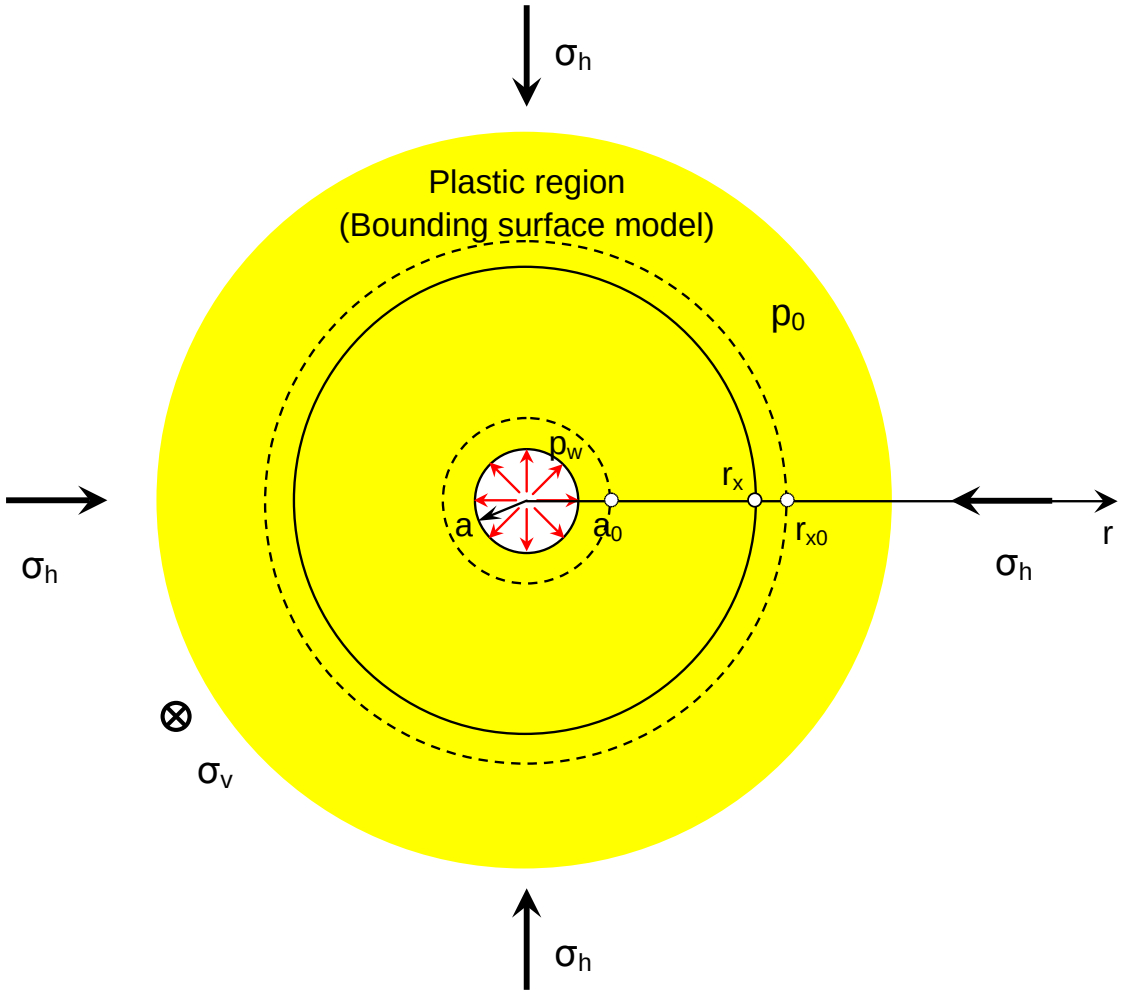

Fig. 5.2. Wellbore boundary value problem (bounding surface model)

direct result of using bounding surface model for which as described earlier yielding may occur as soon as loading commences in the stress space.

5.3.1 General Plastic Constitutive Relations

As in Dafalias & Herrmann (1980; 1982), the bounding surface, and thus the loading surface, are assumed to be surfaces of revolution about the hydrostatic axis in the principal stress space. In other words, $\bar{F}$ and F are independent of the Lode's angle θ and therefore take the forms of $\bar{F}\left(\bar{\sigma}_{ij}^{'}, e^{p}\right) \equiv \bar{F}(\bar{P}^{'}, \bar{q}, e^{p}) = 0$ and $F\left(\sigma_{ij}^{'}\right) \equiv F(P^{'}, q) = 0$, respectively, as shown in Fig. 5.3. According to Eqs. (5.4)-(5.6), the three components of incremental plastic strain can be expressed as

$$d\varepsilon_r^p = \frac{1}{K}(d\sigma_r^{'} n_r + d\sigma_\theta^{'} n_\theta + d\sigma_z^{'} n_z) n_r = \frac{1}{K}\frac{g_1}{g_2}\left(dP^{'} n_p + dq n_q\right) n_r \tag{5.10a}$$

$$d\varepsilon_\theta^p = \frac{1}{K}(d\sigma_r^{'} n_r + d\sigma_\theta^{'} n_\theta + d\sigma_z^{'} n_z) n_\theta = \frac{1}{K}\frac{g_1}{g_2}\left(dP^{'} n_p + dq n_q\right) n_\theta \tag{5.10b}$$

$$d\varepsilon_z^p = \frac{1}{K}(d\sigma_r^{'} n_r + d\sigma_\theta^{'} n_\theta + d\sigma_z^{'} n_z) n_z = \frac{1}{K}\frac{g_1}{g_2}\left(dP^{'} n_p + dq n_q\right) n_z \tag{5.10c}$$

where

$$n_r = \frac{1}{g_2}\left[\frac{1}{3}\frac{\partial F}{\partial P^{'}} + \frac{3(\sigma_r^{'} - P^{'})}{2q}\frac{\partial F}{\partial q}\right] \tag{5.11a}$$

$$n_\theta = \frac{1}{g_2}\left[\frac{1}{3}\frac{\partial F}{\partial P^{'}} + \frac{3(\sigma_\theta^{'} - P^{'})}{2q}\frac{\partial F}{\partial q}\right] \tag{5.11b}$$

$$n_z = \frac{1}{g_2}\left[\frac{1}{3}\frac{\partial F}{\partial P^{'}} + \frac{3(\sigma_z^{'} - P^{'})}{2q}\frac{\partial F}{\partial q}\right] \tag{5.11c}$$

are the components of the unit normal to the loading surface $F(P^{'}, q) = 0$ or to the bounding surface $\bar{F}(\bar{P}^{'}, \bar{q}, e^{p}) = 0$ in r, θ, and z directions, respectively;

$$n_p = \frac{1}{g_1}\frac{\partial F}{\partial P^{'}} \tag{5.11d}$$

$$n_q = \frac{1}{g_1}\frac{\partial F}{\partial q} \tag{5.11e}$$

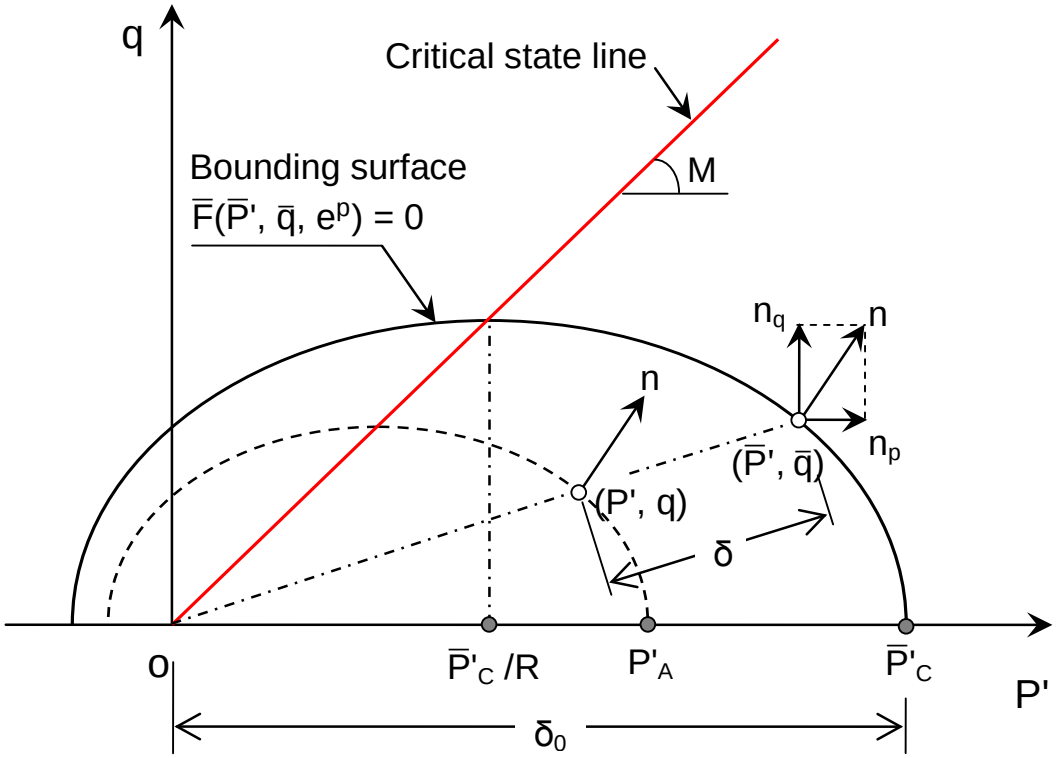

Fig. 5.3. Single ellipse bounding surface model in P'-q stress space

are the components of the unit normal along P' and q axes

$$g_1 = \sqrt{\left(\frac{\partial F}{\partial P'}\right)^2 + \left(\frac{\partial F}{\partial q}\right)^2} \tag{5.11f}$$

$$g_2 = \sqrt{\frac{1}{3}\left(\frac{\partial F}{\partial P'}\right)^2 + \frac{3}{2}\left(\frac{\partial F}{\partial q}\right)^2} \tag{5.11g}$$

and K, according to Eqs. (5.8) and (5.9), is of the form

$$K = K_b + H(\sigma_r', \sigma_\theta', \sigma_z', e^p)\frac{\delta}{\delta_0(\sigma_r', \sigma_\theta', \sigma_z', e^p) - \delta} \tag{5.12}$$

with

$$K_b = \frac{1+e}{\bar{g}_2^2}\frac{\partial \bar{F}}{\partial e^p}\frac{\partial \bar{F}}{\partial \bar{P}'} \tag{5.13}$$

Here, $\bar{g}_2$ is similar to g_2 given by Eq. (5.11g) but evaluated at the image point $(\bar{P}^{'}, \bar{q})$ on the bounding surface, i.e.,

$$\bar{g}_2 = \sqrt{\frac{1}{3}\left(\frac{\partial \bar{F}}{\partial \bar{P}^{'}}\right)^2 + \frac{3}{2}\left(\frac{\partial \bar{F}}{\partial \bar{q}}\right)^2} \tag{5.14}$$

Now introducing the following representations

$$K_b = \frac{g_1^2}{g_2^2}K_b^*, \quad H(\sigma_r^{'}, \sigma_\theta^{'}, \sigma_z^{'}, e^p) = \frac{g_1^2}{g_2^2}H^*(\sigma_r^{'}, \sigma_\theta^{'}, \sigma_z^{'}, e^p), \quad K = \frac{g_1^2}{g_2^2}K^* \tag{5.15}$$

and their substitution into Eqs. (5.10a)-(5.10c) yields

$$d\varepsilon_r^p = \frac{1}{K^*}\left(dP^{'}n_p + dqn_q\right)\frac{\frac{1}{3}\frac{\partial F}{\partial P^{'}} + \frac{3(\sigma_r^{'} - P^{'})}{2q}\frac{\partial F}{\partial q}}{\frac{\partial F}{\partial P^{'}}}n_p \tag{5.16a}$$

$$d\varepsilon_\theta^p = \frac{1}{K^*}\left(dP^{'}n_p + dqn_q\right)\frac{\frac{1}{3}\frac{\partial F}{\partial P^{'}} + \frac{3(\sigma_\theta^{'} - P^{'})}{2q}\frac{\partial F}{\partial q}}{\frac{\partial F}{\partial P^{'}}}n_p \tag{5.16b}$$

$$d\varepsilon_z^p = \frac{1}{K^*}\left(dP^{'}n_p + dqn_q\right)\frac{\frac{1}{3}\frac{\partial F}{\partial P^{'}} + \frac{3(\sigma_z^{'} - P^{'})}{2q}\frac{\partial F}{\partial q}}{\frac{\partial F}{\partial P^{'}}}n_p \tag{5.16c}$$

where

$$K^* = K_b^* + H^*(\sigma_r^{'}, \sigma_\theta^{'}, \sigma_z^{'}, e^p)\frac{\delta}{\delta_0(\sigma_r^{'}, \sigma_\theta^{'}, \sigma_z^{'}, e^p) - \delta} \tag{5.17}$$

and

$$K_b^* = \frac{g_2^2}{g_1^2}K_b = \frac{\bar{g}_2^2}{\bar{g}_1^2}\cdot\frac{1+e}{\bar{g}_2^2}\frac{\partial \bar{F}}{\partial e^p}\frac{\partial \bar{F}}{\partial \bar{P}^{'}} = \frac{1+e}{\bar{g}_1^2}\frac{\partial \bar{F}}{\partial e^p}\frac{\partial \bar{F}}{\partial \bar{P}^{'}} \tag{5.18}$$

In this expression, $\bar{g}_1$ is defined as

$$\bar{g}_1 = \sqrt{\left(\frac{\partial \bar{F}}{\partial \bar{P}^{'}}\right)^2 + \left(\frac{\partial \bar{F}}{\partial \bar{q}}\right)^2} \tag{5.19}$$

and the relation $\frac{g_2^2}{g_1^2} = \frac{\bar{g}_2^2}{\bar{g}_1^2}$ holds due to the geometric similarities between the loading and bounding surfaces, i.e.

$$\frac{\frac{\partial F}{\partial q}}{\frac{\partial F}{\partial P'}} = \frac{\frac{\partial \bar{F}}{\partial \bar{q}}}{\frac{\partial \bar{F}}{\partial \bar{P}'}} = \frac{n_q}{n_p} \tag{5.20}$$

Making further use of the above equation, Eqs. (5.16a)-(5.16c) can be recast in the form

$$d\varepsilon_r^p = \frac{1}{K^*}\left(dP' n_p + dq n_q\right)\left[\frac{1}{3}n_p + \frac{3(\sigma_r' - P')}{2q}n_q\right] \tag{5.21a}$$

$$d\varepsilon_\theta^p = \frac{1}{K^*}\left(dP' n_p + dq n_q\right)\left[\frac{1}{3}n_p + \frac{3(\sigma_\theta' - P')}{2q}n_q\right] \tag{5.21b}$$

$$d\varepsilon_z^p = \frac{1}{K^*}\left(dP' n_p + dq n_q\right)\left[\frac{1}{3}n_p + \frac{3(\sigma_z' - P')}{2q}n_q\right] \tag{5.21c}$$

and therefore the expressions of plastic volumetric and deviatoric strain increments, $d\varepsilon_p^p$ and $d\varepsilon_q^p$ are shown to be

$$d\varepsilon_p^p = d\varepsilon_r^p + d\varepsilon_\theta^p + d\varepsilon_z^p = \frac{1}{K^*}\left(dP' n_p + dq n_q\right)n_p \tag{5.22a}$$

$$d\varepsilon_q^p = \frac{\sqrt{2}}{3}\sqrt{(d\varepsilon_r^p - d\varepsilon_\theta^p)^2 + (d\varepsilon_\theta^p - d\varepsilon_z^p)^2 + (d\varepsilon_r^p - d\varepsilon_z^p)^2}$$

$$= \frac{1}{K^*}\left(dP' n_p + dq n_q\right)n_q \tag{5.22b}$$

which are consistent with the plastic constitutive relations in Dafalias & Herrmann (1980) for the triaxial loading case.

Noting that

$$dP' = \frac{1}{3}(d\sigma_r' + d\sigma_\theta' + d\sigma_z') \tag{5.23a}$$

$$dq = \frac{\partial q}{\partial \sigma_r'}d\sigma_r' + \frac{\partial q}{\partial \sigma_\theta'}d\sigma_\theta' + \frac{\partial q}{\partial \sigma_z'}d\sigma_z' \tag{5.23b}$$

and, once again, introducing the notations

$$a_r = \frac{1}{3}n_p + \frac{3(\sigma_r' - P')}{2q}n_q \tag{5.24a}$$

$$a_\theta = \frac{1}{3}n_p + \frac{3(\sigma_\theta' - P')}{2q}n_q \tag{5.24b}$$

$$a_z = \frac{1}{3} n_p + \frac{3(\sigma_z^{'} - P^{'})}{2q} n_q \tag{5.24c}$$

$$y = \frac{1}{K^*} \tag{5.24d}$$

the plastic stress strain response can be written in a matrix form

$$\begin{Bmatrix} d\varepsilon_r^p \\ d\varepsilon_\theta^p \\ d\varepsilon_z^p \end{Bmatrix} = y \begin{bmatrix} a_r^2 & a_r a_\theta & a_r a_z \\ a_\theta a_r & a_\theta^2 & a_\theta a_z \\ a_z a_r & a_z a_\theta & a_z^2 \end{bmatrix} \cdot \begin{Bmatrix} d\sigma_r^{'} \\ d\sigma_\theta^{'} \\ d\sigma_z^{'} \end{Bmatrix} \tag{5.25}$$

It should be remarked here that, in order to proceed further to solve the wellbore drilling problem, it is important that a_r, a_θ, a_z, and y on the right hand side of Eq. (5.25) all could finally be explicitly expressed as functions of the three stress components $\sigma_r^{'}$, $\sigma_\theta^{'}$, and $\sigma_z^{'}$. This is discussed in the next section specifically for a single elliptical bounding surface.

5.3.2 SINGLE ELLIPTICAL BOUNDING SURFACE

In order to simplify the formulation, here the bounding surface is assumed to consist of a single ellipse (see Fig. 5.3). However, extension of the formulation should be straightforward to the composite form of the bounding surface which may include two ellipses and one hyperbola (Dafalias & Herrmann, 1980; 1982). In terms of the mean effective stress $\bar{P}^{'}$ and deviatoric stress q, the bounding surface can be expressed as (Dafalias & Herrmann, 1980)

$$\bar{F}(\bar{P}^{'}, \bar{q}, e^p) = \left(\frac{\bar{P}^{'}}{\bar{P}_C^{'}}\right)^2 + \frac{(R-1)^2}{M^2}\left(\frac{\bar{q}}{\bar{P}_C^{'}}\right)^2 - \frac{2}{R}\frac{\bar{P}^{'}}{\bar{P}_C^{'}} + \frac{2-R}{R} = 0 \tag{5.26}$$

where M is the slope of critical state line; R is a constant model parameter which completely defines the shape of the bounding surface; $\bar{P}_C^{'}$ represents the intersection of the current bounding surface with the $P^{'}$ axis, which is, in fact, the value of $P^{'}$ for

isotropic consolidation and is connected with the plastic volumetric strain by

$$\frac{d\bar{P}_C^{'}}{\bar{P}_C^{'}} = \frac{(1+e)}{\lambda-\kappa} d\varepsilon_p^p \tag{5.27}$$

where λ and κ are the slopes of normal compression and swelling lines in $v - \ln P^{'}$ plane (Wood 1990).

For undrained condition, $d\varepsilon_v = d\varepsilon_p^e + d\varepsilon_p^p = 0$ where $d\varepsilon_p^e$ denotes the elastic volumetric strain increment, hence

$$\frac{d\bar{P}_C^{'}}{\bar{P}_C^{'}} = -\frac{(1+e)}{\lambda-\kappa} d\varepsilon_p^e = -\frac{(1+e)}{\lambda-\kappa} \frac{dP^{'}}{\frac{(1+e)P^{'}}{\kappa}} = -\frac{\kappa}{\lambda-\kappa} \frac{dP^{'}}{P^{'}} \tag{5.28}$$

which, after integration, yields

$$\bar{P}_C^{'} = \bar{P}_{C,0}^{'} \left(\frac{P^{'}}{P_0^{'}}\right)^{-\frac{\kappa}{\lambda-\kappa}} \tag{5.29}$$

Here $P_0^{'}$ corresponds to the in situ mean effective stress and $\bar{P}_{C,0}^{'}$ is the initial value of $\bar{P}_C^{'}$ before the drilling of wellbore.

Note further that in Fig. 5.3, $P_A^{'}$ is determined as the intersection between an ellipse passing through the current stress point $(P^{'}, q)$ and the P' axis. Its initial value of $P_{A,0}^{'}$ relevant to the in situ stress state $(P_0^{'}, q_0)$, together with $\bar{P}_{C,0}^{'}$, thus define the useful concept of overconsolidation ratio for the shale formations

$$OCR = \frac{\bar{P}_{C,0}^{'}}{P_{A,0}^{'}} \tag{5.30}$$

For the bounding surface of elliptic form, namely Eq. (5.26), the components of the unit vector turn out to be (Dafalias & Herrmann, 1980)

$$n_p = \frac{1}{g_1}\frac{\partial F}{\partial P^{'}} = \frac{1}{\bar{g}_1}\frac{\partial \bar{F}}{\partial \bar{P}^{'}} = \frac{1}{g}\left[f(\eta) - \frac{1}{R}\right] \tag{5.31a}$$

$$n_q = \frac{1}{g_1}\frac{\partial F}{\partial q} = \frac{1}{\bar{g}_1}\frac{\partial \bar{F}}{\partial q} = \frac{1}{g}\eta f(\eta)\left(\frac{R-1}{M}\right)^2 \tag{5.31b}$$

where $\eta = \frac{q}{P'}$; $x = \frac{\eta}{M}$; and

$$f(\eta) = \frac{1+(R-1)\sqrt{1+R(R-2)x^2}}{R[1+x^2+R(R-2)x^2]} \tag{5.32}$$

$$g = \frac{\bar{P}_C'}{2}\bar{g}_1 = \sqrt{\left[f(\eta) - \frac{1}{R}\right]^2 + \eta^2 f^2(\eta)\left(\frac{R-1}{M}\right)^4} \tag{5.33}$$

On the other hand, the bounding surface plastic modulus K_b^* is derived from Eqs. (5.18) and (5.27) as follows

$$K_b^* = \frac{1+e}{\lambda-\kappa}\frac{\bar{P}_C'}{R}\frac{1}{g^2}[R + f(\eta) - 2]\left[f(\eta) - \frac{1}{R}\right] \tag{5.34}$$

where $\bar{P}_C'$ has been related to the current mean effective stress through Eq. (5.29).

Finally, as with Dafalias & Herrmann (1982), the following form of $H^*(\sigma_r', \sigma_\theta', \sigma_z', e^p)$ is proposed for the hardening function

$$H^*(\sigma_r', \sigma_\theta', \sigma_z', e^p) = \frac{1+e}{\lambda-\kappa} h p_a \left(1 + \left|\frac{M}{\eta}\right|^m\right) \tag{4.35}$$

where h and m are dimensionless material constants; p_a represents the atmospheric pressure with the proper stress unit. The desired plastic modulus K^* according to Eq. (5.17) now becomes

$$K^* = K_b^* + \frac{1+e}{\lambda-\kappa} h p_a \left(1 + \left|\frac{M}{\eta}\right|^m\right)\frac{\delta}{\delta_0 - \delta} \tag{5.36}$$

where δ_0 is defined as the maximum isotropic stress, i.e., $\delta_0 = \bar{P}_C'$; and δ can be calculated as

$$\delta = \sqrt{1+\eta^2}[f(\eta)\bar{P}_C' - P'] \tag{5.37}$$

5.3.3 ELASTOPLASTIC WELLBORE DRILLING ANALYSIS

First, the elastic stress strain relationship can be written in incremental form as

$$\begin{Bmatrix} d\varepsilon_r^e \\ d\varepsilon_\theta^e \\ d\varepsilon_z^e \end{Bmatrix} = \frac{1}{E}\begin{bmatrix} 1 & -\nu & -\nu \\ -\nu & 1 & -\nu \\ -\nu & -\nu & 1 \end{bmatrix} \cdot \begin{Bmatrix} d\sigma_r^{'} \\ d\sigma_\theta^{'} \\ d\sigma_z^{'} \end{Bmatrix} \tag{5.38}$$

where $d\varepsilon_r^e$, $d\varepsilon_\theta^e$, and $d\varepsilon_z^e$ are the elastic strain increments in r, θ, and z directions, respectively; ν is the Poisson's ratio; and the Young's modulus E [or shear modulus $G = \frac{E}{2(1+\nu)}$], as in the case of modified Cam Clay model, is a function of the mean stress $P^{'}$ and specific volume v:

$$E = \frac{3(1-2\nu)vP^{'}}{\kappa} \tag{5.39}$$

Now combining Eqs. (5.25) and (5.38), and by inverting, one has

$$\begin{Bmatrix} d\sigma_r^{'} \\ d\sigma_\theta^{'} \\ d\sigma_z^{'} \end{Bmatrix} = \frac{1}{\Delta}\begin{bmatrix} b_{11} & b_{12} & b_{13} \\ b_{21} & b_{22} & b_{23} \\ b_{31} & b_{32} & b_{33} \end{bmatrix} \cdot \begin{Bmatrix} d\varepsilon_r \\ d\varepsilon_\theta \\ d\varepsilon_z \end{Bmatrix} \tag{5.40}$$

where b_{11} and Δ assume the same forms as those defined in Eqs. (2.29a)-(2.29j). Moreover, the three first order governing differential equations (2.33a)-(2.33c), rearranged basically from the elastoplastic constitutive relations, can be directly used without any modification, i.e.,

$$\frac{D\sigma_r^{'}}{Dr} - \frac{b_{11}-b_{12}}{\Delta r} = 0 \tag{5.41a}$$

$$\frac{D\sigma_\theta^{'}}{Dr} - \frac{b_{21}-b_{22}}{\Delta r} = 0 \tag{5.41b}$$

$$\frac{D\sigma_z^{'}}{Dr} - \frac{b_{31}-b_{32}}{\Delta r} = 0 \tag{5.41c}$$

The final point that needs to be addressed now is the specification of suitable initial conditions for the above differential equations. Recall that, for the bounding surface model, there is no purely elastic deformation zone existing around the wellbore. Therefore, Eqs. (5.41a)-(5.41c) are in principle valid for any material point with current

position r_x, whose original position, r_{x0}, can be identified from the kinematic constraint of undrained deformation as

$$\frac{r_{x0}}{a} = \sqrt{\left(\frac{r_x}{a}\right)^2 + \left(\frac{a_0}{a}\right)^2 - 1} \tag{5.42}$$

and the corresponding initial stress conditions are simply given by

$$\sigma_r^{'}(r_{x0}) = \sigma_{r0}^{'}, \quad \sigma_\theta^{'}(r_{x0}) = \sigma_{\theta 0}^{'}, \quad \sigma_z^{'}(r_{x0}) = \sigma_{z0}^{'} \tag{5.43}$$

where $\sigma_{r0}^{'}$, $\sigma_{\theta 0}^{'}$, and $\sigma_{z0}^{'}$ are the in situ effective stresses.

Once the effective stresses are solved from Eqs. (5.41a)-(5.41c), subject to the initial condition (5.43), the distribution of pore pressure $p(r_x)$ can be easily calculated from the equilibrium equation

$$\frac{\partial \sigma_r^{'}}{\partial r} + \frac{\partial p}{\partial r} + \frac{\sigma_r^{'} - \sigma_\theta^{'}}{r} = 0 \tag{5.44}$$

and the excess pore pressure then determined from

$$\Delta p(r_x) = p(r_x) - p_0 \tag{5.45}$$

5.4 Drained Solution

For the drained situation, one can still obtain a formally identical equation for the plastic stress strain response, i.e., Eq. (5.25). However, it should be kept in mind that in this case the void ratio e (or specific volume v), is no longer a constant but instead changes with the deformation so itself needs to be determined during the wellbore drilling. The influences of varying e (or v) are well reflected in Eqs. (5.34) and (5.36) for the plastic moduli K_b^* and K^*. Additionally, it will indirectly affect the hardening parameter $\bar{P}_C^{'}$ which essentially controls the size of the current bounding surface. As a matter of fact, Eq. (5.29) for the determination of $\bar{P}_C^{'}$ is no more applicable for the drained

case since this equation is derived based on the constant specific volume condition, $d\varepsilon_v = 0$.

Consider now the expression of $\bar{P}_C^{'}$ for the drained condition. Substituting Eq. (5.2) into (5.27), and integrating, gives

$$\ln \frac{\bar{P}_C^{'}}{\bar{P}_{C,0}^{'}} = -\frac{1}{\lambda-\kappa} e^p \tag{5.46}$$

Using Eq. (5.3), thus,

$$\ln \frac{\bar{P}_C^{'}}{\bar{P}_{C,0}^{'}} = -\frac{1}{\lambda-\kappa} (v - v_0 - \int_0^{e^e} de^e) \tag{5.47}$$

Here

$$\int_0^{e^e} de^e = \int_0^{e^e} -(1+e) d\varepsilon_p^e = \int_0^{e^e} -(1+e) \frac{dP^{'} \cdot \kappa}{(1+e)P^{'}} = -\kappa \ln \frac{P^{'}}{P_0^{'}} \tag{5.48}$$

so that

$$\frac{\bar{P}_C^{'}}{\bar{P}_{C,0}^{'}} = e^{-\frac{v-v_0}{\lambda-\kappa}} \left(\frac{P^{'}}{P_0^{'}}\right)^{-\frac{\kappa}{\lambda-\kappa}} \tag{5.49}$$

which expresses $\bar{P}_C^{'}$ as a function of the current stress state as well as the specific volume v. Note that when $v = v_0$, the above equation correctly reduces to Eq. (5.29) for the undrained case.

Let us now move on to the formulation of the governing differential equations for the drained condition. Given the elastoplastic incremental constitutive relation, Eq. (5.40), and noting that $d\varepsilon_v = -\frac{dv}{v}$ and $d\varepsilon_\theta = -\frac{dr}{r}$, it follows that

$$d\sigma_r^{'} = \frac{1}{\Delta}[b_{11} d\varepsilon_v + (b_{12} - b_{11}) d\varepsilon_\theta] = \frac{1}{\Delta}[b_{11}(-\frac{dv}{v}) + (b_{12} - b_{11})(-\frac{dr}{r})] \tag{5.50a}$$

$$d\sigma_\theta^{'} = \frac{1}{\Delta}[b_{21} d\varepsilon_v + (b_{22} - b_{21}) d\varepsilon_\theta] = \frac{1}{\Delta}[b_{21}(-\frac{dv}{v}) + (b_{22} - b_{21})(-\frac{dr}{r})] \tag{5.50b}$$

$$d\sigma_z^{'} = \frac{1}{\Delta}[b_{31} d\varepsilon_v + (b_{32} - b_{31}) d\varepsilon_\theta] = \frac{1}{\Delta}[b_{31}(-\frac{dv}{v}) + (b_{32} - b_{31})(-\frac{dr}{r})] \tag{5.50c}$$

Introduce again the auxiliary independent variable

$$\xi = \frac{u_r}{r} = \frac{r - r_0}{r} \tag{5.51}$$

with u_r known as the radial displacement and r_0 the original position of the particle, and then following exactly the same procedure as outlined in the previous chapter and adopting the logarithmic strain components, one can finally derive the desirable four governing differential equations

$$\frac{D\sigma_r^{'}}{D\xi} = -\frac{\sigma_r^{'} - \sigma_\theta^{'}}{1 - \xi - \frac{v_0}{v(1-\xi)}} \tag{5.52a}$$

$$\frac{D\sigma_\theta^{'}}{D\xi} = -\frac{b_{21}}{b_{11}}\left[\frac{\sigma_r^{'} - \sigma_\theta^{'}}{1 - \xi - \frac{v_0}{v(1-\xi)}} + \frac{b_{11} - b_{12}}{\Delta(1-\xi)}\right] - \frac{b_{22} - b_{21}}{\Delta(1-\xi)} \tag{5.52b}$$

$$\frac{D\sigma_z^{'}}{D\xi} = -\frac{b_{31}}{b_{11}}\left[\frac{\sigma_r^{'} - \sigma_\theta^{'}}{1 - \xi - \frac{v_0}{v(1-\xi)}} + \frac{b_{11} - b_{12}}{\Delta(1-\xi)}\right] - \frac{b_{32} - b_{31}}{\Delta(1-\xi)} \tag{5.52c}$$

$$\frac{Dv}{D\xi} = \frac{v\Delta}{b_{11}}\left[\frac{\sigma_r^{'} - \sigma_\theta^{'}}{1 - \xi - \frac{v_0}{v(1-\xi)}} + \frac{b_{11} - b_{12}}{\Delta(1-\xi)}\right] \tag{5.52d}$$

which can be solved for any material particle r_x as an initial value problem with the independent variable starting at $\xi = \xi_0 = 0$. As in the undrained case, the initial conditions for stresses and specific volume are simply as follows

$$\sigma_r^{'}(0) = \sigma_{r0}^{'}, \quad \sigma_\theta^{'}(0) = \sigma_{\theta 0}^{'}, \quad \sigma_z^{'}(0) = \sigma_{z0}^{'}, \quad v(0) = v_0 \tag{5.53}$$

Finally, as in Chapter 4, the conversion between the auxiliary variable ξ and the radial coordinate r can be expressed as

$$\frac{r}{a} = e^{\int_{\xi(a)}^{\xi} \frac{d\xi}{1 - \frac{v_0}{v(\xi)(1-\xi)} - \xi}} \tag{5.54}$$

5.5 Results and Discussions

The parameters of the bounding surface model used for both undrained and drained wellbore analyses are $R = 2.72$, $M = 1.05$, $\lambda = 0.14$, $\kappa = 0.05$, $\nu = 0.15$, $e_0 =$

0.95 ($v_0 = 1.95$), $m = 0.2$, and $h = 30$, as listed in Table 5.1. Four different values of $OCR = 1, 1.2, 2,$ and 5 are considered to investigate the impact of overconsolidation ratio on the stress and pore pressure distributions around the wellbore. The in situ effective stresses and pore pressure, as well as the relevant values of $\bar{P}'_{C,0}$ are also summarized in Table 5.1.

Table 5.1. Parameters used in example analyses with bounding surface model

$R = 2.72, M = 1.05, \lambda = 0.14, \kappa = 0.05, \nu = 0.15, e_0 = 0.95, m = 0.2, h = 30$									
σ'_{r0} (MPa)	$\sigma'_{\theta 0}$ (MPa)	σ'_{z0} (MPa)	p_0 (MPa)	P'_0 (MPa)	q_0 (MPa)	$\bar{P}'_{C,0}$ (MPa)			
						$OCR = 1$	1.2	2	5
11.25	11.25	15	10	12.5	3.75	14.80	17.76	29.60	74.00

Fig. 5.4 shows the variations of the wellbore pressure p_w and excess pore pressure $\Delta p(a)$ at wellbore surface $r = a$ with the normalized wellbore radius $\frac{a_0}{a}$ for the cases of $R = 1, 1.2, 2,$ and 5. As similar with the modified Cam Clay model, the wellbore pressure decreases very rapidly with the wellbore radius if $\frac{a_0}{a}$ is less than 1.5 but more slowly beyond this value. Both the wellbore pressure and the excess pore pressure build-up are found to decrease significantly as OCR increases from 1 (normally consolidated formation) to 5 (heavily overconsolidated formation).

Figs. 5.5-5.8 show the distributions of σ'_r, σ'_θ, and σ'_z and also of P', q, and Δp along the radial distance corresponding to a reduced wellbore pressure of $p_w = 0$ for all the overconsolidation ratios in the range from 1 to 5, where the radial axis has been

normalized with respect to the current contracted radius a. It can be clearly observed that for the case of $OCR = 1$ (Fig. 5.5), all the radial, tangential, and vertical stresses as well as the mean effective stress and deviatoric stress remain unchanged in the vicinity of the borehole $\frac{r}{a} < 1.3$, indicating the occurrence of critical state failure for the rock of this range. However, for larger values of $OCR = 1.2$, 2, and 5, such an internal critical state zone vanishes and only the plastic zone may be expected outside the wellbore. In fact, for given in situ stresses ($\sigma_{r0}^{'} = \sigma_{\theta 0}^{'} = 11.25$ MPa, $\sigma_{z0}^{'} = 15$ MPa, and $p_0 = 10$ MPa), the lower the value of OCR, the closer the stress state at the wellbore surface will approach the critical state. Figs. 5.5-5.8 also clearly show that the negative excess pore pressure increase rapidly near the wellbore and becomes virtually equal to zero at the far field. Especially, for normally consolidated formation with $OCR = 1$, Δp varies linearly with the logarithm of $\frac{r}{a}$ in the critical state failure zone, which is again consistent with the finite element results for cavity expansion problem reported by Randolph et al. (1979).

Figs. 5.9-5.12 present the effective stress path (ESP) followed in the $P^{'} - q$ plane invariably for a material particle at the wellbore surface. For $OCR = 1$, recalling Eq. (5.30), the initial bounding surface must pass through the in situ stress point (Fig. 5.9). In this case the stress path will start from $P_0^{'} = 12.5$ MPa and $q_0 = 3.75$ MPa, continue to move upper-left and finally stop at point F on the critical state line, which also lies on the failure bounding surface with $\bar{P}_C^{'} = 19.92$MPa (see Fig. 5.9). Since at point F, $\eta = M$ and $\delta = 0$ so $K^* = K_b^*$ while the latter is equal to zero following Eq. (5.34) [$f(M) = \frac{1}{R}$], the actual plastic modulus K^* must also vanish. This explains why the stress path terminates on the critical state line and remains stationary there. For OCR greater than 1, the in situ stress point is always located within the initial bounding surface, as shown in

Figs. 5.10-5.12. Note that in the overconsolidation cases ($OCR > 1$), the stress paths all initially cross the critical state line parallel to the q axis. As noted in Dafalias & Herrmann (1980), this is a property for any shape of bounding surface which has $n_p = 0$ at $\eta = M$. In fact, at these cross points, $\delta > 0$ and $K^* > K_b^* = 0$, so the material at this moment has not reached the failure state and therefore the stress paths may bend over and continue to move towards the critical state line. To see this point more clearly, in Fig. 5.12 for the case of $OCR = 5$, the stress path is extended from point B ($p_w = 0$) to F which corresponds to a sufficiently contracted wellbore radius of $\frac{a}{a_0} = 5$. Also included in this figure is the trajectory of the image stress ($\bar{P}^{'}, \bar{q}$) on the expanding/contracting bounding surface, represented by the curve $A'B'F'$. As expected, the two points F and F' coincide and both lie on the critical state line again. This implies that the material has truly reached the failure state and that failure can occur only if the loading surface is consistent with the bounding surface.

Figs. 5.13-5.20 show the calculation results for the drained condition, again corresponding to an effective wellbore pressure $p_w^{'} = 0$. Throughout the range of OCR from 1 to 5, it is observed that (Fig. 5.13-5.16) the rock undergoes dilation during the drilling process and the change in the specific volume decreases with increasing OCR. As regarding the $P^{'} - q$ stress paths for different values of OCR, Figs. 5.17-5.20 illustrates that the rock particles all first harden plastically from the wet side of the critical state line ($\eta < M$), the bounding surface expanding simultaneously to accommodate the new stress state. After hitting the critical state line, the rocks start to soften plastically in the dry side ($\eta > M$) and the bounding surface must decrease in size. One may expect that for sufficiently small value of the wellbore pressure, the stress path will be brought to the

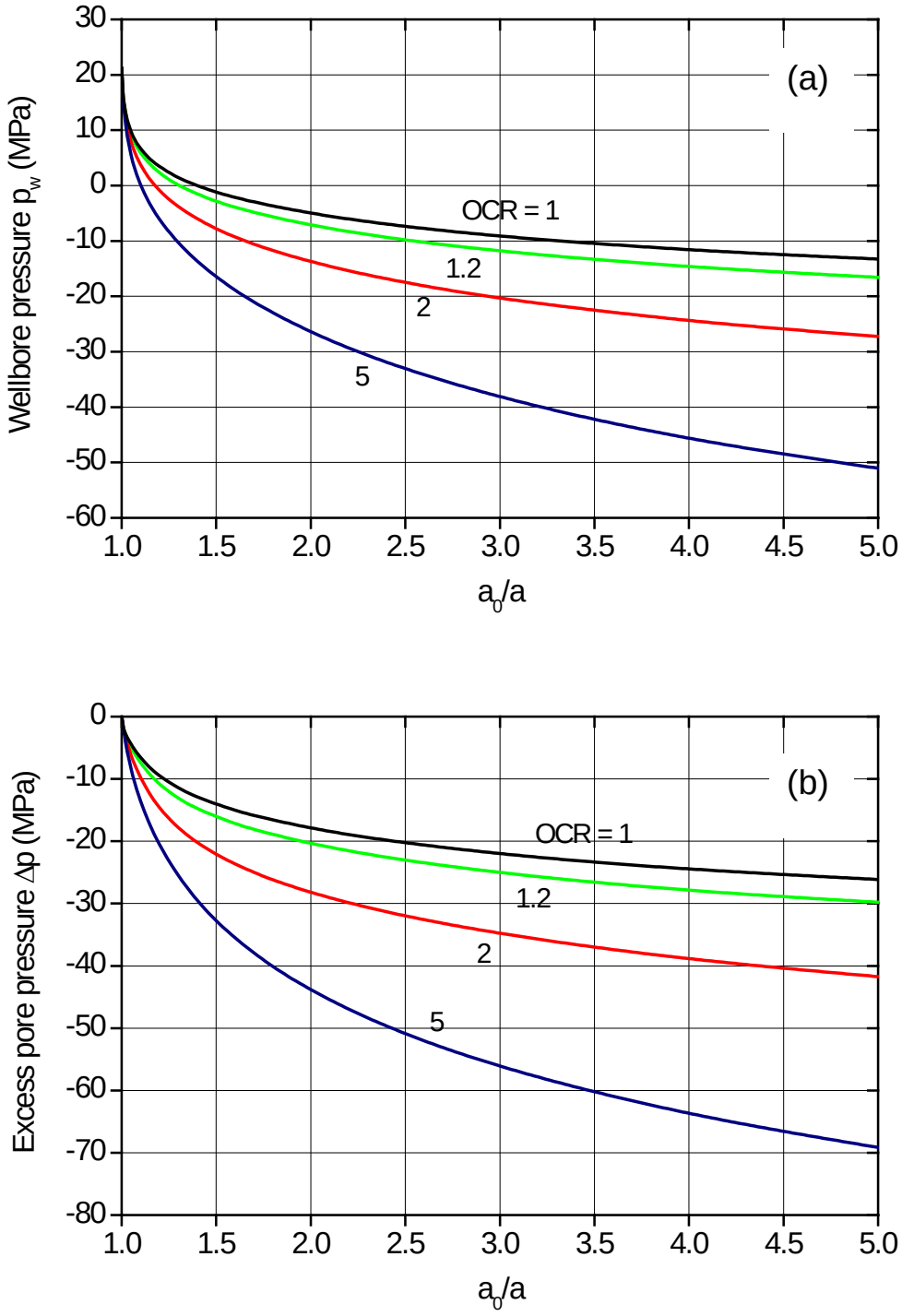

Fig. 5.4. Variations of (a) wellbore pressure; (b) pore pressure with normalized wellbore radius for undrained case

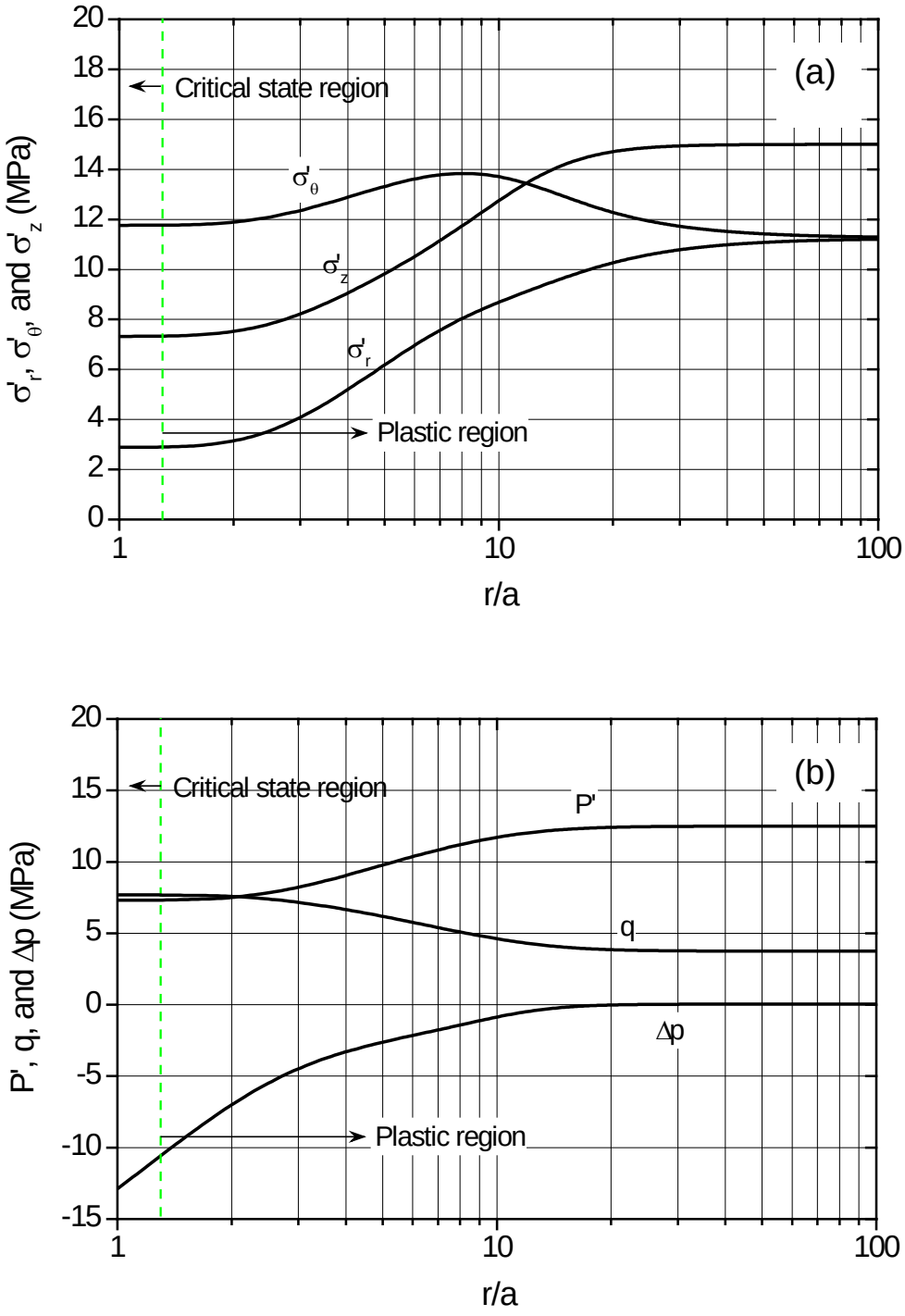

Fig. 5.5. Distributions of (a) effective radial, tangential, and vertical stresses; (b) effective mean, deviatoric stresses and excess pore pressure around the wellbore for OCR = 1, undrained case

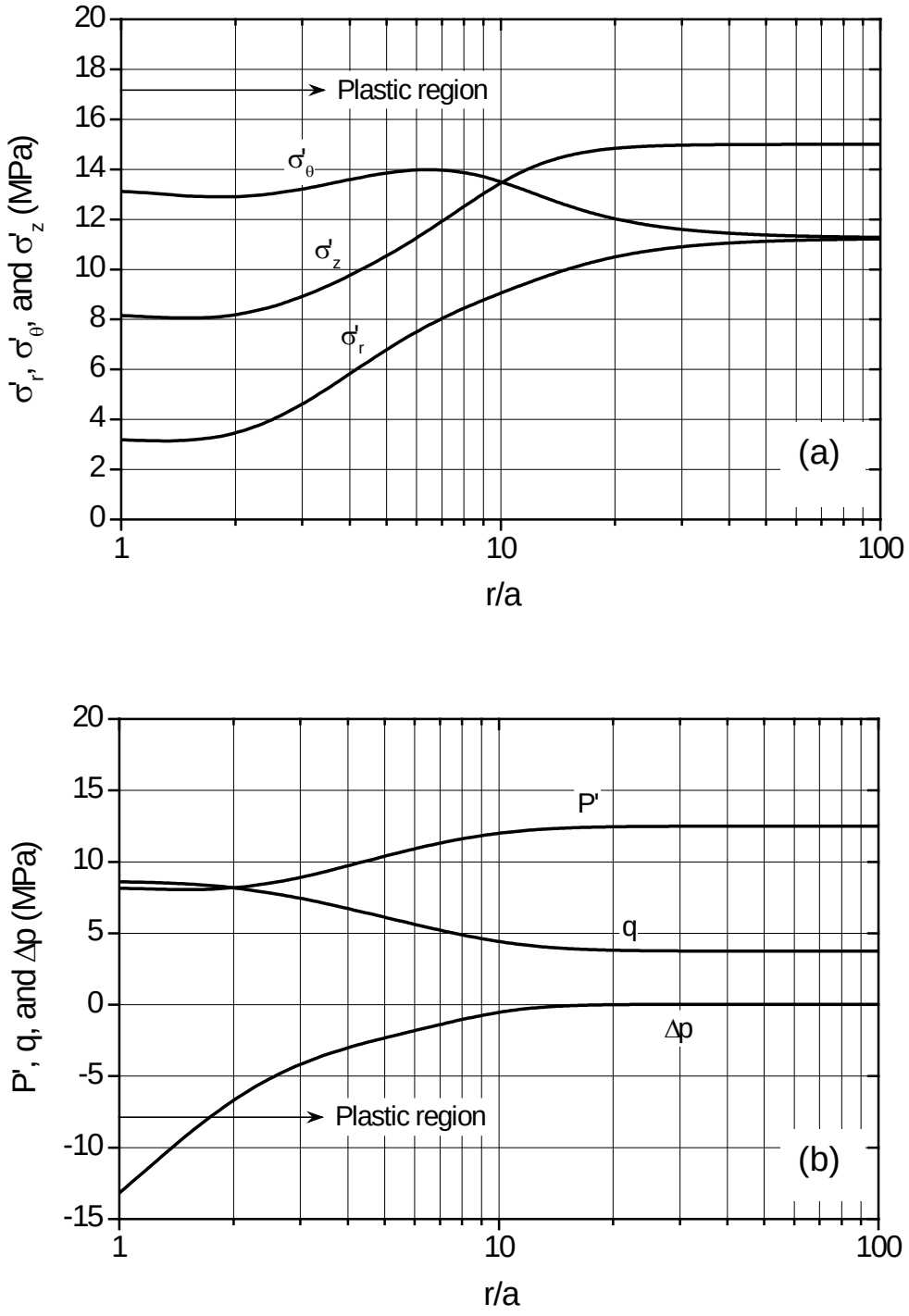

Fig. 5.6. Distributions of (a) effective radial, tangential, and vertical stresses; (b) effective mean, deviatoric stresses and excess pore pressure around the wellbore for OCR = 1.2, undrained case

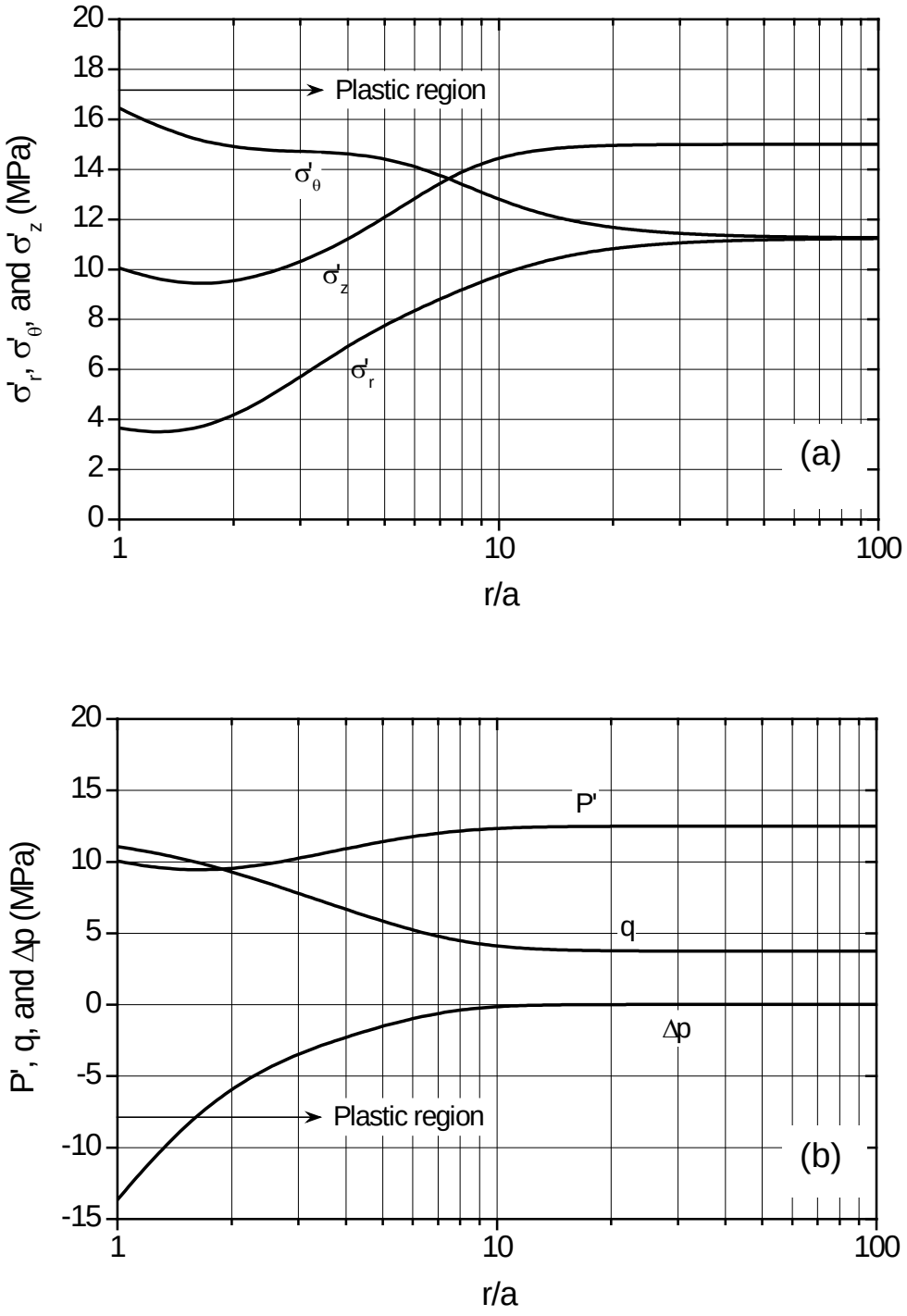

Fig. 5.7. Distributions of (a) effective radial, tangential, and vertical stresses; (b) effective mean, deviatoric stresses and excess pore pressure around the wellbore for OCR = 2, undrained case

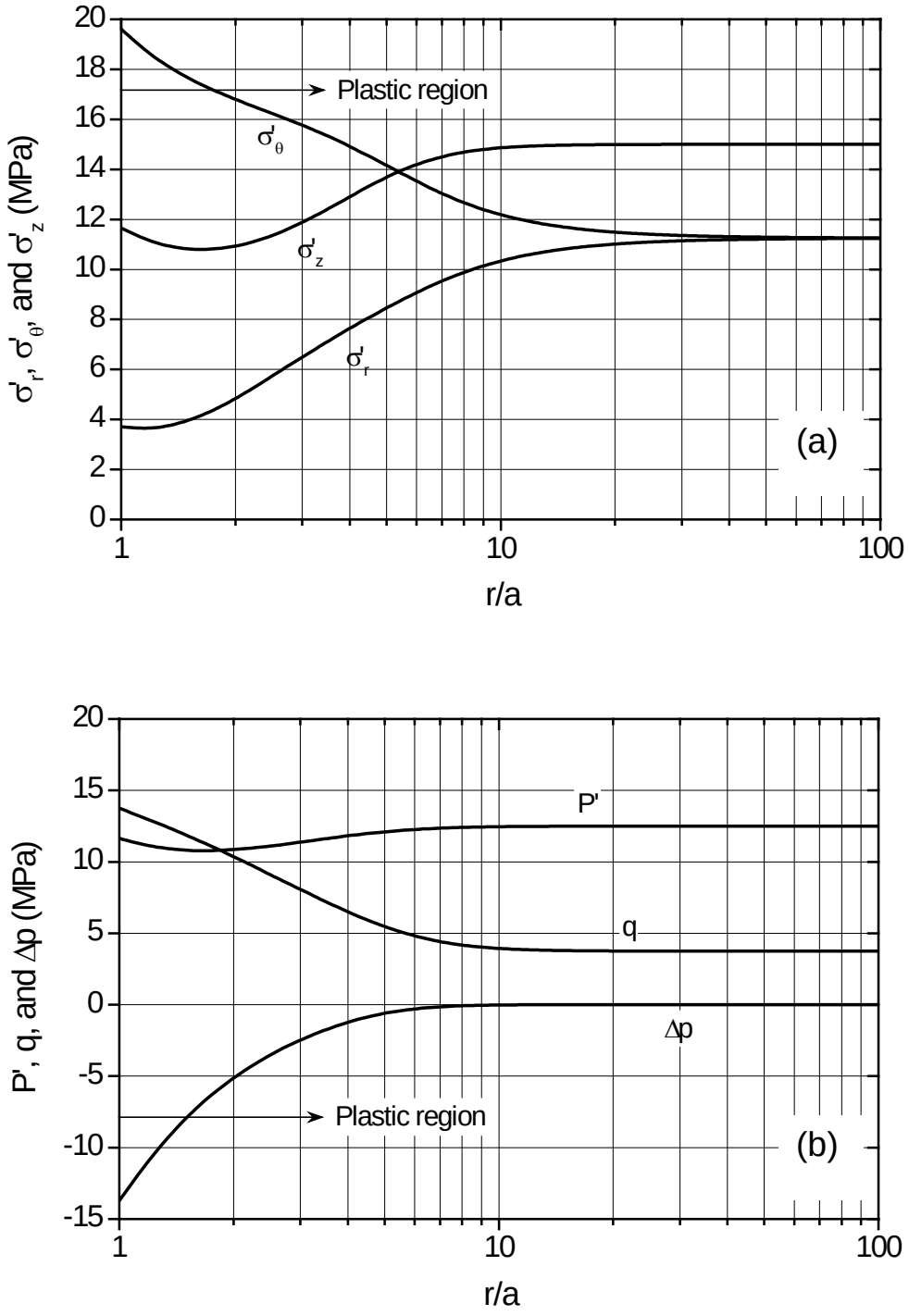

Fig. 5.8. Distributions of (a) effective radial, tangential, and vertical stresses; (b) effective mean, deviatoric stresses and excess pore pressure around the wellbore for OCR = 5, undrained case

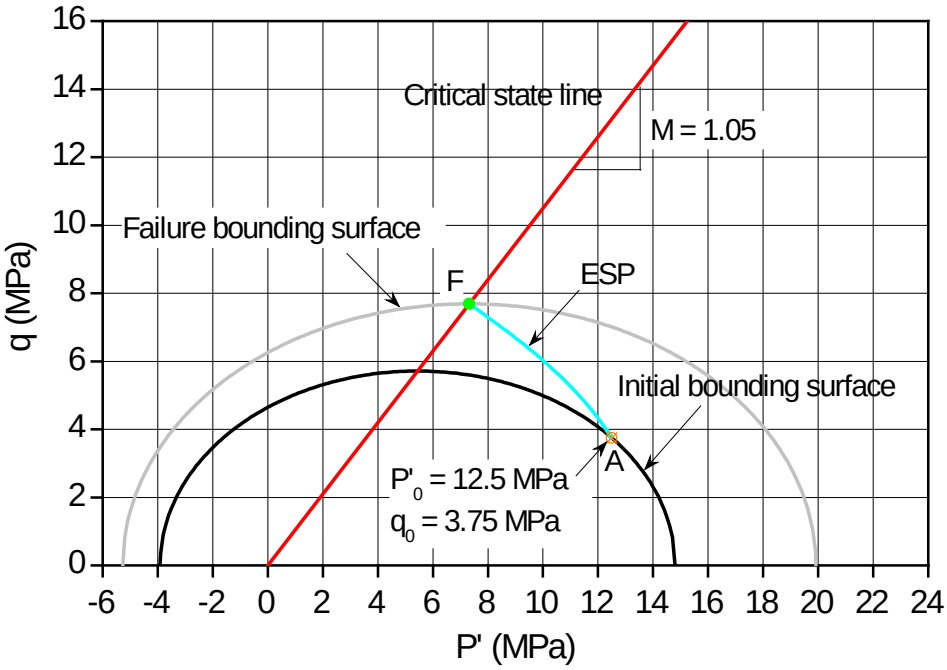

Fig. 5.9. P'-q stress path at wellbore surface for OCR = 1, undrained case

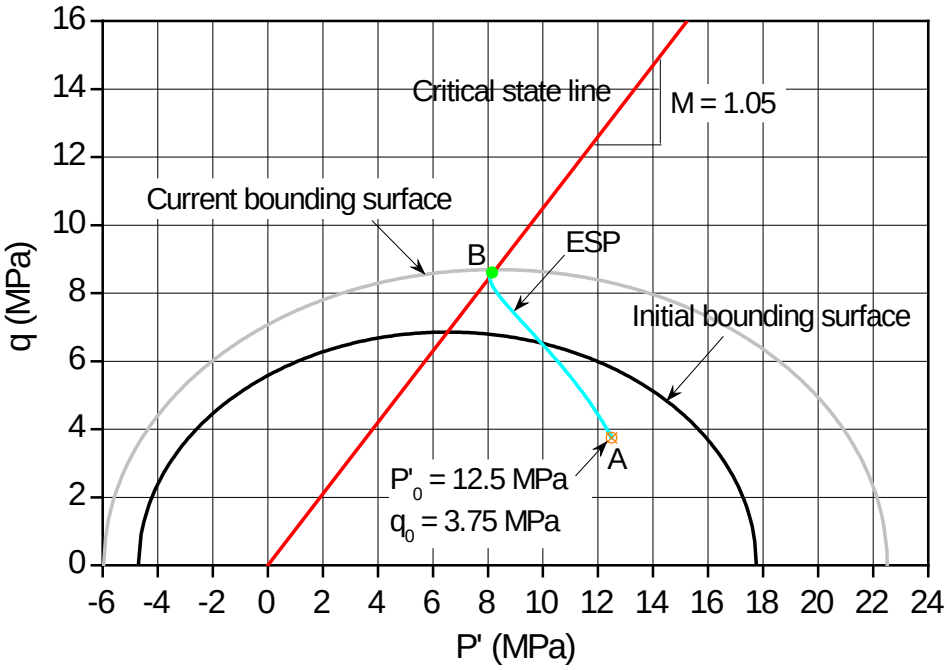

Fig. 5.10. P'-q stress path at wellbore surface for OCR = 1.2, undrained case

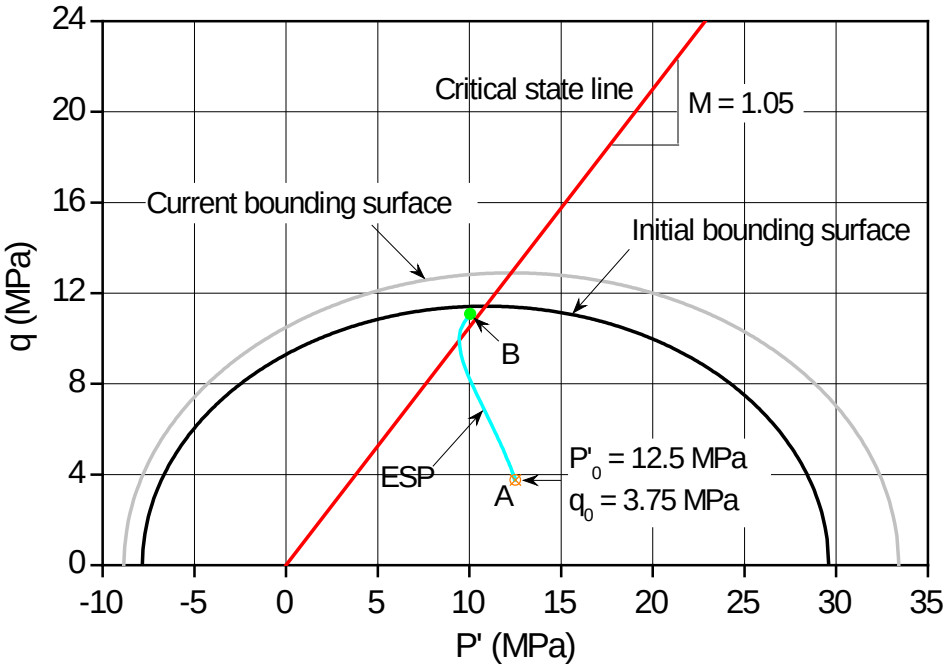

Fig. 5.11. P'-q stress path at wellbore surface for OCR = 2, undrained case

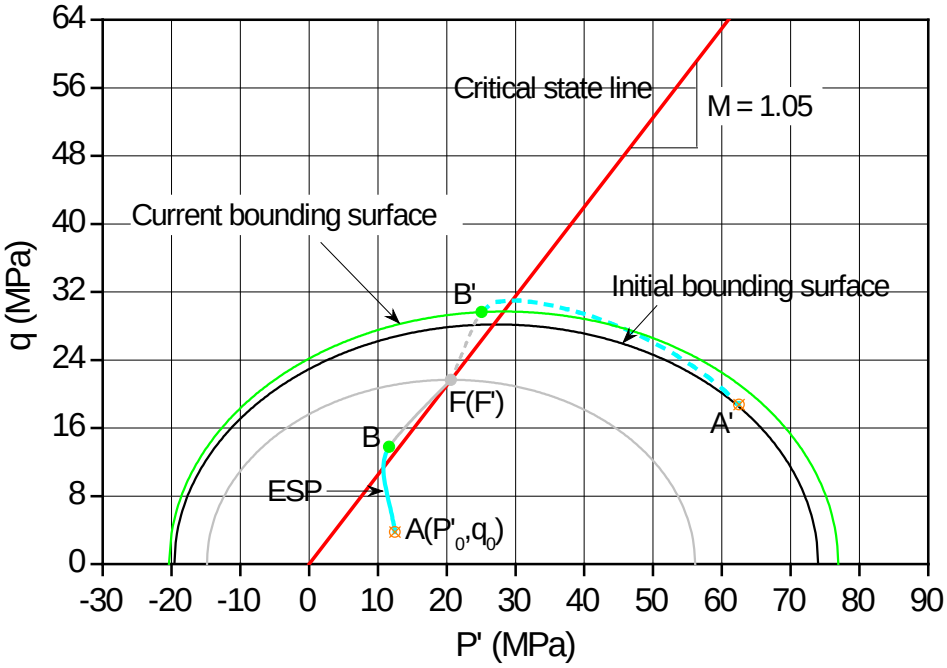

Fig. 5.12. P'-q stress path at wellbore surface for OCR = 5, undrained case

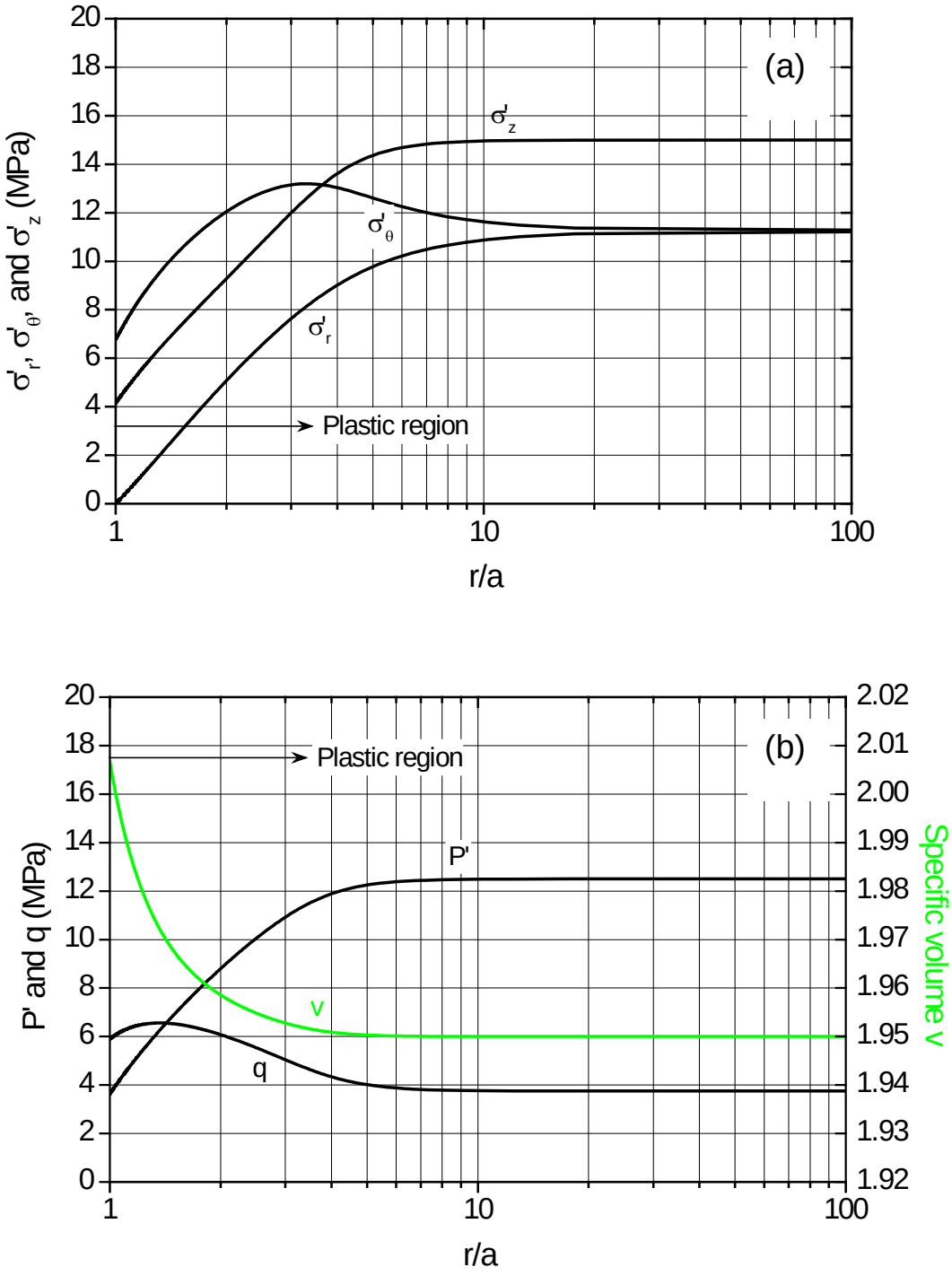

Fig. 5.13. Distributions of (a) effective radial, tangential, and vertical stresses; (b) effective mean, deviatoric stresses and specific volume around the wellbore for OCR = 1, drained case

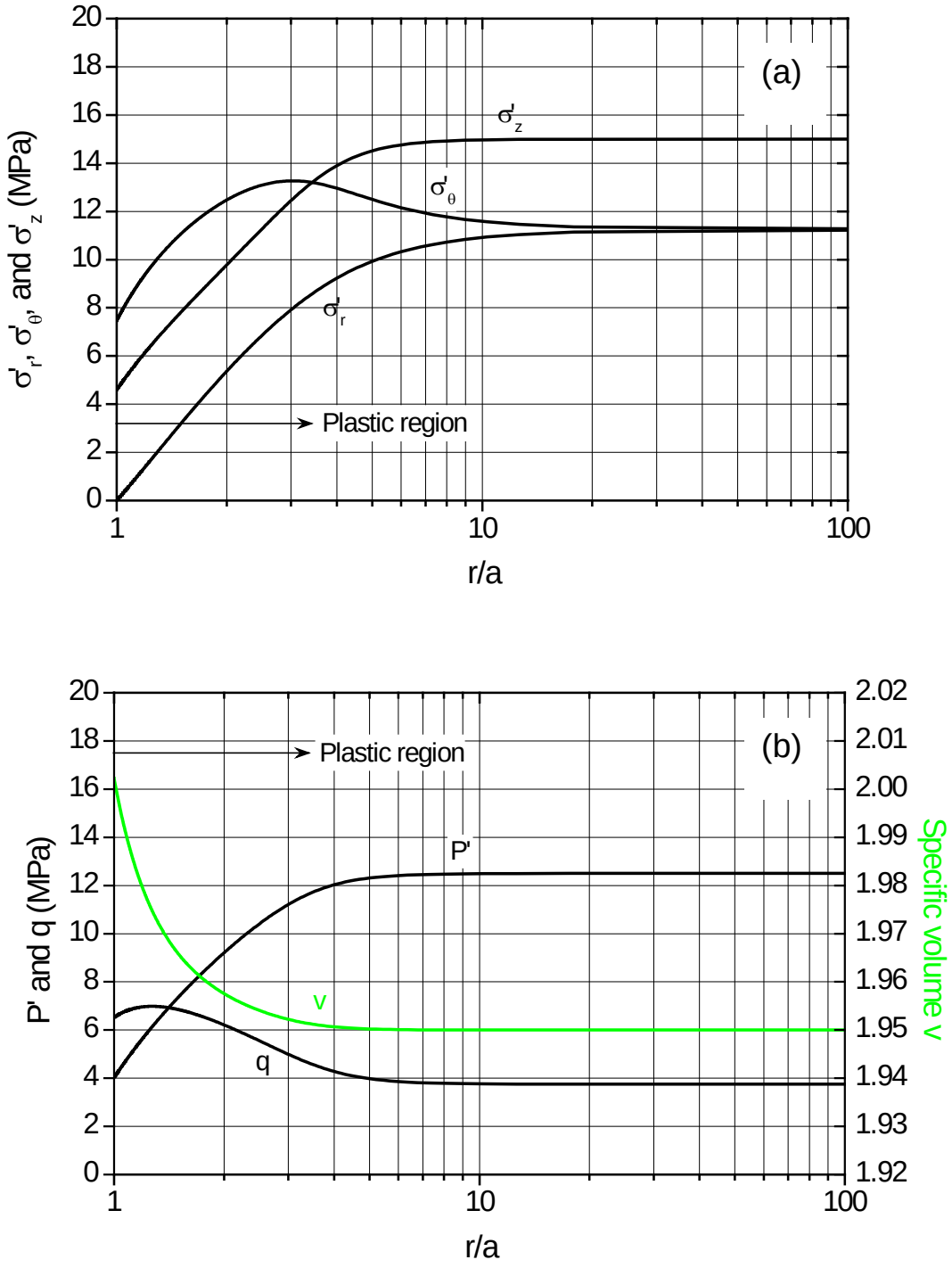

Fig. 5.14. Distributions of (a) effective radial, tangential, and vertical stresses; (b) effective mean, deviatoric stresses and specific volume around the wellbore for OCR = 1.2, drained case

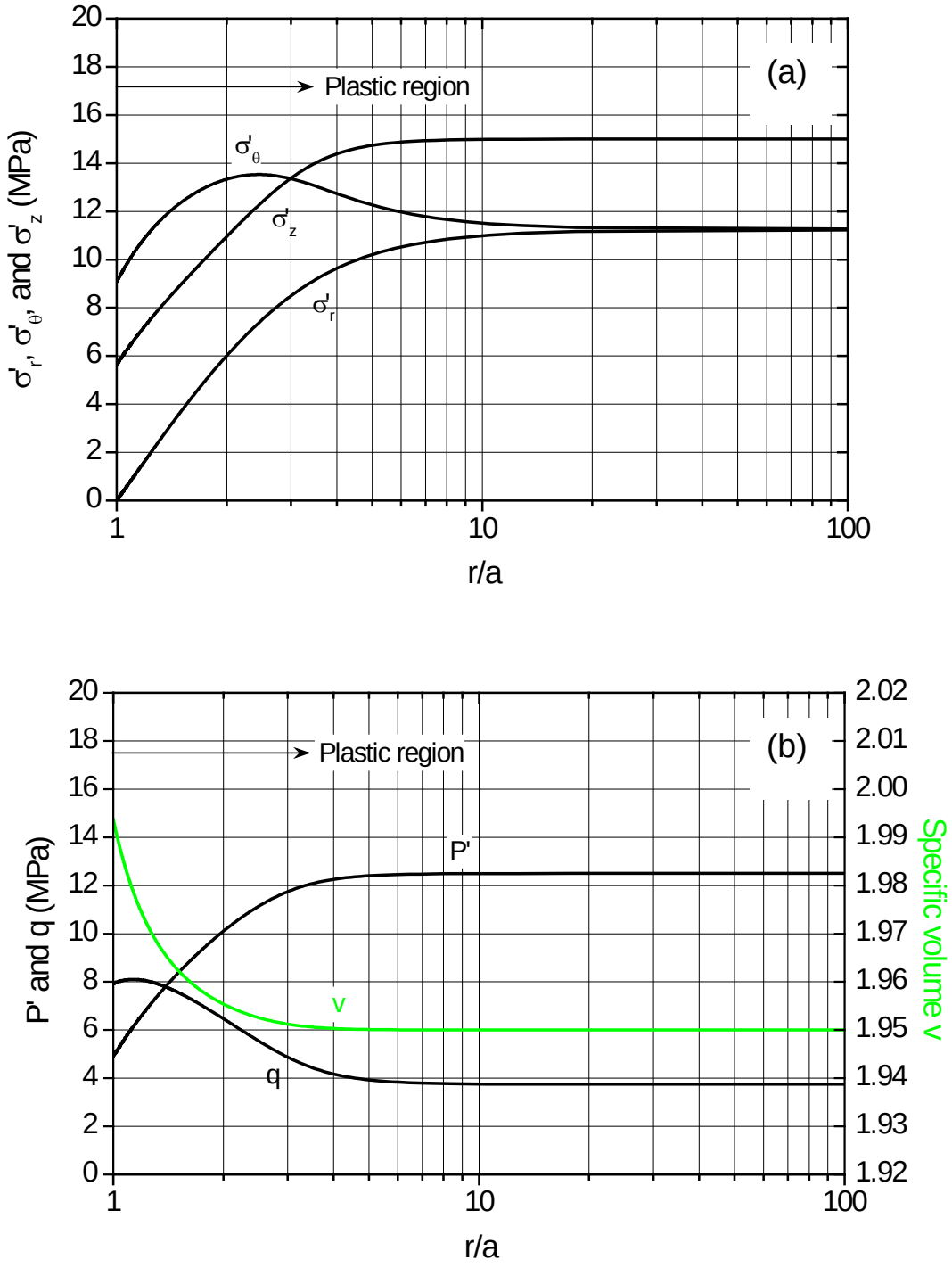

Fig. 5.15. Distributions of (a) effective radial, tangential, and vertical stresses; (b) effective mean, deviatoric stresses and specific volume around the wellbore for OCR = 2, drained case

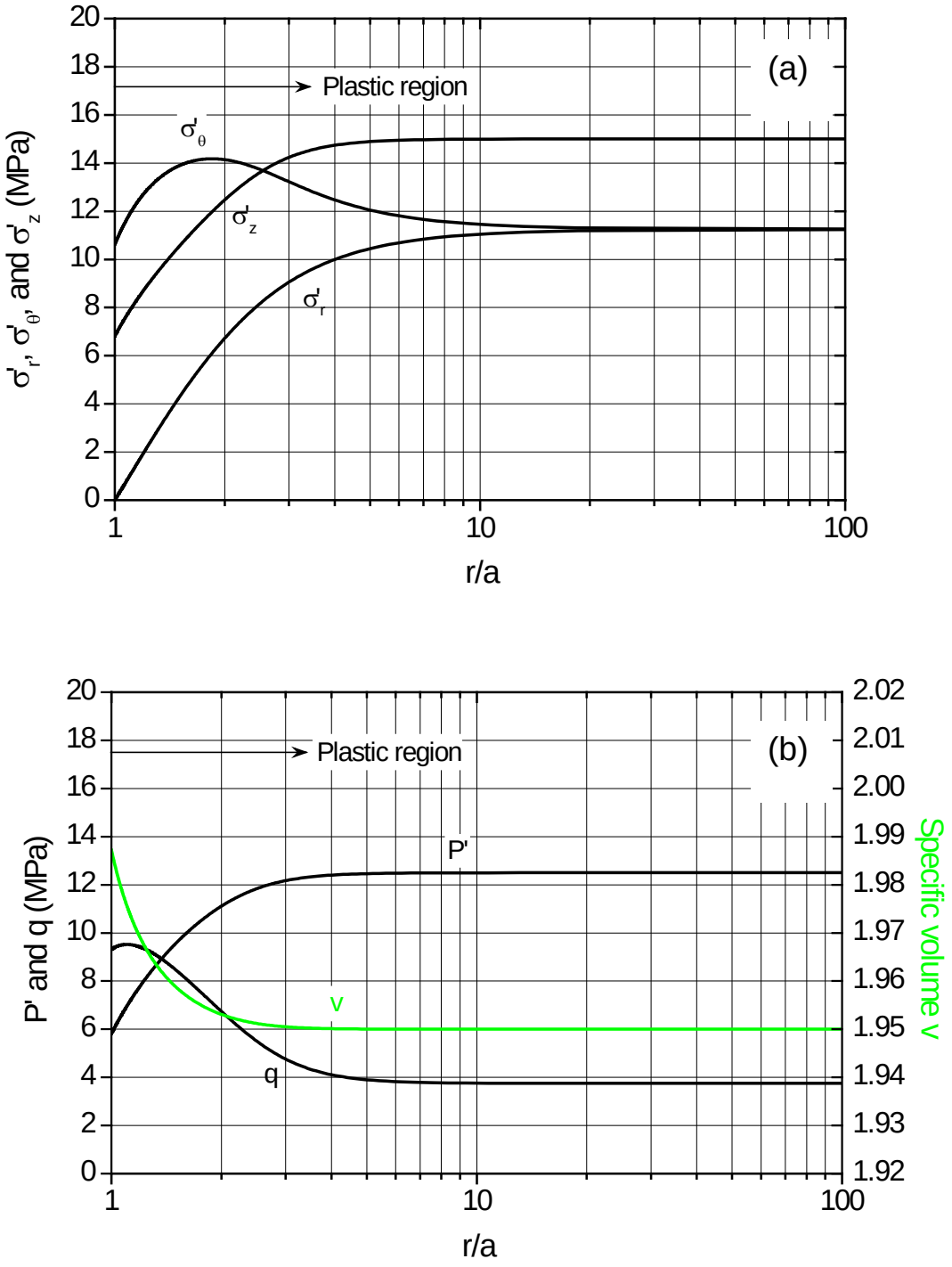

Fig. 5.16. Distributions of (a) effective radial, tangential, and vertical stresses; (b) effective mean, deviatoric stresses and specific volume around the wellbore for OCR = 5, drained case

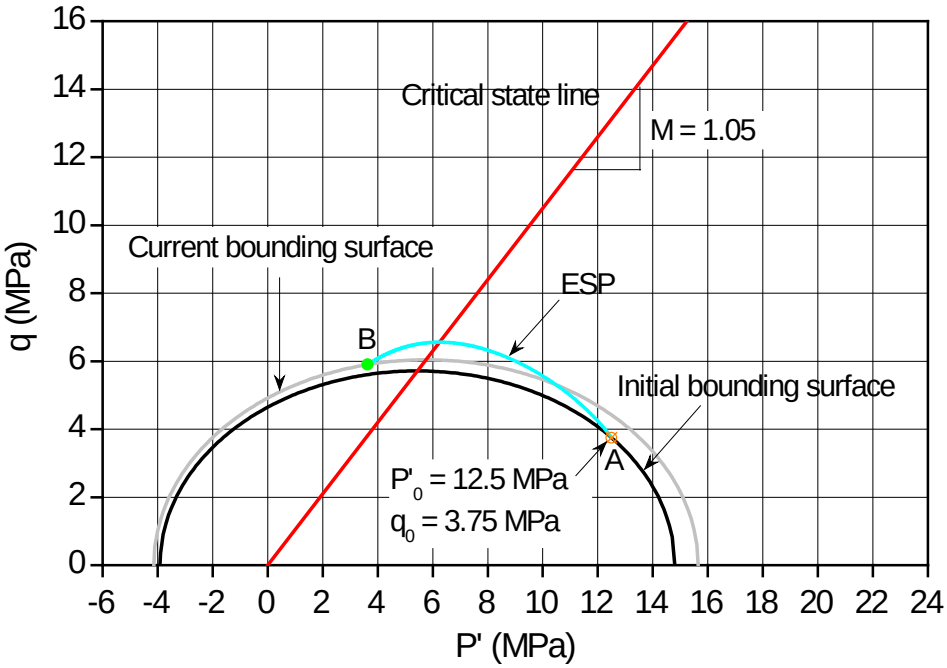

Fig. 5.17. P'-q stress path at wellbore surface for OCR = 1, drained case

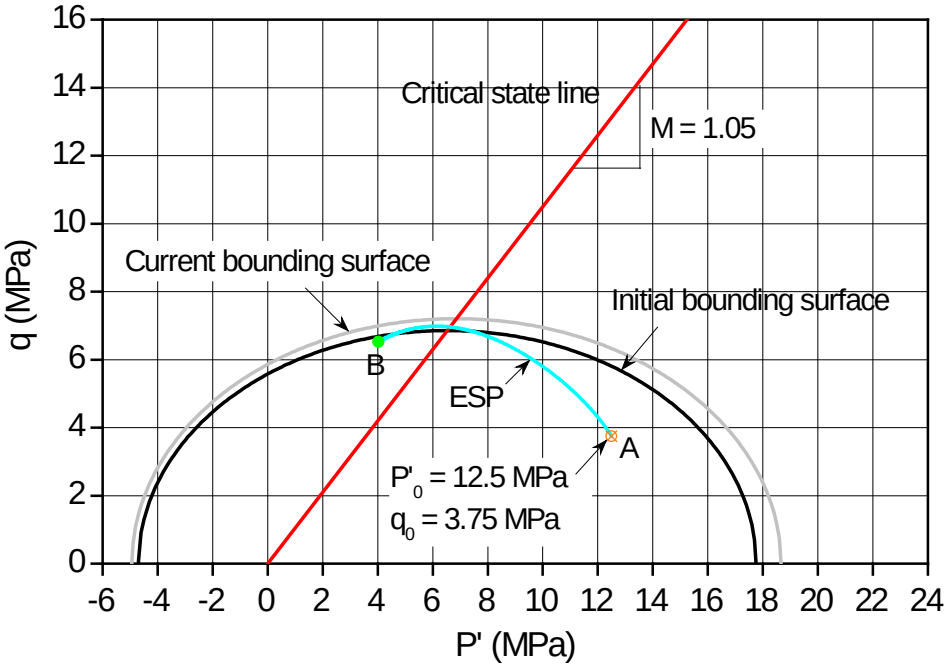

Fig. 5.18. P'-q stress path at wellbore surface for OCR = 1.2, drained case

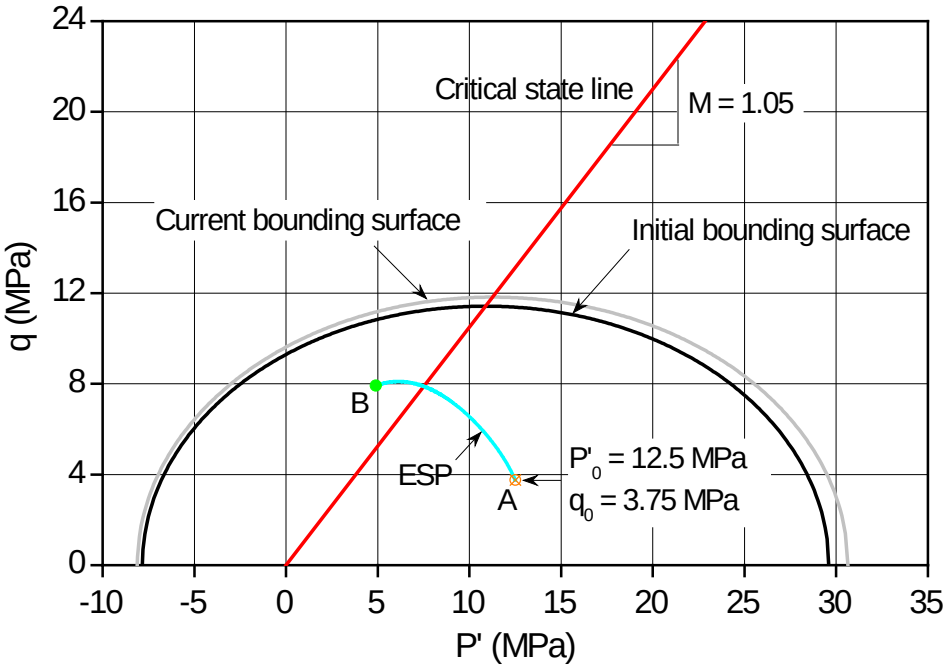

Fig. 5.19. P'-q stress path at wellbore surface for OCR = 2, drained case

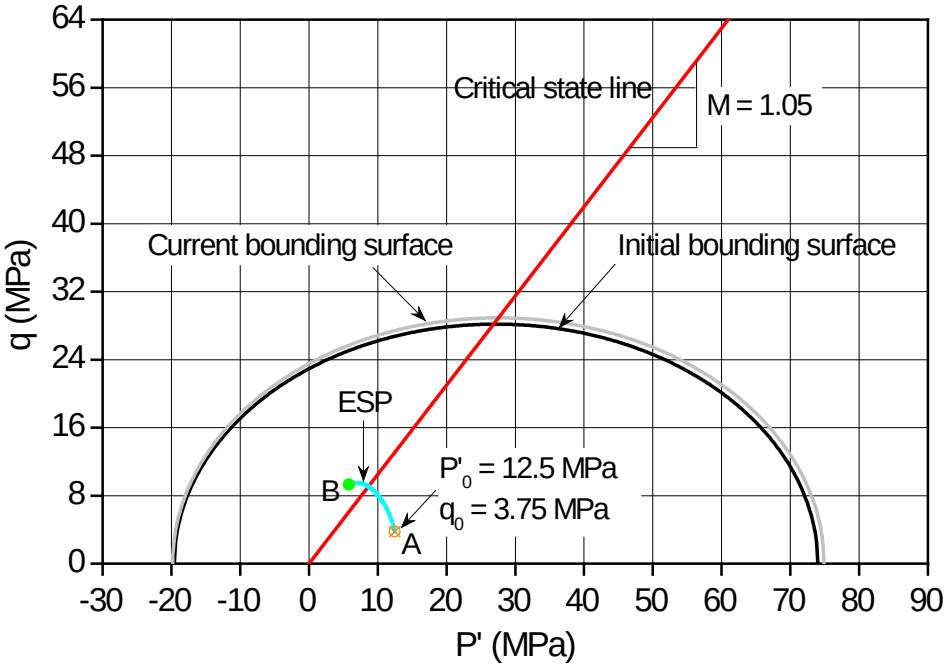

Fig. 5.20. P'-q stress path at wellbore surface for OCR = 5, drained case

critical failure state again at lower values of P' and q.

5.6 Summary

This chapter is devoted to extending the analytical solution procedure to the wellbore drilling in the bounding surface rock formation. One of the important features of the bounding surface model is that yielding could occur as soon as loading commences in the stress space. Therefore, there is no purely elastic zone existing outside the wellbore during the drilling process. Extensive parametric studies show that, for undrained problem, both the wellbore pressure and the induced excess pore pressure decrease significantly as the overconsolidation ratio increases. The lower the value of OCR, the closer the stress state at the wellbore surface will approach the critical state. In the overconsolidation cases, it is found that the undrained stress paths all initially cross the critical state line parallel to the q axis, then bend over and continue to move towards the critical state line until they truly reach the failure state. For the drained case, the rock generally undergoes dilation during the wellbore drilling and the change in the specific volume decreases with increasing OCR. The stress paths first head towards the critical state line from the wet side, so the rock harden plastically accompanied by progressive expansion of the bounding surface. After passing through the critical state line, the rock however tends to soften in the dry side and the bounding surface gradually decreases in size.

CHAPTER 6
FINITE ELEMENT ANALYSES FOR WELLBORE STABILITY PROBLEMS

6.1 Introduction

In Chapters 2-5, a generic class of analytical solutions were derived for a wellbore drilled in elastoplastic rock formations, with both drained and undrained conditions and various types of plasticity models (ranging from the strain hardening Drucker-Prager and Mohr-Coulomb models to critical state based Cam Clay and bounding surface models) taken into account. These solutions are rigorous and provide an envelope for the elastoplastic analysis of the wellbore stability problem. As a matter of fact, the developed analytical approach is theoretically applicable to all the elastoplastic models provided that the yield surface and plastic potential surface considered are sufficiently smooth and differentiable. The main limitation of the analytical solutions, however, is that it requires an equal horizontal in situ stress to make full use of the geometric symmetry of the boundary value problem. For the general case of a fully anisotropic in situ stress state which is commonly encountered in practice, it is inevitable that numerical methods must be used and this is particularly true when an inclined wellbore is drilled.

This chapter recalculates the same wellbore drilling problems using ABAQUS, the finite element analysis commercial program. For demonstration, only the drained case

and the two critical state based elastoplastic models, i.e., modified Cam Clay and bounding surface models, are considered in the numerical analysis. Since the bounding surface model is not directly available in the ABAQUS commercial software, a user defined material subroutine (UMAT) will need to be developed for this constitutive model and implemented into the ABAQUS finite element models. The finite element analysis results are compared with the previously derived analytical solutions, to test the capability of ABAQUS in handling the wellbore drilling problem involving the critical state plasticity models as well as the validity of the UMAT code written for the boundary surface model, and in turn to justify the accuracy of the proposed analytical method. The numerical simulations are clearly possible to be extended to deal with the more realistic situations including the impacts of wellbore inclination and the in situ stress anisotropy.

6.2 The Finite Element Program ABAQUS/Standard

ABAQUS/Standard is a general-purpose analysis product that can solve a wide range of linear and nonlinear problems involving the static, dynamic, thermal, and electrical response of components. It is particularly powerful for nonlinear simulations of geotechnical and petroleum geomechanical problems as it can take into consideration the large deformation and coupled behaviour of porous soils and rocks, and contains extensive lists of material models and interface elements that can simulate the behaviour of most typical geomaterials. The reader may refer to the ABAQUS manuals (ABAQUS, 2011) for further details. Here only a brief introduction is given to the solution strategy used by ABAQUS/Standard for the nonlinear finite element formulations and to the material models available in ABAQUS particularly for elastoplastic soils and rocks.

6.2.1 NONLINEAR FINITE ELEMENT ANALYSIS

In a nonlinear analysis (material and/or geometric nonlinearity) the solution cannot be calculated by solving a single system of linear equations. Instead, it is found by specifying the loading as a function of time and incrementing time to obtain the nonlinear response. Therefore, ABAQUS/Standard breaks the simulation into a number of time increments and finds the approximate equilibrium configuration at the end of each time increment. Using the Newton-Raphson method, it often takes Abaqus/Standard several iterations to determine an acceptable solution to each time increment.

To illustrate the Newton-Raphson algorithm, a simple nonlinear response of a structure to a small load increment, ΔP, is considered, as shown in Fig. 6.1a (ABAQUS, 2011). ABAQUS/Standard uses the structure's tangent stiffness, K_0, which is based on its configuration at u_0, and ΔP to make a first estimate of the displacement correction, c_a. The structure's configuration is then updated to $u_a = u_0 + c_a$, see Fig. 6.1a.

However, ABAQUS/Standard recognizes that the solution is likely to be in error due to the nonlinear nature of the structure stiffness. It therefore calculates the structure's internal forces, I_a, in this updated configuration and further the residual force $R_a = P - I_a$, the latter of which is a measure of the error in the linearized analysis. Note that in a nonlinear problem R_a will never be exactly zero, so ABAQUS/Standard compares it to a (default) tolerance value. If R_a is less than this residual force tolerance at all nodes, ABAQUS/Standard accepts the solution as being in equilibrium. Otherwise, ABAQUS/Standard uses this residual R_a, together with the new stiffness K_a based on the updated configuration u_a, to perform the iteration and determine another displacement correction, c_b (see Fig. 6.1b). This process brings the system closer to equilibrium (point b in Fig.

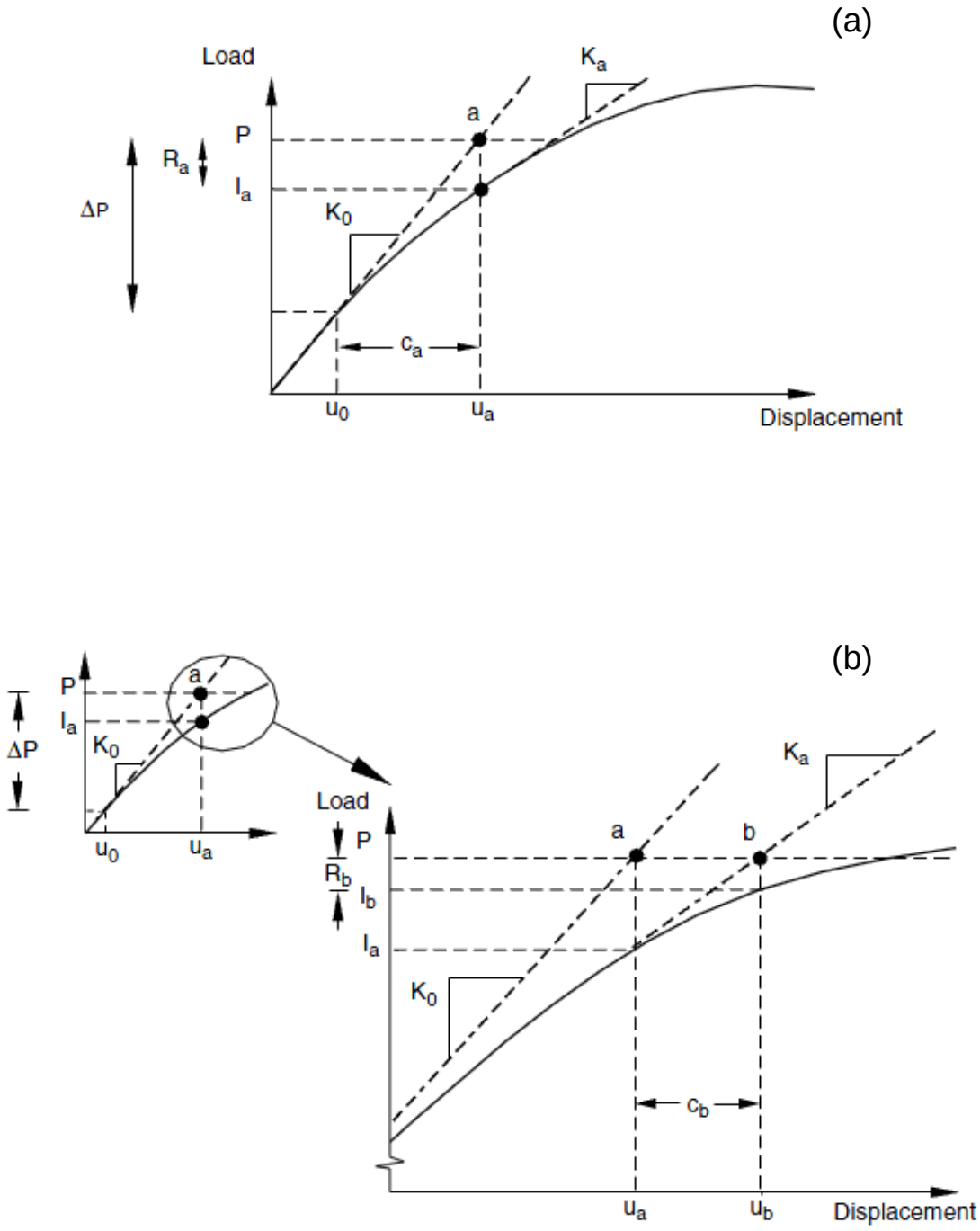

Figure 7.1.1–4 Second iteration.

Fig. 6.1. Nonlinear response of structure to small load increment: (a) first iteration in an increment; (b) second increment (after ABAQUS, 2011)

6.1b).

ABAQUS/Standard now proceeds to calculate a new force residual, R_b, using the internal forces from the structure's new configuration, u_b. Again, the updated residual force, R_b, should be compared against the force residual tolerance. If necessary, ABAQUS/Standard performs further iterations until the residual force is sufficiently small and the solution is then said to have converged for that time increment.

6.2.2 MATERIAL MODELS

One of the most important characteristics of the real soil and rocks are their elastoplastic mechanical behaviour. The material library in ABAQUS offers four commonly used plasticity models for geomaterials, i.e., extended Drucker-Prager models, modified Drucker-Prager/Cap model, Mohr-Coulomb plasticity model, and clay plasticity model (ABAQUS, 2011).

The extended Drucker-Prager models are useful for representing the yielding and frictional behaviour of pressure sensitive materials such as granular soils and rocks. This class of models generally allow for volume change with plastic behaviour and can include the creep effect in ABAQUS/Standard if the material exhibits long-term inelastic deformations. In ABAQUS/Standard the yield surface of the extended Drucker-Prager models can have a linear form, a hyperbolic form, or a general exponent form depending on the shape of the yield surface in the meridional plane (ABAQUS, 2011). The models allow a material to harden/soften isotropically with the yield surface evolving with the material cohesion through the equivalent plastic strain.

The modified Drucker-Prager/Cap model is based on the addition of a cap yield surface to the Drucker-Prager plasticity model, which provides an inelastic hardening

mechanism to account for plastic compaction and helps to control volume dilatancy when the material yields in shear (ABAQUS, 2011). The yield surface is composed of two principal segments: a pressure-dependent Drucker-Prager shear failure segment and a compression cap segment. The former segment is a perfectly plastic yield surface (no hardening). Plastic flow on this segment produces inelastic volume increase (dilation) that causes the cap to soften. On the latter cap surface plastic flow causes the material to compact. In ABAQUS/Standard inelastic time-dependent (creep) behaviour coupled with the plastic behaviour is also available for this model.

The Mohr-Coulomb plasticity model provided in ABAQUS/Standard can be employed for design applications in the geotechnical and petroleum engineering areas. The model uses the classical Mohr-Coloumb yield criterion, i.e., a straight line in the meridional plane and an irregular hexagonal section in the deviatoric plane. However, the ABAQUS/Standard Mohr-Coulomb model has a completely smooth flow potential instead of the classical hexagonal pyramid, the plastic flow in the deviatoric stress plane therefore is always nonassociated. The flow potential is chosen as a hyperbolic function in the meridional plane and the smooth elliptic function proposed by Menetrey & Willam (1995) in the deviatoric stress plane (ABAQUS, 2011). As with the extended Drucker-Prager model, this model assumes an isotropic cohesion hardening and/or softening behaviour of the material.

The clay plasticity model in ABAQUS/Standard is essentially an extension of the Cam Clay critical state models originally developed by Roscoe and his collaborators at the University of Cambridge. The model is based on a yield surface which depends on the three stress invariants and can be expressed as (Helwany, 2007; ABAQUS, 2011)

$$f(P^{'},q,\theta)=\frac{1}{\beta}\left(\frac{P^{'}}{b}-1\right)^{2}+\left(\frac{t}{Mb}\right)^{2}-1=0 \tag{6.1}$$

where $P^{'}$, q, and θ are the mean effective stress, deviatoric stress, and Lode's angle, respectively; $t=\frac{1}{2}q\left[1+\frac{1}{K}-\left(1-\frac{1}{K}\right)\cos(3\theta)\right]$ is a measure of shear stress where K is the ratio of the flow stress in triaxial tension to the flow stress in triaxial compression and determines the shape of the yield surface in the plane of principal deviatoric stresses (ABAQUS/Standard requires a range of $0.778\leq K\leq 1$ to ensure convexity of the yield surface); M is the slope of the critical state line; b is a parameter that defines the size of the yield surface; β is a constant that is equal to 1.0 on the "dry" side of the critical state line but may be less than 1.0 on the "wet" side ($\beta<1.0$ introduces a different elliptic arc on the wet side). Fig. 6.2 shows the projections of the general yield surface on the $P^{'}-t$ plane and the deviatoric plane with different parameters involved for illustration. Note that by setting $K=\beta=1$, Eq. (6.1) will become independent of the third stress invariant and reduce to the yield surface for the classical modified Cam Clay model (Wood, 1990).

It should be pointed out that, in addition to the above built-in plasticity models for typical geomaterials, ABAQUS/Standard also provides a very powerful and flexible user subroutine, UMAT, which allows users to create and implement new material constitutive model into the software. The main function of the UMAT is to integrate the constitutive models along the incremental strain path to obtain an estimate of the stress change (R_a and R_b in Fig. 6.1), and to update the stresses and solution-dependent state variables at the end of the increment. Also, it must provide the material Jacobian or tangential stiffness matrix for the mechanical constitutive model. As a demonstration, the integration algorithm for the bounding surface model and its implementation into the ABAQUS will be elaborated later in this chapter within the context of wellbore drilling

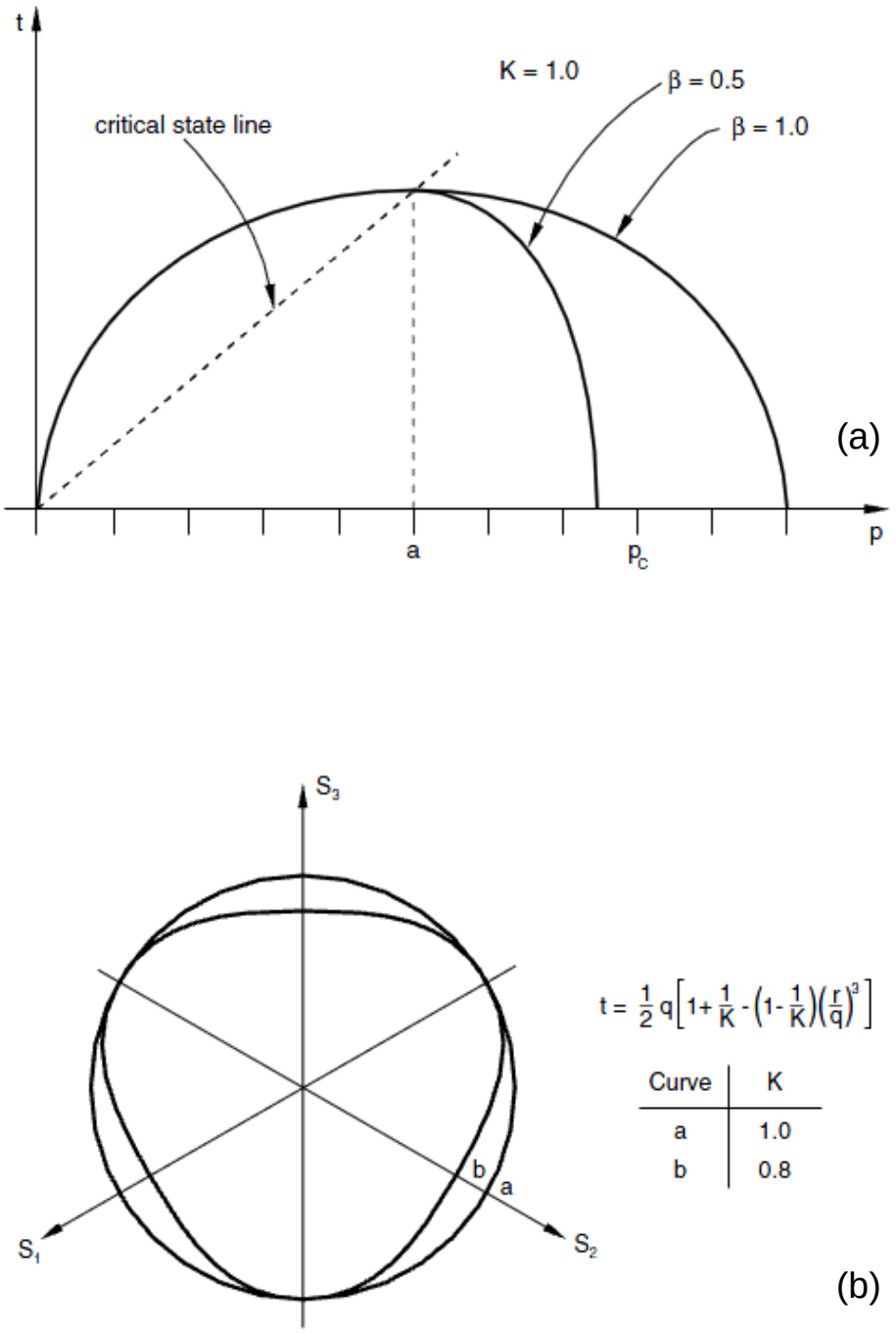

Fig. 6.2. Projections of general yield surface of clay plasticity model on (a) P'-t plane; (b) deviatoric plane (after ABAQUS, 2011)

problem.

6.3 Numerical Analyses of Wellbore Problem with Modified Cam Clay Model

In this section the drained wellbore drilling boundary value problems in the modified Cam Clay rock formations are re-examined using the commercial finite element code ABAQUS. The same rock properties and initial conditions as those given in Table 4.1, i.e., $M = 0.88$, $\lambda = 0.25$, $\kappa = 0.05$, $\nu = 0.16$, and $v_{cs} = 4.04$; $\sigma_{r0}^{'} = \sigma_{\theta 0}^{'} = 11.25$ MPa, $\sigma_{z0}^{'} = 15$ MPa, $P_0^{'} = 12.5$ MPa, and $q_0 = 3.75$ MPa; and $OCR = 1$, 1.2, 3, and 5, have been employed in the numerical simulations. The initial size of the yield surface, b_0, can be calculated from Eqs. (4.4) and (4.74) as

$$b_0 = \frac{1}{2}\left[OCR P_0^{'}\left(1 + \frac{q_0^2}{M^2 P_0^{'2}}\right)\right] = \frac{1}{2} e^{\frac{v_{cs} + (\lambda - \kappa)\ln 2 - v_0 - v \ln P_0^{'}}{\lambda - \kappa}} \tag{6.2}$$

In the ABAQUS simulations, a square computation domain with side length $L = 100a_0$ is adopted, as shown in Fig. 6.3, which is discretized into 16000 8-node biquadratic, reduced integration elements with a refined mesh near the wellbore surface. A sensitivity analysis shows that such a choice of the calculation domain and mesh size is large and fine enough to obtain satisfactory numerical results. The modified Cam Clay model is specified by the keyword *CLAY PLASTICITY followed sequentially by the parameters $\lambda = 0.25$, $M = 0.88$, the initial yield surface size b_0 determined from Eq. (6.2), $\beta = 1.0$, and $K = 1.0$, as well as the keyword *POROUS ELASTIC followed by the nonlinear elastic parameters $\kappa = 0.05$ and $\nu = 0.16$. The initial in-situ stresses of $\sigma_{r0}^{'} = \sigma_{\theta 0}^{'} = 11.25$ MPa and $\sigma_{z0}^{'} = 15$ MPa are defined through the keyword *INITIAL CONDTIONS, TYPE = STRESS.

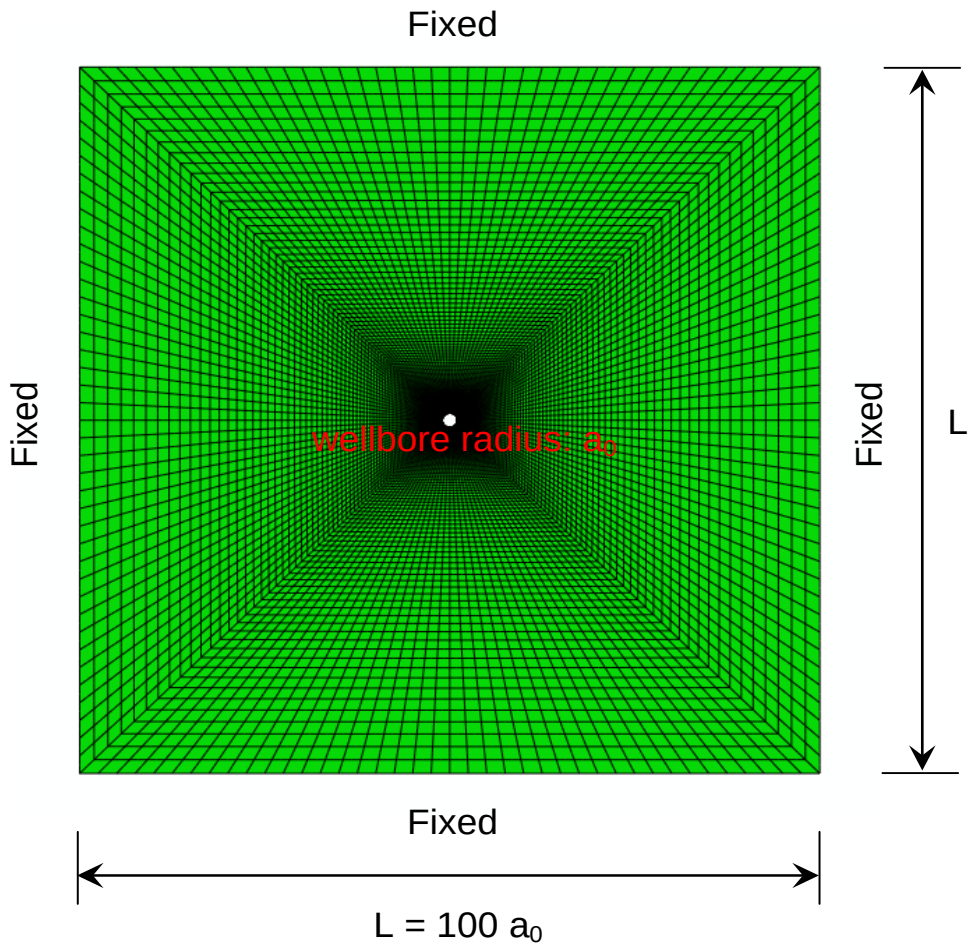

Fig. 6.3. Finite element mesh for wellbore drilling problem

The analysis procedure for the wellbore drilling problem is divided into two steps. The first one should be a *GEOSTATIC step in which the keyword *BOUNDARY is used to fix the displacement and rotation at all nodes on the borehole surface and outer boundaries as well. In this step ABAQUS will check whether the initial stress state (as given on the *INITIAL CONDTIONS keyword) is in equilibrium with these constraints. The next step is defined as the "DRILLING" step using a *STATIC procedure. During

this analysis step the boundary condition at the borehole surface defined in the *GEOSTATIC step is removed, but simultaneously a pressure loading will be assigned over the borehole surface through the *DSLOAD keyword to reflect the mud pressure effect. As described previously in Section 6.2.1, due to the nonlinear nature of the modified Cam Clay elastoplastic model involved, ABAQUS needs to break the "DRILLING" simulation step into a number of small increments and use a Newton iteration scheme to find the approximate equilibrium configuration at the end of each increment.

Figs. 6.4-6.7 show the drained $P' - q$ stress paths and $P' - v$ plots ($p_w' = 0$) obtained from the ABAQUS analyses pertaining to a point at the wellbore surface for OCR ranging from 1 to 5. Also shown in these figures are the analytical solutions. Recall that all the material particles at different locations follow exactly the same curves on the stress and compression planes, yet only end at different positions. It is clear that the two predictions are in excellent agreement, though for the cases of $OCR = 1$ and 1.2, ABAQUS aborts analyses at the effective wellbore pressure of $p_w' = 0.37$ MPa and $p_w' = 0.51$ MPa, respectively, rather than the target value of $p_w' = 0$. This justifies the validity and accuracy of the proposed analytical method and in turn indicates the general capability of ABAQUS in handling the wellbore drilling problem involving the critical state plasticity model. The termination of the ABAQUS running, as is seen under the normally consolidated and slightly overconsolidated situations, is believed to be caused by the convergence problem that frequently occurs in the nonlinear elastoplastic finite element analysis particularly when the critical state models are involved (Potts & Zdravkovic, 1999; 2000).

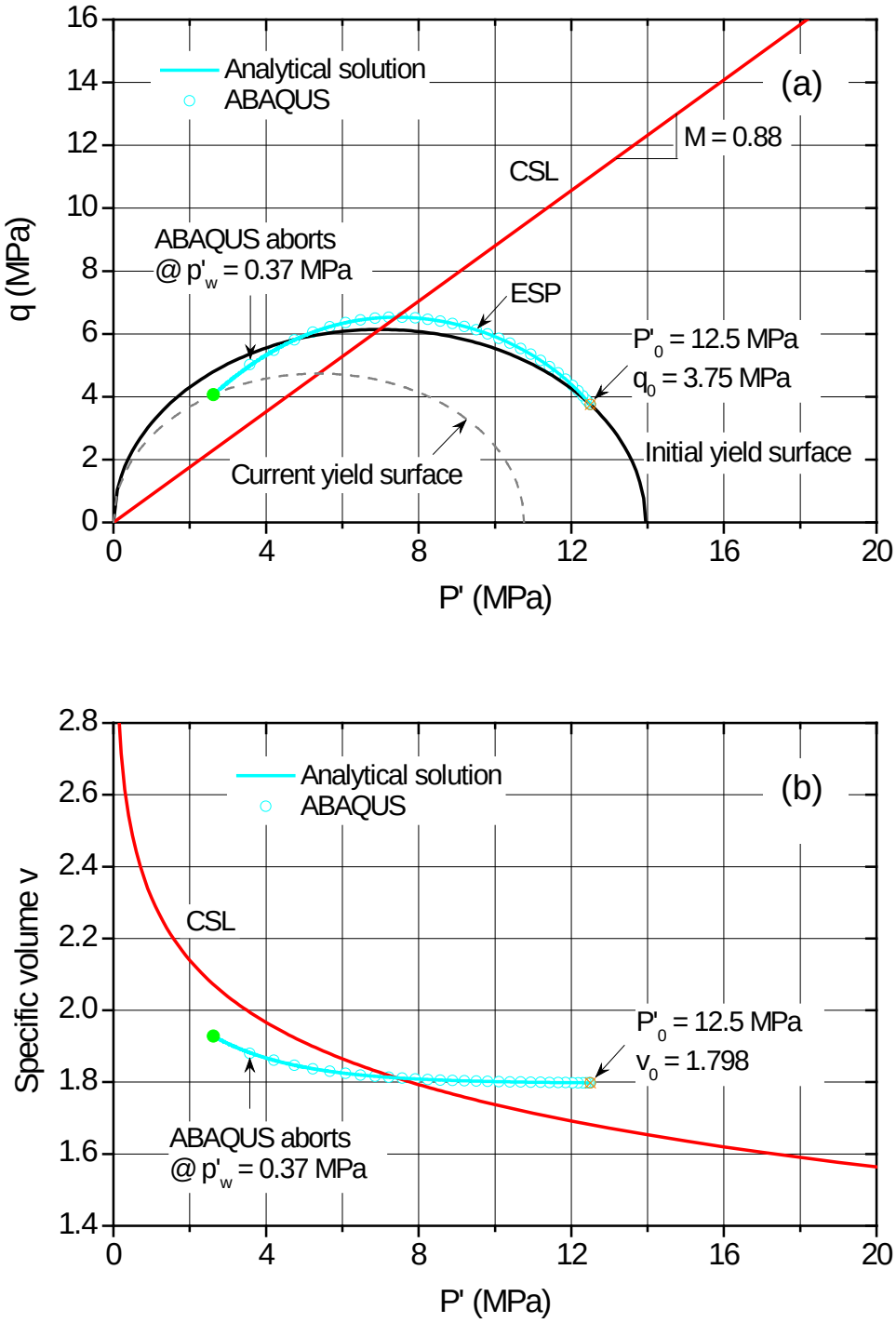

Fig. 6.4. Comparison of drained (a) P'-q stress path and (b) v-P' plot at wellbore surface between ABAQUS and exact analytical solutions for normally consolidated (OCR = 1) rock, modified Cam Clay model

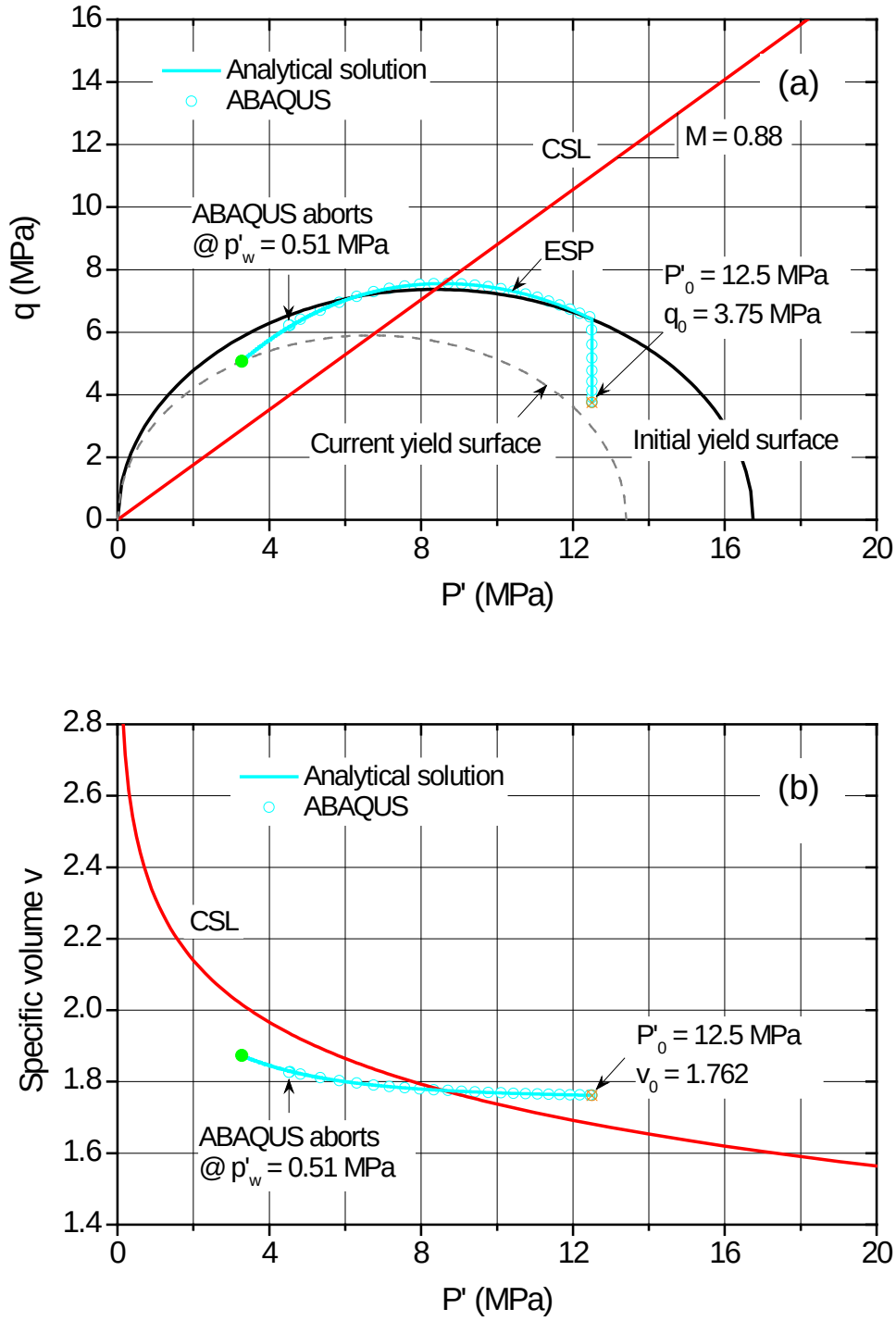

Fig. 6.5. Comparison of drained (a) P'-q stress path and (b) v-P' plot at wellbore surface between ABAQUS and exact analytical solutions for lightly overconsolidated (OCR = 1.2) rock, modified Cam Clay model

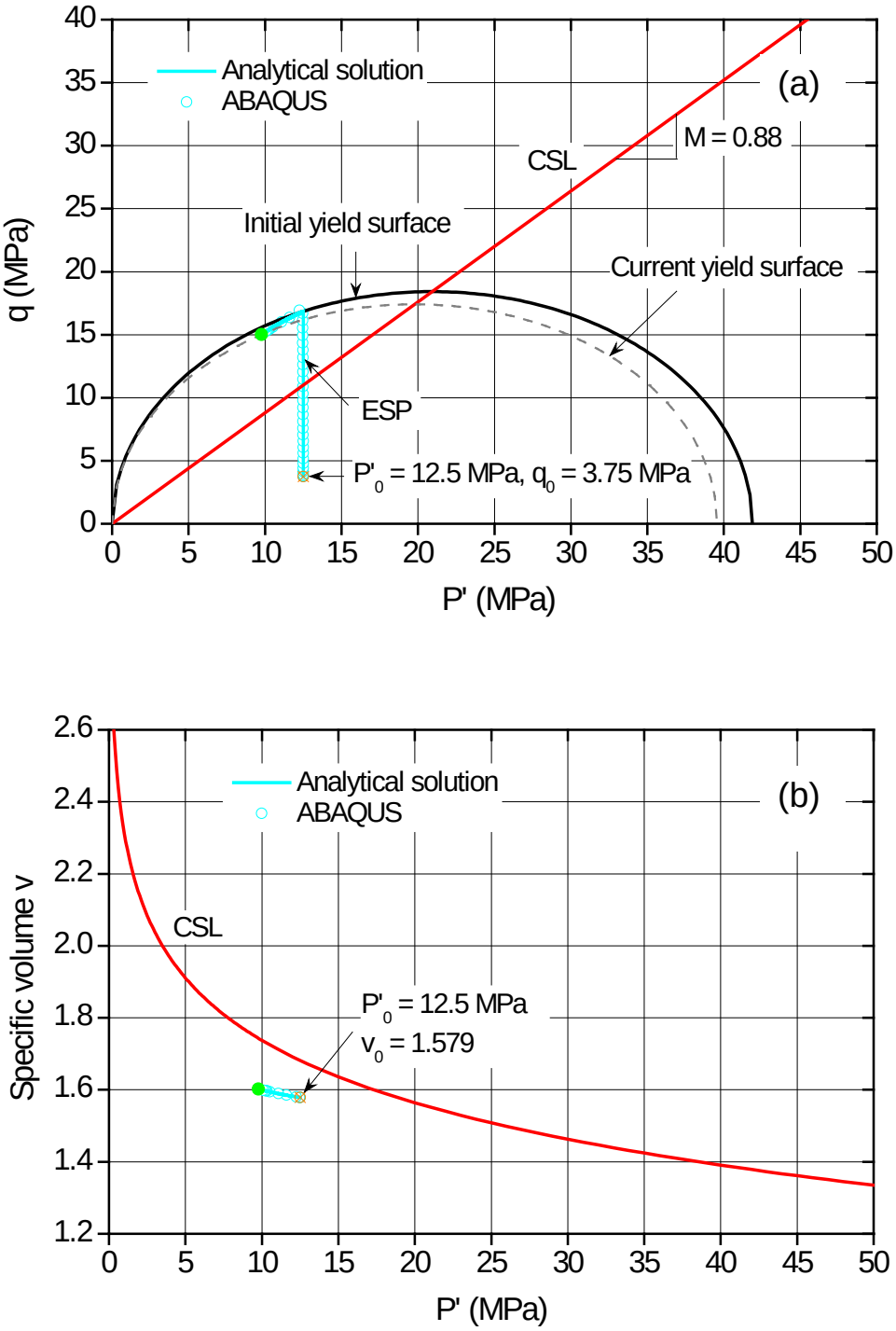

Fig. 6.6. Comparison of drained (a) P'-q stress path and (b) v-P' plot at wellbore surface between ABAQUS and exact analytical solutions for moderately overconsolidated (OCR = 3) rock, modified Cam Clay model

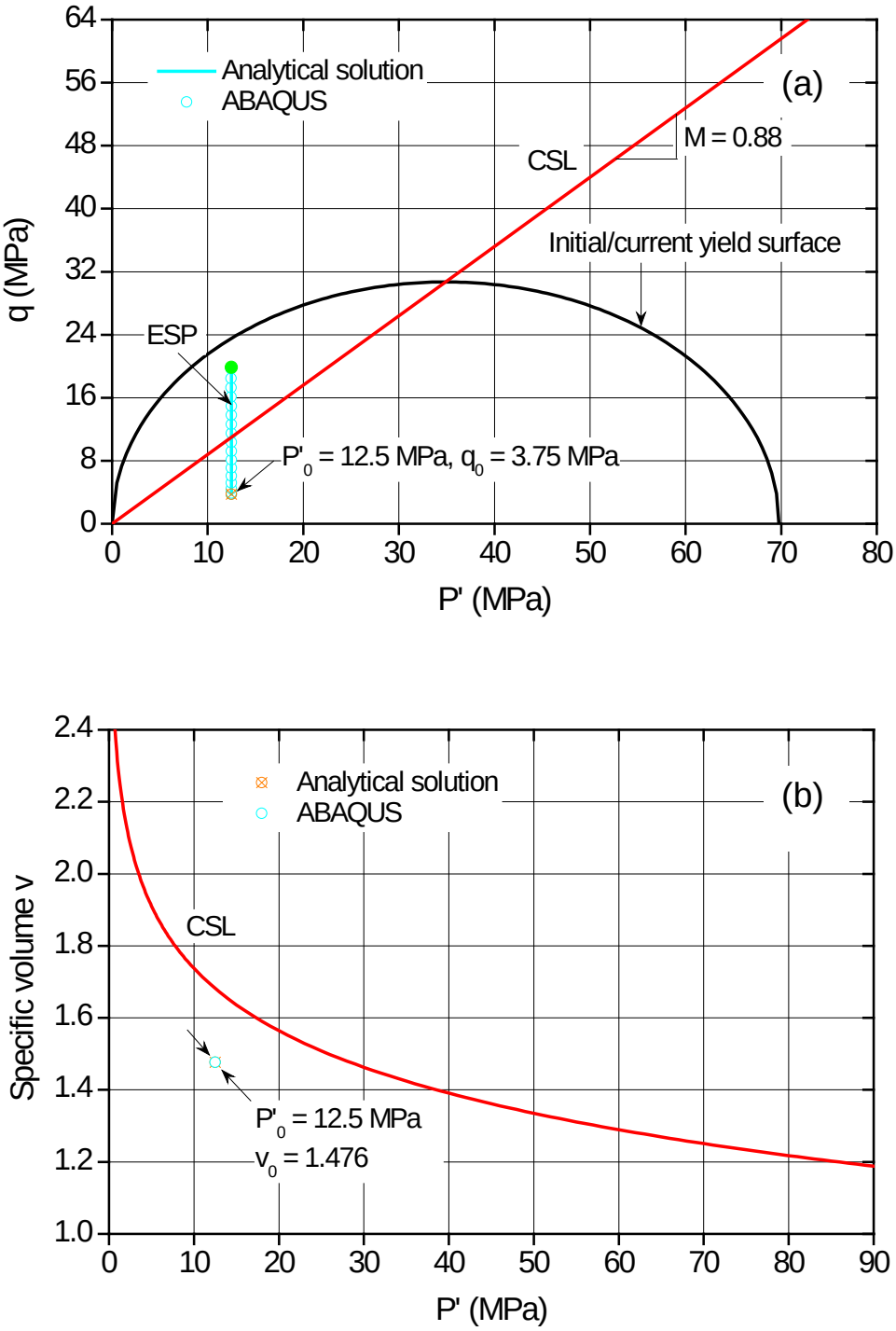

Fig. 6.7. Comparison of drained (a) P'-q stress path and (b) v-P' plot at wellbore surface between ABAQUS and exact analytical solutions for heavily overconsolidated (OCR = 5) rock, modified Cam Clay model

6.4 Numerical Analyses of Wellbore Problem with Bounding Surface Model

When using the bounding surface plasticity model to analyze the wellbore drilling problem with ABAQUS, implementation work has to be done through the user subroutine UMAT as the commercial code ABAQUS does not include this specific elastoplastic model. As already mentioned, a key step for the development of UMAT is to integrate the constitutive equations and update the stresses and state variables at the end of the increment. Methods of performing this integration are termed stress point algorithms and both explicit and implicit approaches have been proposed in the literature (Sloan, 1987; Borja & Lee, 1990; Simo & Hughes, 1998; Potts & Zdravkovic, 1999; Neto et al., 2008). Here the implicit type return mapping algorithm, which is widely used in practice (Simo & Hughes, 2000; Neto et al., 2008), will be adopted because of its attractive properties of accuracy, robustness, and unconditional stability.

6.4.1 RETURN MAPPING ALGORITHM

The return mapping algorithm basically involves some form of elastic predictor to give a trial estimate of the stress changes, and a plastic corrector algorithm to pull these stresses back to the yield surface. The strategy adopted in a return scheme is as follows (Potts & Zdravkovic, 1999; Neto et al., 2008).

(a) Elastic trial step

First, assume that the deformation in step $[t_n, t_{n+1}]$ is purely elastic. Given the values of $\boldsymbol{\varepsilon}_n^e$, $\boldsymbol{\varepsilon}_n^p$, and $\boldsymbol{\alpha}_n$, of the elastic strains, plastic strains, and internal variables set at the beginning of the pseudo-time interval $[t_n, t_{n+1}]$, and given the prescribed incremental strains $\Delta\boldsymbol{\varepsilon}$ for this interval, the elastic trial solution for the strains, state variables, and

stresses at the end of the increment can be obtained as

$$\boldsymbol{\varepsilon}_{n+1}^{e,trial} = \boldsymbol{\varepsilon}_{n}^{e} + \Delta\boldsymbol{\varepsilon} \tag{6.3a}$$

$$\boldsymbol{\varepsilon}_{n+1}^{p,trial} = \boldsymbol{\varepsilon}_{n}^{p} \tag{6.3b}$$

$$\boldsymbol{\alpha}_{n+1}^{trial} = \boldsymbol{\alpha}_{n} \tag{6.3c}$$

$$\boldsymbol{\sigma}_{n+1}^{trial} = \boldsymbol{\sigma}_{n} + \boldsymbol{D}^{e} : \Delta\boldsymbol{\varepsilon} \tag{6.3d}$$

where $\boldsymbol{D}^{e}$ is the elastic constitutive matrix (fourth-order tensor); $\boldsymbol{\sigma}_{n}$ denotes the stress state at the beginning of the increment; and the superscript "trial" refers to the trial solutions.

(b) Check plastic admissibility

If the above trial elastic solution satisfies

$$f(\boldsymbol{\sigma}_{n+1}^{trial}, \boldsymbol{\alpha}_{n+1}^{trial}) \leq 0 \tag{6.4}$$

i.e., lies within the elastic domain or on the yield surface, it is accepted as a solution. Therefore

$$\boldsymbol{\varepsilon}_{n+1}^{e} = \boldsymbol{\varepsilon}_{n+1}^{e,trial}, \quad \boldsymbol{\varepsilon}_{n+1}^{p} = \boldsymbol{\varepsilon}_{n+1}^{p,trial}, \quad \boldsymbol{\alpha}_{n+1} = \boldsymbol{\alpha}_{n+1}^{trial}, \quad \boldsymbol{\sigma}_{n+1} = \boldsymbol{\sigma}_{n+1}^{trial} \tag{6.5}$$

and there is no need to proceed with the algorithm. Otherwise, the elastic trial solution is not plastically admissible, the solution then must be obtained from the plastic corrector step as described below.

(c) Plastic corrector step

The goal of this step is to ensure that the stress state, $\boldsymbol{\sigma}_{n+1}$, at the end of interval $[t_n, t_{n+1}]$ lies on the updated yield surface, that is, the elastic stresses return to the yield surface so that plastic consistency is re-established in the updated state. These stresses, together with the strains and state variables, are calculated from the following nonlinear algebraic equations

$$\boldsymbol{\varepsilon}_{n+1}^{e} = \boldsymbol{\varepsilon}_{n+1}^{e,trial} - \Lambda \frac{\partial f(\boldsymbol{\sigma},\boldsymbol{\alpha})}{\partial \boldsymbol{\sigma}}\Big|_{\boldsymbol{\sigma}=\boldsymbol{\sigma}_{n+1},\boldsymbol{\alpha}=\boldsymbol{\alpha}_{n+1}} \tag{6.6a}$$

$$\boldsymbol{\varepsilon}_{n+1}^{p} = \boldsymbol{\varepsilon}_{n+1}^{p,trial} + \Lambda \frac{\partial f(\boldsymbol{\sigma},\boldsymbol{\alpha})}{\partial \boldsymbol{\sigma}}\Big|_{\boldsymbol{\sigma}=\boldsymbol{\sigma}_{n+1},\boldsymbol{\alpha}=\boldsymbol{\alpha}_{n+1}} \tag{6.6b}$$

$$\boldsymbol{\alpha}_{n+1} = \boldsymbol{\alpha}_{n+1}^{trial} + \Lambda \frac{\partial f(\boldsymbol{\sigma},\boldsymbol{\alpha})}{\partial \boldsymbol{\alpha}}\Big|_{\boldsymbol{\sigma}=\boldsymbol{\sigma}_{n+1},\boldsymbol{\alpha}=\boldsymbol{\alpha}_{n+1}} \tag{6.6c}$$

$$\boldsymbol{\sigma}_{n+1} = \boldsymbol{\sigma}_{n+1}^{trial} - \Lambda \boldsymbol{D}^{e} : \frac{\partial f(\boldsymbol{\sigma},\boldsymbol{\alpha})}{\partial \boldsymbol{\sigma}}\Big|_{\boldsymbol{\sigma}=\boldsymbol{\sigma}_{n+1},\boldsymbol{\alpha}=\boldsymbol{\alpha}_{n+1}} \tag{6.6d}$$

$$f(\boldsymbol{\sigma}_{n+1}, \boldsymbol{\alpha}_{n+1}) = 0 \tag{6.6e}$$

where Λ is the incremental plastic multiplier. Note that in Eqs. (6.6b) and (6.6c) a backward Euler method is adopted to calculate the increments in plastic strains and internal variables, hence a fully implicit nature of the scheme. Fig. 6.8 gives a geometric illustration of the concept of the return mapping algorithm in stress space.

6.4.2 DESCRIPTION OF BOUNDING SURFACE MODEL

Details of the bounding surface model has been described in Chapter 5. In this section the main ingredients of this elastoplastic model are briefly outlined as follows.

Elastic stress-strain relations

The nonlinear elastic rate constitutive relations can be split into volumetric and deviatoric parts, as follows

$$dP' = Kd\varepsilon_p^e = \frac{v}{\kappa} P' (d\varepsilon_v - d\varepsilon_p^p) \tag{6.7a}$$

$$ds_{ij} = 2Gde_{ij}^e = 2G(de_{ij} - de_{ij}^p) \tag{6.7b}$$

where K and $G = \frac{3(1-2\nu)vP'}{2(1+\nu)\kappa}$ are the elastic bulk modulus and shear modulus, respectively; κ denotes the slope of the rebound line in the $v - \ln P'$ plot; v is the specific volume; $ds_{ij} = d\sigma_{ij}' - dP'\delta_{ij}$ is the deviatoric of the incremental stresses $d\sigma_{ij}'$ with δ_{ij} denoting

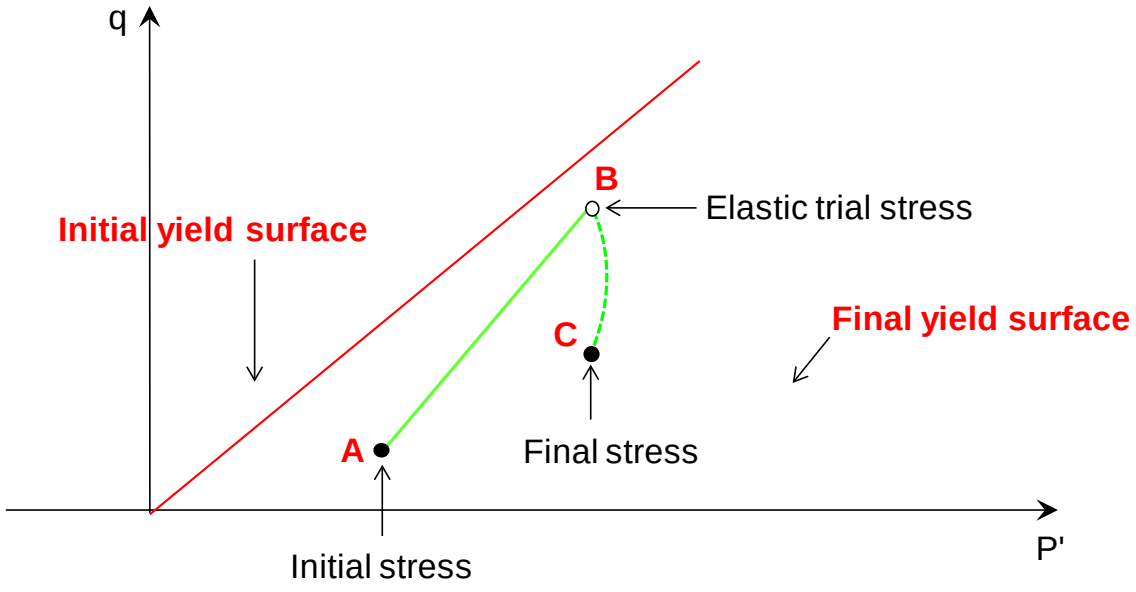

Fig. 6.8. Return mapping algorithm approach

the Kronecker delta; $d\varepsilon_v$ is the change of the volumetric strain; and $de_{ij} = d\varepsilon_{ij} - \frac{1}{3}d\varepsilon_v\delta_{ij}$ is the deviatoric of the incremental strains $d\varepsilon_{ij}$.

Single elliptical bounding surface

Repeating Eq. (5.26), the bounding surface assumes the form

$$\bar{F}\left(\bar{\sigma}_{ij}^{'}, \bar{p}_C^{'}\right) = \bar{F}(\bar{P}^{'}, \bar{q}, \bar{P}_C^{'}) = \frac{2}{3}\bar{q}^2 + \frac{2}{3}\frac{M^2}{(R-1)^2}\left(\bar{P}^{'2} - \frac{2}{R}\bar{P}^{'}\bar{P}_C^{'} + \frac{2-R}{R}\bar{P}_C^{'2}\right)$$

$$= \bar{s}_{ij}\bar{s}_{ij} + \frac{2}{3}\frac{M^2}{(R-1)^2}\left(\bar{P}^{'2} - \frac{2}{R}\bar{P}^{'}\bar{P}_C^{'} + \frac{2-R}{R}\bar{P}_C^{'2}\right) = 0 \qquad (6.8)$$

where the superposed bar represents the stress quantities on the bounding surface and repeated indices appearing as subscripts (i, j) imply summation; $\bar{s}_{ij}$ is the image deviatoric stress state; M and R, as shown in Fig. 5.3, are the model parameters; and $\bar{P}_C^{'}$ denotes the size of the current bounding surface.

Loading surface

The loading surface has the same shape as the bounding surface, and hence is given under the form of

$$F\left(\sigma_{ij}^{'}, P_A^{'}\right) = F(P^{'}, q, P_A^{'}) = s_{ij}\, s_{ij} + \frac{2}{3}\frac{M^2}{(R-1)^2}\left(P^{'2} - \frac{2}{R}P^{'}P_A^{'} + \frac{2-R}{R}P_A^{'2}\right) = 0 \qquad (6.9)$$

where s_{ij} is the actual deviatoric stress state and $P_A^{'}$ denotes the size of the loading surface (Fig. 5.3).

Hardening law

Hardening/softening of the bounding surface is assumed to be isotropic and depend only on the parameter $\bar{P}_C^{'}$, which is related to the plastic volumetric strain, ε_p^p, by

$$\frac{d\bar{P}_C^{'}}{\bar{P}_C^{'}} = \frac{(1+e)}{\lambda-\kappa}\, d\varepsilon_p^p = \frac{v}{\lambda-\kappa}\, d\varepsilon_p^p \qquad (6.10)$$

where λ denotes the slope of normal compression line in $v - \ln P^{'}$ plane.

Radial mapping rule

The simple radial mapping rule used in the current bounding surface model can be expressed as (Dafalias & Herrmann, 1982)

$$\bar{\sigma}_{ij}^{'} = \varrho\sigma_{ij}^{'} \qquad (6.11)$$

where $\varrho = \varrho(\sigma_{ij}^{'}, \varepsilon_p^p)$ is the ratio between the image stress and the current stress quantities. From Eq. (6.11), it can be easily obtained the following representation

$$\bar{P}^{'} = \varrho P^{'}, \quad \bar{s}_{ij} = \varrho s_{ij}, \quad \bar{P}_C^{'} = \varrho P_A^{'} \qquad (6.12)$$

Flow rule and plastic modulus

The plastic strain rates under the normality condition are given by Eqs. (5.5) and (5.6), namely

$$d\varepsilon_{ij}^p = \frac{1}{K_p}\, d\sigma_{kl}^{'}\, n_{kl} = \frac{1}{K_b}\, d\bar{\sigma}_{kl}^{'} n_{kl} \qquad (6.13)$$

where K_b, the plastic modulus on the bounding surface, can be obtained from Eqs. (5.13), (5.14), and (6.10) as follows

$$K_b = \frac{1+e}{\bar{g}_2^2}\frac{\partial \bar{F}}{\partial e^p}\frac{\partial \bar{F}}{\partial \bar{P}'} = -\frac{1}{\bar{g}_2^2}\frac{\partial \bar{F}}{\partial \varepsilon_p^p}\frac{\partial \bar{F}}{\partial \bar{P}'} = -\frac{1}{\bar{g}_2^2}\frac{\partial \bar{F}}{\partial \bar{P}_C'}\frac{d\bar{P}_C'}{d\varepsilon_p^p}\frac{\partial \bar{F}}{\partial \bar{P}'}$$

$$= -\frac{1}{\bar{g}_2^2}\frac{16}{9}\frac{M^4}{\lambda-\kappa}\frac{v}{(R-1)^4}\bar{P}_C'\left(\bar{P}' - \frac{\bar{P}_C'}{R}\right)\left(\frac{2-R}{R}\bar{P}_C' - \frac{\bar{P}'}{R}\right) \tag{6.14}$$

with

$$\bar{g}_2 = \sqrt{\frac{1}{3}\left(\frac{\partial \bar{F}}{\partial \bar{P}'}\right)^2 + \frac{3}{2}\left(\frac{\partial \bar{F}}{\partial \bar{q}}\right)^2} \tag{6.15}$$

and K_p, the actual plastic modulus on the loading surface, takes the following form according to Eqs. (5.15) and (5.36)

$$K_p = K_b + K_h \tag{6.16}$$

where

$$K_h = \frac{\left(\frac{\partial \bar{F}}{\partial \bar{P}'}\right)^2 + \left(\frac{\partial \bar{F}}{\partial \bar{q}}\right)^2}{\bar{g}_2^2}\frac{v}{\lambda-\kappa}hp_a\left(1 + \left|\frac{M\bar{P}'}{\bar{q}}\right|^m\right)\frac{\delta}{\delta_0-\delta} \tag{6.17}$$

With the aid of Eqs. (5.19), (5.37), and (6.8), the above equation becomes

$$K_h = \frac{1}{\bar{g}_2^2}\left\{\frac{4}{9}\frac{M^4}{(R-1)^4}\left(2\bar{P}' - \frac{2\bar{P}_C'}{R}\right)^2 + \frac{16}{9}\bar{q}^2\right\}\left\{\frac{v}{\lambda-\kappa}hp_a\left(1 + \left|\frac{M\bar{P}'}{\bar{q}}\right|^m\right)\right\}\frac{(\varrho-1)\bar{P}'Q}{\varrho\bar{P}_C' - (\varrho-1)\bar{P}'Q} \tag{6.18}$$

where $\varrho = \frac{\bar{P}'}{P'}$ and

$$Q = \sqrt{1 + \frac{q^2}{P'^2}} \tag{6.19}$$

6.4.3 IMPLICIT INTEGRATION OF THE MODEL

This section describes the implicit integration algorithm for the bounding surface model which follows the popular cutting-plane algorithm (Ortiz & Simo, 1986; Hashash & Whittle, 1992), and is essentially an extension of the integration scheme proposed by

Manzari & Nour (1997) used for the simple bounding surface version of modified Cam Clay associated with a substantially simplified hardening rule. As mentioned earlier, the main purpose of the integration procedure is to obtain the updated stress state, $\boldsymbol{\sigma}_{n+1}$, at the end of a typical interval $[t_n, t_{n+1}]$ for the given increments of strain, $\Delta\boldsymbol{\varepsilon}$, corresponding to this interval. It involves an elastic predictor phase and a subsequent plastic corrector phase.

Elastic predictor

In the first estimate for the updated stresses $\boldsymbol{\sigma}'^{trial}_{n+1} = \{P'^{trial}_{n+1}, s^{trial}_{ij,n+1}\}$ (the superscript prime represents the effective stress), the response is assumed to be fully elastic so there are neither any incremental plastic strains $\Delta\varepsilon^{p}_{ij}$ nor any incremental change in the hardening parameter $\Delta\bar{P}'_{C}$. Thus,

$$\Delta\varepsilon^{p,trial}_{p,n+1} = \Delta e^{p,trial}_{ij,n+1} = 0, \quad \Delta\bar{P}'^{trial}_{C,n+1} = 0 \tag{6.20}$$

Here $\Delta\varepsilon^{p,trial}_{p,n+1}$ corresponds to the trial plastic volumetric strain increment in step $[t_n, t_{n+1}]$ and $\Delta e^{p,trial}_{ij,n+1}$ to the deviatoric part of the plastic strain increments defined as

$$\Delta e^{p,trial}_{ij,n+1} = \Delta\varepsilon^{p,trial}_{ij,n+1} - \frac{1}{3}\Delta\varepsilon^{p,trial}_{p,n+1}\,\delta_{ij} \tag{6.21}$$

The updated hardening parameter and stress state at t_{n+1} now can be calculated by integrating the stress-strain relations (6.7a) and (6.7b), which gives

$$\bar{P}'^{trial}_{C,n+1} = \bar{P}'_{C,n} \tag{6.22a}$$

$$P'^{trial}_{n+1} = P'_{n} e^{\frac{v_n}{\kappa}\Delta\varepsilon_{v,n+1}} \tag{6.22b}$$

$$s^{trial}_{ij,n+1} = s_{ij,n} + \frac{3(1-2\nu)}{1+\nu}\frac{P'_n}{\Delta\varepsilon_{v,n+1}}\left(e^{\frac{v_n}{\kappa}\Delta\varepsilon_{v,n+1}} - 1\right)\Delta e_{ij,n+1} \tag{6.22c}$$

Plastic corrector

If the above trial stress solution exceeds the yield surface, i.e.,

$f\left(P_{n+1}^{'trial}, s_{ij,n+1}^{trial}, \bar{P}_{C,n+1}^{'trial}\right) > 0$, plastic straining then occurs. In this case the stress state and hardening parameter should be corrected by imposing the flow and hardening rule together with the consistency requirement. This can be achieved by applying Eqs. (6.6a)-(6.6e), which for the specific bounding surface model take the form

$$P_{n+1}^{'} = P_n^{'} e^{\frac{v_n}{\kappa}(\Delta\varepsilon_{v,n+1} - \Delta\varepsilon_{p,n+1}^{p})} \tag{6.23a}$$

$$\Delta\varepsilon_{p,n+1}^{p} = \Lambda_{n+1} \frac{4}{3} \frac{M^2}{(R-1)^2} \left(\bar{P}_{n+1}^{'} - \frac{\bar{P}_{C,n+1}^{'}}{R}\right) \tag{6.23b}$$

$$s_{ij,n+1} = s_{ij,n} + \frac{3(1-2\nu)}{1+\nu} P_n^{'} \frac{\Delta e_{ij,n+1} - \Delta e_{ij,n+1}^{p}}{\Delta\varepsilon_{v,n+1} - \Delta\varepsilon_{p,n+1}^{p}} \left\{ e^{\frac{v_n}{\kappa}(\Delta\varepsilon_{v,n+1} - \Delta\varepsilon_{p,n+1}^{p})} - 1 \right\} \tag{6.23c}$$

$$\Delta e_{ij,n+1}^{p} = 2\Lambda_{n+1} \bar{s}_{ij,n+1} \tag{6.23d}$$

$$\bar{P}_{C,n+1}^{'} = \bar{P}_{C,n}^{'} e^{\frac{v_n}{\lambda-\kappa}\Delta\varepsilon_{p,n+1}^{p}} \tag{6.23e}$$

$$\bar{s}_{ij,n+1}\bar{s}_{ij,n+1} + \frac{2}{3} \frac{M^2}{(R-1)^2} \left(\bar{P}_{n+1}^{'2} - \frac{2}{R} \bar{P}_{n+1}^{'} \bar{P}_{C,n+1}^{'} + \frac{2-R}{R} \bar{P}_{C,n+1}^{'2}\right) = 0 \tag{6.23f}$$

By substitution of the relations $\bar{P}_{n+1}^{'} = \varrho_{n+1} P_{n+1}^{'}$ and $\bar{s}_{ij,n+1} = \varrho_{n+1} s_{ij,n+1}$ from Eq. (6.12) into Eqs. (6.23d) and (6.23f), one obtains the plastic deviatoric stains and consistency condition without involving the use of the image states as follows

$$\Delta e_{ij,n+1}^{p} = 2\Lambda_{n+1} \varrho_{n+1} s_{ij,n+1} \tag{6.23g}$$

$$\varrho_{n+1}^2 s_{ij,n+1} s_{ij,n+1} + \frac{2}{3} \frac{M^2}{(R-1)^2} \left(\varrho_{n+1}^2 P_{n+1}^{'2} - \frac{2}{R} \varrho_{n+1} P_{n+1}^{'} \bar{P}_{C,n+1}^{'} + \frac{2-R}{R} \bar{P}_{C,n+1}^{'2}\right) = 0 \tag{6.23h}$$

Eqs. (6.23a)-(6.23c) and (6.23e) together with (6.23g)-(6.23h) provide a set of 16 nonlinear algebra equations, but contain totally 17 ($P_{n+1}^{'}$, $\Delta\varepsilon_{p,n+1}^{p}$, 6 $s_{ij,n+1}$, 6 $\Delta e_{ij,n+1}^{p}$, $\bar{P}_{C,n+1}^{'}$, and ϱ_{n+1}) unknowns to be solved for. Therefore, one additional equation is required to complete the formulation. As pointed out by Manzari & Nour (1997) for the simple modified Cam Clay bounding surface, such an equation should be obtained by

considering the essential feature of the bounding surface plasticity, defined in Eq. (6.13). It is found that, for the general bounding surface considered in this work, a differential equation may still be derived for ϱ in an exactly similar way as in Manzari & Nour (1997). Details of the derivation of this equation is given in the following section.

Differential equation governing ϱ

Let the plastic constitutive relation, i.e., Eq. (6.13), be rewritten in the following form

$$d\bar{\sigma}_{kl}^{'}\frac{\partial \bar{F}}{\partial \bar{\sigma}_{ij}^{'}} = k_p\, d\sigma_{kl}^{'}\ \frac{\partial \bar{F}}{\partial \bar{\sigma}_{ij}^{'}} \tag{6.24}$$

where k_p is the ratio between the bounding surface plastic modulus and the actual plastic modulus

$$k_p = \frac{K_b}{K_p} = \frac{-\frac{M^4}{(R-1)^4}\bar{P}_C^{'}\left(\bar{P}^{'}-\frac{\bar{P}_C^{'}}{R}\right)\left(\frac{2-R}{R}\bar{P}_C^{'}-\frac{\bar{P}^{'}}{R}\right)}{-\frac{M^4}{(R-1)^4}\bar{P}_C^{'}\left(\bar{P}^{'}-\frac{\bar{P}_C^{'}}{R}\right)\left(\frac{2-R}{R}\bar{P}_C^{'}-\frac{\bar{P}^{'}}{R}\right)+\left\{\frac{M^4}{(R-1)^4}\left(\bar{P}^{'}-\frac{\bar{P}_C^{'}}{R}\right)^2+\bar{q}^2\right\}\left\{hp_a\left(1+\left|\frac{M\bar{P}^{'}}{\bar{q}}\right|^m\right)\right\}\frac{(\varrho-1)\bar{P}^{'}Q}{\varrho\bar{P}_C^{'}-(\varrho-1)\bar{P}^{'}Q}} \tag{6.25}$$

and from Eq. (6.8)

$$\frac{\partial \bar{F}}{\partial \bar{\sigma}_{ij}^{'}} = \frac{\partial \bar{F}}{\partial \bar{s}_{ij}} + \frac{\partial \bar{F}}{\partial \bar{P}}\frac{1}{3}\delta_{ij}\ = 2\bar{s}_{ij}\ + \frac{4}{9}\frac{M^2}{(R-1)^2}\left(\bar{P}^{'}-\frac{\bar{P}_C^{'}}{R}\right)\delta_{ij} \tag{6.26}$$

Substituting Eq. (6.26) and making use of the first two components of Eq. (6.12), Eq. (6.24) then becomes

$$2\varrho\left(\varrho-k_p\right)\left\{s_{ij}\,ds_{ij}\ +\frac{2}{3}\frac{M^2}{(R-1)^2}P^{'}dP^{'}\right\}+2\varrho d\varrho\left\{s_{ij}\,s_{ij}\ +\frac{2}{3}\frac{M^2}{(R-1)^2}P^{'2}\right\}$$

$$-\frac{4}{3}\frac{M^2}{(R-1)^2}\frac{\bar{P}_C^{'}}{R}(\varrho dP^{'}+P^{'}d\varrho)+\frac{4}{3}k_p\frac{M^2}{(R-1)^2}\frac{\bar{P}_C^{'}}{R}dP^{'}=0 \tag{6.27}$$

Considering now the loading surface representation (6.9), and noting that $\bar{P}_C^{'}=\varrho P_A^{'}$, it then follows

$$s_{ij}\,s_{ij} + \frac{2}{3}\frac{M^2}{(R-1)^2}\left(P'^2 - \frac{2}{R}P'\frac{\bar{P}_C'}{\varrho} + \frac{2-R}{R}\frac{\bar{P}_C'^2}{\varrho^2}\right) = 0 \tag{6.28}$$

or in the differential form

$$s_{ij}\,ds_{ij} + \frac{2}{3}\frac{M^2}{(R-1)^2}P'\,dP' = \frac{2}{3}\frac{M^2}{(R-1)^2}\frac{1}{R}\frac{\varrho P'\,d\bar{P}_C' + \varrho d\,P'\bar{P}_C' - P'\bar{P}_C' d\varrho}{\varrho^2}$$

$$- \frac{2}{3}\frac{M^2}{(R-1)^2}\frac{2-R}{R}\frac{\bar{P}_C'}{\varrho}\frac{\varrho d\,\bar{P}_C' - \bar{P}_C' d\varrho}{\varrho^2} \tag{6.29}$$

Substituting Eq. (6.29) into Eq. (6.27) and after some algebra operations, one obtains

$$\left(\varrho - k_p\right)P'\,d\bar{P}_C' - \left(\varrho - k_p\right)\frac{2-R}{\varrho}\bar{P}_C' d\bar{P}_C' = \frac{k_p}{\varrho}\left(-P'\,d\bar{P}_C' d\varrho + \frac{2-R}{\varrho}\bar{P}_C'^2 d\varrho\right) \tag{6.30}$$

and therefore

$$\frac{d\bar{P}_C'}{\bar{P}_C'} = \left(\frac{1}{\varrho} - \frac{1}{\varrho - k_p}\right)d\varrho \tag{6.31}$$

It is interesting to note that the above differential equation for ϱ has the same form as the one for the bounding surface modified Cam Clay model with specific value of $R = 2$ (Manzari & Nour, 1997). Integrating Eq. (6.31) over the time step $[t_n, t_{n+1}]$, with an assumption of constant plastic modulus ratio $k_p = k_{p,n+1}$ evaluated at the end of the increment, results in

$$\varrho_{n+1} = -\frac{\varrho_n k_{p,n+1}\frac{\bar{P}_{C,n+1}'}{\bar{P}_{C,n}'}}{\varrho_n - k_{p,n+1} - \varrho_n\frac{\bar{P}_{C,n+1}'}{\bar{P}_{C,n}'}} \tag{6.32}$$

where, according to Eqs. (6.12), (6.19), and (6.25),

$$k_{p,n+1} = \frac{X_1}{X_1 + X_{21}X_{22}X_{23}} \tag{6.33a}$$

$$X_1 = -\frac{M^4}{(R-1)^4}\bar{P}_{C,n+1}'\left(\varrho_{n+1}P_{n+1}' - \frac{\bar{P}_{C,n+1}'}{R}\right)\left(\frac{2-R}{R}\bar{P}_{C,n+1}' - \frac{\varrho_{n+1}P_{n+1}'}{R}\right) \tag{6.33b}$$

$$X_{21} = \frac{M^4}{(R-1)^4}\left(\varrho_{n+1}P_{n+1}' - \frac{\bar{P}_{C,n+1}'}{R}\right)^2 + \varrho_{n+1}^2\frac{3}{2}s_{ij,n+1}s_{ij,n+1} \tag{6.33c}$$

$$X_{22} = hp_a \left(1 + \left|\frac{MP'_{n+1}}{\sqrt{(3/2)s_{ij,n+1}s_{ij,n+1}}}\right|^m\right) \tag{6.33d}$$

$$X_{23} = \frac{(\varrho_{n+1}-1)P'_{n+1}\sqrt{1+\frac{\frac{3}{2}s_{ij,n+1}s_{ij,n+1}}{P'^2_{n+1}}}}{\bar{P}'_{C,n+1}-(\varrho_{n+1}-1)P'_{n+1}\sqrt{1+\frac{\frac{3}{2}s_{ij,n+1}s_{ij,n+1}}{P'^2_{n+1}}}} \tag{6.33e}$$

Eqs. (6.32) and (6.33) complete the set of Eq. (6.23) which now offers 18 equations and simultaneously includes the same number of unknowns with the addition of the variable $k_{p,n+1}$. Solution of these nonlinear equations to obtain the updated states at t_{n+1} requires the use of a Newton-type iterative procedure (Neto et al., 2008). The algorithm for solving these equations in accordance with the implicit integration of the bounding surface model is presented in detail in Appendix A.

Jacobian stiffness matrix

The Jacobian stiffness matrix (or consistent tangent operator) is defined as (Manzari & Nour, 1997)

$$\boldsymbol{J} = \begin{bmatrix} \frac{\partial \Delta P'}{\partial \Delta \varepsilon_v} & \frac{\partial \Delta P'}{\partial \Delta e_{ij}} \\ \frac{\partial \Delta s_{ij}}{\partial \Delta \varepsilon_v} & \frac{\partial \Delta s_{ij}}{\partial \Delta e_{kl}} \end{bmatrix} \tag{6.34}$$

which is found to be derivable from Eqs. (6.23) and (6.32) in analytical expressions in terms of the stress state at the end of the increment. However, it is well known that the Jacobian matrix does not influence the accuracy of the solution, but only the rate at which convergence is achieved (Dunne & Petrinic, 2005; ABAQUS, 2011). For this reason, and for the sake of simplicity, the material Jacobian in the present integration scheme is calculated using the elastic constitutive matrix, $\boldsymbol{J}_e$, rather than the elastoplastic matrix, $\boldsymbol{J}_{ep}$, as follows

$$\boldsymbol{J} = \boldsymbol{J}_e = \begin{bmatrix} \frac{\partial \Delta P'}{\partial \Delta \varepsilon_v} & \frac{\partial \Delta P'}{\partial \Delta e_{ij}} \\ \frac{\partial \Delta s_{ij}}{\partial \Delta \varepsilon_v} & \frac{\partial \Delta s_{ij}}{\partial \Delta e_{kl}} \end{bmatrix} = \begin{bmatrix} K & \mathbf{0} \\ \mathbf{0} & G(\delta_{ik}\delta_{jl} + \delta_{il}\delta_{jk}) \end{bmatrix} \tag{6.35}$$

where $K = \frac{P'^{trial}_{n+1} - P'_n}{\Delta \varepsilon_{v,n+1}}$ and $G = \frac{3(1-2\nu)}{2(1+\nu)} \frac{P'^{trial}_{n+1} - P'_n}{\Delta \varepsilon_{v,n+1}}$.

6.4.4 Implementation in ABAQUS and Numerical Results

The above implicit return mapping algorithm for the general bounding surface model is coded using Fortran and implemented in ABAQUS through the material interface UMAT. The UMAT subroutine is called at each material integration point of every element and returns the updated stresses and solution-dependent state variables at the end of each iteration/increment.

To call the UMAT subroutine, the following keyword is used in the ABAQUS input file: *USER MATERIAL, TYPE = MECHANICAL, CONSTANTS = *number-of-constants*. Here for the bounding surface model the number of constants is set equal to 8, which, in sequence, includes the slope of critical state line, M; hardening parameter h; the slope of rebound line, κ; Poisson's ratio ν; the slope of normal compression line λ; atmosphere pressure p_a; hardening parameter m; and bounding surface shape parameter R. On the other hand, ABAQUS needs to specify the number of solution-dependent state variables (required at each integration point) through the command *DEPVAR. Considering the wellbore drilling plane strain condition, the state variables consist of only 4 elastic strains (ε_r^e, ε_θ^e, ε_z^e, and $\varepsilon_{r\theta}^e$) and 4 plastic strains (ε_r^p, ε_θ^p, ε_z^p, and $\varepsilon_{r\theta}^p$), in addition to the bounding surface hardening parameter $\bar{P}_C'$ and specific volume v.

The ABAQUS finite element analysis for the wellbore drilling problem again proceeds in two steps, namely the standard *GEOSTATIC step and the subsequent

"DRILLING" step, as explained in Section 6.3 for the modified Cam Clay model. The initial stress conditions and bounding surface rock parameters are basically the same as those used in the analytical solutions (Chapter 5), but here two different values of $R = 2$ and 2.72 have been considered in performing the numerical simulations (under drained condition), see Table 6.1. Note that $R = 2$ reduces to the simple bounding surface version of modified Cam Clay.

Table 6.1. Parameters used in ABAQUS simulations with bounding surface model

$\sigma_{r0}^{'} = \sigma_{\theta 0}^{'} = 11.25$ MPa, $\sigma_{z0}^{'} = 15$ MPa, $p_0 = 10$ MPa $P_0^{'} = 12.5$ MPa, $q_0 = 3.75$ MPa				
$M = 1.05, \lambda = 0.14, \kappa = 0.05, \nu = 0.15, e_0 = 0.95, m = 0.2, h = 30$				
R	$\bar{P}_{C,0}^{'}$ (MPa)			
	$OCR = 1$	1.2	2	5
2	13.52	16.22	27.04	67.60
2.72	14.80	17.76	29.60	74.00

Figs. 6.9-6.12 and 6.13-15 present the ABAQUS predictions of the $P^{'} - q$ stress paths at the wellbore surface and compare with the analytical solutions for $R = 2$ and 2.72, respectively. Again, excellent agreement could be observed between these two results, thus indicating the accuracy of the exact analytical approach developed for the wellbore drilling boundary value problem, and simultaneously the validity of the UMAT code written for the bounding surface model. It should, however, be noted that for OCR greater than 1, ABAQUS simulations again terminate running before the effective

wellbore pressure of $p_w^{'} = 0$ can finally be achieved, a phenomenon due to the convergence and stability problems which also has occurred for the modified Cam Clay model. Note further that the $P^{'} - q$ stress path corresponding to $R = 2.72$ and relatively large value of $OCR = 5$ has not been presented herein, as in this case ABAQUS encounters severe convergence difficulties and actually breaks down in the first increment during the "DRILLING" step.

6.5 Summary

This chapter revisits the wellbore drilling boundary value problem in modified Cam Clay and bounding surface rocks using the finite element program ABAQUS/Standard. In particular, a UMAT subroutine has been developed and incorporated into ABAQUS for

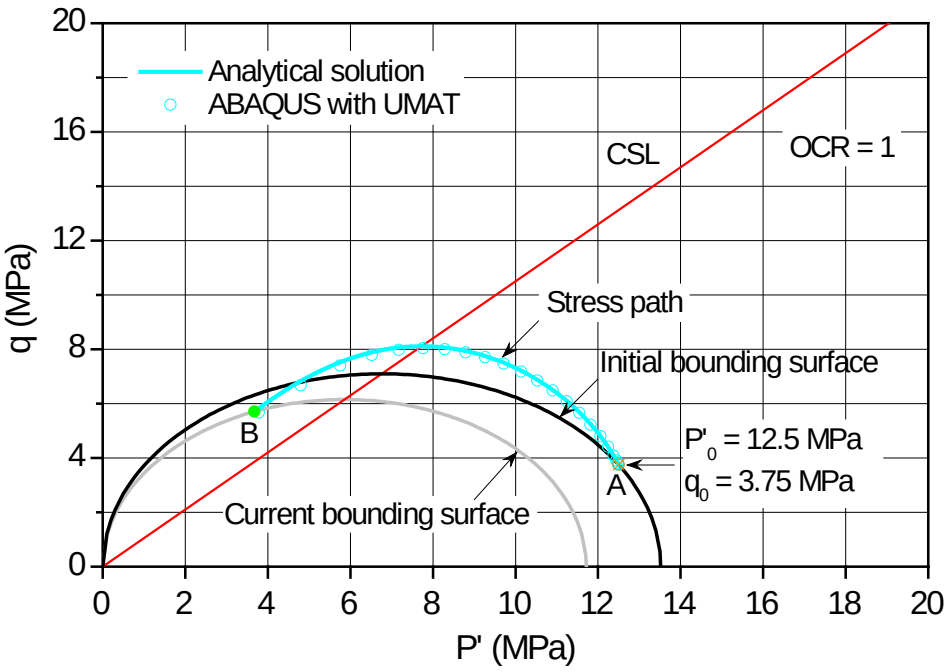

Fig. 6.9. Comparison of drained P'-q stress path at wellbore surface between ABAQUS and exact solutions for OCR = 1, bounding surface model with R = 2

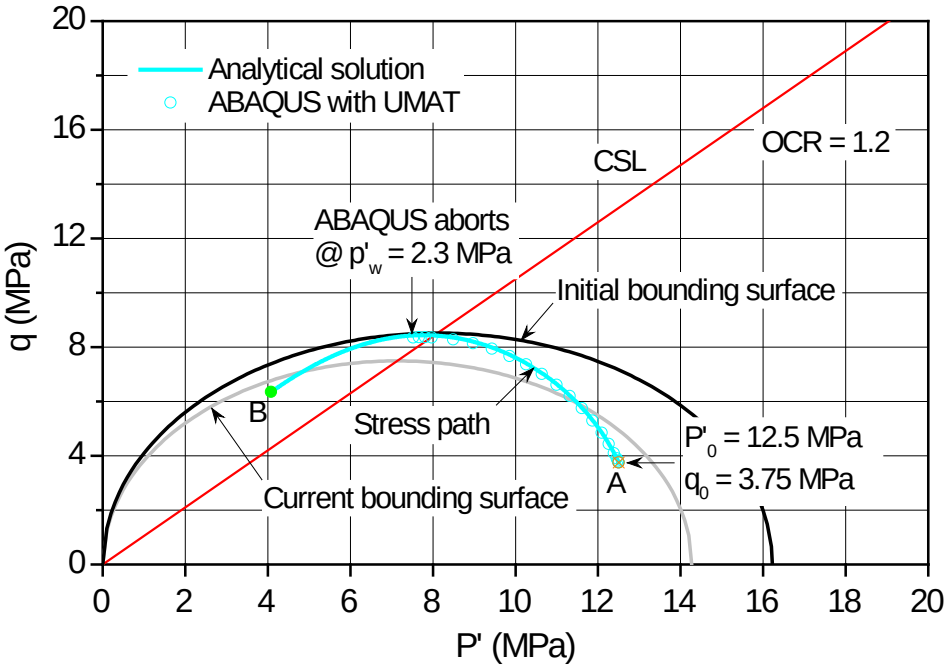

Fig. 6.10. Comparison of drained P'-q stress path at wellbore surface between ABAQUS and exact solutions for OCR = 1.2, bounding surface model with R = 2

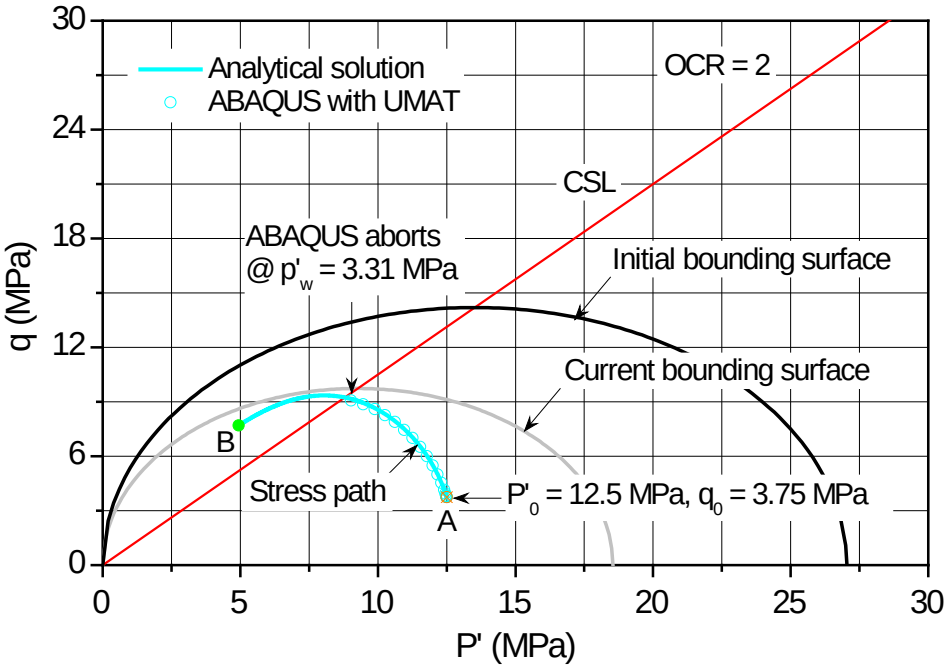

Fig. 6.11. Comparison of drained P'-q stress path at wellbore surface between ABAQUS and exact solutions for OCR = 2, bounding surface model with R = 2

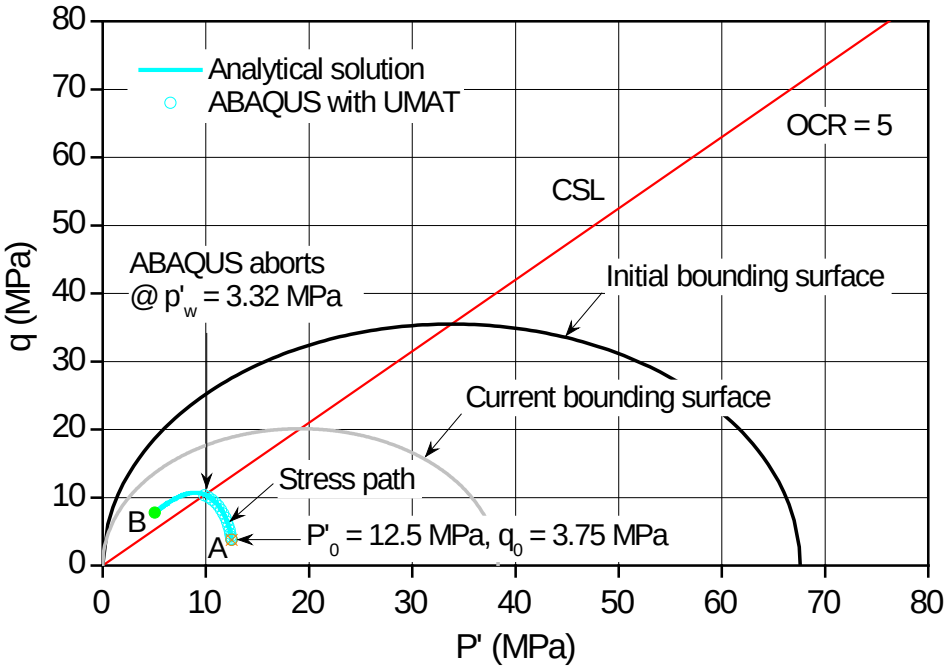

Fig. 6.12. Comparison of drained P'-q stress path at wellbore surface between ABAQUS and exact solutions for OCR = 5, bounding surface model with R = 2

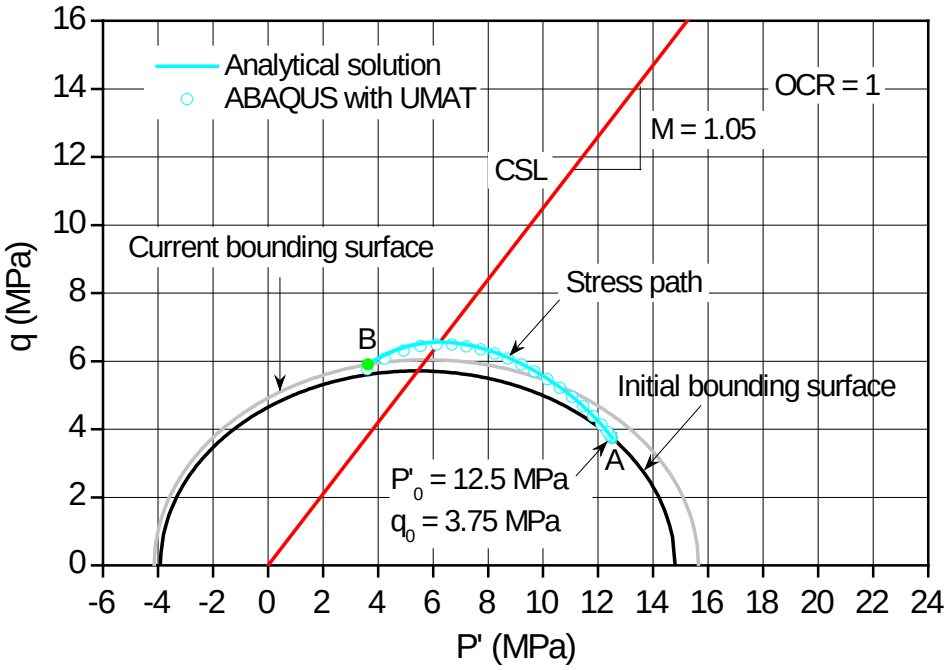

Fig. 6.13. Comparison of drained P'-q stress path at wellbore surface between ABAQUS and exact solutions for OCR = 1, bounding surface model with R = 2.72

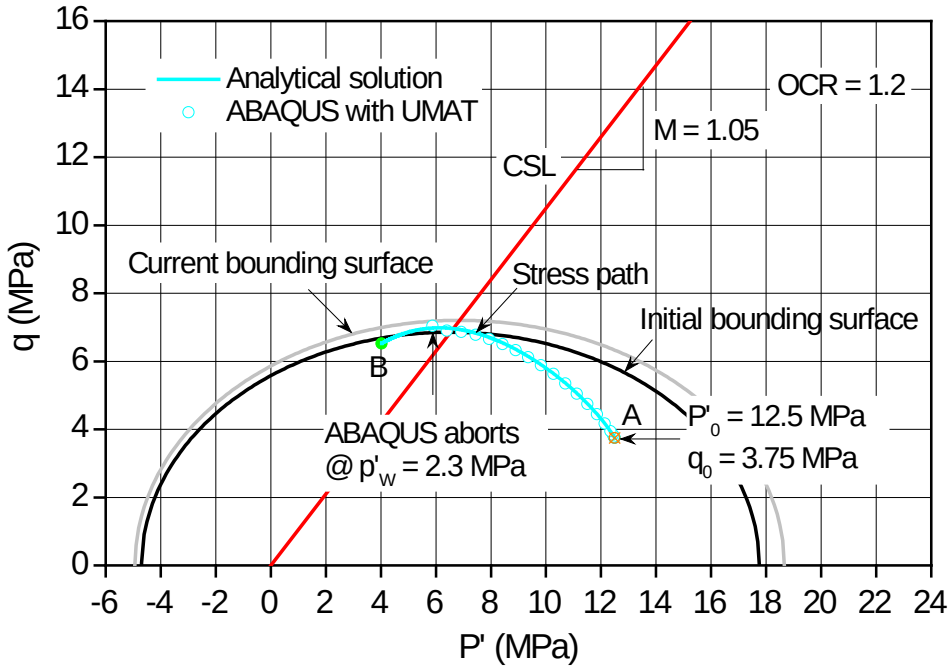

Fig. 6.14. Comparison of drained P'-q stress path at wellbore surface between ABAQUS and exact solutions for OCR = 1.2, bounding surface model with R = 2.72

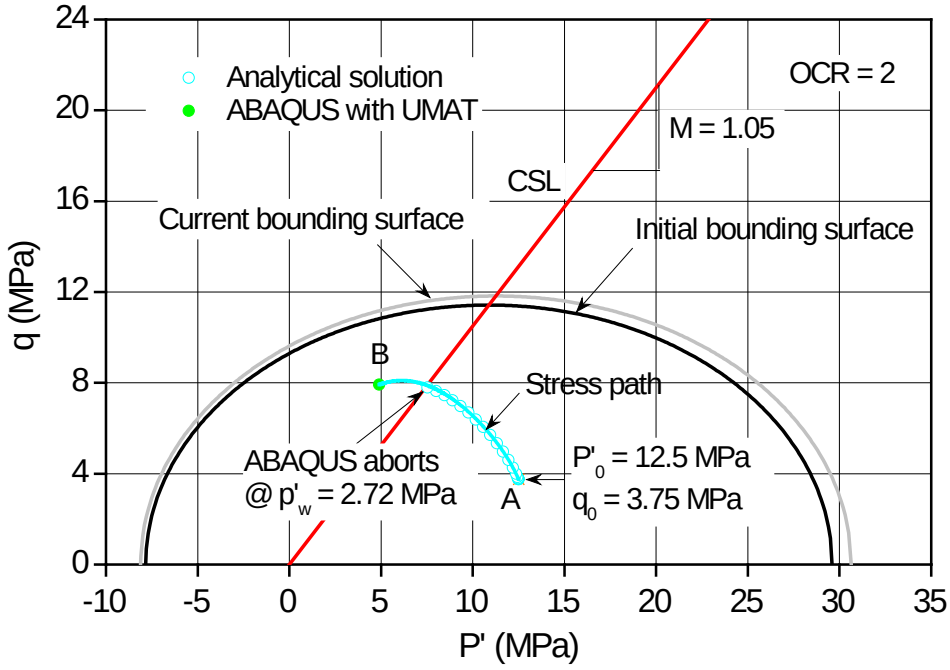

Fig. 6.15. Comparison of drained P'-q stress path at wellbore surface between ABAQUS and exact solutions for OCR = 2, bounding surface model with R = 2.72

the bounding surface constitutive model. Comparisons between the numerical and exact analytical solutions in general show excellent agreement, which therefore justifies the accuracy of the proposed analytical method, and in turn indicates the capability of ABAQUS in handling the wellbore drilling problem involving the critical state plasticity as well as the validity of the UMAT code written for the boundary surface model. However, under some circumstances, ABAQUS suffers from the convergence and stability problems and tend to terminate the analyses before the target (zero) wellbore pressure can be reached. The extension of the current numerical simulations will be a trivial matter to deal with the more realistic situations including the impacts of wellbore inclination and the in situ stress anisotropy.

CHAPTER 7
APPLICATIONS

7.1 Introduction

This chapter is dedicated to the applications of the analytical solutions developed in previous chapters, with main attention focused on the prediction of critical mud pressure required to maintain the wellbore stability. For illustration purpose, only the undrained condition has been considered for the four plasticity models, i.e., the strain hardening Drucker-Prager, strain hardening Mohr-Coulomb, modified Cam Clay, and bounding surface models.

7.2 Critical Mud Pressure

The critical mud pressure $p_{mud,cr}$ could be defined in three different ways depending on the stability criterion used for the wellbore design. The first criterion based on the elastic theory is a conventional one which assumes that the wellbore will approach collapse condition once the yielding criterion is satisfied anywhere in the rocks. With reference to this criterion the critical mud pressure therefore must correspond to the wellbore pressure for which the plastic deformation begins to take place at the wellbore surface. The other two criteria require the analysis of the wellbore instability as an

elastoplastic problem (Charlez, 1997; Yu, 2000), as is elaborated in this dissertation. The wellbore is regarded as unstable either when the borehole surface reaches the failure state (failure yield surface in Drucker-Prager and Mohr-Coulomb models or critical state in the modified Cam Clay and bounding surface models) or when the inward borehole displacement is too large to satisfy the allowable deformation criterion, the latter probably resulting from the consideration of the casing design.

Recall now that the wellbore drilling curves plotting the reduced wellbore pressure as a function of the contracted wellbore radius, from the elastic phase to elastoplastic or even failure phase of the deformation, have been presented in Figs. 2.5, 3.3, 4.4, and 5.4 for the four typical plasticity models considered. As a consequence, the critical mud pressure $p_{mud\,,cr}$ can be directly obtained from these curves for the first and third (allowable displacement) stability criteria. The value of $p_{mud\,,cr}$ corresponding to the second stability criterion (wellbore surface reaching the critical state), however, needs to be determined from the associated critical state conditions.

Table 7.1-7.4 compares the calculated results of $p_{mud\,,cr}$ using the strain hardening Drucker-Prager, strain hardening Mohr-Coulomb, modified Cam Clay, and bounding surface models, based on the three stability criteria mentioned above. The rock parameters used in the analyses are the same as those listed in Tables 2.1, 3.1, 4.1, and 5.1. In all these tables two strain values of 2% and 5% at the wellbore surface have been identified as controlling thresholds. This follows from the practical consideration that the tolerance for the maximum inward borehole displacement is usually somewhere between 2% and 5% of the wellbore radius (Charlez & Heugas, 1991; Charlez, 1997). Note that here the borehole surface strain is defined as $\varepsilon = \frac{a_0 - a}{a_0}$.

Table 7.1. Predicted $p_{mud,cr}$ using three different stability criteria, strain hardening Drucker -Prager model

Elastic analysis	Allowable deformation $\varepsilon = 2\%$	Allowable deformation $\varepsilon = 5\%$	Wellbore surface reaches critical state
17.69 MPa ($\varepsilon = 0.6\%$)	10.64 MPa	-2.64 MPa	-1210.72 MPa ($\varepsilon = 80\%$)

Table 7.2. Predicted $p_{mud,cr}$ using three different stability criteria, strain hardening Mohr-Coulomb model

Elastic analysis	Allowable deformation $\varepsilon = 2\%$	Allowable deformation $\varepsilon = 5\%$	Wellbore surface reaches critical state
18.55 MPa ($\varepsilon = 0.45\%$)	11.06 MPa	-1.48 MPa	-1062.94 MPa ($\varepsilon = 80\%$)

Table 7.3. Predicted $p_{mud,cr}$ using three different stability criteria, Modified Cam Clay model

OCR	Elastic analysis	Allowable deformation $\varepsilon = 2\%$	Allowable deformation $\varepsilon = 5\%$	Wellbore surface reaches critical state
1	21.25 MPa ($\varepsilon = 0$)	13.36 MPa	9.79 MPa	3.14 MPa ($\varepsilon = 24\%$)
1.2	18.25 MPa ($\varepsilon = 0.39\%$)	11.95 MPa	7.79 MPa	-0.07 MPa ($\varepsilon = 25\%$)
3	11.76 MPa ($\varepsilon = 1.37\%$)	8.08 MPa	-1.04 MPa	-17.80 MPa ($\varepsilon = 26\%$)
5	7.83 MPa ($\varepsilon = 2.07\%$)	8.27 MPa	-4.87 MPa	-33.51 MPa ($\varepsilon = 32\%$)

Table 7.4. Predicted $p_{mud,cr}$ using three different stability criteria, bounding surface model

OCR	Elastic analysis	Allowable deformation $\varepsilon = 2\%$	Allowable deformation $\varepsilon = 5\%$	Wellbore surface reaches critical state
1	21.25 MPa ($\varepsilon = 0$)	13.34 MPa	9.50 MPa	2.96 MPa ($\varepsilon = 18\%$)
1.2	21.25 MPa ($\varepsilon = 0$)	13.12 MPa	9.00 MPa	0.55 MPa ($\varepsilon = 25\%$)
3	21.25 MPa ($\varepsilon = 0$)	12.48 MPa	7.58 MPa	-7.46 MPa ($\varepsilon = 35\%$)
5	21.25 MPa ($\varepsilon = 0$)	11.32 MPa	5.10 MPa	-27.62 MPa ($\varepsilon = 53\%$)

From Tables 7.1-7.4, it is observed that for all the four plasticity models adopted, a very large strain at the wellbore surface (contraction) must have been mobilized before the wellbore surface finally reach the failure or critical state, and therefore the critical state-based stability criterion is not controlling. Of course, which stability criterion, i.e., wellbore deformation exceeding the allowable limit or wellbore stress reaching the critical state, will control the design will be dependent on the actual rock properties. In spite of this, the values of the critical mud pressure based on the elasticity theory are always well above those predicted from the elastoplastic analyses, indicating that neglect of the elastoplastic feature of rock formations does lead to a substantial overestimation of the critical mud pressure. Tables 7.3 and 7.4 also show that the predicted $p_{mud\,,cr}$ in general decreases with the overconsolidation ratio, which is reasonably expected as the higher the value of OCR, the stiffer the rock. The only exception is the predicted value of

$p_{mud,cr} = 8.27$ MPa pertaining to the 2% displacement criterion for the modified Cam Clay model with $OCR = 5$, which is found slightly greater than the one of 8.08 MPa for the case of $OCR = 3$. This is probably because in the former ($OCR = 5$) the rock formation still behaves elastically corresponding to the allowable deformation of 2% and it has smaller shear modulus of $G_0 = 325$ MPa. Note that for the normally consolidated modified Cam Clay formation ($OCR = 1$) and for all cases of the bounding surface model, the material points around the wellbore harden plastically immediately after the wellbore pressure drops below the in situ horizontal stress σ_h, so the critical mud pressure from the elastic analysis is $p_{mud,cr} = \sigma_h = 21.25$ MPa.

7.3 Summary

As an application to the wellbore instability analysis, the analytical elastoplastic solutions developed for the wellbore drilling problem has been used to predict the critical mud pressure in this chapter. Two types of stability criteria, i.e., wellbore displacement exceeding the allowable limit or wellbore stress reaching the critical state, have been considered in conjunction with the elastoplastic analysis. Comparison with the elastic results shows that ignoring the elastoplastic feature of the rock formations gives conservative solutions and would lead to a substantial overestimation of the critical mud pressure (density).

CHAPTER 8
CONCLUDING REMARKS

8.1 Conclusions

This research develops a rigorous analytical approach for solving the wellbore stability problem drilled in elastoplastic rock formations. The key step in the formulation of the wellbore boundary value problem is to establish an incremental relationship between the effective radial, tangential, and vertical stresses and the corresponding stain components, i.e., the elastoplastic constitutive equations, and then reduce them to a set of differential equations valid for any material point in the plastic zone. For undrained condition, the three stresses can be directly solved from these governing differential equations as an initial value problem, the excess pore pressure then being determined from the radial equilibrium equation. Whereas for the drained condition, the Eulerian radial equilibrium equation must be first transformed into an equivalent one in Lagrangian description, which can be accomplished with the introduction of an auxiliary variable. This transformed equation, together with the aforementioned elastoplastic constitutive relation, again constitute a set of differential equations. The three stress components as well as the volumetric strain or specific volume thus can be readily solved.

In this dissertation various elastoplastic models including the strain hardening

Drucker-Prager and Mohr-Coulomb models as well as the critical state based modified Cam Clay and bounding surface models have been considered to cover a wide range of rock formations. Using the solution scheme described above, it is found that the wellbore drilling analyses involving different types of plasticity models can be performed in a theoretically consistent way. The computed stress distributions and in particular the stress paths capture well the anticipated elastoplastic to failure behaviour of the rocks surrounding the wellbore, the solutions thus is able to contribute to better prediction and design of the wellbore instability problems.

Regarding the critical state elastoplastic models, finite element numerical simulations have also been carried out for the drained wellbore problem using the commercial software ABAQUS. Of importance, a user defined material subroutine (UMAT) for the bounding surface model is coded with FORTRAN following the widely used return mapping algorithm and implemented into the ABAQUS finite element models. The predictions from the analytical solutions and the ABAQUS analyses are generally in excellent agreement for both modified Cam Clay and bounding surface models, though under some circumstances, ABAQUS may break down before the target wellbore pressure can finally be reached.

8.2 Recommendations

Although various types of elastoplastic models have been covered, the rock formations in the present work are basically treated as isotropic materials. However, mechanical anisotropy has been long recognized for soils and rocks, due to the fabric orientation developed during their deposition and the subsequent alteration induced by the applied loading (Banerjee & Butterfield, 1985). In the future, the wellbore stability

analysis may be extended to taking into account the anisotropic elastoplastic behaviour of rocks. The anisotropic modified Cam Clay and bounding surface models proposed, respectively, by Dafalias (1987) and Banerjee & Yousif (1986), the yield surfaces of which consist of rotated and distorted ellipses and the degree of rotation/distortion is determined by the introduced variables, might be adopted for further investigation.

As shown in Chapter 6, when conducting the numerical simulations for the wellbore drilling problem with the critical state models, computational difficulties could occur under certain conditions accompanied by the termination of ABAQUS analyses. The author is aware that this happens because of the convergence and stability issues that frequently arise in the nonlinear finite element analysis, however, the reason has not been fully understood and this aspect should be addressed more thoroughly and improved in future studies.

For the sandstone-like formations, it will be useful to compare the present analytical results using macroscale material properties with the numerical predictions from the discrete element method (DEM) at the microscopic level (Itasca, 2004). The exact solutions will serve as good benchmarks to evaluate the capability of DEM in handling the elastoplastic wellbore drilling problems.

Finally, it is recommended that the wellbore stability analyses be extended to the more realistic and general situation of fully anisotropic in situ stress state, both analytically and numerically. Also, given the three phase nature of the reservoir formations (oil, gas, and rock skeleton), it will be desirable to make a further extension of the current solutions to unsaturated porous media.

REFERENCES

ABAQUS (2011). *ABAQUS user's manual, version 6.9-EF*. Hibbitt, Karlsson & Sorensen, Inc.

Abousleiman, N. Y. & Cui, L. (1998). Poroelastic solutions in transversely isotropic media for wellbore and cylinder. *Int. J. Solids Struct.*, **35**, 4905-4929.

Abousleiman, N. Y. & Cui, L. (2000). The theory of anisotropic poroelasticity with applications. In *Modeling in Geomechanics*, Eds: Zaman, M., Gioda, G. & Booker, J. R., Chichester: John Wiley & Sons, 559-593.

Al-Wardy, W. & Urdaneta, O. P. (2010). Geomechanical modeling for wellbore stability during drilling Nahr Umr shales in a field in petroleum development Oman. *Paper SPE 138214 presented at the Abu Dhabi International Petroleum Exhibition & Conference*, Abu Dhabi, UAE, 1-4, November.

Banerjee, P. K. & Butterfield, R. (1985). *Developments in soil mechanics and foundation engineering, Vol. 2*. Elsevier Applied Science Publishers.

Banerjee, P. K. & Yousif, N. B. (1986). A plasticity model for the mechanical behavior of anisotropically consolidated clay. *Int. J. Numer. Anal. Meth. Geomech.*, **16**, 521-541.

Bigoni, D. & Laudiero, F. (1989). The quasi-static finite cavity expansion in a non-standard elasto-plastic medium. *Int. J. Mech. Sci.*, **31**, No. 11/12, 825-837.

Bishop, R. F., Hill, R. & Mott, N. F. (1945). The theory of indentation and hardness tests. *Proc. Phys. Soc.*, **57**, 147-159.

Bobet, A. (2010). Characteristic curves for deep circular tunnels poroplastic rock. *Roc Mech. Rock Eng.*, **43**, 185-200.

Borja, R. I. & Lee, S. R. (1990). Cam Clay plasticity, part I: Implicit integration of constitutive relations. *Comput. Meth. Appl. Mech. Eng*., **78**, 49-72.

Bradley, W. B. (1979). Failure of inclined boreholes. *J. Energy Resour. Tech., ASME*, **101**, 232-239.

Brown, E. T., Bray, J. W., Ladanyi, B. & Hoek, E. (1983). Ground response curves for rock tunnels. *J. Geotech. Eng. Div., ASCE*, **109**, No. 1, 15-39.

Cao, L. F., Teh, C. I. & Chang, M. F. (2001). Undrained cavity expansion in modified Cam clay I: Theoretical analysis. *Geotechnique*, **51**, No. 4, 323-334.

Carter, J. P. (1978). *CAMFE: A computer program for the analysis of a cylindrical cavity expansion in soil*. Report CUED/C-Soils TR52, Department of Engineering, University of Cambridge.

Carter, J. P., Booker, J. R. & Yeung, S. K. (1986). Cavity expansion in cohesive frictional soils. *Geotechnique*, **36**, No. 3, 345-358.

Chadwick, P. (1959). The quasi-static expansion of a spherical cavity in metals and ideal soils. *Q. J. Mech. Appl. Math.*, **12**, No. 52-71.

Charlez, P. A. (1991). *Rock mechanics Vol. 1: Theoretical Fundamentals*. Editions Technip, Paris.

Charlez, P. A. (1994). The impact of constitutive laws on wellbore stability: A general review. *SPE/ISRM Rock Mechanics in Petroleum Engineering Conference*, 29-31. Delft, The Netherlands.

Charlez, P. A. (1997). *Rock mechanics Vol. 2: petroleum application*. Editions Technip, Paris.

Charlez, P. A. & Heugas, O. (1991). Evaluation of optimal mud weight in soft shale

levels. *Rock Mechanics as a Multidisciplinary Science* (Editor: Roegiers, J. C.), 1005-1014. Balkema, Rotterdam.

Charlez, P. A. & Roatesi, S. (1999). A fully analytical solution of the wellbore stability problem under undrained conditions using a linearized Cam-Clay model. *Oil Gas Sci. Tech.*, **54**, No. 5, 551-563.

Chen, S. L. & Abousleiman, N. Y. (2012a). Exact undrained elastoplastic solution for cylindrical cavity expansion in modified Cam Clay soil. *Geotechnique*, **62**, No. 5, 447-456.

Chen, S. L. & Abousleiman, N. Y. (2012b). Exact drained solution for cylindrical cavity expansion in modified Cam Clay soil. *Geotechnique,* ahead of print, doi:10.1680/geot.11.P.088.

Chen, S. L., Abousleiman, N. Y. & Muraleetharan, K. K. (2012). A closed-form elastoplastic solution for the wellbore problem in strain hardening/softening rock formations. *Int. J. Geomech.,* **12**, No. 4, 494-507.

Collins, I. F., Pender, M. J. & Wang, Y. (1992). Cavity expansion in sands under drained loading conditions. *Int. J. Numer. Anal. Meth. Geomech.*, **16**, 3-23.

Collins, I. F. & Stimpson, J. R. (1994). Similarity solutions for drained and undrained cavity expansions in soils. *Geotechnique,* **44**, No. 1, 21-34.

Collins, I. F. & Yu, H. S. (1996). Undrained cavity expansions in critical state soils. *Int. J. Numer. Anal. Meth. Geomech.*, **20**, 489-516.

Cui, L., Abousleiman, Y., Cheng, A. H-D. & Roegiers, J.-C. (1999). Time-dependent failure analysis of inclined boreholes in fluid-saturated formations. *J. Energy Resour. Tech., ASME*, **121**, 31-39.

Cui, L., Cheng, A. H-D. & Abousleiman, Y. (1997). Poroelastic solution for an inclined borehole. *J. Appl. Mech., ASME,* **64**, 32-38.

Dafalias, Y. F. (1987). An anisotropic critical state clay plasticity model. *Constitutive laws for engineering materials: theory and applications* (Editors: Desai, C. S., Krempl, E., Kiousis, P. D., and Kundu, T.), **1**, 513-521.

Dafalias, Y. F. & Herrmann, L. R. (1980). A bounding surface soil plasticity model. *Proceedings of the International Symposium on Soils Under Cyclic and Transient Loading* (Editors: Pande, G. N. and Zienkiewicz, O. Z.), 335-345. Balkema, Rotterdam.

Dafalias, Y. F. & Herrmann, L. R. (1982). Bounding surface formulation of soil plasticity. *Soil Mechanics-Transient and Cyclic Loads* (Editors: Pande, G. N. and Zienkiewicz, O. Z.), 253-282. Wiley, Chichester.

Davis, R. O. & Selvadurai, A. P. S. (2002). *Plasticity and geomechanics*. Cambridge, UK: Cambridge University Press.

Diwan, P., Pandey, B. P.& Gupta, D. K. (2011). A fresh look at wellbore stability analysis to sustainable development of natural resources: issues and opportunities. *International Journal of Science Technology & Management*, **2**, No. 1, 55−63.

Dunne, F. & Petrinic, N. (2005). *Introduction to computational plasticity*. Oxford University Press.

Durban, D. & Fleck, N. A. (1997). Spherical cavity expansion in a Drucker-Prager solid. *J. Appl. Mech., ASME,* **64**, 743-750.

Durban, D. & Kubi, M. (1992). A general solution for the pressurized elastoplastic tube. *J. Appl. Mech.*, **59**, No. 1, 20-26.

Dusseault, M. B. (1994). Analysis of borehole stability. *Computer methods and advances in geomechancis* (Editors: Siriwardane and Zaman), 125-137. Balkema.

Gibson, R. E. & Anderson, W. F. (1961). In situ measurement of soil properties with the pressuremeter. *Civ. Engng Public Works Rev.* **56**, 615-618.

Graziani, A. & Ribacchi, R. (1993). Critical conditions for a tunnel in a strain softening rock. *Assessment and Prevention of Failure Phenomena in Rock Engineering*, 199-204. Istanbul. A. A. Balkema.

Hashash, Y. M. A. & Whittle, A. J. (1992). Integration of the modified Cam-clay model in nonlinear finite element analysis. *Comput. Geotech*., **14**, 59-83.

Helwany, S. (2007). *Applied soil mechanics with ABAQUS applications*. John Wiley & Son, Inc.

Hicher, P. Y. & Shao, J. F. (2008). *Constitutive modeling of soils and rocks*. John Wiley & Sons, Inc.

Hill, R. (1950). *The mathematical theory of plasticity*. Oxford University Press.

Hoang, S. (2011). *Poroviscoelasticity and analytical solutions of selected problems in engineering*. PhD thesis, University of Oklahoma, USA.

Hughes, J. M. O., Wroth, C. P. & Windle, D. (1977). Pressuremeter tests in sands. *Geotechnique*, **27**, No. 4, 455-477.

iPMI. (2011). *PBORE-3D: Poromechanics wellbore stability simulator*. integrated PoroMechanics Institute, University of Oklahoma.

Itasca. (2004). *PFC2D 3.10 particle flow code in two dimensions, theory and background volume*. Minneapolis, Minnesota.

Jiang, M. J. & Sun, Y. G. (2011). Cavity expansion analyses of crushable granular

materials with state-dependent dilatancy. *Int. J. Numer. Anal. Meth. Geomech.*, **36**, 723-742.

Kaliakin, V. N., Dafalias, Y. F. & Herrmann, L. R. (1987). *Time dependent bounding surface model for isotropic cohesive soils, Note for a short course*. Tucson, Arizona.

Kavvadas, M. (1982). *Nonlinear consolidation around driven piles in clays*. PhD thesis, Massachusetts Institute of Technology.

Manzari, M. T. & Nour, M. A. (1997). On implicit integration of bounding surface plasticity models. *Comput. & Struct.*, **63**, No. 3, 385-395.

Matsuoka, T. & Nakai, K. (1974). Stress-deformation and stress strain theory for cohesionless soil under three different principal stresses. *Proc. Japan. Soc. Civil Engineers*, **232**, 59-70.

Menetrey, Ph. & Willam, K. J. (1995). Triaxial failure criterion for concrete and its generalization. *ACI. Structures Journal*, **92**, 311-318.

Ortiz, M. & Simo, J. C. (1986). An analysis of a new class of integration algorithms for elastoplastic constitutive relations. *Int. J. Num. Meth. Eng.*, **23**, 353–366

Neto, E. A. S., Peric, D. & Owen, D. R. J. (2008). *Computational methods for plasticity: theory and applications*. John Wiley & Sons Ltd.

Nova, R. (2010). *Soil mechanics*. John Wiley & Sons, Inc.

Palmer, A. C. & Mitchell, R.J. (1972). Plane-strain expansion of a cylindrical cavity in clay. *Stress-strain behaviour of soils: proceedings of the Roscoe Memorial Symposium*, Cambridge, pp. 588-599.

Papanastasiou, P. & Durban, D. (1997). Elastoplastic analysis of cylindrical cavity problems in geomaterials. *Int. J. Numer. Anal. Meth. Geomech.*, **21**, 133-149.

Papanastasiou, P. & Zervos, A. (2004). Wellbore stability analysis: from linear elasticity to postbifurcation modeling. *Int. J. Geomech., ASCE*, **4**, No. 1, 2-12.

Potts, D. M. & Zdravkovic, L. (1999). *Finite element analysis in geotechnical engineering: theory*. Thomas Telford Ltd.

Potts, D. M. & Zdravkovic, L. (2000). Some pitfalls when using Modified Cam clay. *Soil-structure interaction in urban civil engineering*, Editor(s): Avdelas, European Commision.

Prevost, J. H. & Hoeg, K. (1975). Analysis of pressuremeter in strain strain softening soil. *J. Geotech. Engng ASCE*, **101**, No. 8, 717-732.

Randolph, M. F., Carter, J. P. & Wroth, C. P. (1979). Driven piles in clay-the effects of installation and subsequent consolidation. *Geotechnique*, **29**, No. 4, 361-393.

Reed, M. B. (1988). The influence of out-of-plane stress on a plane strain problem in rock mechanics. *Int. J. Numer. Anal. Meth. Geomech.*, **12**, 173-181.

Roscoe, K. H. & Burland, J. B. (1968). On the generalized stress-strain behaviour of 'wet' clay. *Engineering Plasticity*, 535-609, Cambridge Univ. Press.

Russell, A. R. & Khalili, N. (2002). Drained cavity expansion in sands exhibiting particle crushing. *Int. J. Numer. Anal. Meth. Geomech.*, **26**, 323-340.

Russell, A. R. & Khalili, N. (2006). On the problem of cavity expansion in unsaturated soils. *Comput. Mech.*, **37**, No. 4, 311-330.

Salgado, R. & Randolph, M. F. (2001). Analysis of cavity expansion in sand. *Int. J. Geomech.*, **1**, No. 2, 175-192.

Schofield, A. N. & Wroth, C. P. (1968). *Critical state soil mechanics.* McGraw-Hill, England.

Sharan, S. K. (2005). Exact and approximate solutions for displacements around circular openings in elastic-brittle-plastic Hoek-Brown rock. *Int. J. Rock Mech. Min. Sci.*, **42**, 542-549.

Sheng, D., Sloan, S. W., & Yu, H. S. (2000). Aspects of finite element implementation of critical state models. *Comput. Mech.*, **26**, 185-196.

Silvestri, V. & Abou-Samra, G. (2011). Application of the exact constitutive relationship of modified Cam clay to the undrained expansion of a spherical cavity. *Int. J. Numer. Anal. Meth. Geomech.*, **35**, No. 1, 53-66.

Silvestri, V. & Abou-Samra, G. (2012). Analytical solution for undrained plane strain expansion of a cylindrical cavity in modified cam clay. *Geomechanics and Engineering*, **4**, No. 1, 19-37.

Simo, J. C. & Hughes, T. J. R. (1998). *Computational inelasticity*. Springer.

Sloan, S. W. (1987). Substepping schemes for numerical integration of elasto-plastic stress-strain realations. *Int. J. Num. Meth. Eng.*, **24**, 893-911.

Timoshenko, S. P. & Goodier, J. N. (1970). *Theory of elasticity*. McGraw-Hill Book Company.

Vesic, A. C. (1972). Expansion of cavities in infinite soil mass. *J. Soil Mech. Found. Div., ASCE* **98**, No. SM3, 265-290.

Wang, Y. (1996). Ground response of circular tunnel in poorly consolidated rock. *J. Geotech. Eng. Div., ASCE*, **122**, No. 9, 703-708.

Whittle, A. J. (1987). *A constitutive model for overconsolidated clays with application to the cyclic loading of friction piles*. PhD thesis, Massachusetts Institute of Technology.

Wolfram, S. (2008). *Matehmatica 7.0*. Wolfram Research Inc.

Wood, D. M. (1990). *Soil behaviour and critical state soil mechanics*. Cambridge, UK: Cambridge University Press.

Wood, D. M. (2004). *Geotechnical modelling*. Spon Press, Taylor & Francis Group.

Yu, H. S. (1990). *Cavity expansion theory and its application to the analysis of pressuremeters*. PhD thesis, University of Oxford, UK.

Yu, H. S. (2000). *Cavity expansion methods in geomechancis*. Dordrecht: Kluwer Academic Publishers.

Yu, H. S. (2006). *Plasticity and geotechnics*. Springer.

Yu, H. S. & Houlsby, G. T. (1991). Finite cavity expansion in dilatants soils: loading analysis. *Geotechnique*, **41**, No. 2, 173-183.

Yu, H. S. & Rowe, R. K. (1999). Plasticity solutions for soil behavior around contracting cavities and tunnels. *Int. J. Numer. Anal. Meth. Geomech.*, **23**, 1245-1279.

APPENDIX A

ALGORITHM FOR IMPLICIT INTEGRATION OF BOUNDING SURFACE MODEL

(1) INITIALIZATION

$$\Delta\varepsilon^{p}_{p,n+1} = 0, \quad \Delta e^{p}_{ij,n+1} = 0, \quad \bar{P}'_{C,n+1} = \bar{P}'_{C,n}, \quad \Lambda_{n+1} = 0 \tag{A.1}$$

$$\varrho_{n+1} = \varrho_n \tag{A.2}$$

where ϱ_n is determined from Eq. (6.23h), given by

$$\varrho_n = \frac{-B+\sqrt{B^2-4AC}}{2A} \tag{A.3a}$$

$$A = s_{ij,n}s_{ij,n} + \frac{2}{3}\frac{M^2}{(R-1)^2}P_n'^2 \tag{A.3b}$$

$$B = -\frac{2}{3}\frac{M^2}{(R-1)^2}\frac{2}{R}P_n'\bar{P}'_{C,n} \tag{A.3c}$$

$$C = \frac{2}{3}\frac{M^2}{(R-1)^2}\frac{2-R}{R}\bar{P}'^2_{C,n} \tag{A.3d}$$

and

$$k_{p,n+1} = k_{p,n} \tag{A.4}$$

where, according to Eq. (6.25),

$$k_{p,n} = \frac{T_1}{T_1+T_{21}T_{22}T_{23}} \tag{A.5a}$$

$$T_1 = -\frac{M^4}{(R-1)^4}\bar{P}'_{C,n}\left(\varrho_n P_n' - \frac{\bar{P}'_{C,n}}{R}\right)\left(\frac{2-R}{R}\bar{P}'_{C,n} - \frac{\varrho_n P_n'}{R}\right) \tag{A.5b}$$

$$T_{21} = \frac{M^4}{(R-1)^4}\left(\varrho_n P_n' - \frac{\bar{P}'_{C,n}}{R}\right)^2 + \varrho_n^2\frac{3}{2}s_{ij,n}s_{ij,n} \tag{A.5c}$$

$$T_{22} = hp_a\left(1 + \left|\frac{MP_n'}{\sqrt{(3/2)s_{ij,n}s_{ij,n}}}\right|^m\right) \tag{A.5d}$$

$$T_{23} = \frac{(\varrho_n - 1)\varrho_n P_n^{'} \sqrt{1 + \frac{\frac{3}{2} s_{ij,n} s_{ij,n}}{P_n^{'2}}}}{\varrho_n \bar{P}_{C,n}^{'} - (\varrho_n - 1)\varrho_n P_n^{'} \sqrt{1 + \frac{\frac{3}{2} s_{ij,n} s_{ij,n}}{P_n^{'2}}}} \tag{A.5e}$$

(2) ELASTIC PREDICTION AND PLASTIC ADMISSIBILITY CHECK

$$P_{n+1}^{'} = P_n^{'} e^{\frac{v_n}{\kappa} \Delta\varepsilon_{v,n+1}} \tag{A.6}$$

$$s_{ij,n+1} = s_{ij,n+1} + \frac{3(1-2\nu)}{1+\nu} P_n^{'} \frac{\Delta e_{ij,n+1}}{\Delta\varepsilon_{v,n+1}} \left(e^{\frac{v_n}{\kappa} \Delta\varepsilon_{v,n+1}} - 1 \right) \tag{A.7}$$

IF $f\left(P_{n+1}^{'}, s_{ij,n+1}, \bar{P}_{C,n+1}^{'}\right) < 0$, THEN GO TO **(7)** final stresses (elastic increment), ELSE

(3) PLASTIC CORRECTION

Find the solution vector $\boldsymbol{U}$ by solving 18 simultaneous equations, i.e., Eqs. (6.23a)-(6.23c), (6.23e), (6.23g)-(6.23h), (6.32), and (6.33), using a local (full) Newton scheme:

$$\boldsymbol{U} = \left\{ \Delta\varepsilon_{p,n+1}^{p}, \Delta e_{ij,n+1}^{p}, \bar{P}_{C,n+1}^{'}, \Lambda_{n+1}, P_{n+1}^{'}, s_{ij,n+1}, \varrho_{n+1}, k_{p,n+1} \right\}^T \tag{A.8}$$

The residuals vector:

$$\boldsymbol{R} = \{R_1, R_2, R_3, R_4, R_5, R_6, R_7, R_8\}^T \tag{A.9}$$

where

$$R_1 = P_{n+1}^{'} - P_n^{'} e^{\frac{v_n}{\kappa} (\Delta\varepsilon_{v,n+1} - \Delta\varepsilon_{p,n+1}^{p})} \tag{A.10a}$$

$$R_2 = \Delta\varepsilon_{p,n+1}^{p} - \Lambda_{n+1} \frac{4}{3} \frac{M^2}{(R-1)^2} \left(\varrho_{n+1} P_{n+1}^{'} - \frac{\bar{P}_{C,n+1}^{'}}{R} \right) \tag{A.10b}$$

$$R_3 = s_{ij,n+1} - s_{ij,n} - \frac{3(1-2\nu)}{1+\nu} P_n^{'} \frac{\Delta e_{ij,n+1} - \Delta e_{ij,n+1}^{p}}{\Delta\varepsilon_{v,n+1} - \Delta\varepsilon_{p,n+1}^{p}} \left\{ e^{\frac{v_n}{\kappa} (\Delta\varepsilon_{v,n+1} - \Delta\varepsilon_{p,n+1}^{p})} - 1 \right\} \tag{A.10c}$$

$$R_4 = \Delta e_{ij,n+1}^{p} - 2\Lambda_{n+1} \varrho_{n+1} s_{ij,n+1} \tag{A.10d}$$

$$R_5 = \bar{P}'_{C,n+1} - \bar{P}'_{C,n} e^{\frac{v_n}{\lambda-\kappa}\Delta\varepsilon^p_{p,n+1}} \tag{A.10e}$$

$$R_6 = \varrho^2_{n+1} s_{ij,n+1} s_{ij,n+1} + \frac{2}{3}\frac{M^2}{(R-1)^2}\left(\varrho^2_{n+1} P'^2_{n+1} - \frac{2}{R}\varrho_{n+1} P'_{n+1} \bar{P}'_{C,n+1} + \frac{2-R}{R}\bar{P}'^2_{C,n+1}\right) \tag{A.10f}$$

$$R_7 = \varrho_{n+1} + \frac{\varrho_n k_{p,n+1} \frac{\bar{P}'_{C,n+1}}{\bar{P}'_{C,n}}}{\varrho_n - k_{p,n+1} - \varrho_n \frac{\bar{P}'_{C,n+1}}{\bar{P}'_{C,n}}} \tag{A.10g}$$

$$R_8 = k_{p,n+1} - \frac{X_1}{X_1 + X_{21} X_{22} X_{23}} \tag{A.10h}$$

IF $|\boldsymbol{R}|$ less than tolerance, THEN GO TO **(7)** final stresses (converged solution), ELSE

(4) CONSISTENT TANGENT MATRIX

Calculate consistent tangent matrix $\boldsymbol{T} = \frac{\partial \boldsymbol{R}}{\partial \boldsymbol{U}}$ for the local Newton iteration

$$\frac{\partial R_1}{\partial \Delta\varepsilon^p_{p,n+1}} = \frac{v_n}{\kappa} P'_n e^{\frac{v_n}{\kappa}(\Delta\varepsilon_{v,n+1} - \Delta\varepsilon^p_{p,n+1})}, \quad \frac{\partial R_1}{\partial \Delta e^p_{ij,n+1}} = \mathbf{0} \tag{A.11a}$$

$$\frac{\partial R_1}{\partial \bar{P}'_{C,n+1}} = 0, \quad \frac{\partial R_1}{\partial \Lambda_{n+1}} = 0, \quad \frac{\partial R_1}{\partial P'_{n+1}} = 1, \tag{A.11b}$$

$$\frac{\partial R_1}{\partial s_{ij,n+1}} = \mathbf{0}, \quad \frac{\partial R_1}{\partial \varrho_{n+1}} = 0, \quad \frac{\partial R_1}{\partial k_{p,n+1}} = 0 \tag{A.11c}$$

$$\frac{\partial R_2}{\Delta\partial \varepsilon^p_{p,n+1}} = 1, \quad \frac{\partial R_2}{\partial \Delta e^p_{ij,n+1}} = \mathbf{0}, \quad \frac{\partial R_2}{\partial \bar{P}'_{C,n+1}} = \Lambda_{n+1}\frac{4}{3}\frac{M^2}{R(R-1)^2} \tag{A.12a}$$

$$\frac{\partial R_2}{\partial \Lambda_{n+1}} = -\frac{4}{3}\frac{M^2}{(R-1)^2}\left(\varrho_{n+1} P'_{n+1} - \frac{\bar{P}'_{C,n+1}}{R}\right) \tag{A.12b}$$

$$\frac{\partial R_2}{\partial P'_{n+1}} = -\Lambda_{n+1}\frac{4}{3}\frac{M^2}{(R-1)^2}\varrho_{n+1} P'_{n+1}, \quad \frac{\partial R_2}{\partial s_{ij,n+1}} = \mathbf{0}, \tag{A.12c}$$

$$\frac{\partial R_2}{\partial \varrho_{n+1}} = -\Lambda_{n+1}\frac{4}{3}\frac{M^2}{(R-1)^2} P'_{n+1}, \quad \frac{\partial R_2}{\partial k_{p,n+1}} = 0 \tag{A.12d}$$

$$\frac{\partial R_3}{\partial \Delta\varepsilon^p_{p,n+1}} = 0 \tag{A.13a}$$

$$\frac{\partial R_3}{\partial \Delta e^p_{ij,n+1}} = -\frac{3(1-2\nu)}{1+\nu}\frac{P'_n}{\Delta\varepsilon_{v,n+1}-\Delta\varepsilon^p_{p,n+1}}\left\{e^{\frac{v_n}{\kappa}(\Delta\varepsilon_{v,n+1}-\Delta\varepsilon^p_{p,n+1})}-1\right\}\delta_{ki}\delta_{lj} \tag{A.13b}$$

$$\frac{\partial R_3}{\partial \bar{P}'_{C,n+1}} = 0, \quad \frac{\partial R_3}{\partial \Lambda_{n+1}} = 0, \quad \frac{\partial R_3}{\partial P'_{n+1}} = 1, \tag{A.13c}$$

$$\frac{\partial R_3}{\partial s_{ij,n+1}} = \delta_{ki}\delta_{lj}, \quad \frac{\partial R_3}{\partial \varrho_{n+1}} = 0, \quad \frac{\partial R_3}{\partial k_{p,n+1}} = 0 \tag{A.13d}$$

$$\frac{\partial R_4}{\Delta\partial \varepsilon^p_{p,n+1}} = 1, \quad \frac{\partial R_4}{\partial \Delta e^p_{ij,n+1}} = \delta_{ki}\delta_{lj}, \quad \frac{\partial R_4}{\partial \bar{P}'_{C,n+1}} = 0 \tag{A.14a}$$

$$\frac{\partial R_4}{\partial \Lambda_{n+1}} = -2\varrho_{n+1}s_{ij,n+1}, \quad \frac{\partial R_4}{\partial P'_{n+1}} = 0, \quad \frac{\partial R_4}{\partial s_{ij,n+1}} = -2\Lambda_{n+1}\varrho_{n+1}\delta_{ki}\delta_{lj} \tag{A.14b}$$

$$\frac{\partial R_4}{\partial \varrho_{n+1}} = -2\Lambda_{n+1}s_{ij,n+1}, \quad \frac{\partial R_4}{\partial k_{p,n+1}} = 0 \tag{A.14c}$$

$$\frac{\partial R_5}{\partial \Delta\varepsilon^p_{p,n+1}} = -\frac{v_n}{\lambda-\kappa}\bar{P}'_{C,n}e^{\frac{v_n}{\lambda-\kappa}\Delta\varepsilon^p_{p,n+1}}, \quad \frac{\partial R_5}{\partial \Delta e^p_{ij,n+1}} = \mathbf{0}, \quad \frac{\partial R_5}{\partial \bar{P}'_{C,n+1}} = 1 \tag{A.15a}$$

$$\frac{\partial R_5}{\partial \Lambda_{n+1}} = 0, \quad \frac{\partial R_5}{\partial P'_{n+1}} = 0, \quad \frac{\partial R_5}{\partial s_{ij,n+1}} = \mathbf{0}, \tag{A.15b}$$

$$\frac{\partial R_5}{\partial \varrho_{n+1}} = 0, \quad \frac{\partial R_5}{\partial k_{p,n+1}} = 0 \tag{A.15c}$$

$$\frac{\partial R_6}{\partial \Delta\varepsilon^p_{p,n+1}} = 0, \quad \frac{\partial R_6}{\partial \Delta e^p_{ij,n+1}} = \mathbf{0} \tag{A.16a}$$

$$\frac{\partial R_6}{\partial \bar{P}'_{C,n+1}} = \frac{2}{3}\frac{M^2}{(R-1)^2}\left\{-\frac{2}{R}\varrho_{n+1}P'_{n+1}+\frac{2(2-R)}{R}\bar{P}'_{C,n+1}\right\}, \quad \frac{\partial R_6}{\partial \Lambda_{n+1}} = 0 \tag{A.16b}$$

$$\frac{\partial R_6}{\partial P'_{n+1}} = +\frac{2}{3}\frac{M^2}{(R-1)^2}\left(2\varrho^2_{n+1}P'_{n+1}-\frac{2}{R}\varrho_{n+1}\bar{P}'_{C,n+1}\right) \tag{A.16c}$$

$$\frac{\partial R_6}{\partial s_{ij,n+1}} = \begin{cases} 2\varrho^2_{n+1}s_{ij,n+1} & (i=j) \\ 4\varrho^2_{n+1}s_{ij,n+1} & (i\neq j) \end{cases} \tag{A.16d}$$

$$\frac{\partial R_6}{\partial \varrho_{n+1}} = 2\varrho_{n+1}s_{ij,n+1}s_{ij,n+1}+\frac{2}{3}\frac{M^2}{(R-1)^2}\left(2\varrho_{n+1}P'^2_{n+1}-\frac{2}{R}P'_{n+1}\bar{P}'_{C,n+1}\right) \tag{A.16e}$$

$$\frac{\partial R_6}{\partial k_{p,n+1}} = 0 \tag{A.16f}$$

$$\frac{\partial R_7}{\partial \Delta\varepsilon^p_{p,n+1}} = 0, \quad \frac{\partial R_7}{\partial \Delta e^p_{ij,n+1}} = \mathbf{0} \tag{A.17a}$$

$$\frac{\partial R_7}{\partial \bar{P}'_{C,n+1}} = \frac{\left(\varrho_n - k_{p,n+1} - \varrho_n \frac{\bar{P}'_{C,n+1}}{\bar{P}'_{C,n}}\right)\frac{\varrho_n k_{p,n+1}}{\bar{P}'_{C,n}} + \varrho_n^2 k_{p,n+1}\frac{\bar{P}'_{C,n+1}}{\bar{P}'^2_{C,n}}}{\left(\varrho_n - k_{p,n+1} - \varrho_n \frac{\bar{P}'_{C,n+1}}{\bar{P}'_{C,n}}\right)^2} \tag{A.17b}$$

$$\frac{\partial R_7}{\partial \Lambda_{n+1}} = 0, \quad \frac{\partial R_7}{\partial P'_{n+1}} = 0, \quad \frac{\partial R_7}{\partial s_{ij,n+1}} = \mathbf{0}, \quad \frac{\partial R_7}{\partial \varrho_{n+1}} = 1 \tag{A.17c}$$

$$\frac{\partial R_7}{\partial k_{p,n+1}} = \frac{\left(\varrho_n - k_{p,n+1} - \varrho_n \frac{\bar{P}'_{C,n+1}}{\bar{P}'_{C,n}}\right)\frac{\varrho_n \bar{P}'_{C,n+1}}{\bar{P}'_{C,n}} + \varrho_n k_{p,n+1}\frac{\bar{P}'_{C,n+1}}{\bar{P}'_{C,n}}}{\left(\varrho_n - k_{p,n+1} - \varrho_n \frac{\bar{P}'_{C,n+1}}{\bar{P}'_{C,n}}\right)^2} \tag{A.17d}$$

$$\frac{\partial R_8}{\partial \Delta \varepsilon^p_{p,n+1}} = 0, \quad \frac{\partial R_8}{\partial \Delta e^p_{ij,n+1}} = \mathbf{0} \tag{A.18a}$$

$$\frac{\partial R_8}{\partial \bar{P}'_{C,n+1}} = -\frac{(X_1 + X_{21}X_{22}X_{23})Y_1 - X_1(Y_1 + X_{21}X_{22}Y_{23} + X_{21}Y_{22}X_{23} + Y_{21}X_{22}X_{23})}{(X_1 + X_{21}X_{22}X_{23})^2} \tag{A.18b}$$

where

$$Y_1 = \frac{\partial X_1}{\partial \bar{P}'_{C,n+1}} = -\frac{M^4}{(R-1)^4}\left\{\left(\varrho_{n+1}P'_{n+1} - \frac{2\bar{P}'_{C,n+1}}{R}\right)\left(\frac{2-R}{R}\bar{P}'_{C,n+1} - \frac{\varrho_{n+1}P'_{n+1}}{R}\right) + \left(\bar{P}'_{C,n+1}\varrho_{n+1}P'_{n+1} - \frac{\bar{P}'^2_{C,n+1}}{R}\right)\frac{2-R}{R}\right\} \tag{A.18b-1}$$

$$Y_{21} = \frac{\partial X_{21}}{\partial \bar{P}'_{C,n+1}} = 2\frac{M^4}{(R-1)^4}\left(\varrho_{n+1}P'_{n+1} - \frac{\bar{P}'_{C,n+1}}{R}\right)\left(-\frac{1}{R}\right) \tag{A.18b-2}$$

$$Y_{22} = \frac{\partial X_{22}}{\partial \bar{P}'_{C,n+1}} = 0 \tag{A.18b-3}$$

$$Y_{23} = \frac{\partial X_{23}}{\partial \bar{P}'_{C,n+1}} = -\frac{(\varrho_{n+1}-1)P'_{n+1}\sqrt{1 + \frac{\frac{3}{2}s_{ij,n+1}s_{ij,n+1}}{P'^2_{n+1}}}}{\left\{\bar{P}'_{C,n+1} - (\varrho_{n+1}-1)P'_{n+1}\sqrt{1 + \frac{\frac{3}{2}s_{ij,n+1}s_{ij,n+1}}{P'^2_{n+1}}}\right\}^2} \tag{A.18b-4}$$

$$\frac{\partial R_8}{\partial \Lambda_{n+1}} = 0 \tag{A.18c}$$

$$\frac{\partial R_8}{\partial P'_{n+1}} = -\frac{(X_1 + X_{21}X_{22}X_{23})Z_1 - X_1(Z_1 + X_{21}X_{22}Z_{23} + X_{21}Z_{22}X_{23} + Z_{21}X_{22}X_{23})}{(X_1 + X_{21}X_{22}X_{23})^2} \tag{A.18d}$$

where

$$Z_1 = \frac{\partial X_1}{\partial P'_{n+1}} = -\frac{M^4}{(R-1)^4}\bar{P}'_{C,n+1}\left\{\varrho_{n+1}\left(\frac{2-R}{R}\bar{P}'_{C,n+1} - \frac{\varrho_{n+1}P'_{n+1}}{R}\right) + \left(\varrho_{n+1}P'_{n+1} - \frac{\bar{P}'_{C,n+1}}{R}\right)\left(-\frac{\varrho_{n+1}}{R}\right)\right\} \quad \text{(A.18d-1)}$$

$$Z_{21} = \frac{\partial X_{21}}{\partial P'_{n+1}} = 2\frac{M^4}{(R-1)^4}\left(\varrho_{n+1}P'_{n+1} - \frac{\bar{P}'_{C,n+1}}{R}\right)\varrho_{n+1} \quad \text{(A.18d-2)}$$

$$Z_{22} = \frac{\partial X_{22}}{\partial P'_{n+1}} = hp_a m\frac{1}{P'_{n+1}}\left(\frac{MP'_{n+1}}{\sqrt{(3/2)s_{ij,n+1}s_{ij,n+1}}}\right)^m \quad \text{(A.18d-3)}$$

$$Z_{23} = \frac{\partial X_{23}}{\partial P'_{n+1}} = -\frac{\bar{P}'_{C,n+1}(\varrho_{n+1}-1)\left\{\sqrt{1+\frac{3s_{ij,n+1}s_{ij,n+1}}{2P'^2_{n+1}}} - \frac{\frac{3}{2}s_{ij,n+1}s_{ij,n+1}}{P'^2_{n+1}\sqrt{1+\frac{3s_{ij,n+1}s_{ij,n+1}}{2P'^2_{n+1}}}}\right\}}{\left\{\bar{P}'_{C,n+1} - (\varrho_{n+1}-1)P'_{n+1}\sqrt{1+\frac{3s_{ij,n+1}s_{ij,n+1}}{2P'^2_{n+1}}}\right\}^2} \quad \text{(A.18d-4)}$$

$$\frac{\partial R_8}{\partial s_{ij,n+1}} = -\frac{(X_1+X_{21}X_{22}X_{23})V_1 - X_1(V_1+X_{21}X_{22}V_{23}+X_{21}V_{22}X_{23}+V_{21}X_{22}X_{23})}{(X_1+X_{21}X_{22}X_{23})^2} \quad \text{(A.18e)}$$

where

$$V_1 = \frac{\partial X_1}{\partial s_{ij,n+1}} = 0 \quad \text{(A.18e-1)}$$

$$V_{21} = \frac{\partial X_{21}}{\partial s_{ij,n+1}} = \begin{cases} 3\varrho_{n+1}^2 s_{ij,n+1} & (i=j) \\ 6\varrho_{n+1}^2 s_{ij,n+1} & (i\neq j) \end{cases} \quad \text{(A.18e-2)}$$

$$V_{22} = \frac{\partial X_{22}}{\partial s_{ij,n+1}} = \begin{cases} -hp_a m\left(\frac{MP'_{n+1}}{\sqrt{(3/2)s_{ij,n+1}s_{ij,n+1}}}\right)^m \frac{s_{ij,n+1}}{s_{ij,n+1}s_{ij,n+1}} & (i=j) \\ -hp_a m\left(\frac{MP'_{n+1}}{\sqrt{(3/2)s_{ij,n+1}s_{ij,n+1}}}\right)^m \frac{2s_{ij,n+1}}{s_{ij,n+1}s_{ij,n+1}} & (i\neq j) \end{cases} \quad \text{(A.18e-3)}$$

$$V_{23} = \frac{\partial X_{23}}{\partial P'_{n+1}} = \begin{cases} \frac{\bar{P}'_{C,n+1}(\varrho_{n+1}-1)3s_{ij,n+1}}{2P'_{n+1}\sqrt{1+\frac{3s_{ij,n+1}s_{ij,n+1}}{2P'^2_{n+1}}}\left\{\bar{P}'_{C,n+1} - (\varrho_{n+1}-1)P'_{n+1}\sqrt{1+\frac{\frac{3}{2}s_{ij,n+1}s_{ij,n+1}}{P'^2_{n+1}}}\right\}^2} & (i=j) \\ \frac{\bar{P}'_{C,n+1}(\varrho_{n+1}-1)3s_{ij,n+1}}{P'_{n+1}\sqrt{1+\frac{3s_{ij,n+1}s_{ij,n+1}}{2P'^2_{n+1}}}\left\{\bar{P}'_{C,n+1} - (\varrho_{n+1}-1)P'_{n+1}\sqrt{1+\frac{\frac{3}{2}s_{ij,n+1}s_{ij,n+1}}{P'^2_{n+1}}}\right\}^2} & (i\neq j) \end{cases} \quad \text{(A.18e-4)}$$

$$\frac{\partial R_8}{\partial \varrho_{n+1}} = -\frac{(X_1+X_{21}X_{22}X_{23})W_1 - X_1(W_1+X_{21}X_{22}W_{23}+X_{21}W_{22}X_{23}+W_{21}X_{22}X_{23})}{(X_1+X_{21}X_{22}X_{23})^2} \tag{A.18f}$$

where

$$W_1 = \frac{\partial X_1}{\partial \varrho_{n+1}} = -\frac{M^4}{(R-1)^4}\left\{\bar{P}'_{C,n+1}P'_{n+1}\left(\frac{2-R}{R}\bar{P}'_{C,n+1} - \frac{\varrho_{n+1}P'_{n+1}}{R}\right) + \bar{P}'_{C,n+1}\left(\varrho_{n+1}P'_{n+1} - \frac{\bar{P}'_{C,n+1}}{R}\right)\left(-\frac{P'_{n+1}}{R}\right)\right\} \tag{A.18f-1}$$

$$W_{21} = \frac{\partial X_{21}}{\partial \varrho_{n+1}} = 2\frac{M^4}{(R-1)^4}\left(\varrho_{n+1}P'_{n+1} - \frac{\bar{P}'_{C,n+1}}{R}\right)P'_{n+1} + 3s_{ij,n+1}s_{ij,n+1}\varrho_{n+1} \tag{A.18f-2}$$

$$W_{22} = \frac{\partial X_{22}}{\partial \varrho_{n+1}} = 0 \tag{A.18f-3}$$

$$W_{23} = \frac{\partial X_{23}}{\partial \varrho_{n+1}} = -\frac{\bar{P}'_{C,n+1}P'_{n+1}\sqrt{1+\frac{\frac{3}{2}s_{ij,n+1}s_{ij,n+1}}{P'^2_{n+1}}}}{\left\{\bar{P}'_{C,n+1}-(\varrho_{n+1}-1)P'_{n+1}\sqrt{1+\frac{\frac{3}{2}s_{ij,n+1}s_{ij,n+1}}{P'^2_{n+1}}}\right\}^2} \tag{A.18f-4}$$

$$\frac{\partial R_8}{\partial k_{p,n+1}} = 0 \tag{A.18g}$$

(5) SOLVING FOR $\boldsymbol{T\delta U = -R}$

$$\delta \boldsymbol{U} = \left\{\delta\Delta\varepsilon^p_{p,n+1}, \delta\Delta e^p_{ij,n+1}, \delta\bar{P}'_{C,n+1}, \delta\Lambda_{n+1}, \delta P'_{n+1}, \delta s_{ij,n+1}, \delta\varrho_{n+1}, \delta k_{p,n+1}\right\}^T \tag{A.19}$$

(6) UPDATE OF SOLUTION VECTOR $\boldsymbol{U}$

$$\Delta\varepsilon^p_{p,n+1} = \Delta\varepsilon^p_{p,n+1} + \delta\Delta\varepsilon^p_{p,n+1}, \quad \Delta e^p_{ij,n+1} = \Delta e^p_{ij,n+1} + \delta\Delta e^p_{ij,n+1} \tag{A.20a}$$

$$\bar{P}'_{C,n+1} = \bar{P}'_{C,n+1} + \delta\bar{P}'_{C,n+1}, \quad \Lambda_{n+1} = \Lambda_{n+1} + \delta\Lambda_{n+1} \tag{A.20b}$$

$$P'_{n+1} = P'_{n+1} + \delta P'_{n+1}, \quad s_{ij,n+1} = s_{ij,n+1} + \delta s_{ij,n+1} \tag{A.20c}$$

$$\varrho_{n+1} = \varrho_{n+1} + \delta\varrho_{n+1}, \quad k_{p,n+1} = k_{p,n+1} + \delta k_{p,n+1} \tag{A.20d}$$

GO TO **(3)**

(7) FINAL STRESSES (CONVERGED SOLUTION)

$$\Delta\varepsilon^{p}_{p,n} = \Delta\varepsilon^{p}_{p,n+1}, \quad \Delta e^{p}_{ij,n} = \Delta e^{p}_{ij,n+1} \tag{A.21a}$$

$$\bar{P}'_{C,n} = \bar{P}'_{C,n+1}, \quad \Lambda_n = \Lambda_{n+1} \tag{A.21b}$$

$$P'_n = P'_{n+1}, \quad s_{ij,n} = s_{ij,n+1} \tag{A.21c}$$

$$\varrho_n = \varrho_{n+1}, \quad k_{p,n} = k_{p,n+1} \tag{A.21d}$$

END